Lecture Notes in Physics 875

Christian Beck *Editor*

# Clusters in Nuclei, Volume 3

Springer

# Lecture Notes in Physics

## Volume 875

For further volumes:
www.springer.com/series/5304

# The Lecture Notes in Physics

The series Lecture Notes in Physics (LNP), founded in 1969, reports new developments in physics research and teaching—quickly and informally, but with a high quality and the explicit aim to summarize and communicate current knowledge in an accessible way. Books published in this series are conceived as bridging material between advanced graduate textbooks and the forefront of research and to serve three purposes:

- to be a compact and modern up-to-date source of reference on a well-defined topic
- to serve as an accessible introduction to the field to postgraduate students and nonspecialist researchers from related areas
- to be a source of advanced teaching material for specialized seminars, courses and schools

Both monographs and multi-author volumes will be considered for publication. Edited volumes should, however, consist of a very limited number of contributions only. Proceedings will not be considered for LNP.

Volumes published in LNP are disseminated both in print and in electronic formats, the electronic archive being available at springerlink.com. The series content is indexed, abstracted and referenced by many abstracting and information services, bibliographic networks, subscription agencies, library networks, and consortia.

Proposals should be sent to a member of the Editorial Board, or directly to the managing editor at Springer:

Christian Caron
Springer Heidelberg
Physics Editorial Department I
Tiergartenstrasse 17
69121 Heidelberg/Germany
christian.caron@springer.com

Christian Beck
Editor

# Clusters in Nuclei, Volume 3

Springer

*Editor*
Christian Beck
Dept. de Recherches Subatomiques
Institut Pluridisciplinaire Hubert Curien
Strasbourg, France

ISSN 0075-8450 ISSN 1616-6361 (electronic)
Lecture Notes in Physics
ISBN 978-3-319-01076-2 ISBN 978-3-319-01077-9 (eBook)
DOI 10.1007/978-3-319-01077-9
Springer Cham Heidelberg New York Dordrecht London

Library of Congress Control Number: 2010932330

© Springer International Publishing Switzerland 2014
This work is subject to copyright. All rights are reserved by the Publisher, whether the whole or part of the material is concerned, specifically the rights of translation, reprinting, reuse of illustrations, recitation, broadcasting, reproduction on microfilms or in any other physical way, and transmission or information storage and retrieval, electronic adaptation, computer software, or by similar or dissimilar methodology now known or hereafter developed. Exempted from this legal reservation are brief excerpts in connection with reviews or scholarly analysis or material supplied specifically for the purpose of being entered and executed on a computer system, for exclusive use by the purchaser of the work. Duplication of this publication or parts thereof is permitted only under the provisions of the Copyright Law of the Publisher's location, in its current version, and permission for use must always be obtained from Springer. Permissions for use may be obtained through RightsLink at the Copyright Clearance Center. Violations are liable to prosecution under the respective Copyright Law.
The use of general descriptive names, registered names, trademarks, service marks, etc. in this publication does not imply, even in the absence of a specific statement, that such names are exempt from the relevant protective laws and regulations and therefore free for general use.
While the advice and information in this book are believed to be true and accurate at the date of publication, neither the authors nor the editors nor the publisher can accept any legal responsibility for any errors or omissions that may be made. The publisher makes no warranty, express or implied, with respect to the material contained herein.

Printed on acid-free paper

Springer is part of Springer Science+Business Media (www.springer.com)

*The third volume of the Series Lecture Notes in Physics "Clusters in Nuclei" is dedicated to the memory of Professor Marten Brenner (1926–2012) as well as to Professor V.V. Volkov for his 90th anniversary and to Professor D.M. Brink*

# Preface

This is the third volume in the series of *Lecture Notes in Physics* entitled “Clusters in Nuclei” based on the well known Cluster Conferences that have been running since decades, on two recent “State Of The Art in Nuclear Cluster Physics” Workshops, as well as on successfull Theoretical Winter Schools, tradionnally held on the Campus of the Université de Strasbourg, Strasbourg, France.

A great deal of research work has been accomplished in the field of alpha clustering and in cluster studies of light neutron-rich nuclei. The scope of this Series of lecture notes is to deepen our knowledge of the field of nuclear cluster physics which is one of the domains of heavy-ion nuclear physics facing the greatest challenges and opportunities.

The purpose of this third and last volume of *Lecture Notes in Physics* “Clusters in Nuclei”, is to promote the exchange of ideas and discuss new developments in “Clustering Phenomena in Nuclear Physics and Nuclear Astrophysics” from both the theoretical and experimental points of views. It is aimed to retain the pedagogical nature of our earlier Theoretical Winter Schools and should provide a helpful reference for young researchers entering the field and wishing to get a feel of contemporary research in a number of areas.

The various aspects of the main topics in this last volume of “Clusters in Nuclei” are divided into six chapters, each highlighting new ideas that have emerged in recent years:

- Faddeev Equation Approach for Three-Cluster Nuclear Reactions
- Electromagnetic Transitions as a Probe of Nuclear Clustering
- “Tomography” of the Cluster Structure of Light Nuclei via Relativistic Dissociation
- From Light to Hyper-heavy Molecules and Neutron-Star Crusts in a Dynamical Mean-Field Approach
- Covalent Binding on the Femtometer Scale: Nuclear Molecules
- Clusterization in Ternary Fission

The first chapter entitled *Faddeev Equation Approach for Three-Cluster Nuclear Reactions* by Deltuva, Fonseca and Lazauskas shows how well the formalism based on Faddeev-like equations is capable to describe nuclear three-cluster reactions, which include elastic, break-up and transfer channels. For the sake of pedagogy, the formalism is presented in two different techniques based on momentum space and configuration space representions explained in detail. Comparison with previous calculations based on approximate methods used in nuclear reaction theory is discussed.

The second chapter of Jenkins on *Electromagnetic Transitions as a Probe of Nuclear Clustering* investigates a number of cases where electromagnetic transitions can be used to further our understanding of clustering, from heavy-ion radiative capture to superdeformation in alpha-conjugate nuclei.

"*Tomography*" *of the Cluster Structure of Light Nuclei via Relativistic Dissociation* is deeply discussed in Chap. 3 by Zarubin to demonstrate the capabilities of relativistic nuclear physics for the development of the physics of nuclear clusters. Nuclear track emulsion is an effective technique for pilot studies to study the cluster dissociation of a wide variety of light relativistic nuclei within a common approach. Analysis of the peripheral interactions of relativistic isotopes of beryllium, boron, carbon and nitrogen, including radioactive ones, with nuclei of the emulsion composition, allows the clustering pattern to be presented for a whole family of light nuclei.

The Chap. 4 entitled *From Light to Hyper-Heavy Molecules in Dynamical Mean-Field Approach* by Simenel describes a microscopic approach for low-energy collisions between atomic nuclei is the time-dependent Hartree-Fock theory, providing a mean-field dynamics of the system. This approach and some of its extensions are used to predict the evolution of out-of-equilibrium nuclear systems. The formation of light molecules and the dynamics of $\alpha$-clustering are discussed. Di-nuclear systems formed in transfer, deep-inelastic, and quasi-fission reactions, as well as hyper-heavy molecules produced in reactions between actinides are also investigated. The formation and stability of structures in neutron star crusts are finally discussed.

von Oertzen and Milin are trying in Chap. 5 (*Covalent Binding on the Femtometer Scale: Nuclear Molecules*) to definitively demontrate that Nuclear molecules are objects having two or more individual clusters as centres with extra nucleons (usually neutrons) binding them. The clusters have to be strongly bound themselves, while they get bound into molecules due to the specific properties of the nucleus-nucleus potentials and exchange of nucleons. A large number of strongly deformed nuclear states in light nuclei with neutron excess have been experimentally identified in the last decades, and some of them have been associated with covalent structures, mainly via their grouping into rotational bands.

Finally, the last chapter *Clusterization in Ternary Fission* proposed by Kamanin and Pyatkov treats most of experimental findings of the new kind of ternary decay of low excited heavy nuclei called "collinear cluster tri-partition" due to the features of the effect observed namely decay partners fly away almost collinearly and at least one of them has magic nucleon composition. At the early stage of our work the process of "true ternary fission" (fission of the nucleus into three fragments of comparable masses) was considered to be undiscovered for low excited heavy nuclei.

Manifestations of new decay channel observed in the frame of different experimental approaches are discussed. Special attention is paid to the connection between conventional binary fission and ternary fission processes.

Each of the three volumes contains lectures covering a wide range of topics from nuclear cluster theory to experimental applications that have gained a renewed interest with available Radioactive Ion Beams facilities and modern detection techniques. We stress that the contributions in these volumes are not review articles and so are not meant to contain all the latest results or to provide an exhaustive coverage of the field but are written instead in the pedagogical style of graduate lectures and thus have a reasonable long ‘shelf life’.

The edition of this book could not have been possible without stimulous discussions with Profs. Greiner, Horiuchi, Schuck and Zagrebaev. Our appreciation goes to all our co-lectures for their valuable contributions. We acknowledge also all the referees for their comments on the Chapters that are included in this volume. I would like here to thank, more particularly, Prof. Poenaru for his constant helpful suggestions from the beginning to the end. Special thanks go Dr. Christian Caron and all the members of his Springer-Verlag team (in particular, Mrs Angela Schulze-Thomin, Gabriele Hakuba, and Donatas Akmanavičius) for their help, fruitful collaboration and continued support for this ongoing project.

Strasbourg, France Christian Beck
May 2013

# Contents

# Chapter 1
# Faddeev Equation Approach for Three-Cluster Nuclear Reactions

**A. Deltuva, A.C. Fonseca, and R. Lazauskas**

## 1.1 Introduction

Nuclear collision experiments, performed at ion accelerators, are a very powerful tool to study nuclear properties at low and intermediate energies. In order to interpret accumulated experimental data appropriate theoretical methods are necessary enabling the simultaneous description of the available elastic, rearrangement and breakup reactions.

Regardless of its importance, the theoretical description of quantum-mechanical collisions turns out to be one of the most complex and slowly advancing problems in theoretical physics. If during the last decade accurate solutions for the nuclear bound state problem became available, full solution of the scattering problem (containing elastic, rearrangement and breakup channels) remains limited to the three-body case.

The main difficulty is related to the fact that, unlike the bound state wave functions, scattering wave functions are not localized. In configuration space one is obliged to solve multidimensional differential equations with extremely complex boundary conditions; by formulating the quantum-mechanical scattering problem in momentum space one has to deal with non-trivial singularities in the kernel of multivariable integral equations.

A rigorous mathematical formulation of the quantum mechanical three-body problem in the framework of non relativistic dynamics has been introduced by Faddeev in the early sixties [1], in the context of the three-nucleon system with short range interactions. In momentum space these equations might be slightly modified

---

A. Deltuva · A.C. Fonseca
Centro de Física Nuclear da Universidade de Lisboa, 1649-003 Lisbon, Portugal

A. Deltuva
e-mail: deltuva@cii.fc.ul.pt

R. Lazauskas (✉)
IPHC, IN2P3-CNRS, Université Louis Pasteur, BP 28, 67037 Strasbourg Cedex 2, France
e-mail: rimantas.lazauskas@ires.in2p3.fr

C. Beck (ed.), *Clusters in Nuclei, Volume 3*, Lecture Notes in Physics 875,
DOI 10.1007/978-3-319-01077-9_1,

by formulating them in terms of three-particle transition operators that are smoother functions compared to the system wave functions. Such a modification was proposed by Alt, Grassberger, and Sandhas [2] (AGS).

Solutions of the AGS equations with short range interactions were readily obtained in the early seventies. As large computers became available progress followed leading, by the end eighties, to fully converged solutions of these equations for neutron-deuteron ($n$-$d$) elastic scattering and breakup using realistic short range nucleon-nucleon ($N$-$N$) interactions. Nevertheless the inclusion of the long range Coulomb force in momentum space calculations of proton-deuteron ($p$-$d$) elastic scattering and breakup with the same numerical reliability as calculations with short range interactions alone, only become possible in the last decade.

Significant progress has been achieved [3, 4] by developing the screening and renormalization procedure for the Coulomb interaction in momentum space using a smooth but at the same time sufficiently rapid screening. This technique permitted to extend the calculations to the systems of three-particles with arbitrary masses above the breakup threshold [5, 6].

However it has taken some time to formulate the appropriate boundary conditions in configuration space for the three-body problem [7–9] and even longer to reformulate the original Faddeev equations to allow the incorporation of long-range Coulomb like interactions [10, 11]. Rigorous solution of the three-body problem with short range interactions has been achieved just after these theoretical developments, both below and above breakup threshold. On the other hand the numerical solution for the three-body problem including charged particles above the three-particle breakup threshold has been achieved only recently. First it has been done by using approximate Merkuriev boundary conditions in configuration space [12]. Nevertheless this approach proved to be a rather complex task numerically, remaining unexplored beyond the $p$-$d$ scattering case, but not yet for the $p$-$d$ breakup.

Finally, very recently configuration space method based on complex scaling have been developed and applied for $p$-$d$ scattering [13]. This method allows to treat the scattering problem using very simple boundary conditions, equivalent to the ones employed to solve the bound-state problem.

The aim of this lecture is to present these two recently developed techniques, namely the momentum-space method based on screening and renormalization as well as the configuration-space complex scaling method. This lecture is structured as follows: the first part serves to introduce theoretical formalisms for momentum space and configuration space calculations; in the second part we present some selected calculations with an aim to test the performance and validity of the two presented methods.

## 1.2 Momentum-Space Description of Three-Particle Scattering

We describe the scattering process in a system of three-particles interacting via pairwise short-range potentials $v_\alpha$, $\alpha = 1, 2, 3$; we use the odd-man-out notation, that is, $v_1$ is the potential between particles 2 and 3. In the framework of nonrelativistic quantum mechanics the center-of-mass (*c.m.*) and the internal motion can be separated by introducing Jacobi momenta

$$\mathbf{p}_\alpha = \frac{m_\gamma \mathbf{k}_\beta - m_\beta \mathbf{k}_\gamma}{m_\beta + m_\gamma}, \tag{1.1}$$

$$\mathbf{q}_\alpha = \frac{m_\alpha(\mathbf{k}_\beta + \mathbf{k}_\gamma) - (m_\beta + m_\gamma)\mathbf{k}_\alpha}{m_\alpha + m_\beta + m_\gamma}, \tag{1.2}$$

with $(\alpha\beta\gamma)$ being cyclic permutations of (123); $\mathbf{k}_\alpha$ and $m_\alpha$ are the individual particle momenta and masses, respectively. The c.m. motion is free and in the following we consider only the internal motion; the corresponding kinetic energy operator is $H_0$ while the full Hamiltonian is

$$H = H_0 + \sum_{\alpha=1}^{3} v_\alpha. \tag{1.3}$$

### 1.2.1 Alt, Grassberger, and Sandhas Equations

We consider the particle $\alpha$ scattering from the pair $\alpha$ that is bound with energy $\varepsilon_\alpha$. The initial channel state $|b_\alpha \mathbf{q}_\alpha\rangle$ is the product of the bound state wave function $|b_\alpha\rangle$ for the pair $\alpha$ and a plane wave with the relative particle-pair $\alpha$ momentum $\mathbf{q}_\alpha$; the dependence on the discrete quantum numbers is suppressed in our notation. $|b_\alpha \mathbf{q}_\alpha\rangle$ is the eigenstate of the corresponding channel Hamiltonian $H_\alpha = H_0 + v_\alpha$ with the energy eigenvalue $E = \varepsilon_\alpha + q_\alpha^2/2M_\alpha$ where $M_\alpha$ is the particle-pair $\alpha$ reduced mass. The final channel state is the particle-pair state in the same or different configuration $|b_\beta \mathbf{q}_\beta\rangle$ in the case of elastic and rearrangement scattering or, in the case of breakup, it is the state of three free particles $|\mathbf{p}_\gamma \mathbf{q}_\gamma\rangle$ with the same energy $E = p_\gamma^2/2\mu_\gamma + q_\gamma^2/2M_\gamma$ and pair $\gamma$ reduced mass $\mu_\gamma$; any set of Jacobi momenta can be used equally well for the breakup state.

The stationary scattering states [14, 15] corresponding to the above channel states are eigenstates of the full Hamiltonian; they are obtained from the channel states using the full resolvent $G = (E + i0 - H)^{-1}$, i.e.,

$$|b_\alpha \mathbf{q}_\alpha\rangle^{(+)} = i0G|b_\alpha \mathbf{q}_\alpha\rangle, \tag{1.4}$$

$$|\mathbf{p}_\alpha \mathbf{q}_\alpha\rangle^{(+)} = i0G|\mathbf{p}_\alpha \mathbf{q}_\alpha\rangle. \tag{1.5}$$

The full resolvent $G$ may be decomposed into the channel resolvents $G_\beta = (E + i0 - H_\beta)^{-1}$ and/or free resolvent $G_0 = (E + i0 - H_0)^{-1}$ as

$$G = G_\beta + G_\beta \bar{v}_\beta G, \tag{1.6}$$

with $\beta = 0, 1, 2, 3$ and $\bar{v}_\beta = \sum_{\gamma=1}^{3} \bar{\delta}_{\beta\gamma} v_\gamma$ where $\bar{\delta}_{\beta\gamma} = 1 - \delta_{\beta\gamma}$. Furthermore, the channel resolvents

$$G_\beta = G_0 + G_0 T_\beta G_0, \tag{1.7}$$

can be related to the corresponding two-particle transition operators

$$T_\beta = v_\beta + v_\beta G_0 T_\beta, \tag{1.8}$$

embedded into three-particle Hilbert space. Using these definitions Eqs. (1.4) and (1.5) can be written as triads of Lippmann-Schwinger equations

$$|b_\alpha \mathbf{q}_\alpha\rangle^{(+)} = \delta_{\beta\alpha} |b_\alpha \mathbf{q}_\alpha\rangle + G_\beta \bar{v}_\beta |b_\alpha \mathbf{q}_\alpha\rangle^{(+)}, \tag{1.9}$$

$$|\mathbf{p}_\alpha \mathbf{q}_\alpha\rangle^{(+)} = (1 + G_0 T_\beta)|\mathbf{p}_\alpha \mathbf{q}_\alpha\rangle + G_\beta \bar{v}_\beta |\mathbf{p}_\alpha \mathbf{q}_\alpha\rangle^{(+)}, \tag{1.10}$$

with $\alpha$ being fixed and $\beta = 1, 2, 3$; they are necessary and sufficient to define the states $|b_\alpha \mathbf{q}_\alpha\rangle^{(+)}$ and $|\mathbf{p}_\alpha \mathbf{q}_\alpha\rangle^{(+)}$ uniquely. However, in scattering problems it may be more convenient to work with the multichannel transition operators $U_{\beta\alpha}$ defined such that their on-shell elements yield scattering amplitudes, i.e.,

$$U_{\beta\alpha} |b_\alpha \mathbf{q}_\alpha\rangle = \bar{v}_\beta |b_\alpha \mathbf{q}_\alpha\rangle^{(+)}. \tag{1.11}$$

Our calculations are based on the AGS version [2] of three-particle scattering theory. In accordance with Eq. (1.11) it defines the multichannel transition operators $U_{\beta\alpha}$ by the decomposition of the full resolvent $G$ into channel and/or free resolvents as

$$G = \delta_{\beta\alpha} G_\alpha + G_\beta U_{\beta\alpha} G_\alpha. \tag{1.12}$$

The multichannel transition operators $U_{\beta\alpha}$ with fixed $\alpha$ and $\beta = 1, 2, 3$ are solutions of three coupled integral equations

$$U_{\beta\alpha} = \bar{\delta}_{\beta\alpha} G_0^{-1} + \sum_{\gamma=1}^{3} \bar{\delta}_{\beta\gamma} T_\gamma G_0 U_{\gamma\alpha}. \tag{1.13}$$

The transition matrix $U_{0\alpha}$ to final states with three free particles can be obtained from the solutions of Eq. (1.13) by quadrature, i.e.,

$$U_{0\alpha} = G_0^{-1} + \sum_{\gamma=1}^{3} T_\gamma G_0 U_{\gamma\alpha}. \tag{1.14}$$

The on-shell matrix elements $\langle b_\beta \mathbf{q}'_\beta | U_{\beta\alpha} | b_\alpha \mathbf{q}_\alpha\rangle$ are amplitudes (up to a factor) for elastic ($\beta = \alpha$) and rearrangement ($\beta \neq \alpha$) scattering. For example, the differential cross section for the $\alpha + (\beta\gamma) \to \beta + (\gamma\alpha)$ reaction in the c.m. system is given by

$$\frac{d\sigma_{\alpha\to\beta}}{d\Omega_\beta} = (2\pi)^4 M_\alpha M_\beta \frac{q'_\beta}{q_\alpha} \left|\langle b_\beta \mathbf{q}'_\beta \middle| U_{\beta\alpha} \middle| b_\alpha \mathbf{q}_\alpha\rangle\right|^2. \tag{1.15}$$

The cross section for the breakup is determined by the on-shell matrix elements $\langle \mathbf{p}'_\gamma \mathbf{q}'_\gamma | U_{0\alpha} | b_\alpha \mathbf{q}_\alpha \rangle$. Thus, in the AGS framework all elastic, rearrangement, and breakup reactions are calculated on the same footing.

Finally we note that the AGS equations can be extended to include also the three-body forces as done in Ref. [16].

### *1.2.2 Inclusion of the Coulomb Interaction*

The Coulomb potential $w_C$, due to its long range, does not satisfy the mathematical properties required for the formulation of standard scattering theory as given in the previous subsection for short-range interactions $v_\alpha$. However, in nature the Coulomb potential is always screened at large distances. The comparison of the data from typical nuclear physics experiments and theoretical predictions with full Coulomb is meaningful only if the full and screened Coulomb become physically indistinguishable. This was proved in Refs. [17, 18] where the screening and renormalization method for the scattering of two charged particles was proposed. We base our treatment of the Coulomb interaction on that idea.

Although we use momentum-space framework, we first choose the screened Coulomb potential in configuration-space representation as

$$w_R(r) = w_C(r) e^{-(r/R)^n}, \tag{1.16}$$

and then transform it to momentum-space. Here $R$ is the screening radius and $n$ controls the smoothness of the screening. The standard scattering theory is formally applicable to the screened Coulomb potential $w_R$, i.e., the Lippmann-Schwinger equation yields the two-particle transition matrix

$$t_R = w_R + w_R g_0 t_R, \tag{1.17}$$

where $g_0$ is the two-particle free resolvent. It was proven in Ref. [17] that in the limit of infinite screening radius $R$ the on-shell screened Coulomb transition matrix (screened Coulomb scattering amplitude) $\langle \mathbf{p}' | t_R | \mathbf{p} \rangle$ with $p' = p$, renormalized by an infinitely oscillating phase factor $z_R^{-1}(p) = e^{2i\phi_R(p)}$, approaches the full Coulomb amplitude $\langle \mathbf{p}' | t_C | \mathbf{p} \rangle$ in general as a distribution. The convergence in the sense of distributions is sufficient for the description of physical observables in a real experiment where the incoming beam is not a plane wave but wave packet and therefore the cross section is determined not directly by the scattering amplitude but by the outgoing wave packet, i.e., by the scattering amplitude averaged over the initial state physical wave packet. In practical calculations [3, 19] this averaging is carried out implicitly, replacing the renormalized screened Coulomb amplitude in the $R \to \infty$ limit by the full one, i.e.,

$$\lim_{R\to\infty} z_R^{-1}(p) \langle \mathbf{p}' | t_R | \mathbf{p} \rangle \to \langle \mathbf{p}' | t_C | \mathbf{p} \rangle. \tag{1.18}$$

Since $z_R^{-1}(p)$ is only a phase factor, the above relations indeed demonstrate that the physical observables become insensitive to screening provided it takes place at sufficiently large distances $R$ and, in the $R \to \infty$ limit, coincide with the corresponding quantities referring to the full Coulomb. Furthermore, renormalization by $z_R^{-\frac{1}{2}}(p_i)$ in the $R \to \infty$ limit relates also the screened and full Coulomb wave functions [20], i.e.,

$$\lim_{R\to\infty}(1+g_0 t_R)|\mathbf{p}\rangle z_R^{-\frac{1}{2}}(p) = \big|\psi_C^{(+)}(\mathbf{p})\big\rangle. \tag{1.19}$$

The screening and renormalization method based on the above relations can be extended to more complicated systems, albeit with some limitations. We consider the system of three-particles with charges $z_\alpha$ of equal sign interacting via pairwise strong short-range and screened Coulomb potentials $v_\alpha + w_{\alpha R}$ with $\alpha$ being 1, 2, or 3. The corresponding two-particle transition matrices are calculated with the full channel interaction

$$T_\alpha^{(R)} = (v_\alpha + w_{\alpha R}) + (v_\alpha + w_{\alpha R}) G_0 T_\alpha^{(R)}, \tag{1.20}$$

and the multichannel transition operators $U_{\beta\alpha}^{(R)}$ for elastic and rearrangement scattering are solutions of the AGS equation

$$U_{\beta\alpha}^{(R)} = \bar{\delta}_{\beta\alpha} G_0^{-1} + \sum_{\gamma=1}^{3} \bar{\delta}_{\beta\gamma} T_\gamma^{(R)} G_0 U_{\gamma\alpha}^{(R)}; \tag{1.21}$$

all operators depend parametrically on the Coulomb screening radius $R$.

In order to isolate the screened Coulomb contributions to the transition amplitude that diverge in the infinite $R$ limit we introduce an auxiliary screened Coulomb potential $W_{\alpha R}^{c.m.}$ between the particle $\alpha$ and the center of mass (*c.m.*) of the remaining pair. The same screening function has to be used for both Coulomb potentials $w_{\alpha R}$ and $W_{\alpha R}^{c.m.}$. The corresponding transition matrix

$$T_{\alpha R}^{c.m.} = W_{\alpha R}^{c.m.} + W_{\alpha R}^{c.m.} G_\alpha^{(R)} T_{\alpha R}^{c.m.}, \tag{1.22}$$

with $G_\alpha^{(R)} = (E + i0 - H_0 - v_\alpha - w_{\alpha R})^{-1}$ is a two-body-like operator and therefore its on-shell and half-shell behavior in the limit $R \to \infty$ is given by Eqs. (1.18) and (1.19). As derived in Ref. [3], the three-particle transition operators may be decomposed as

$$U_{\beta\alpha}^{(R)} = \delta_{\beta\alpha} T_{\alpha R}^{c.m.} + \big[1 + T_{\beta R}^{c.m.} G_\beta^{(R)}\big] \tilde{U}_{\beta\alpha}^{(R)} \big[1 + G_\alpha^{(R)} T_{\alpha R}^{c.m.}\big] \tag{1.23}$$

$$= \delta_{\beta\alpha} T_{\alpha R}^{c.m.} + \big(U_{\beta\alpha}^{(R)} - \delta_{\beta\alpha} T_{\alpha R}^{c.m.}\big). \tag{1.24}$$

where the auxiliary operator $\tilde{U}_{\beta\alpha}^{(R)}$ is of short range when calculated between on-shell screened Coulomb states. Thus, the three-particle transition operator $U_{\beta\alpha}^{(R)}$ has a long-range part $\delta_{\beta\alpha} T^{c.m.}_{\alpha R}$ whereas the remainder $U^{(R)}_{\beta\alpha} - \delta_{\beta\alpha} T^{c.m.}_{\alpha R}$ is a short-range operator that is externally distorted due to the screened Coulomb waves generated by $[1 + G^{(R)}_{\alpha} T^{c.m.}_{\alpha R}]$. On-shell, both parts do not have a proper limit as $R \to \infty$ but the limit exists after renormalization by an appropriate phase factor, yielding the transition amplitude for full Coulomb

$$\begin{aligned} \langle b_\beta \mathbf{q}'_\beta \big| U^{(C)}_{\beta\alpha} |b_\alpha \mathbf{q}_\alpha\rangle &= \delta_{\beta\alpha} \langle b_\alpha \mathbf{q}'_\beta \big| T^{c.m.}_{\alpha C} |b_\alpha \mathbf{q}_\alpha\rangle \\ &\quad + \lim_{R\to\infty} \big[ Z^{-\frac{1}{2}}_{\beta R}(q'_\beta) \langle b_\beta \mathbf{q}'_\beta \big| \big(U^{(R)}_{\beta\alpha} - \delta_{\beta\alpha} T^{c.m.}_{\alpha R}\big) |b_\alpha \mathbf{q}_\alpha\rangle Z^{-\frac{1}{2}}_{\alpha R}(q_\alpha)\big]. \end{aligned} \tag{1.25}$$

The first term on the right-hand side of Eq. (1.25) is known analytically [17]; it corresponds to the particle-pair $\alpha$ full Coulomb transition amplitude that results from the implicit renormalization of $T^{c.m.}_{\alpha R}$ according to Eq. (1.18). The $R \to \infty$ limit for the remaining part $(U^{(R)}_{\beta\alpha} - \delta_{\beta\alpha} T^{c.m.}_{\alpha R})$ of the multichannel transition matrix is performed numerically; due to the short-range nature of this term the convergence with the increasing screening radius $R$ is fast and the limit is reached with sufficient accuracy at finite $R$; furthermore, it can be calculated using the partial-wave expansion. We emphasize that Eq. (1.25) is by no means an approximation since it is based on the obviously exact identity (1.24) where the $R \to \infty$ limit for each term exists and is calculated separately.

The renormalization factor for $R \to \infty$ is a diverging phase factor

$$Z_{\alpha R}(q_\alpha) = e^{-2i\Phi_{\alpha R}(q_\alpha)}, \tag{1.26}$$

where $\Phi_{\alpha R}(q_\alpha)$, though independent of the particle-pair relative angular momentum $l_\alpha$ in the infinite $R$ limit, may be realized by

$$\Phi_{\alpha R}(q_\alpha) = \sigma^\alpha_{l_\alpha}(q_\alpha) - \eta^\alpha_{l_\alpha R}(q_\alpha), \tag{1.27}$$

with the diverging screened Coulomb phase shift $\eta^\alpha_{l_\alpha R}(q_\alpha)$ corresponding to standard boundary conditions and the proper Coulomb one $\sigma^\alpha_{l_\alpha}(q_\alpha)$ referring to the logarithmically distorted proper Coulomb boundary conditions. For the screened Coulomb potential of Eq. (1.16) the infinite $R$ limit of $\Phi_{\alpha R}(q_\alpha)$ is known analytically,

$$\Phi_{\alpha R}(q_\alpha) = \mathcal{K}_\alpha(q_\alpha)\big[\ln(2q_\alpha R) - C/n\big], \tag{1.28}$$

where $C \approx 0.5772156649$ is the Euler number and $\mathcal{K}_\alpha(q_\alpha) = \alpha_{e.m.} z_\alpha \sum_\gamma \bar{\delta}_{\gamma\alpha} z_\gamma \times M_\alpha / q_\alpha$ is the Coulomb parameter with $\alpha_{e.m.} \approx 1/137$. The form of the renormalization phase $\Phi_{\alpha R}(q_\alpha)$ to be used in the actual calculations with finite screening radii $R$ is not unique, but the converged results show independence of the chosen form of $\Phi_{\alpha R}(q_\alpha)$.

For breakup reactions we follow a similar strategy. However, the proper three-body Coulomb wave function and its relation to the three-body screened Coulomb wave function is, in general, unknown. This prevents the application of the screening and renormalization method to the reactions involving three free charged particles (nucleons or nuclei) in the final state. However, in the system of two charged particles and a neutral one with $z_\rho = 0$, the final-state Coulomb distortion becomes again a two-body problem with the screened Coulomb transition matrix

$$T_{\rho R} = w_{\rho R} + w_{\rho R} G_0 T_{\rho R}. \tag{1.29}$$

This makes the channel $\rho$, corresponding to the correlated pair of charged particles, the most convenient choice for the description of the final breakup state. As shown in Ref. [4], the AGS breakup operator

$$U^{(R)}_{0\alpha} = G_0^{-1} + \sum_{\gamma=1}^{3} T^{(R)}_{\gamma} G_0 U^{(R)}_{\gamma\alpha}, \tag{1.30}$$

can be decomposed as

$$U^{(R)}_{0\alpha} = (1 + T_{\rho R} G_0) \tilde{U}^{(R)}_{0\alpha} \big(1 + G^{(R)}_{\alpha} T^{c.m.}_{\alpha R}\big), \tag{1.31}$$

where the reduced operator $\tilde{U}^{(R)}_{0\alpha}(Z)$ calculated between screened Coulomb distorted initial and final states is of finite range. In the full breakup operator $U^{(R)}_{0\alpha}(Z)$ the external distortions show up in screened Coulomb waves generated by $(1 + G^{(R)}_{\alpha} T^{c.m.}_{\alpha R})$ in the initial state and by $(1 + T_{\rho R} G_0)$ in the final state; both wave functions do not have proper limits as $R \to \infty$. Therefore the full breakup transition amplitude in the case of the unscreened Coulomb potential is obtained via the renormalization of the on-shell breakup transition matrix $U^{(R)}_{0\alpha}$ in the infinite $R$ limit

$$\langle \mathbf{p}'_\rho \mathbf{q}'_\rho | U^{(C)}_{0\alpha} | b_\alpha \mathbf{q}_\alpha \rangle = \lim_{R\to\infty} \big[ z^{-\frac{1}{2}}_{\rho R}(p'_\rho) \langle \mathbf{p}'_\rho \mathbf{q}'_\rho | U^{(R)}_{0\alpha} | b_\alpha \mathbf{q}_\alpha \rangle Z^{-\frac{1}{2}}_{\alpha R}(q_\alpha) \big], \tag{1.32}$$

where $\mathbf{p}'_\rho$ is the relative momentum between the charged particles in the final state, $\mathbf{q}'_\rho$ the corresponding particle-pair relative momentum, and

$$z_{\rho R}\big(p'_\rho\big) = e^{-2i\kappa_\rho(p'_\rho)[\ln(2p'_\rho R) - C/n]}, \tag{1.33}$$

the final-state renormalization factor with the Coulomb parameter $\kappa_\rho(p'_\rho)$ for the pair $\rho$. The limit in Eq. (1.32) has to be performed numerically, but, due to the short-range nature of the breakup operator, the convergence with increasing screening radius $R$ is fast and the limit is reached with sufficient accuracy at finite $R$. Thus, to include the Coulomb interaction via the screening and renormalization method one only needs to solve standard scattering theory equations.

### *1.2.3 Practical Realization*

We calculate the short-range part of the elastic, rearrangement, and breakup scattering amplitudes (1.25) and (1.32) by solving standard scattering equations (1.21), (1.22), and (1.30) with a finite Coulomb screening radius $R$. We work in the momentum-space partial-wave basis [21], i.e., we use three sets $|p_\alpha q_\alpha \nu_\alpha\rangle \equiv |p_\alpha q_\alpha (l_\alpha\{[L_\alpha(s_\beta s_\gamma)S_\alpha]I_\alpha s_\alpha\}K_\alpha)JM\rangle$ with $(\alpha, \beta, \gamma)$ being cyclic permutations of $(1, 2, 3)$. Here $s_\alpha$ is the spin of particle $\alpha$, $L_\alpha$ and $l_\alpha$ are the orbital angular momenta associated with $p_\alpha$ and $q_\alpha$ respectively, whereas $S_\alpha$, $I_\alpha$, and $K_\alpha$ are intermediate angular momenta that are coupled to a total angular momentum $J$ with projection $M$. All discrete quantum numbers are abbreviated by $\nu_\alpha$. The integration over the momentum variables is discretized using Gaussian quadrature rules thereby converting a system of integral equations for each $J$ and parity $\Pi = (-)^{L_\alpha + l_\alpha}$ into a very large system of linear algebraic equations. Due to the huge dimension those linear systems cannot be solved directly. Instead we expand the AGS transition operators (1.21) into the corresponding Neumann series

$$U^{(R)}_{\beta\alpha} = \bar{\delta}_{\beta\alpha} G_0^{-1} + \sum_{\gamma=1}^{3} \bar{\delta}_{\beta\gamma} T^{(R)}_{\gamma} \bar{\delta}_{\gamma\alpha} + \sum_{\gamma=1}^{3} \bar{\delta}_{\beta\gamma} T^{(R)}_{\gamma} G_0 \sum_{\sigma=1}^{3} \bar{\delta}_{\gamma\sigma} T^{(R)}_{\sigma} \bar{\delta}_{\sigma\alpha} + \cdots , \tag{1.34}$$

that are summed up by the iterative Pade method [22]; it yields an accurate solution of Eq. (1.21) even when the Neumann series (1.34) diverges. Each two-particle transition operator $T^{(R)}_{\gamma}$ is evaluated in its proper basis $|p_\gamma q_\gamma \nu_\gamma\rangle$, thus, transformations between all three bases are needed. The calculation of the involved overlap functions $\langle p_\beta q_\beta \nu_\beta | p_\alpha q_\alpha \nu_\alpha\rangle$ follows closely the calculation of three-nucleon permutation operators discussed in Refs. [15, 21]. A special treatment [21, 22] is needed for the integrable singularities arising from the pair bound state poles in $T^{(R)}_{\gamma}$ and from $G_0$. Furthermore, we have to make sure that $R$ is large enough to achieve (after renormalization) the $R$-independence of the results up to a desired accuracy. However, those $R$ values are larger than the range of the nuclear interaction resulting in a slower convergence of the partial-wave expansion. As we found in Ref. [3], the practical success of the screening and renormalization method depends very much on the choice of the screening function, in our case on the power $n$ in Eq. (1.16). We want to ensure that the screened Coulomb potential $w_R$ approximates well the true Coulomb one $w_C$ for distances $r < R$ and simultaneously vanishes rapidly for $r > R$, providing a comparatively fast convergence of the partial-wave expansion. As shown in Ref. [3], this is not the case for simple exponential screening ($n = 1$) whereas the sharp cutoff ($n \to \infty$) yields slow oscillating convergence with the screening radius $R$. However, we found that values of $3 \le n \le 8$ provide a sufficiently smooth and rapid screening around $r = R$. The screening functions for different $n$ values are compared in Ref. [3] together with the results demonstrating the superiority of our optimal choice: using $3 \le n \le 8$ the convergence with the screening radius $R$, at which the short range part of the amplitudes was calculated, is fast enough such that the convergence of the partial-wave expansion, though being slower than for the nuclear interaction alone, can be achieved and there is no need to work in a plane-wave basis. Here we use $n = 4$ and show in Figs. 1.1 and 1.2 few examples for the $R$-convergence of the $\alpha$-deuteron scattering observables calculated in a three-body model $(\alpha, p, n)$; the nuclear interaction is taken from Ref. [5]. The

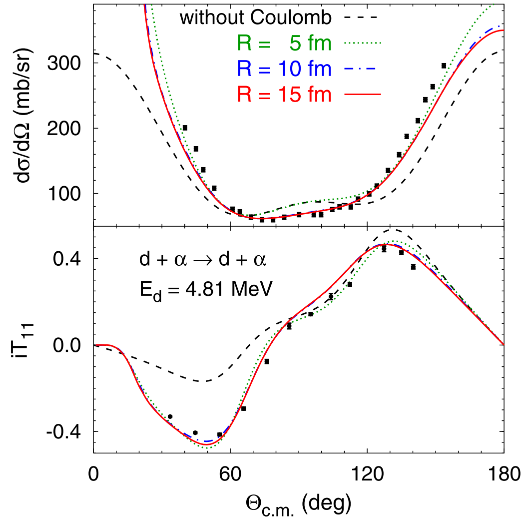

**Fig. 1.1** Differential cross section and deuteron vector analyzing power $iT_{11}$ of the $\alpha d$ elastic scattering at 4.81 MeV deuteron lab energy as functions of the c.m. scattering angle. Convergence with the screening radius $R$ used to calculate the short-range part of the amplitudes is studied: $R = 5$ fm (*dotted curves*), $R = 10$ fm (*dash-dotted curves*), and $R = 15$ fm (*solid curves*). Results without Coulomb are given by *dashed curves*. The experimental data are from Refs. [23, 24]

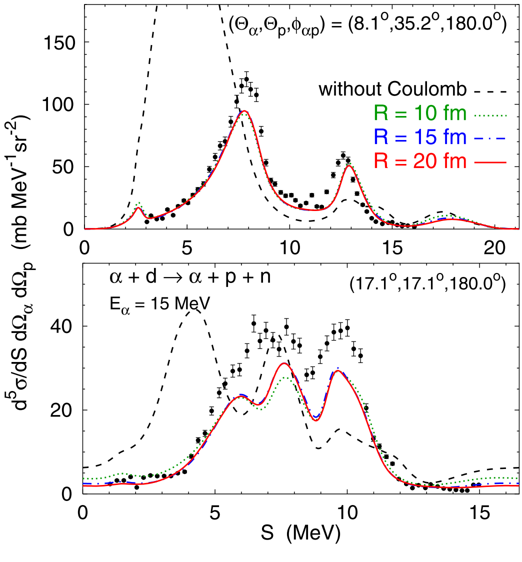

**Fig. 1.2** Fivefold differential cross section of the $\alpha d$ breakup reaction at 15 MeV $\alpha$ lab energy for several combinations of $\alpha$ and proton scattering angles as function of the final-state energy variable $S$ with $dS = (dE_\alpha^2 + dE_p^2)^{1/2}$. Convergence with the screening radius $R$ is studied: $R = 10$ fm (*dotted curves*), $R = 15$ fm (*dash-dotted curves*), and $R = 20$ fm (*solid curves*). Results without Coulomb are given by *dashed curves*. The experimental data are from Ref. [25]

convergence with $R$ is impressively fast for both $\alpha$-deuteron elastic scattering and breakup. In addition we note that the Coulomb effect is very large and clearly improves the description of the experimental data, especially for the differential cross section in $\alpha$-deuteron breakup reaction. This is due to the shift of the $\alpha p$ $P$-wave resonance position when the $\alpha p$ Coulomb repulsion is included that leads to the corresponding changes in the structure of the observables.

In addition to the internal reliability criterion of the screening and renormalization method—the convergence with $R$—we note that our results for proton-deuteron elastic scattering [26] agree well over a broad energy range with those of Ref. [27] obtained from the variational configuration-space solution of the three-nucleon Schrödinger equation with unscreened Coulomb potential and imposing the proper Coulomb boundary conditions explicitly.

## 1.3 Configuration Space

In contrast to the momentum-space representation, the Coulomb interaction has a trivial expression in configuration space and thus may seem to be easier to handle. However the major obstacle for configuration-space treatment of the scattering problem is related with the complexity of the wave function asymptotic structure, which strongly complicates once three-particle breakup is available. Although for short range interactions the analytical behavior of the breakup asymptote of the configuration space wave function is well established, this is not a case once long range interactions (like Coulomb) are present. Therefore a method which enables the scattering problem to be solved without explicit use of the wave function asymptotic form is of great importance. The complex scaling method has been proposed [28, 29] and successfully applied to calculate the resonance positions [30] by using bound state boundary conditions. As has been demonstrated recently this method can be extended also for the scattering problem [31, 32]. We demonstrate here that this method may be also successfully applied to solve three-particle scattering problems which include the long-range Coulomb interaction together with short range optical potentials.

### 1.3.1 Faddeev-Merkuriev Equations

Like in the momentum space formalism described above Jacobi coordinates are also used in configuration space to separate the center of mass of the three-particle system. One has three equivalent sets of three-particle Jacobi coordinates

$$
\begin{aligned}
\mathbf{x}_\alpha &= \sqrt{\frac{2m_\beta m_\gamma}{(m_\beta + m_\gamma)m}}(\mathbf{r}_\gamma - \mathbf{r}_\beta), \\
\mathbf{y}_\alpha &= \sqrt{\frac{2m_\beta(m_\beta + m_\gamma)}{(m_\alpha + m_\beta + m_\gamma)m}}\left(\mathbf{r}_\alpha - \frac{m_\beta \mathbf{r}_\beta + m_\gamma \mathbf{r}_\gamma}{m_\beta + m_\gamma}\right),
\end{aligned}
\tag{1.35}
$$

here $r_\alpha$ and $m_\alpha$ are individual particle position vectors and masses, respectively. The choice of a mass scale $m$ is arbitrary. The three-particle problem is formulated here using Faddeev-Merkuriev (FM) equations [10]:

$$
\left(E - H_0 - \sum_{\kappa=1}^{3} w_i^l\right)\psi_\alpha = \left(v_\alpha + w_\alpha^s\right)(\psi_\alpha + \psi_\beta + \psi_\gamma),
$$

$$\left(E - H_0 - \sum_{\kappa=1}^{3} w_i^l\right)\psi_\beta = \left(v_\beta + w_\beta^s\right)(\psi_\alpha + \psi_\beta + \psi_\gamma), \tag{1.36}$$

$$\left(E - H_0 - \sum_{\kappa=1}^{3} w_i^l\right)\psi_\gamma = \left(v_\gamma + w_\gamma^s\right)(\psi_\alpha + \psi_\beta + \psi_\gamma),$$

where the Coulomb interaction is split in two parts (short and long range), $w_\alpha = w_\alpha^s + w_\alpha^l$, by means of some arbitrary cut-off function $\chi_\alpha(x_\alpha, y_\alpha)$:

$$w_\alpha^s(x_\alpha, y_\alpha) = w_\alpha(x_\alpha)\chi_\alpha(x_\alpha, y_\alpha), \qquad w_\alpha^l(x_\alpha, y_\alpha) = w_\alpha(x_\alpha)\left[1 - \chi_\alpha(x_\alpha, y_\alpha)\right] \tag{1.37}$$

This cut-off function intends to shift the full Coulomb interaction in the $w_\alpha^s$ term if $x_\alpha$ is small, whereas the $w_\alpha^l$ term acquires the full Coulomb interaction if $x_\alpha$ becomes large and $y_\alpha < x_\alpha$. The practical choice of function $\chi_\alpha(x_\alpha, y_\alpha)$ has been proposed in [10]:

$$\chi_\alpha(x_\alpha, y_\alpha) = \frac{2}{[1 + \exp\left(\frac{[x_\alpha/x_0]^\mu}{1+y_\alpha/y_0}\right)]}, \tag{1.38}$$

with free parameters $x_0, y_0$ having size comparable with the charge radii of the respective binary systems; the value of parameter $\mu$ must be larger than 1 and is usually set $\mu \approx 2$. In such a way the so-called Faddeev amplitude $\psi_\alpha$ intends to acquire full asymptotic behavior of the binary $\alpha - (\beta\gamma)$ channels, i.e:

$$\begin{aligned}\psi_\alpha(\mathbf{x}_\alpha, \mathbf{y}_\alpha \to \infty) = \delta_{\kappa,\alpha}\psi_\alpha^{i_\kappa}(\mathbf{x}_\alpha)\phi_\alpha^{i_\kappa,in}(\mathbf{y}_\alpha) + \sum_{j_\alpha} f_{j_\alpha i_\kappa}(\mathbf{x}_\alpha.\mathbf{y}_\alpha)\psi_\alpha^{j_\alpha}(\mathbf{x}_\alpha)\phi_\alpha^{j_\alpha,out}(\mathbf{y}_\alpha)\\ + A_{i_\kappa}(\mathbf{x}_\alpha, \mathbf{y}_\alpha)\Phi_{i_\kappa}^{out}(\rho),\end{aligned} \tag{1.39}$$

where the hyperradius is $\rho = \sqrt{x_\alpha^2 + y_\alpha^2}$. An expression $\varphi_\alpha^{i_\alpha}(\mathbf{x}_\alpha)\phi_\alpha^{i_\kappa,in}(\mathbf{y}_\alpha)$ represents the incoming wave for particle $\alpha$ on pair $(\beta\gamma)$ in the bound state $i_\alpha$, with $\varphi_\alpha^{i_\alpha}(\mathbf{x}_\alpha)$ representing the normalized wave function of bound state $i_\alpha$. This wave function is a solution of the $(E - H_0 - w_\alpha - v_\alpha - W_\alpha^{c.m.})$ two-body Hamiltonian. The $\phi_\alpha^{j_\alpha,out}(\mathbf{y}_\alpha)$ and $\Phi_{i_\kappa}^{out}(\rho_\alpha)$ represent outgoing waves for binary and three-particle breakup channels respectively. In the asymptote, one has the following behavior:

$$\begin{aligned}\varphi_\alpha^{i_\alpha}(x_\alpha \to \infty) &\propto \exp(-k_{i_\alpha}x_\alpha),\\ \phi_\alpha^{i_\alpha,out}(y_\alpha \to \infty) &\propto \exp(iq_{i_\alpha}y_\alpha),\end{aligned} \tag{1.40}$$

$$\Phi_{i_\alpha}^{out}(\rho \to \infty) \propto \exp(iK\rho), \tag{1.41}$$

with $k_{i_\alpha} = \sqrt{-\varepsilon_{i_\alpha}m}$ representing momentum of 2-body bound state $i_\alpha$ with a negative binding energy $\varepsilon_{i_\alpha}$; $q_{i_\alpha} = \sqrt{(E - \varepsilon_{i_\alpha})m}$ is relative scattering momentum for the $\alpha - (\beta\gamma)$ binary channel, whereas $K = \sqrt{mE}$ is a three-particle breakup momentum (three-particle breakup is possible only if energy value $E$ is positive).

When considering particle's $\alpha$ scattering on the bound state $i_\alpha$ of the pair $(\beta\gamma)$, it is convenient to separate readily incoming wave $\psi_\alpha^{i_\alpha,in} = \psi_\alpha^{i_\alpha}(\mathbf{x}_\alpha)\phi_\alpha^{i_\alpha,in}(\mathbf{y}_\alpha)$, by introducing:

$$\begin{aligned} \psi_\alpha^{i_\alpha,out} &= \psi_\alpha^{i_\alpha} - \psi_\alpha^{i_\alpha}(\mathbf{x}_\alpha)\phi_\alpha^{i_\alpha,in}(\mathbf{y}_\alpha), \\ \psi_\beta^{i_\alpha,out} &= \psi_\beta^{i_\alpha} \quad \beta \neq \alpha, \end{aligned} \tag{1.42}$$

Then Faddeev-Merkuriev equations might be rewritten in a so-called driven form:

$$\begin{aligned} \left(E - H_0 - \sum_{\kappa=1}^{3} w_\kappa^l\right)\psi_\alpha^{out} &= \left(v_\alpha + w_\alpha^s\right)\left(\psi_\alpha^{out} + \psi_\beta^{out} + \psi_\gamma^{out}\right) \\ &\quad + \left[\sum_{\kappa=1}^{3} w_\kappa^l - w_\alpha - W_\alpha^{c.m.}\right]\psi_\alpha^{in}, \\ \left(E - H_0 - \sum_{\kappa=1}^{3} w_\kappa^l\right)\psi_\beta^{out} &= \left(v_\beta + w_\beta^s\right)\left(\psi_\alpha^{out} + \psi_\beta^{out} + \psi_\gamma^{out} + \psi_\alpha^{in}\right), \\ \left(E - H_0 - \sum_{\kappa=1}^{3} w_\kappa^l\right)\psi_\gamma^{out} &= \left(v_\gamma + w_\gamma^s\right)\left(\psi_\alpha^{out} + \psi_\beta^{out} + \psi_\gamma^{out} + \psi_\alpha^{in}\right). \end{aligned} \tag{1.43}$$

In this expression index of the incoming state $i_\alpha$ has been omitted in all Faddeev component expressions $\psi_\alpha^{in}$ and $\psi_\alpha^{out}$.

### 1.3.2 Complex Scaling

Next step is to perform the complex scaling operations i.e. scale all the distances $x$ and $y$ by a constant complex factor $e^{i\theta}$, so that both $\mathrm{Re}(e^{i\theta})$ and $\mathrm{Im}(e^{i\theta})$ are positive (angle $\theta$ must be chosen in the first quartet in order to satisfy this condition). The complex scaling operation, in particular, implies that the analytical continuation of the interaction potentials is performed: $v_\alpha(x_\alpha e^{i\theta})$ and $w_\alpha(x_\alpha e^{i\theta})$. Therefore the complex scaling method may be used only if these potentials are analytic. It is easy to see that the solutions of the complex scaled equations coincide with the ones obtained without complex scaling but to which the complex scaling operation is applied: $[\psi(x_\alpha, y_\alpha)]^{CS} = \psi(x_\alpha e^{i\theta}, y_\alpha e^{i\theta})$.

Namely, it is easy to demonstrate that all the outgoing wave functions of Eq. (1.41) becomes exponentially bound after the complex scaling operation:

$$\begin{aligned} \left[\varphi_\alpha^{i_\alpha}(x_\alpha \to \infty)\right]^{CS} &\propto \exp(-k_{i_\alpha} x_\alpha \cos\theta), \\ \left[\phi_\alpha^{i_\alpha,out}(y_\alpha \to \infty)\right]^{CS} &\propto \exp(-q_{i_\alpha} y_\alpha \sin\theta), \\ \left[\varPhi_{i_\alpha}^{out}(\rho \to \infty)\right]^{CS} &\propto \exp(-K\rho \sin\theta). \end{aligned} \tag{1.44}$$

Nevertheless an incoming wave diverges in $y_\alpha$ after the complex scaling:

$$\left[\phi_\alpha^{i_\alpha,out}(y_\alpha \to \infty)\right]^{CS} \propto \exp(+q_{i_\alpha} y_\alpha \sin\theta). \tag{1.45}$$

However these terms appear only on the right hand sides of the driven Faddeev-Merkuriev equation (1.43) being pre-multiplied with the potential terms and under certain conditions they may vanish outside of some finite (resolution) domain $x_\alpha \in [0, x^{\max}]$ and $y_\alpha \in [0, y^{\max}]$. Let us consider the long range behavior of the term $[(v_\beta + w_\beta^s)\psi_\alpha^{in}]^{CS}$. Since the interaction terms $v_\beta$ and $w_\beta^s$ are of short range, the only region the former term might not converge is along $y_\beta$ axis in $(x_\beta, y_\beta)$ plane, i.e. for $x_\beta \ll y_\beta$. On the other hand $x_\alpha(\mathbf{x}_\beta, \mathbf{y}_\beta) \approx \sqrt{m_\gamma/(m_\gamma + m_\beta)}\sqrt{M/(m_\gamma + m_\alpha)}y_\beta$ and $y_\alpha(\mathbf{x}_\beta, \mathbf{y}_\beta) \approx \sqrt{m_\beta/(m_\gamma + m_\beta)}\sqrt{m_\alpha/(m_\gamma + m_\alpha)}y_\beta$ under condition $x_\beta \ll y_\beta$. Then one has:

$$\begin{aligned}\left[\left(v_\beta + w_\beta^s\right)\psi_\alpha^{i_\alpha,in}\right]^{CS}_{x_\beta \ll y_\beta} \propto \exp\Bigg(&-k_{i_\alpha}\sqrt{\frac{m_\gamma M}{(m_\gamma + m_\beta)(m_\gamma + m_\alpha)}}y_\beta \cos\theta \\ &+ q_{i_\alpha}\sqrt{\frac{m_\alpha m_\beta}{(m_\gamma + m_\beta)(m_\gamma + m_\alpha)}}y_\beta \sin\theta\Bigg).\end{aligned} \tag{1.46}$$

This term becomes bound to finite domain in $(x_\beta, y_\beta)$ plane, if condition:

$$\tan\theta < \sqrt{\frac{m_\gamma M}{m_\alpha m_\beta}}\frac{k_{i_\alpha}}{q_{i_\alpha}} = \sqrt{\frac{m_\gamma M}{m_\alpha m_\beta}}\sqrt{\frac{|B_{i_\alpha}|}{E + |B_{i_\alpha}|}}, \tag{1.47}$$

is satisfied. This implies that for rather large scattering energies $E$, above the break-up threshold, one is obliged to use rather small complex scaling parameter $\theta$ values.

The term $[\sum_{\kappa=1}^3 w_\kappa^l - w_\alpha - W_\alpha^{c.m.}]\psi_\alpha^{i_\alpha,in}$, in principle, is not exponentially bound after the complex scaling. It represents the higher order corrections to the residual Coulomb interaction between particle $\alpha$ and bound pair $(\beta\gamma)$. These corrections are weak $o(1/y^2)$ and might be neglected by suppressing this term close to the border of the resolution domain. Alternative possibility might be to use incoming wave functions, which account not only for the bare $\alpha - (\beta\gamma)$ Coulomb interaction but also takes into account higher order polarization corrections.

Extraction of the scattering observables is realized by employing Greens theorem. One might demonstrate that strong interaction amplitude for $\alpha - (\beta\gamma)$ collision is:

$$\begin{aligned}f_{j_\alpha i_\kappa}(\mathbf{x}_\alpha.\mathbf{y}_\alpha) = -\frac{m}{q_{j_\alpha}}\int\int &\left[\left(\psi_\alpha^{j_\alpha,in}\right)^*\right]^{CS}\left(\overline{v}_\alpha + \overline{w}_\alpha - W_\alpha^{c.m.}\right)^{CS} \\ &\times [\Psi_{i_\kappa}]^{CS} e^{6i\theta} d^3\mathbf{x}_i d^3\mathbf{y}_i,\end{aligned} \tag{1.48}$$

with $[\Psi_{i_\kappa}]^{CS} = [\psi_\alpha^{i_\kappa,out} + \psi_\beta^{i_\kappa,out} + \psi_\gamma^{i_\kappa,out} + \psi_\alpha^{i_\kappa,in}]^{CS}$ being the total wave function of the three-body system. In the last expression the term containing product of two incoming waves is slowest to converge. Even stronger constraint than Eq. (1.47) should be implied on complex scaling angle in order to make this term integrable on the finite domain. Nevertheless this term contains only the product of two-body wave functions and might be evaluated without using complex scaling prior to three-body solution. Then the appropriate form of the integral (1.48) to be used becomes:

$$\begin{aligned} f_{j_\alpha i_\kappa}(\mathbf{x}_\alpha.\mathbf{y}_\alpha) = & -\frac{m}{q_{j_\alpha}} \int\int \left[\left(\psi_\alpha^{j_\alpha,in}\right)^*\right]^{CS} \left(\overline{v}_\alpha + \overline{w}_\alpha - W_\alpha^{c.m.}\right)^{CS} \\ & \times \left[\Psi_{i_\kappa} - \psi_\alpha^{j_\alpha,in}\right]^{CS} e^{6i\theta} d^3\mathbf{x}_i d^3\mathbf{y}_i \\ & -\frac{m}{q_{j_\alpha}} \int\int \left(\psi_\alpha^{j_\alpha,in}\right)^* \left(\overline{v}_\alpha + \overline{w}_\alpha - W_\alpha^{c.m.}\right) \psi_\alpha^{j_\alpha,in} d^3\mathbf{x}_i d^3\mathbf{y}. \end{aligned} \tag{1.49}$$

## 1.4 Application to Three-Body Nuclear Reactions

The two methods presented in Sects. 1.2 and 1.3 were first applied to the proton-deuteron elastic scattering and breakup [3, 4, 13, 16]. The three-nucleon system is the only nuclear three-particle system that may be considered realistic in the sense that the interactions are given by high precision potentials valid over a broad energy range. Nevertheless, in the same way one considers the nucleon as a single particle by neglecting its inner quark structure, in a further approximation one can consider a cluster of nucleons (composite nucleus) to be a single particle that interacts with other nucleons or nuclei via effective potentials whose parameters are determined from the two-body data. A classical example is the $\alpha$ particle, a tightly bound four-nucleon cluster. As shown in Figs. 1.1 and 1.2 and in Ref. [5], the description of the $(\alpha, p, n)$ three-particle system with real potentials is quite successful at low energies but becomes less reliable with increasing energy where the inner structure of the $\alpha$ particle cannot be neglected anymore. At higher energies the nucleon-nucleus or nucleus-nucleus interactions are modeled by optical potentials (OP) that provide quite an accurate description of the considered two-body system in a given narrow energy range; these potentials are complex to account for the inelastic excitations not explicitly included in the model space. The methods based on Faddeev/AGS equations can be applied also in this case, however, the potentials within the pairs that are bound in the initial or final channel must remain real. The comparison of the two methods based on the AGS and FM equations will be performed in Sect. 1.4.1 for such an interaction model with OP.

In the past the description of three-body-like nuclear reactions involved a number of approximate methods that have been developed. Well-known examples are the distorted-wave Born approximation (DWBA), various adiabatic approaches [33], and continuum-discretized coupled-channels (CDCC) method [34]. Compared to them the present methods based on exact Faddeev or AGS equations, being more technically and numerically involved, have some disadvantages. Namely, their application in the present technical realization is so far limited to a system made of two nucleons and one heavier cluster. The reason is that the interaction between two heavier cluster involves very many angular momentum states and the partial-wave convergence cannot be achieved. The comparison between traditional nuclear reaction approaches and momentum-space Faddeev/AGS methods for various neutron + proton + nucleus systems are summarized in Sect. 1.4.2.

On the other hand, the Faddeev and AGS methods may be more flexible with respect to dynamic input and thereby allows to test novel aspects of the nuclear interaction not accessible with the traditional approaches. Few examples will be presented in Sect. 1.4.3.

### *1.4.1 Numerical Comparison of AGS and FM Methods*

As an example we consider the $n + p + {}^{12}\mathrm{C}$ system. For the $n$-$p$ interaction we use a realistic AV18 model [35] that accurately reproduces the available two-nucleon scattering data and deuteron binding energy. To study not only the $d + {}^{12}\mathrm{C}$ but also $p + {}^{13}\mathrm{C}$ scattering and transfer reactions we use a $n$-${}^{12}\mathrm{C}$ potential that is real in the ${}^2P_{\frac{1}{2}}$ partial wave and supports the ground state of ${}^{13}\mathrm{C}$ with 4.946 MeV binding energy; the parameters are taken from Ref. [36]. In all other partial waves we use the $n$-${}^{12}\mathrm{C}$ optical potential from Ref. [37] taken at half the deuteron energy in the $d + {}^{12}\mathrm{C}$ channel. The $p$-${}^{12}\mathrm{C}$ optical potential is also taken from Ref. [37], however, at the proton energy in the $p + {}^{13}\mathrm{C}$ channel. We admit that, depending on the reaction of interest, other choices of energies for OP may be more appropriate, however, the aim of the present study is comparison of the methods and not the description of the experimental data although the latter are also included in the plots.

We consider $d + {}^{12}\mathrm{C}$ scattering at 30 MeV deuteron lab energy and $p + {}^{13}\mathrm{C}$ scattering at 30.6 MeV proton lab energy; they correspond to the same energy in c.m. system. First we perform calculations by neglecting the $p$-${}^{12}\mathrm{C}$ Coulomb repulsion. One observes a perfect agreement between the AGS and FM methods. Indeed, the calculated S-matrix elements in each three-particle channel considered (calculations have been performed for total three-particle angular momentum states up to $J = 13$) agree within three digits. Scattering observables converge quite slowly with $J$ as different angular momentum state contributions cancel each other at large angles. Nevertheless, the results of the two methods are practically indistinguishable as demonstrated in Fig. 1.3 for $d + {}^{12}\mathrm{C}$ elastic scattering and transfer to $p + {}^{13}\mathrm{C}$.

Next we perform the full calculation including the $p$-${}^{12}\mathrm{C}$ Coulomb repulsion; we note that inside the nucleus the Coulomb potential is taken as the one of a uniformly charged sphere [5]. Once again we obtain good agreement between the AGS and FM methods. However, this time small variations up to the order of 1 % are observed when analyzing separate $S$-matrix elements, mostly in high angular momentum states. This leads to small differences in some scattering observables, e.g., differential cross sections for $d + {}^{12}\mathrm{C}$ elastic scattering (at large angles where the differential cross section is very small) and for the deuteron stripping reaction $d + {}^{12}\mathrm{C} \to p + {}^{13}\mathrm{C}$ shown in Fig. 1.4. The $p + {}^{13}\mathrm{C}$ elastic scattering observables presented in Fig. 1.5 converge faster with $J$. As a consequence, the results of the

**Fig. 1.3** Comparison of momentum- (*solid curves*) and configuration-space (*dashed-dotted curves*) results for the deuteron-$^{12}$C scattering at 30 MeV deuteron lab energy. Differential cross sections for elastic scattering and stripping are shown neglecting the Coulomb interaction

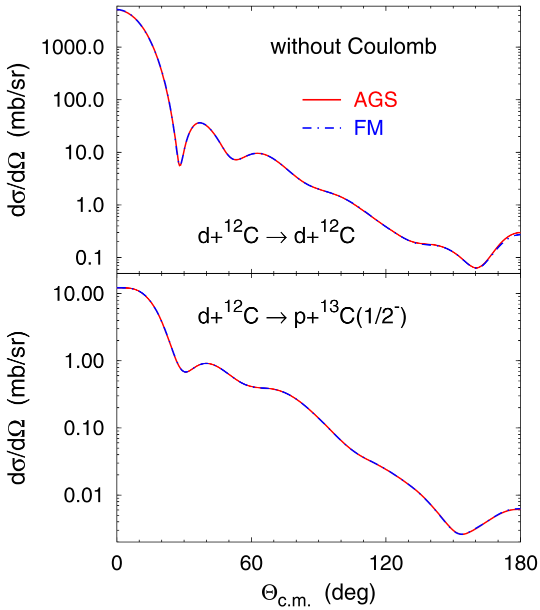

**Fig. 1.4** Comparison of momentum- (*solid curves*) and configuration-space (*dashed-dotted curves*) results for the deuteron-$^{12}$C scattering at 30 MeV deuteron lab energy. Differential cross sections for elastic scattering and stripping are shown, the former in ratio to the Rutherford cross section $d\sigma_R/d\Omega$. The experimental data are from Refs. [38, 39]

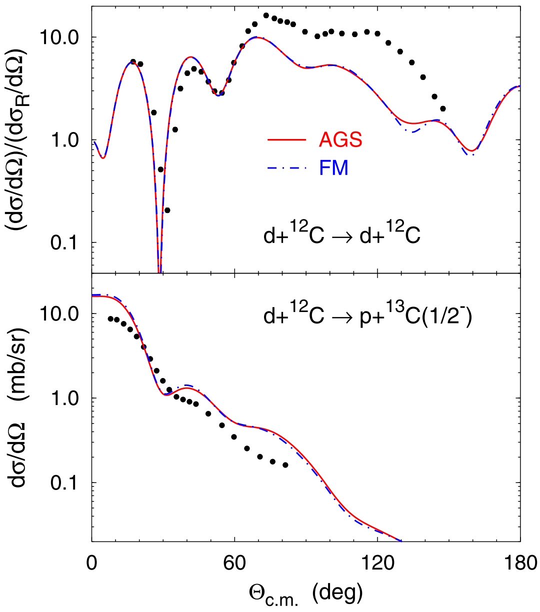

two calculations are indistinguishable for the $p + {}^{13}$C elastic cross section and only tiny differences can be seen for the proton analyzing power at large angles. In any case, the agreement between the AGS and FM methods exceeds both the accuracy

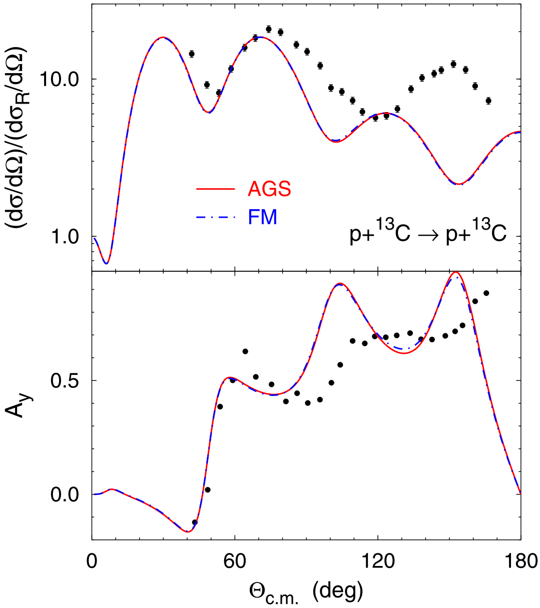

**Fig. 1.5** Comparison of momentum- (*solid curves*) and configuration-space (*dashed-dotted curves*) results for the proton-$^{13}$C elastic scattering at 30.6 MeV proton lab energy. Differential cross section divided by the Rutherford cross section and proton analyzing power are shown. The experimental data are from Ref. [40]

of the data and the existing discrepancies between theoretical predictions and experimental data.

### *1.4.2 Comparison with Traditional Nuclear Reaction Approaches*

The method based on the momentum-space AGS equations has already been used to test the accuracy of the traditional nuclear reaction approaches; limitations of their validity in energy and kinematic range have been established. The distorted-wave impulse approximation for breakup of a one-neutron halo nucleus $^{11}$Be on a proton target has been tested in Ref. [41] while the adiabatic-wave approximation for the deuteron stripping and pickup reactions $^{11}\mathrm{Be}(p,d)^{10}\mathrm{Be}$, $^{12}\mathrm{C}(d,p)^{13}\mathrm{C}$, and $^{48}\mathrm{Ca}(d,p)^{49}\mathrm{Ca}$ in Ref. [36]. However, one of the most sophisticated traditional approaches is the CDCC method [34]. A detailed comparison between CDCC and AGS results is performed in Ref. [6]. The agreement is good for deuteron-$^{12}$C and deuteron-$^{58}$Ni elastic scattering and breakup. In these cases nucleon-nucleus interactions were given by optical potentials; thus, there was no transfer reaction. A different situation takes place in proton-$^{11}$Be scattering where $^{11}$Be nucleus is assumed to be the bound state of a $^{10}$Be core plus a neutron. In this case, where the transfer channel $d + {}^{10}\mathrm{Be}$ is open, the CDCC approach lacks accuracy as shown in Ref. [6]. The semi-inclusive differential cross section for the breakup reaction $p + {}^{11}\mathrm{Be} \to p + n + {}^{10}\mathrm{Be}$ was calculated also using two CDCC versions where the full scattering wave function was expanded into the eigenstates of either the $n + {}^{10}\mathrm{Be}$

**Fig. 1.6** Semi-inclusive differential cross section for the breakup reaction $p + {}^{11}\text{Be} \to p + n + {}^{10}\text{Be}$ at lab energy of 38.4 MeV/nucleon. Results obtained with AGS and CDCC methods are compared

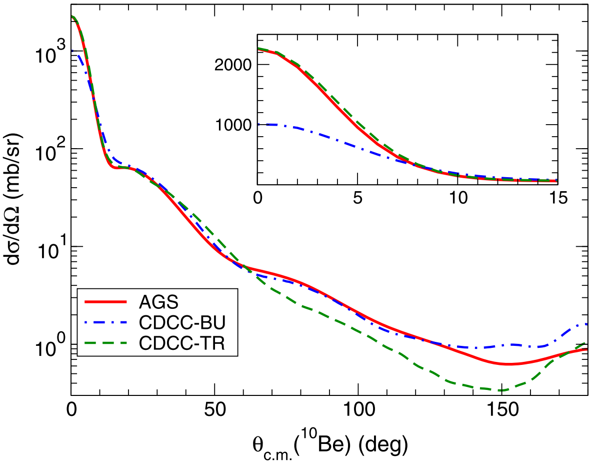

(CDCC-BU) or the $p + n$ (CDCC-TR) pair. Neither of them agrees well with AGS over the whole angular regime as shown in Fig. 1.6. It turns out that, depending on the ${}^{10}$Be scattering angle, the semi-inclusive breakup cross section is dominated by different mechanisms: at small angles it is the proton-neutron quasifree scattering whereas at intermediate and large angles it is the neutron-${}^{10}$Be $D$-wave resonance. However, a proper treatment of proton-neutron interaction in CDCC-BU and of neutron-${}^{10}$Be interaction in CDCC-TR is very hard to achieve since the wave function expansion uses eigenstates of a different pair. No such problem exists in the AGS method that uses simultaneously three sets of basis states and each pair is treated in its proper basis.

### *1.4.3 Beyond Standard Dynamic Models*

The standard nucleon-nucleus optical potentials employed in three-body calculations have central and, eventually, spin-orbit parts that are local. This local approximation yields a tremendous simplification in the practical realization of DWBA, CDCC and other traditional approaches that are based on configuration-space representations where the use of nonlocal optical potentials was never attempted. However, nonlocal optical potentials do not yield any serious technical difficulties in the momentum-space representation. Thus, they can be included quite easily in the AGS framework employed by us.

There are very few nonlocal parametrizations of the optical potentials available. We take the one from Refs. [42, 43] defined in the configuration space as

$$v_\gamma\big(\mathbf{r}', \mathbf{r}\big) = H_c(x)\big[V_c(y) + i\,W_c(y)\big] + 2\mathbf{S}_\gamma \cdot \mathbf{L}_\gamma H_s(x) V_s(y), \tag{1.50}$$

with $x = |\mathbf{r}' - \mathbf{r}|$ and $y = |\mathbf{r}' + \mathbf{r}|/2$. The central part has real volume and imaginary surface parts, whereas the spin-orbit part is real; all of them are expressed

**Fig. 1.7** Differential cross section for $(d, p)$ reaction on $^{16}O$ at 36 MeV deuteron lab energy leading to $^{17}O$ nucleus in the ground state $5/2^+$ (*top*) and first excited state $1/2^+$ (*bottom*). Predictions of nonlocal (*solid curve*) and local (*dashed curve*) optical potentials (OP) are compared with the experimental data from Ref. [45]

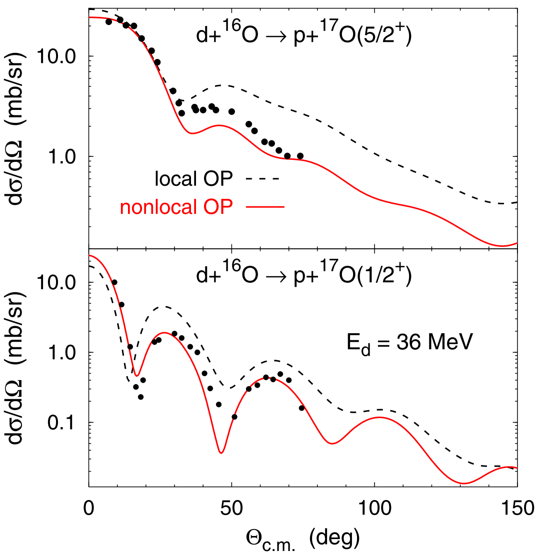

**Fig. 1.8** Differential cross section for $(d, p)$ reaction on $^{14}C$ at 14 MeV deuteron lab energy leading to one-neutron halo nucleus $^{15}C$ in the ground state $1/2^+$ (*top*) and first excited state $5/2^+$ (*bottom*). Curves as in Fig. 1.7 and the experimental data are from Ref. [46]

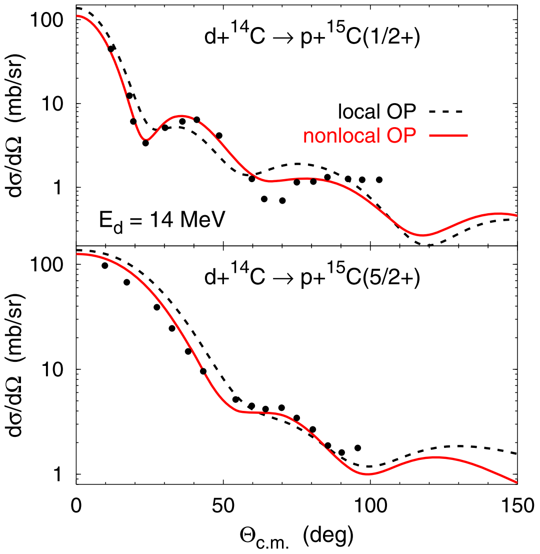

in the standard way by Woods-Saxon functions. Some of their strength parameters were readjusted in Ref. [44] to improve the description of the experimental nucleon-nucleus scattering data. The range of the nonlocality is determined by the functions $H_i(x) = (\pi\beta_i^2)^{-3/2} \exp(-x^2/\beta_i^2)$ with the parameters $\beta_i$ being of the order of 1 fm.

A detailed study of nonlocal optical potentials in three-body reactions involving stable as well as weakly bound nuclei, ranging from $^{10}$Be to $^{40}$Ca, is carried out in Ref. [44]. In order to isolate the nonlocality effect we also performed calculations with a local optical potential that provides approximately equivalent description of the nucleon-nucleus scattering at the considered energy. The nonlocality effect turns out to be very small in the elastic proton scattering from the bound neutron-nucleus system and of moderate size in the deuteron-nucleus scattering. However, the effect of nonlocal proton-nucleus optical potential becomes significant in deuteron stripping and pickup reactions $(d, p)$ and $(p, d)$; in most cases it considerably improves agreement with the experimental data. Examples for $(d, p)$ reactions leading to ground and excited states of the stable nucleus $^{17}$O and one-neutron halo nucleus $^{15}$C are presented in Figs. 1.7 and 1.8. We note that in these transfer reactions the proton-nucleus potential is taken at proton lab energy in the proton channel while the neutron-nucleus potential has to be real in order to support the respective bound states.

Another extension beyond the standard dynamic models includes the AGS method using energy-dependent optical potentials Although such calculations don't correspond to a rigorous Hamiltonian theory, they may shed some light on the shortcomings of the traditional nuclear interaction models. A detailed discussion of the calculations with energy-dependent optical potentials is given in Ref. [47].

## 1.5 Summary

We have presented the results of three-body Faddeev-type calculations for systems of three particles, two of which are charged, interacting through short-range nuclear plus the long-range Coulomb potentials. Realistic applications of three-body theory to three-cluster nuclear reactions—such as scattering of deuterons on a nuclear target or one-neutron halo nucleus impinging on a proton target—only became possible to address in recent years when a reliable and practical momentum-space treatment of the Coulomb interaction has been developed. After the extensive and very complete study of $p$-$d$ elastic scattering and breakup, the natural extension of these calculations was the application to complex reactions such as $d$-$^4$He, $p$-$^{17}$O, $^{11}$Be-$p$, $d$-$^{58}$Ni and many others using a realistic interaction such as AV18 between nucleons, and optical potentials chosen at the appropriate energy for the nucleon-nucleus interactions. The advantage of three-body calculations vis-à-vis traditional approximate reaction methods is that elastic, transfer, and breakup channels are treated on the same footing once the interaction Hamiltonian has been chosen. Another advantage of the three-body Faddeev-AGS approach is the possibility to include nonlocal optical potentials instead of local ones as commonly used in the standard nuclear reaction methods; as demonstrated, this leads to an improvement in the description of transfer reactions in a very consistent way across different energies and mass numbers for the core nucleus.

Although most three-body calculations have been performed in momentum space over a broad range of nuclei from $^4$He to $^{58}$Ni and have encompassed studies of cross sections and polarizations for elastic, transfer, charge exchange, and breakup reactions, coordinate space calculations above breakup threshold are coming to age using the complex scaling method. We have demonstrated here that both calculations agree to within a few percent for all the reactions we have calculated. This is a very promising development that may bring new light to the study of nuclear reactions given that the reduction of the many-body problem to an effective three-body one may be better implemented and understood by the community in coordinate space rather than in momentum space. On the other hand, compared to DWBA, adiabatic approaches, or CDCC, the Faddeev-type three-body methods are computationally more demanding and require greater technical expertise rendering them less attractive to analyze the data. Nevertheless, when benchmark calculations have been performed comparing the Faddeev-AGS results with those obtained using CDCC or adiabatic approaches, some discrepancies were found in transfer and breakup cross sections depending on the specific kinematic conditions. Therefore the Faddeev-AGS approach is imminent in order to calibrate and validate approximate nuclear reaction methods wherever a comparison is possible.

**Acknowledgements** The work of A.D. and A.C.F. was partially supported by the FCT grant PTDC/FIS/65736/2006. The work of R.L. was granted access to the HPC resources of IDRIS under the allocation 2009-i2009056006 made by GENCI (Grand Equipement National de Calcul Intensif). We thank the staff members of the IDRIS for their constant help.

## References

1. L.D. Faddeev, Zh. Eksp. Teor. Fiz. **39**, 1459 (1960) [Sov. Phys. JETP **12**, 1014 (1961)]
2. E.O. Alt, P. Grassberger, W. Sandhas, Nucl. Phys. B **2**, 167 (1967)
3. A. Deltuva, A.C. Fonseca, P.U. Sauer, Phys. Rev. C **71**, 054005 (2005)
4. A. Deltuva, A.C. Fonseca, P.U. Sauer, Phys. Rev. C **72**, 054004 (2005)
5. A. Deltuva, Phys. Rev. C **74**, 064001 (2006)
6. A. Deltuva, A.M. Moro, E. Cravo, F.M. Nunes, A.C. Fonseca, Phys. Rev. C **76**, 064602 (2007)
7. S.P. Merkuriev, Theor. Math. Phys. **8**, 798 (1971)
8. S.P. Merkuriev, Sov. J. Nucl. Phys. **19**, 22 (1974)
9. S.P. Merkuriev, C. Gignoux, A. Laverne, Ann. Phys. **99**, 30 (1976)
10. S.P. Merkuriev, Ann. Phys. (N.Y.) **130**, 395 (1980)
11. S.P. Merkuriev, Acta Phys. Austr. Suppl. **XXIII**, 65 (1981)
12. A. Kievsky, M. Viviani, S. Rosati, Phys. Rev. C **56**, 2987 (1997)
13. R. Lazauskas, J. Carbonell, Phys. Rev. C **84**, 034002 (2011)
14. E.W. Schmid, H. Ziegelmann, *The Quantum Mechanical Three-Body Problem* (Vieweg, Braunschweig, 1974)
15. W. Glöckle, *The Quantum Mechanical Few-Body Problem* (Springer, Berlin, 1983)
16. A. Deltuva, Phys. Rev. C **80**, 064002 (2009)
17. J.R. Taylor, Nuovo Cimento B **23**, 313 (1974)
18. M.D. Semon, J.R. Taylor, Nuovo Cimento A **26**, 48 (1975)
19. E.O. Alt, A.M. Mukhamedzhanov, M.M. Nishonov, A.I. Sattarov, Phys. Rev. C **65**, 064613 (2002)
20. V.G. Gorshkov, Sov. Phys. JETP **13**, 1037 (1961)
21. A. Deltuva, PhD thesis, University of Hanover (2003). http://edok01.tib.uni-hannover.de/edoks/e01dh03/374454701.pdf
22. K. Chmielewski, A. Deltuva, A.C. Fonseca, S. Nemoto, P.U. Sauer, Phys. Rev. C **67**, 014002 (2003)

23. M. Bruno, F. Cannata, M. D'Agostino, C. Maroni, M. Lombardi, Lett. Nuovo Cimento **27**, 265 (1980)
24. V. König, W. Grüebler, P.A. Schmelzbach, P. Marmier, Nucl. Phys. A **148**, 380 (1970)
25. I. Koersner, L. Glantz, A. Johansson, B. Sundqvist, H. Nakamura, H. Noya, Nucl. Phys. A **286**, 431 (1977)
26. A. Deltuva, A.C. Fonseca, A. Kievsky, S. Rosati, P.U. Sauer, M. Viviani, Phys. Rev. C **71**, 064003 (2005)
27. A. Kievsky, M. Viviani, S. Rosati, Phys. Rev. C **64**, 024002 (2001)
28. J. Nuttal, H.L. Cohen, Phys. Rev. **188**, 1542 (1969)
29. E. Balslev, J.M. Combes, Commun. Math. Phys. **22**, 280 (1971)
30. N. Moiseyev, Phys. Rep. **302**, 212 (1998)
31. C.W. McCurdy, M. Baertschy, T.N. Rescigno, J. Phys. B **373**, R137 (2004)
32. M.V. Volkov, N. Elander, E. Yarevsky, S.L. Yakovlev, Europhys. Lett. **85**, 30001 (2009)
33. R.C. Johnson, P.J.R. Soper, Phys. Rev. C **1**, 976 (1970)
34. N. Austern, Y. Iseri, M. Kamimura, M. Kawai, G. Rawitscher, M. Yahiro, Phys. Rep. **154**, 125 (1987)
35. R.B. Wiringa, V.G.J. Stoks, R. Schiavilla, Phys. Rev. C **51**, 38 (1995)
36. F.M. Nunes, A. Deltuva, Phys. Rev. C **84**, 034607 (2011)
37. R.L. Varner, W.J. Thompson, T.L. McAbee, E.J. Ludwig, T.B. Clegg, Phys. Rep. **201**, 57 (1991)
38. G. Perrin, N.V. Sen, J. Arvieux, R. Darves-Blanc, J. Durand, A. Fiore, J. Gondrand, F. Merchez, C. Perrin, Nucl. Phys. A **282**, 221 (1977)
39. H. Ohnuma et al., Nucl. Phys. A **448**, 205 (1986)
40. P.D. Greaves, V. Hnizdo, J. Lowe, O. Karban, Nucl. Phys. A **179**, 1 (1972)
41. R. Crespo, A. Deltuva, E. Cravo, M. Rodriguez-Gallardo, A.C. Fonseca, Phys. Rev. C **77**, 024601 (2008)
42. M.M. Giannini, G. Ricco, Ann. Phys. (N.Y.) **102**, 458 (1976)
43. M.M. Giannini, G. Ricco, A. Zucchiatti, Ann. Phys. (N.Y.) **124**, 208 (1980)
44. A. Deltuva, Phys. Rev. C **79**, 021602(R) (2009)
45. M.D. Cooper, W.F. Hornyak, P.G. Roos, Nucl. Phys. A **218**, 249 (1974)
46. J.D. Goss, P.L. Jolivette, C.P. Browne, S.E. Darden, H.R. Weller, R.A. Blue, Phys. Rev. C **12**, 1730 (1975)
47. A. Deltuva, A.C. Fonseca, Phys. Rev. C **79**, 014606 (2009)

# Chapter 2
# Electromagnetic Transitions as a Probe of Nuclear Clustering

**David G. Jenkins**

## 2.1 Introduction

Nuclear clustering was first suggested as an explanation for anomalous structure in the elastic and inelastic scattering of two $^{12}$C nuclei. This concept has latterly been extended to encompass all light alpha-conjugate nuclei, where bandheads for highly-deformed rotational structures are expected on or near the threshold energies for break-up into different alpha-cluster channels. Traditionally, such cluster states have often been identified on the basis of the position of resonances seen in fusion [1], (in)elastic scattering [2] and break-up reactions [3, 4]. Such states are then assigned to rotational bands, often with the aid of comparison to theoretical expectations. Clustering in nuclei has therefore often been the province of reaction studies but this approach is not without ambiguity, and runs the risk of over-enthusiastic interpretation of experimental data. The states observed may appear to follow a rotational pattern but it is not an obvious step to say that they share the same intrinsic configuration.

This chapter will stress the very important role that the observation of electromagnetic transitions between candidate cluster states or superdeformed states in light alpha-conjugate nuclei could play in securing the whole basis of the cluster model. Since clustering is generally associated with large intrinsic deformations, very enhanced *E2* transitions are expected between states in cluster bands. Moreover, different cluster configurations with large intrinsic deformations may also be connected by *E0* transitions between states of the same angular momentum. The strength of such transitions is related to the difference in the mean squared charge radius [5].

A second topic explored in this chapter will be the electromagnetic decay of cluster resonances into normal states. A very relevant example of this is heavy-ion

---

D.G. Jenkins (✉)
Department of Physics, University of York, York YO10 5DD, UK
e-mail: david.jenkins@york.ac.uk

C. Beck (ed.), *Clusters in Nuclei, Volume 3*, Lecture Notes in Physics 875,
DOI 10.1007/978-3-319-01077-9_2,

radiative capture. In all the cases considered here, the experimental challenges are strong and similar in character, and relate to the fact that:

- States with a strong cluster configuration are often particle-unbound and frequently lie at very high excitation energy. Phase space considerations dictate that electromagnetic branches in such cases will be small, and competition from break-up channels will be strong.
- The relevant transition energies are, in general, high (1 MeV and up) and so are challenging to measure with both high resolution and high efficiency.
- Cluster states, although unbound, are often "narrow", typically 100s of keV wide although in many cases this is most probably an instrumental width and not the true width.

## 2.2 Gamma-Ray Spectroscopy

The principal experimental methodology appropriate to these studies is $\gamma$-ray spectroscopy. This technique is discussed in Chap. 6 of Vol. 2 of this series by Papka and Beck, but it is worth reviewing some of the key aspects of such measurements again here, in terms of the relevant detection technology and some of the methods which can be used to extract important information on the states between which gamma decay takes place.

Gamma-ray spectroscopy supplies information on the energy of electromagnetic transitions, and their relative intensity. Analysis of coincidence data allows a level scheme to be constructed. For reactions where magnetic substate alignment is achieved, it is possible to use the angular distribution of gamma rays to extract the multipolarity of the transition. In addition, gamma-ray spectroscopy can be used to deduce transition strengths from lifetimes (corrected for particle-emission in the case of unbound states). In the case of light alpha-conjugate nuclei where typical lifetimes are in the order of femtoseconds, an appropriate technique is the fractional Doppler-shift technique comparing the reduced Doppler shift observed for transitions with a finite lifetime due to slowing in the target.

There are two principal classes of gamma-ray detector which may be used in the study of gamma rays associated with clustering, and both types have been used in the studies to be described here. The first class of detector employ inorganic scintillators. Such detectors have the advantage of a high intrinsic efficiency but at the expense of limited energy resolution. Typical scintillator materials include sodium iodide, barium fluoride, bismuth germinate (BGO) and caesium iodide. Scintillation light is produced by the interaction of gamma rays in the crystal, and is usually collected and amplified using a photomultiplier tube (PMT). The best resolution for scintillator detectors with conventional scintillator materials is around 6–7 % for 662-keV gamma rays obtained for sodium iodide detectors. Novel materials such as lanthanum bromide are now becoming available which can obtain a resolution below 3 %. The future prospects with such novel scintillators will be reviewed briefly at the end of this chapter.

The second type of detector relevant to gamma-ray spectroscopy are germanium detectors, of which the most modern type are hyper-pure germanium detectors. Such detectors are semiconductor-based and have an extremely high intrinsic energy resolution of the order of a few keV. In general, though, the efficiency of such detectors is considerably lower (typically an order of magnitude) than that achievable with a scintillator detector. The principal reason for this reduced efficiency is the general practice of surrounding germanium crystals with a high efficiency scintillator shield to veto Compton-scattered gamma rays. This ensures an excellent peak-to-total but means that only gamma rays which deposit all of their energy in the germanium crystal are accepted. The degradation in efficiency is energy dependent and is significantly worse for high-energy gamma rays. The next generation of germanium detector array, for example AGATA [6], dispenses with the veto shield and comprises a complete germanium shell. Gamma-ray interactions are then studied through tracking. This approach leads to significantly higher efficiency for detecting a single gamma ray, but orders of magnitude greater efficiency for detecting large multiplicities of gamma rays in coincidence. Such next generation arrays are yet to be applied to studies of nuclear clustering but the prospects are exciting.

## 2.3 Physics Examples

### *2.3.1 Molecular Transitions in* $^{8}$Be

An excellent test case for the cluster model is $^{8}$Be since the ground state is already suggested to be based on alpha-clustering [7, 8]. The unbound excited states built on this configuration have an energy spacing consistent with strong deformation (see Fig. 2.1). In recent years, increase in computer power has made it possible to perform *ab initio* calculations for light nuclei. In the case of $^{8}$Be, they point to a strong $\alpha$-$\alpha$ cluster configuration for its ground state (see Fig. 2.2) [9]. There are, therefore, competing descriptions of $^{8}$Be within very different model prescriptions.

A strong test of the competing models would be to measure the strength of the electromagnetic transitions connecting the states in the ground state band. Langanke and Rolfs have calculated the transition strength for $2^+ \rightarrow 0^+$ [10] and obtain $\Gamma_\gamma =$ 8.3 meV corresponding to a transition of 75 Wu. In a separate work, they calculated the $4^+ \rightarrow 2^+$ transition strength to be 19 Wu [11]. Despite the fact that the in-band transitions are "strong", the gamma branch is such a small fraction of the total width of the state, that it is extremely challenging to attempt to discriminate it. It turns out that the prospects are much more favourable for measuring the $4^+ \rightarrow 2^+$ transition than the $2^+ \rightarrow 0^+$ transition.

Datar et al. have carried out a "brute-force" determination of the $4^+ \rightarrow 2^+$ transition strength in an experiment at the Tata Institute for Fundamental Research in Mumbai [12]. The measurement comprised a coincidence between a detected gamma ray in an array of BGO detectors with alpha particles from the break-up of

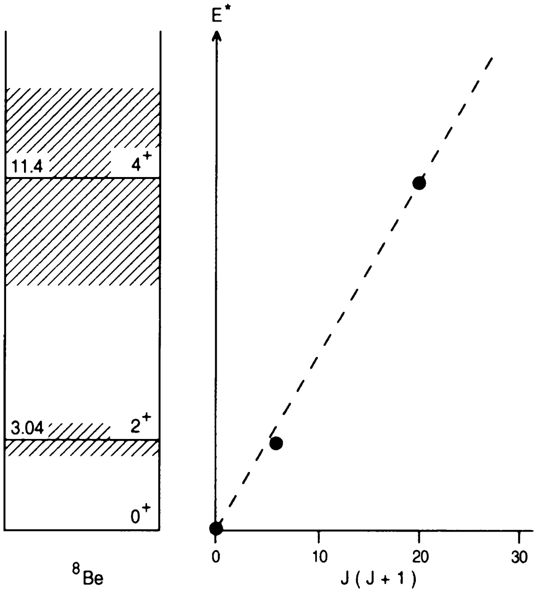

**Fig. 2.1** Level diagram for $^8$Be and excitation energy of states as a function of $J(J+1)$ (taken from [4])

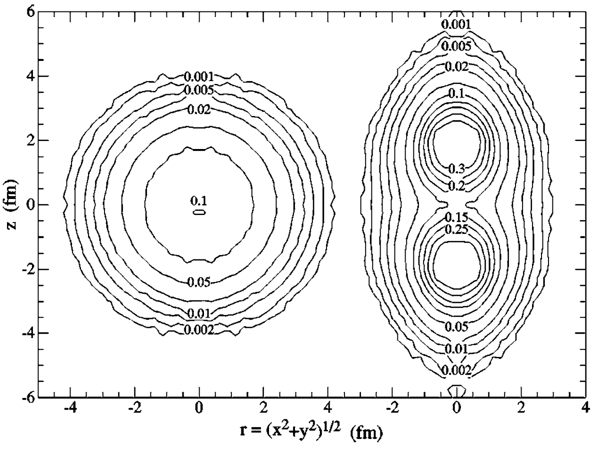

**Fig. 2.2** Contours of constant density for $^8$Be ground state in lab frame (*left*) and intrinsic frame (*right*) taken from Fig. 15 of [9]

the $2^+$ state in $^8$Be. The B(E2) value obtained is 25(8) $e^2\,fm^4$. This value is consistent with the predictions of both *ab initio* and cluster model calculations. The precision of the measurement, however, does not make it possible to discriminate between these two different models. Accordingly, Datar et al. have repeated their $^8$Be experiment in 2010 using superior silicon detectors with the aim of reducing the error bar on the B(E2) value in order to discriminate between different theoretical models. This data is under analysis at the time of writing.

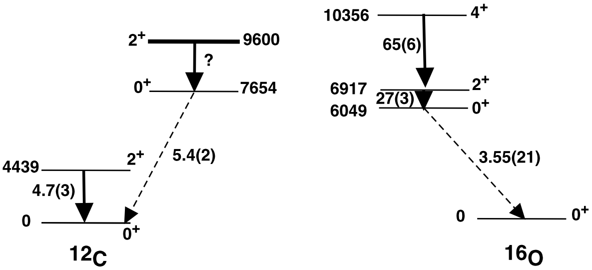

**Fig. 2.3** Selected positive parity states in $^{12}C$ and $^{16}O$. B(E2) values are given in Wu where known. The M(E0) transition strengths are given in $fm^2$

## *2.3.2 Alpha Clustering in $^{12}C$*

A long-discussed and spectacular example of a cluster state is the first-excited $0^+$ state in $^{12}C$. The existence of this state was first hypothesised by Hoyle as a means of explaining the formation of $^{12}C$ in massive stars [13] and latterly observed by Cook et al. [14] close to the triple-alpha threshold in $^{12}C$. The literature on the properties of this state alone is very extensive. The "Hoyle" state clearly has a very complex structure. A shell-model calculation cannot account for its existence but it does appear in various cluster models, and very recently was first described within an *ab initio* model [15]. Recently, Freer et al. [16] reported the possible existence of a $2^+$ state at 9.6(1) MeV in $^{12}C$ with a width of 600(100) keV (see Fig. 2.4). It is argued that this state corresponds to the first member of the rotational band built on the Hoyle state. Locating this state was extremely challenging as it sits underneath an extremely broad $0^+$ state at 10.3 MeV. In the context of the present discussion, the observation of an *E2* transition connecting this $2^+$ state to the $0^+$ "Hoyle" state and measuring its transition strength would be sensational as it would provide extremely important information regarding the nature of the "Hoyle" state. It would, however, be extremely difficult to realise as the gamma width might be expected to be of the order of $10^{-5}$ of the width of the state. A highly efficient particle-gamma experimental setup would be required. It is also not clear what would be the best choice of reaction to selectively populate the $2^+$ state while allowing for $\gamma$-ray detection. For completeness, it is worth mentioning that a deformed band is well known in $^{16}O$ (see Fig. 2.3), and has been described within the cluster model [17].

## *2.3.3 E0 Transitions*

As discussed in the introduction, *E0* transitions are commonly associated with a change in the nuclear radius and may therefore be a relevant observable in terms of nuclear clustering. The width for pair decay of the Hoyle state has recently been extracted from re-analysis of $^{12}C(e,e')$ data as $\Gamma_{\Pi} = (62.3 \pm 2.0)$ μeV which is around $10^{-6}$ of the total width of the state [18]. This corresponds to a monopole strength $M(E0) = 5.4(0.2)$ fm$^2$ (see Fig. 2.4), and exhausts about 7.5 % of the energy-weighted monopole sum rule. In $^{16}O$, the $M(E0)$ value between the ground state and the first and second excited $0^+$ states at $E_{ex} = 6.05$ MeV and 12.05 MeV which are proposed to have $^{12}\mathrm{C} + \alpha$ cluster structure are $3.55 \pm 0.21$ fm$^2$ and $4.03 \pm 0.09$ fm$^2$, respectively, which share about 3 % and 8 % of the energy weighted sum rule value.

At first glance, the large values for the *E0* transitions in these light nuclei are a surprise because the single-particle estimate might be assumed to be a strong overestimate given the very complex structure of the cluster state. Yamada et al. [19] have presented an example calculation for $^{12}$C which tries to account for the strong enhancement of the observed *E0* transition. They attribute it to an excitation of the $3\alpha$ degrees of freedom in the ground state, which then strongly populates the excited "Hoyle" state. These considerations suggest that further experimental investigations of *E0* transitions in alpha-conjugate may pose a strong challenge to theory and be supportive of the complex nature of these states.

## 2.4 $^{12}\mathrm{C} + {}^{12}\mathrm{C}$ Clustering

The clustering hypothesis was first introduced in the 1960s [20] to explain the anomalous behaviour seen in fusion [1] and elastic and inelastic scattering of two $^{12}$C nuclei [2]. Strong resonances were seen below the Coulomb barrier and persisting to the lowest energies considered. The resonances were explained in terms of the formation of short-lived $^{12}\mathrm{C} + {}^{12}\mathrm{C}$ molecules. This system remains the most studied so far as nuclear clustering is concerned and it has strong implications for other related fields such as nuclear astrophysics. The resonances, which persist down into the Gamow window, hinder our understanding of fusion rates in massive stars. In this chapter, we will review two aspects of $^{12}\mathrm{C} + {}^{12}\mathrm{C}$ clustering: the potential for observing transitions between cluster states, and the decay of cluster states into normal states (heavy-ion radiative capture).

### *2.4.1 Searching for Transitions Within* $^{12}\mathrm{C} + {}^{12}\mathrm{C}$ *Cluster Bands*

It is straightforward to access the cluster configuration in $^8$Be as it is expected to already be the configuration of the ground state. In heavier, alpha-conjugate nuclei, this is much more difficult as the cluster states lie at a high excitation energy beyond the particle-breakup thresholds. Nevertheless, a number of attempts have been made to observe transitions within cluster bands, in particular, $^{12}\mathrm{C} + {}^{12}\mathrm{C}$ configurations in $^{24}$Mg. The observation of such transitions would indeed be the "smoking gun" in favour of the molecular hypothesis. Several calculations exist for transition strengths within the $^{12}\mathrm{C} + {}^{12}\mathrm{C}$ cluster bands, for example those by Baye and Descouvemont within the GCM model [21]. Langanke and van Roosmalen [22] have also made such calculations and present predicted gamma widths for cluster states. A complication from the experimental perspective is that in reality the cluster states appear somewhat fragmented and there is often not a unique state of a given spin/parity but rather a number of close-lying resonances. McGrath et al. [23] looked speculatively for gamma transitions between $14^+$ and $12^+$ “gross structure” $^{12}C + {}^{12}C$ resonances. They did not search for the $\gamma$ ray directly but instead looked for evidence of such a transition having taken place through detection of coincident heavy ions and measurement of the reaction Q-value. Haas et al. [24] made a more direct search for the in-band gamma ray in the $^{12}C + {}^{12}C$ cluster band using the Château de Cristal, a large $4\pi$ array of $BaF_2$ scintillators. In particular, this study focussed on a possible $\gamma$-ray transition between $10^+$ and $8^+$ resonant states formed in the $^{12}C + {}^{12}C$ reaction. The bombarding energy, $E_{lab} = 32.9$ MeV, was chosen to populate a known and isolated $10^+$ resonance. The exotic branch of interest was searched for by looking for triple coincidences between $\gamma$ rays and binary (e.g. $^4He + {}^{20}Ne$,$^8Be + {}^{16}O$ or $^{12}C + {}^{12}C$) fragments. A handful of events were observed that fitted the necessary criteria but due to a high background, a clear and positive discrimination of the gamma branch was challenging. Nevertheless, a radiative partial width of $(1.2 \pm 0.4) \times 10^{-5}$ was deduced for the $10^+$ resonance.

There is clearly scope to return to the search for in-band transitions. It might be better, for example, to attempt to locate transitions between lower spin members of the $^{12}C + {}^{12}C$ cluster configuration where the phase space is more restricted. An improved measurement could be made with state-of-the-art detectors such as annular silicon strip detectors and with novel, high energy resolution scintillators like $LaBr_3$(Ce).

### 2.4.2 Connecting Carbon-Carbon Resonances to Low-Lying States: Heavy-Ion Radiative Capture

Heavy-ion radiative capture (HIRC) is an exotic and barely studied process but nevertheless has considerable application to the challenge of clustering in alpha-conjugate nuclei. An extensive review of this technique and of important work at Brookhaven National Laboratory on this topic in the 1980s is given by Sandorfi elsewhere [25] and so it is appropriate only to summarise it here before bringing it up-to-date.

The Brookhaven studies focussed on heavy-ion radiative capture in the $^{12}C + {}^{12}C$ and $^{12}C + {}^{16}O$ reactions. Sandorfi and Nathan employed a single large sodium iodide detector to detect high-energy capture gamma rays [26]. Such an approach is viable because the Q-value for radiative capture is large and positive for the reactions of interest and so the radiative capture events can be readily separated from other gamma rays associated with particle-emission channels, which completely dominate the total reaction cross-section, solely on the basis of their high energy. Sandorfi scanned the region between $E_{c.m.} = 5$ and 11 MeV for radiative capture resonances. The detection method used was sensitive to capture to the ground state, first, second and third (the latter unresolved) excited states (see Fig. 2.4). A series of resonances

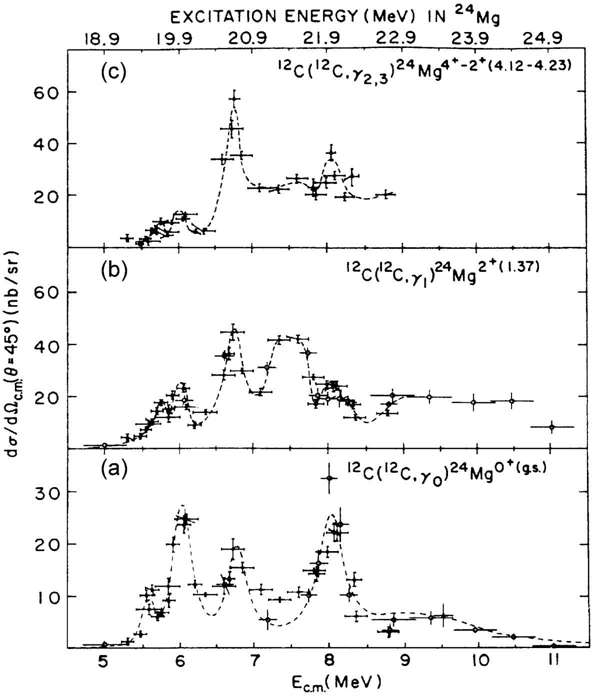

**Fig. 2.4** Cross-sections for radiative capture to low-lying states in $^{24}$Mg taken from [25]

were observed—some in individual channels and some clearly correlated between different channels. The observed resonances were typically 200–300 keV wide and corresponded to cross-sections of 10s of nanobarns per steradian.

By definition, the resonances observed must be low spin since the capture takes place directly to the ground state and first few excited states ($J = 2$ or 4). The resonances disappear towards the upper end of the energy range studied which either indicates that the cross-section begins to be distributed into other exit channels and/or the spin of the capture resonances is increasing and so they no longer directly feed the low-lying states in $^{24}$Mg. The resonances were interpreted as a coupling to the giant quadrupole resonance strength in $^{24}$Mg.

There are other reaction mechanisms which are in some sense the time inverse of the radiative capture process. The break-up of $^{24}$Mg into two $^{12}$C nuclei has been studied through electrofission around 30 years ago [27, 28]. There ought to be a relationship with the radiative capture data where excitation of the fissioning state proceeds through *E2* excitation. This comparison is complicated, however, by the potential to excite also through *E0*, *C0* and *C2* excitations. In addition, capture can proceed to excited states while electrofission is driven up from the ground state. Some structure is seen in the electrofission excitation function in a similar energy range to that seen in radiative capture, but a definitive interpretation of these results is not available [27, 28]. There would be value in repeating these measurements with state-of-the-art detectors.

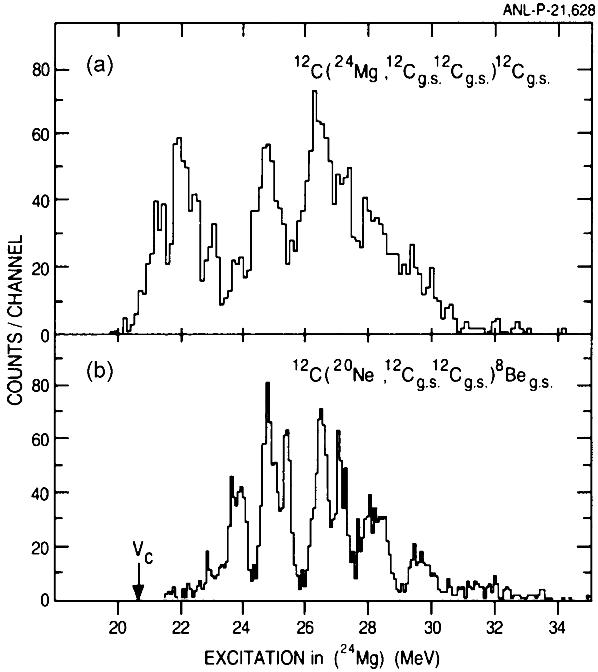

**Fig. 2.5** Excitation energy spectra of $^{24}$Mg in the reaction $^{12}C(^{24}Mg,^{12}C^{12}C)^{12}C$ at 170 MeV (*top*) and in the $^{12}C(^{20}Ne,^{12}C,^{12}C)^{8}Be$ reaction at 180 MeV [29]

The second mechanism related to the radiative capture mechanism is break-up. In such reactions, for example, $^{24}$Mg is broken up into $^{12}$C fragments through interaction with a $^{12}$C target (see Fig. 2.5) [29–31]. This work was carried out around a decade following the initial radiative capture studies at Brookhaven. Qualitatively similar structure is seen in break-up as in the radiative capture but in a higher energy range, and the two sets of data overlap only over a very limited range. Again, the mechanism is roughly a time-inverse of radiative capture to the ground state. It is currently an open question as to how far these different reaction mechanisms explore different aspects of the underlying physics.

Returning to the HIRC mechanism, it is clear that the strong advantage of this approach is that it couples the resonances directly to excited states in $^{24}$Mg. The strong limitation of the Brookhaven studies, however, was that they were restricted to a study of capture transitions to the ground state and the first few excited states, so what was observed might only be the "tip of the iceberg" in terms of the total capture cross-section. Moreover, the Brookhaven work could not search for transitions to highly-excited states in $^{24}$Mg (see Fig. 2.6). An interesting speculation is whether there might be structural selectivity in the capture process so that enhanced transitions are seen to strongly-deformed (superdeformed) bands at high excitation energy. This is plausible for two reasons. Firstly, Collins et al. claimed to see preferential capture in the $^{12}C(^{16}O,\gamma)$ reaction to the excited prolate band rather than the oblate ground state band [32]. Secondly, there are long standing predictions of shape-isomeric/superdeformed (the nomenclature varies) bands with band-heads at

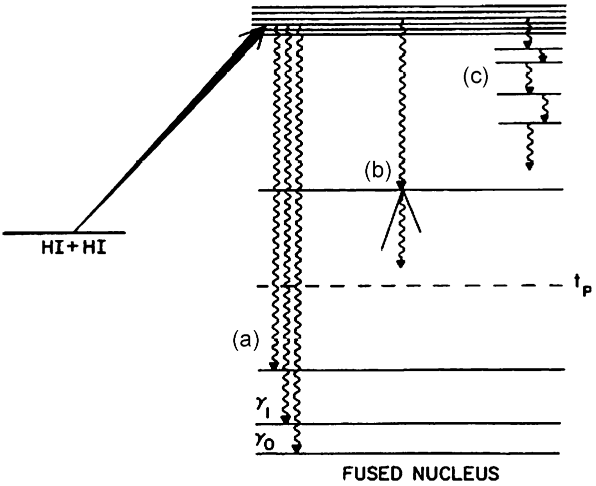

**Fig. 2.6** The three possible modes of heavy ion radiative capture: (**a**) direct transitions to low-lying states (**b**) transitions to high-lying, potentially particle-unbound states (**c**) multi-step decay through yrast states (taken from [25])

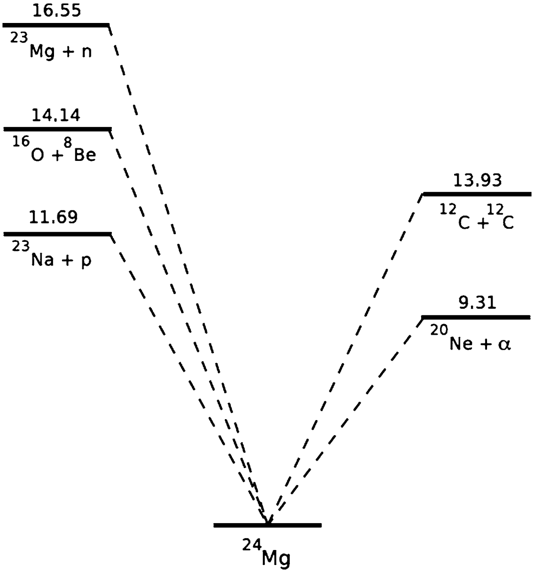

**Fig. 2.7** The excitation energy for break-up of $^{24}$Mg into different channels

around 10 MeV in $^{24}$Mg and $^{28}$Si (see the extensive discussion on candidates for the latter in the section below).

The principal challenge in the study of heavy-ion radiative capture is effectively identifying HIRC events and discriminating them from the overwhelming background due to particle-emission (see Fig. 2.7). This challenge is further complicated by the potential for target impurities, e.g. $^{13}$C and $^{16}$O in a $^{12}$C target which can lead to confusion in the identification of true HIRC events. Two techniques are able to confront these challenges—the first is effectively sum-energy calorimetry, which is related to the original Brookhaven approach [25], while the second is to use a recoil separator to rigorously identify HIRC residues. Both these approaches have been applied in the last ten years in renewed study of HIRC through a series of measurements at different laboratories in North America including Argonne National Laboratory, TRIUMF and Lawrence Berkeley National Laboratory.

### 2.4.3 Total Cross-Section Measurements

Jenkins *et al.* used the Fragment Mass Analyser (FMA) at Argonne National Laboratory to carry out an integrated cross-section measurement for the $^{12}$C($^{12}$C,$\gamma$) reaction at energies around $E_{c.m.} = 7.8$ MeV [33]. The cross-section was found to be around 3 μb which is a factor of three larger than the typical values seen in the earlier Brookhaven work [25, 26]. This coincides with the view that what was measured earlier was only a fraction of the total and that pathways through high-lying states must be important. A follow-up experiment was conducted using the Gammasphere array at Lawrence Berkeley National Laboratory. Gammasphere comprises 100 high-purity germanium detectors arranged in a spherical geometry [33]. Each detector (see Fig. 2.8) comprises a germanium crystal surrounded by a contiguous shield and suppressor plug made from Bismuth Germanate (BGO). The standard mode of operation for such a detector is for the BGO shield to act as a veto detector for gamma rays which scatter out of the germanium crystal. In this way, the peak-to-total can be dramatically improved. The design of Gammasphere, however, is optimised for detection of low energy (100–3000 keV) $\gamma$ rays with high multiplicity. This is the kind of regime typified by a high-spin study of a deformed rare-earth nucleus where a long cascade of gamma rays results from the population of the nucleus of interest at a spin up to $50\hbar$. Unfortunately, HIRC studies have very different characteristics, namely a low multiplicity of gamma rays (including one single gamma ray) and typically high energy (2–20 MeV) gamma rays. The efficiency of Gammasphere for detecting gamma rays above 10 MeV in suppressed germanium detectors is essentially zero. These issues pose strong limitations on what can be achieved with Gammasphere in its conventional mode of operation. It is also possible, however, to operate in an add-back mode where the energy recorded in the BGO shield is added to that recorded in the germanium crystal, so that each element acts as effectively a composite detector module. The sum of such add-back energies recorded in the calorimeter as a whole can be used as a measure of the sum energy of the event. This technique was used in the Gammasphere experiment at Lawrence Berkeley National Laboratory [33], whereby a high-sum energy cut was imposed to separate the radiative capture channel from competing particle-evaporation channels (see Fig. 2.9).

Analysis of the Gammasphere data allowed the capture process to be explored in a limited fashion, and it was found that capture transitions to the $K = 2$ rotational band were prominent on-resonance, but appeared to be strongly suppressed off-resonance. The statistics available did not allow a detailed study of this effect.

**Fig. 2.8** Schematic of a Gammasphere detector module

### 2.4.4 *Strength Distribution Measurements Using DRAGON*

While the FMA measurement showed that a significant part of the capture cross-section was missing, the low statistics of the Gammasphere experiment did not permit a detailed understanding of the decay process. Clearly, much higher efficiency was needed and this motivated a study by Jenkins et al. [34] of decay strength distributions in the $^{12}$C($^{12}$C,$\gamma$) reaction with the DRAGON recoil separator at TRIUMF. DRAGON [35] is specially constructed for nuclear astrophysics experiments, particularly $(p, \gamma)$ reactions in inverse kinematics, e.g. $^{21}$Na$(p, \gamma)$ [36]. An array of close-packed BGO detectors surrounds the target position (normally a windowless gas target for nuclear astrophysics studies) which can be used to detect capture gamma rays (see Fig. 2.10). DRAGON comprises a two-stage recoil mass separator with a total length of 21 m. Separation of recoils from scattered beam is achieved using a combination of electric and magnetic dipoles. A single (optimal) charge state is selected in the first magnetic dipole. Energy dispersion in the electric dipole

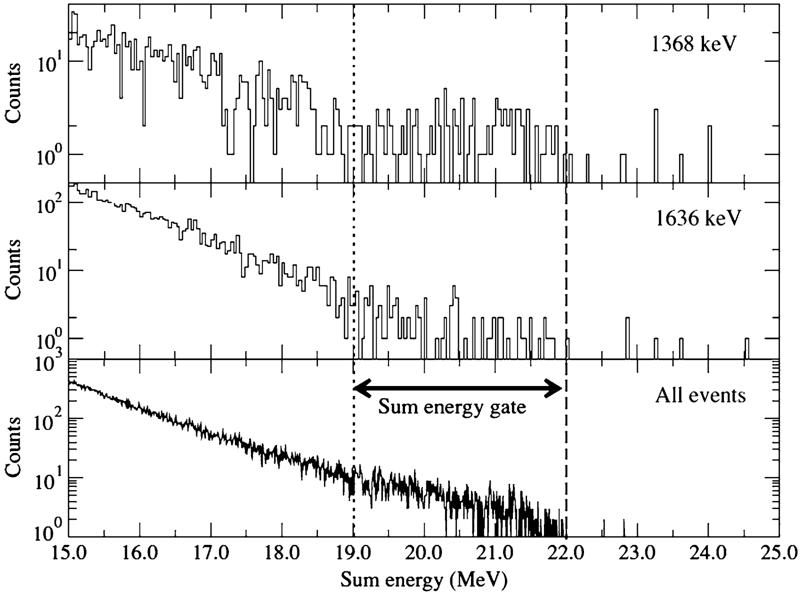

**Fig. 2.9** Sum energy spectra in coincidence with 1368-keV transition in $^{24}$Mg (*top*); 1636 keV transition in $^{23}$Na (*middle*) and all events (*bottom*)

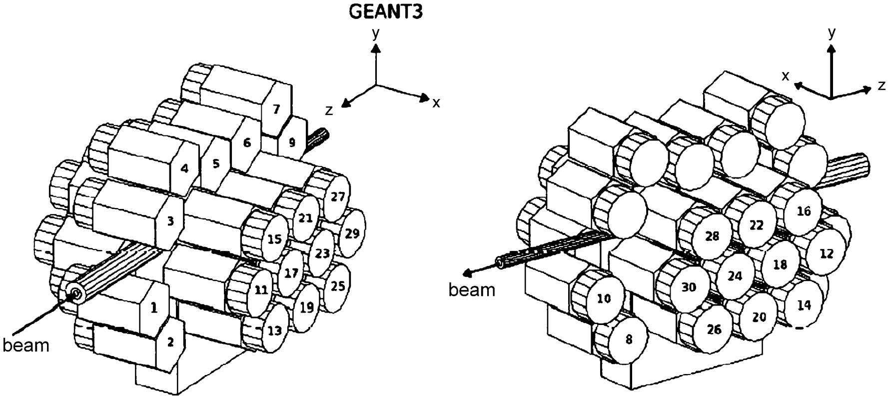

**Fig. 2.10** Arrangement of BGO detectors around the DRAGON target position

separates the residues by mass. The second stage repeats this process, leading to an extremely high beam rejection ratio ($10^{14}$). Such a high rejection ratio is essential to DRAGON's intended application to studying proton capture reactions with short-lived radioactive species in inverse kinematics. Although not specifically designed for such an application, DRAGON is also an excellent tool for studies of heavy-ion radiative capture reactions. A disadvantage of the design, however, is that the angular acceptance of the device is limited due its intended application to $(p, \gamma)$

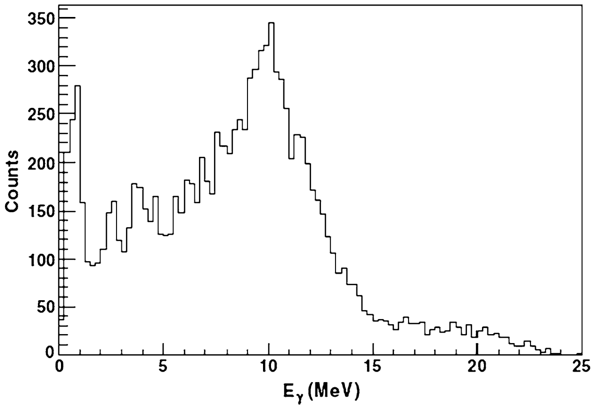

**Fig. 2.11** Total projection of gamma rays in coincidence with recoils at $E_{cm} = 6.0$ MeV

reactions. The maximum recoil cone for $^{12}$C($^{12}$C,$\gamma$) at energies near the Coulomb barrier falls outside of this angular acceptance. In addition the layout of the BGO detectors around the target position is somewhat irregular and designed to maximise efficiency rather than symmetry. As a consequence of the design of DRAGON and the BGO array, it was necessary to carry out detailed GEANT3 simulations in order to understand the efficiency for different types of event. For the HIRC studies, the windowless gas target system was replaced with a solid target ladder.

Measurements of the $^{12}$C($^{12}$C,$\gamma$) reaction were made at a series of energies including the prominent capture resonances at $E_{cm} = 6.0$, 6.7, 7.5 and 8.0 MeV, as well as intermediate off-resonance energies. The radiative capture spectra obtained were compared to the results of a GEANT3 simulation to assist with the interpretation. This simulation incorporated decays to all known bound states via transitions with average transition strength taken from tabulated values.

The data at $E_{cm} = 6.0$, 6.7 MeV were relatively similar in that capture to the low-lying states was observed, consistent with the earlier Sandorfi work but the gamma-ray spectrum was dominated by a peak around 10 MeV (see Fig. 2.11). Such a feature could not have been seen in the earlier HIRC studies of Sandorfi et al. [27] as they only employed a single large sodium iodide detector.

Comparison with simulation suggests that the origin of the peak around 10 MeV is attributed to decay pathways via $T = 1$, $1^+$ states in the region around 10 MeV in $^{24}$Mg. These states are reached via strong isovector *M1* transitions. This previously unseen decay mechanism is analogous to Gamow-Teller beta decay (see Fig. 2.12). In order to populate such states in the decay, the capture resonance must have spin/parity of $0^+$ or $2^+$; the comparison with simulation gives strong preference to the latter. Comparing the capture spectra with simulations for two further resonances at $E_{cm} = 7.5$ and 8.0 MeV suggests $J = 4^+$ assignments (or a mixture of $2^+$ and $4^+$ for $E_{cm} = 8.0$ MeV). It is interesting to cross-reference this new information with break-up data where $J = 4$ resonances are seen at $E_{cm} = 7.3$ and 7.7 MeV [31].

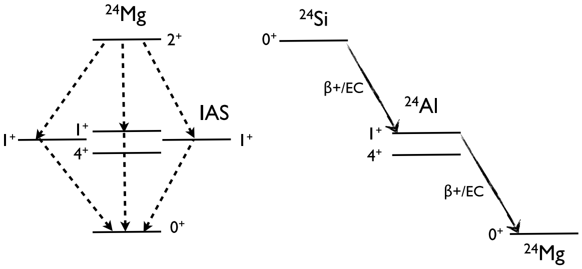

**Fig. 2.12** Comparison between radiative capture via IAS $T = 1$ states (*left*) and Gamow-Teller beta decay (*right*)

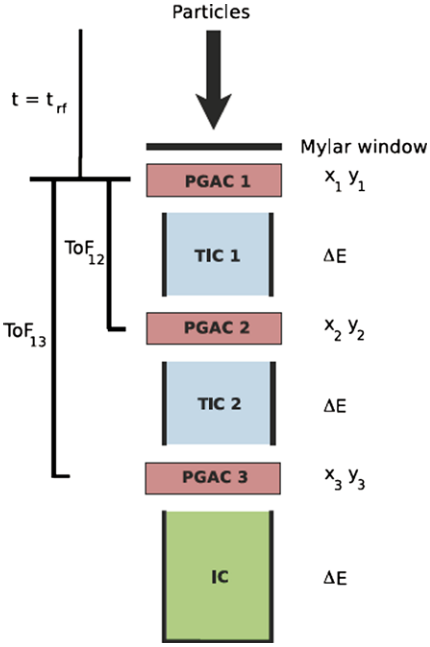

**Fig. 2.13** Multi PGAC-ion chamber system

## 2.4.5 Gammasphere and FMA

The lessons learned from previous techniques applied to the study of the $^{12}$C($^{12}$C,$\gamma$) reaction suggested that the key features needed in any future study would be robust channel selection with no bias towards any class of residues, allied to a high energy resolution for detection of capture gamma rays. In 2007, an experiment was carried out to obtain high statistics for the capture process with high energy resolution by focussing on one specific capture resonance in the $^{12}$C($^{12}$C,$\gamma$) reaction at $E_{c.m.} =$ 8.0 MeV [37]. The Gammasphere array was used to detect the capture gamma rays, while the FMA was used to separate residues by $A/q$. A robust selection of the capture channel was achieved using a multi-step ion chamber/PGAC system [38] illustrated in Fig. 2.13. By producing a 2D spectrum of the energy loss ($\Delta E$) versus

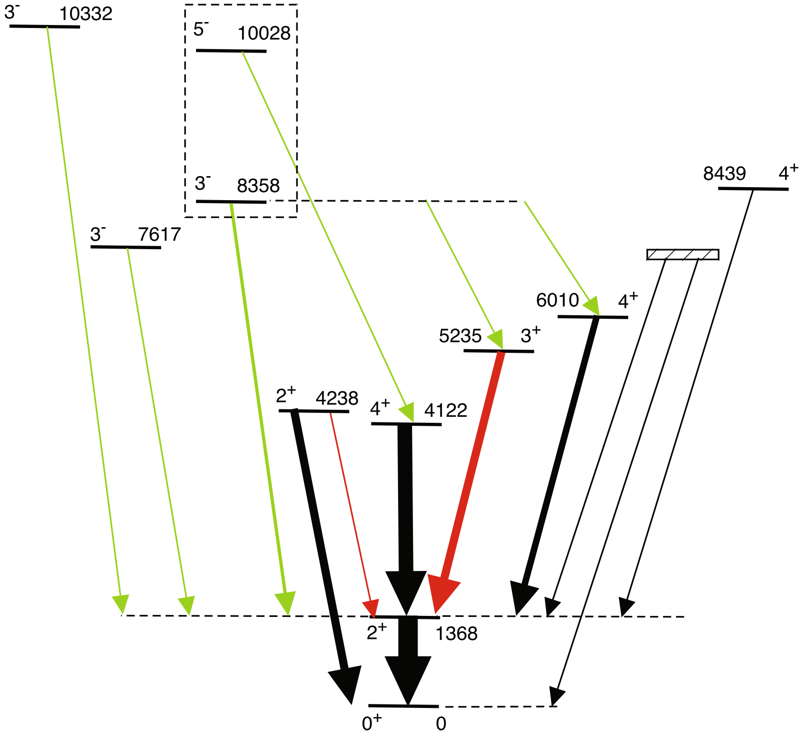

**Fig. 2.14** Levels populated in $^{24}$Mg following radiative capture. The *green* transitions are E1, *red* transitions are M1/E2 and *black* transitions are E2

the time of flight (ToF) through each of the two transmission ionisation chambers (TICs) it was possible to unambiguously identify $^{24}$Mg despite the overwhelming dominance of the particle evaporation channels [37].

The residue selection afforded a reduction in the intensity of contaminant channels by five orders of magnitude. This allowed the decay branching of the capture resonance to be examined in detail (see Fig. 2.14). In general, the population of positive parity states appeared to demonstrate a statistical feeding expected for the decay of the resonance by *E2* transitions. The observed feeding strongly favoured a $J^{\pi} = 4^{+}$ assignment to the capture resonance. There are two aspects in support of this. Firstly, states between $2^{+}$ and $5^{-}$ are fed, but no lower spin states. This strongly disfavours a spin/parity assignment of $0^{+}$ or $2^{+}$ to the capture resonance. Moreover, in the earlier studies with DRAGON discussed above, capture resonances with $J^{\pi} = 0^{+}$ and $2^{+}$ had very strong decays to $1^{+}$, $T = 1$ states via isovector *M1* transitions. These were not observed in the Gammasphere study.

The surprising feature of the data was the strong population of the $3^{-}$ state at 8358 keV and $5^{-}$ level at 10028 keV, amounting to a total of ~18 % of the feeding intensity (see Fig. 2.15). These states were identified as members of a

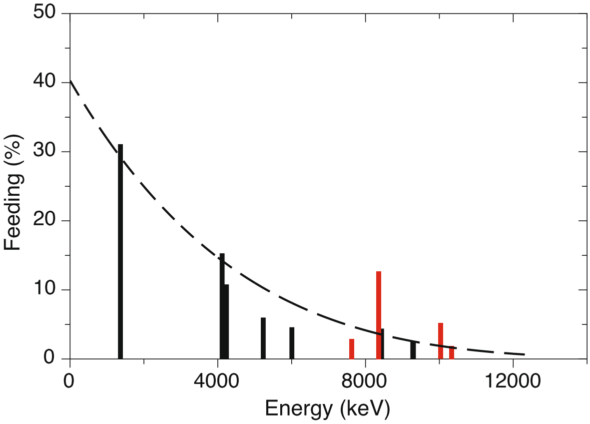

**Fig. 2.15** Feeding pattern for population of states following radiative capture for the $^{12}C(^{12}C,\gamma)$ reaction at $E_{c.m.} = 8.0$ MeV. Cascade feeding has been removed. The population of negative parity states is shown in red

$K^{\pi} = 0^{-}$ band by Branford et al. on the basis of the strong *E2* transition connecting the two states [39]. It is notable that the feeding of the $3^{-}$ and $5^{-}$ states in the $K^{\pi} = 0^{-}$ band is enhanced 3–5 times relative to the other $3^{-}$ states observed. An open question is whether this enhancement is structural in origin. Kato and Bando [40] find in their cluster calculations that the $K^{\pi} = 0^{-}$ band corresponds to the parity doublet of the ground state band. As discussed by Butler and Nazarewicz in their review of octupole phenomena in nuclei [41], there are similar predictions of low-lying $K^{\pi} = 0^{-}$ bands in many light alpha-conjugate nuclei. Branford et al. note that while the candidate $K^{\pi} = 3^{-}$ band has a similar moment-of-inertia to the ground-state band, the moment-of-inertia of their candidate $K^{\pi} = 0^{-}$ band is more than double that of the ground-state band. This would imply that the $K^{\pi} = 0^{-}$ band is associated with a large deformation.

In their transfer-reaction study, Tribble et al. showed that the lowest $3^{-}$ state in $^{24}$Mg had a structure mostly related to a hole in the $1p$ shell, while the second $3^{-}$ state appeared to be better explained as a particle-hole excitation into the *fp* shell [42]. This observation seems to be borne out by $1\hbar\omega$ PSDPF shell model calculations which indicate that the lowest $3^{-}$ state is clearly associated with a $1p$ hole, while the first $5^{-}$ state is clearly associated with a particle in the *fp* shell. The second $3^{-}$ state is a mixture of these two configurations. Naturally, the model space is somewhat restricted and, in a deformed nucleus, the $1p$-$1h$ configurations might also be expected to have significant $3p$-$3h$ components. It is interesting that in a two-centre shell model study of the $^{12}C + {}^{12}C$ system, Chandra and Mosel [43] pointed to a major component for configuration for the molecular resonances of $4p$-$4h$. Again, such configurations would be expected to have $2p$-$2h$ components as well. Favoured decay between these particle-hole excitations might, therefore, be anticipated in comparison to decay to the configurations based on a $1p$ shell hole. This could explain the favoured decay to the second $3^{-}$ and first $5^{-}$ states.

### 2.4.6 *Studies of the* $^{12}$C($^{16}$O,$\gamma$) *Reaction*

The $^{12}$C($^{16}$O,$\gamma$) reaction was also investigated at Brookhaven National Laboratory in the 1980s [32]. A more sophisticated set-up was used compared to the $^{12}$C($^{12}$C,$\gamma$) studies, in that a Wien filter and ionisation chamber were coupled to a single sodium iodide detector. This allowed capture residues to be more rigorously identified but the single detector involved still posed a limitation in that only gamma-ray singles could be studied and not coincidence data. The $^{12}$C($^{16}$O,$\gamma$) data were qualitatively different to the earlier $^{12}$C($^{12}$C,$\gamma$) study in that there appeared to be preferred feeding of the $0_3^+$ state which is the bandhead of the prolate (normal-deformed) band in $^{28}$Si [32]. This preferential feeding was attributed to the greater structural overlap between the entry resonance and the prolate band, as opposed to the oblate, ground-state band.

The $^{12}$C($^{16}$O,$\gamma$) reaction has also been reinvestigated in the last few years using the DRAGON recoil separator and its associated BGO array. In certain respects, the situation is less straightforward since non-identical bosons are involved and so negative-parity resonances are also possible, effectively doubling the number of potential resonances. In addition, E1 transitions are much more important.

Three energies were investigated using DRAGON [44, 45], corresponding to $E_{cm} = 8.5$, 8.8 and 9.0 MeV coinciding with the region explored earlier by Collins et al. [32]. The data obtained were analysed in a similar manner to the $^{12}$C($^{12}$C,$\gamma$) study, using a Monte Carlo simulation of the full electromagnetic elements of the DRAGON separator and the BGO array. This is important as the acceptance into DRAGON is not 100 % for this class of reaction. The $E_{cm} = 9.0$ MeV resonance appears to have a clear unique spin of $6^+$, while the other resonances are best fit with a mixture of contributions from spins of $5^-$ and $6^+$.

The key result of the recent $^{12}$C($^{16}$O,$\gamma$) study was to show that what was earlier interpreted as feeding of the excited prolate bandhead was incorrect, and that the feeding in fact proceeds to a close-lying $3^-$ state which is the bandhead of a $K^\pi = 3^-$ band. The change in the interpretation of the data is a feature of the availability of $\gamma$-$\gamma$ coincidence data, which were not available in the original studies in the 1980s.

## 2.5 Superdeformed Bands and Clustering

The term “superdeformed” is most generally associated with the discovery of bands in rare-earth nuclei like $^{152}$Dy [46]. This term has also been applied, however, to rotational bands in the light, alpha-conjugate nuclei, $^{36}$Ar [47] and $^{40}$Ca [48], which were identified around ten years ago, in $\gamma$-ray spectroscopy studies. Figure 2.16 shows the level scheme for $^{40}$Ca, where there is shape coexistence between the spherical ground state, a prolate deformed band with a band-head at 3.352 MeV and the superdeformed (SD) band with its band-head at 5.213 MeV. It is instructive to compare the gamma-ray spectroscopy work with earlier transfer reaction studies as the latter can point to the clustering structure of the states. Middleton et al. [49]

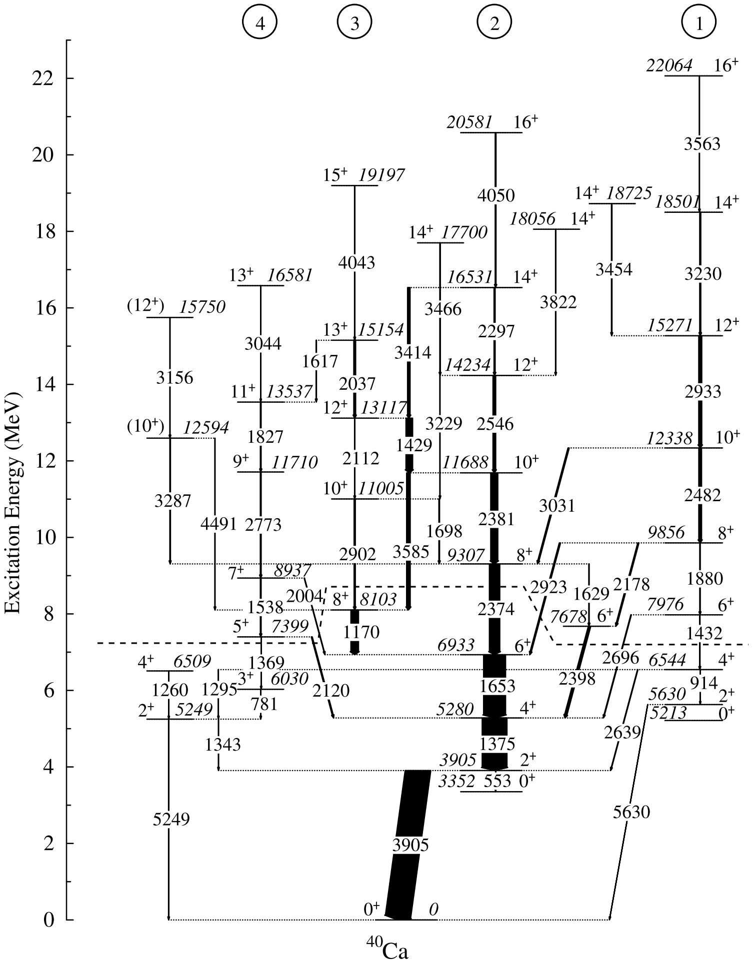

**Fig. 2.16** Level scheme for $^{40}$Ca. The prolate ($4p$-$4h$) is labelled as band 2. The superdeformed ($8p$-$8h$) band is labelled as band 1 (taken from [48])

studied the $^{32}$S($^{12}$C,$\alpha$)$^{40}$Ca reaction, where the $0^+$ state at 3.352 MeV attributed to the $4p$-$4h$ configuration is excited ten times more strongly than the $0p$-$0h$ configuration, and the $8p$-$8h$ is excited 1.5 times more strongly than the $4p$-$4h$ (see Fig. 2.17). Indeed, the state most strongly excited in this reaction is at 7.98 MeV in $^{40}$Ca, which has latterly been shown to be the $6^+$ state in the superdeformed band in $^{40}$Ca based on the $8p$-$8h$ configuration [48].

The superdeformed bands in $^{36}$Ar and $^{40}$Ca are of particular interest, since a complementary description can be found both in terms of particle-hole excitations in the shell model, and from cluster model calculations such as antisymmetrized molecular dynamics (AMD) e.g. [50]. This raises the question of whether clustering is the correct description or whether cluster models simply agree with the appear-

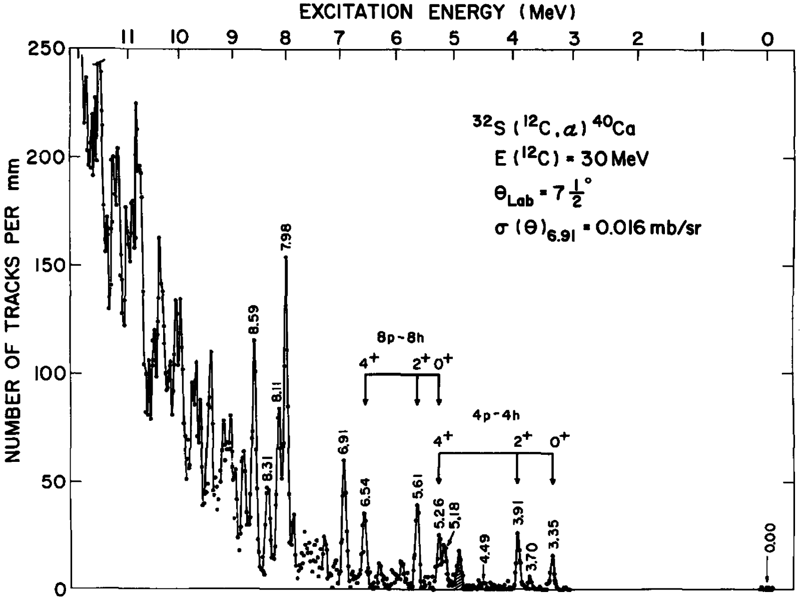

**Fig. 2.17** Particle spectrum taken from [49]

ances. One way to test this is to observe the evolution from clustered to deformed regimes. For this, it would be highly desirable to locate superdeformed bands in lighter, alpha-conjugate nuclei such as $^{32}$S and $^{28}$Si for which long-standing theoretical predictions of superdeformed configurations exist and which remain a hot topic for theoretical study e.g. $^{32}$S [51]. From the experimental perspective, such an extension is very challenging as the superdeformed bands in $^{28}$Si and $^{32}$S are predicted to lie at much higher excitation energy than those in $^{36}$Ar and $^{40}$Ca. This leads to two consequences: Firstly, that phase space favours high energy out-of-band transitions compared to low energy in-band transitions despite the strong collective character of the latter. Secondly, the bandhead lies on or above the particle-decay thresholds meaning that there is competition with particle emission.

Recently, Taniguchi et al. [52] have made an extensive study of collective structures in $^{28}$Si using the AMD model. They explored clustering degrees of freedom of the type: $^{24}$Mg $+ \alpha$ and $^{12}$C $+$ $^{16}$O. These studies reveal a rich diversity of rotational behaviour (see Fig. 2.18). There is shape coexistence between the oblate ground state band and a prolate (ND) band. An SD band is identified in the calculations with a strong $^{24}$Mg $+ \alpha$ configuration as well as some component of $^{12}$C $+$ $^{16}$O.

The AMD calculations show good correspondence with the known band structure of $^{28}$Si, which comprises an oblate ground state band, co-existing with a prolate rotational band. It is more difficult to find states forming likely candidates for the SD band. In their recent paper, Taniguchi et al. [52] compare their predictions for the SD band in $^{28}$Si with the properties of a so-called "excited prolate" band identified in the early 1980s by Kubono et al. [53] using the $^{12}$C($^{20}$Ne,$\alpha$)$^{28}$Si reac-

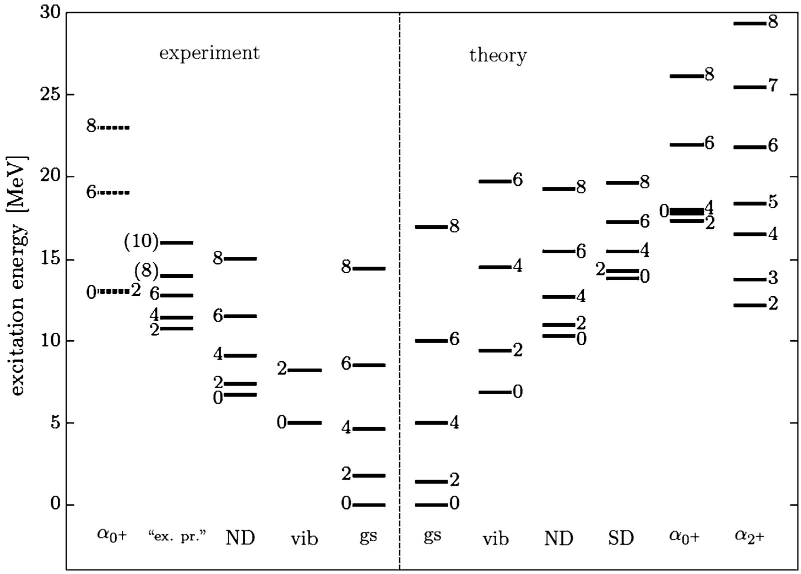

Fig. 2.18 Comparison of known experimental bands in $^{28}$Si with predictions of the AMD model (taken from [52])

tion. The experimental assignment of this "excited prolate" band rests on peaks in a charged particle spectrum, many of which do not have well-established spin/parity. These states, however, do not form a smooth sequence characteristic of a rotational band even making plausible allowance for mixing (see Fig. 2.19), and the suggested moments of inertia are rather higher than the calculated values. Moreover, $\gamma$-ray transitions between these states are not observed, and, as a consequence, transition strengths are unknown. Without the observation of in-band transitions, assigning candidate rotational bands is difficult and potentially ambiguous, although such an approach has been a common procedure in the past for "cluster" bands in light nuclei.

The striking feature of the AMD calculations, however, is the dominant $^{24}$Mg $+\alpha$ component and this poses the question as to whether the $^{24}$Mg($\alpha$,$\gamma$) radiative capture reaction might prove to be a favoured reaction mechanism for selectively populating SD states in $^{28}$Si. A review of the literature on this reaction suggests some possible candidate SD states, in particular, the 12.86 MeV state which has decay branches to a number of states including a $4^+$ state at 10.945 MeV, via a 1.921 MeV transition; the associated B(E2) value exceeds 25 Wu [55–57]. Comparison with the USD shell model leads to the conclusion that the respective $6^+$ and $4^+$ states as well as a $2^+$ state at 9796 keV are not consistent with expected shell model states but are more likely to be intruder states. They suggest, accordingly, that the states they have identified form a candidate $K^\pi = 0^+$ intruder band. If this set of states did form a rotational band then the kinematic moment of inertia would be $6\hbar^2$/MeV, in good conformity to that predicted by the AMD calculation (see Fig. 2.19).

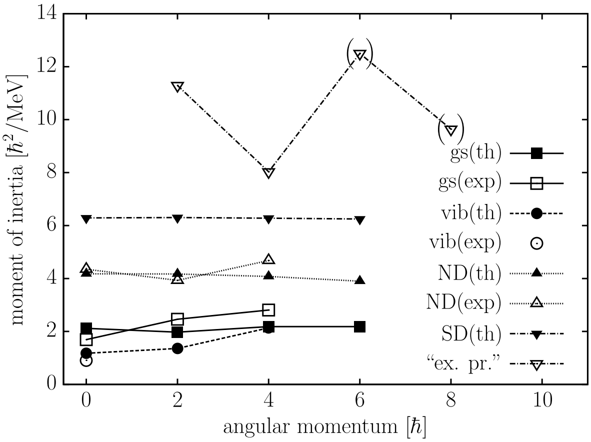

**Fig. 2.19** Calculated and experimental moments-of-inertia for rotational bands in $^{28}$Si taken from [52]

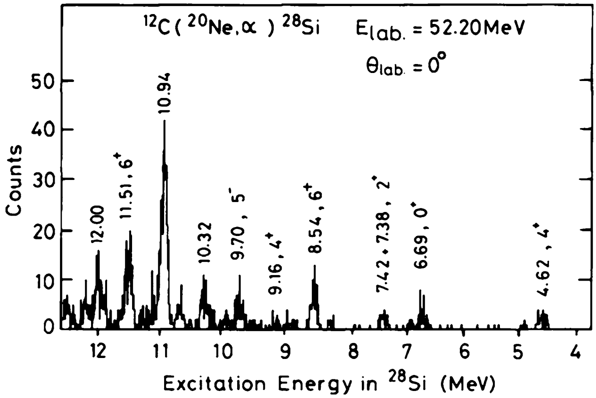

**Fig. 2.20** Particle spectrum from the $^{12}$C($^{20}$Ne,$\alpha$)$^{28}$Si reaction taken from [53]

The unusual character of the 10.94 MeV and 12.86 MeV states becomes clear when cross-referenced with other work such as the $^{12}$C($^{20}$Ne,$\alpha$)$^{28}$Si reaction studied by Kubono et al. [53]. In this reaction, the 10.94 MeV state is the most strongly populated state below 12 MeV (see Fig. 2.20). This $4^+$ state is populated with more than ten times the cross-section of the $4^+$ states in the prolate and oblate ground state bands. The reaction mechanism is likely to favourably populate multi particle-hole states or in other words, those with substantial alpha clustering component.

Analysis of the $^{12}$C($^{20}$Ne,$\alpha$)$^{28}$Si reaction provides a strong assignment of $6^+$ to a 12.8 MeV state [53]. This state is also shown to have a direct proton branch to the $5/2^+$ ground state of $^{27}$Al [53] which implies $L = 4$ and so there must be an associated $g_{9/2}$ component, corresponding to $S = 0.3$ [54]. This result is reinforced by a parallel $^{24}$Mg($\alpha$, $t$) study by Kubono et al. [53, 54] which also indicated a sizeable $g_{9/2}$ component to the 12.82 MeV state. This is an unusually large component possibly reflecting a strong associated deformation. A consistent picture emerges, therefore, where the candidate intruder states discussed by Brenneisen et al. appear with unusual selectivity in the $^{12}$C($^{20}$Ne,$\alpha$)$^{28}$Si reaction, and with the suggestion of

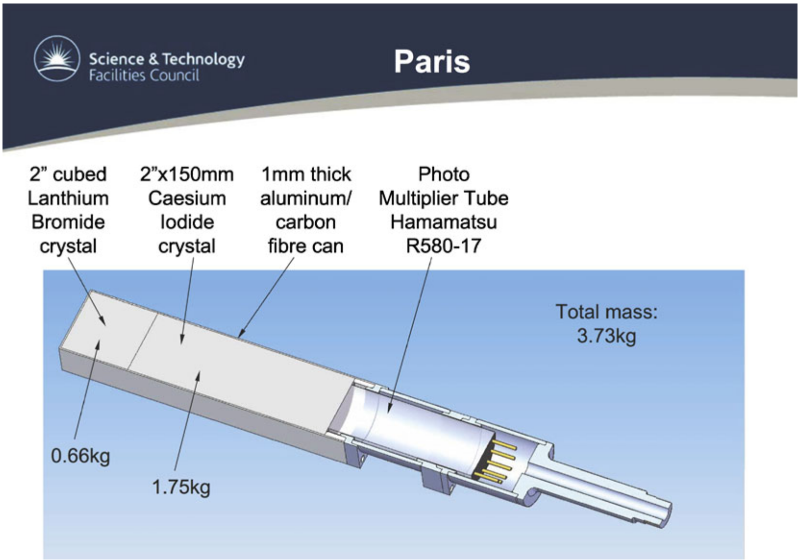

**Fig. 2.21** PARIS phoswich design

very strong deformation, in the case of the 12.86 MeV state. Further work in this area is clearly warranted.

In the future, it would be of great interest to extend the knowledge of superdeformed bands to $^{24}$Mg and $^{32}$S. Given the synergies between transfer reactions and $\gamma$-ray spectroscopy discussed for the extant cases, it might be interesting to consider a particle-gamma study, where an alpha-particle transfer reaction is chosen to selectively populate the states of interest, and gamma-ray branches measured to confirm the band structure and extract B(E2) strengths.

## 2.6 Future Prospects and New Detector Materials

In all of the examples discussed above, gamma-ray spectroscopy studies related to clustering are restricted by the desire to achieve both high energy resolution and high efficiency. High energy resolution can be achieved with Compton-suppressed germanium detectors but at the expense of efficiency. Scintillator detectors provide much higher efficiency but at the expense of relatively poor energy resolution. Novel scintillator materials such as lanthanum bromide and cerium bromide are now becoming available which promise energy resolutions of around 3 %. They also have very fast time response which can be used to reject neutrons. The difficulty at the time of writing, however, is the high cost of such next generation detectors relative to conventional materials.

The PARIS collaboration (http://paris.ifj.edu.pl) intends to build a $4\pi$ calorimeter using novel scintillators. In particular, they are investigating using phoswich de-

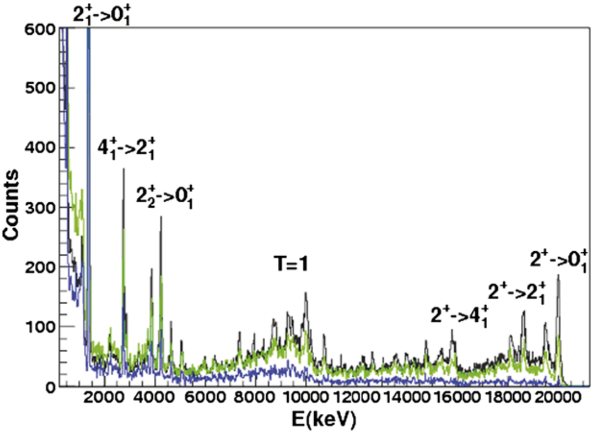

**Fig. 2.22** Simulation of the performance of PARIS for the study of the $^{12}$C($^{12}$C,$\gamma$) reaction

tectors where a 2″ cubic crystal of LaBr$_3$(Ce) is backed by a longer crystal of a conventional scintillator like sodium iodide (see Fig. 2.21). The advantage of such an arrangement is that it obtains most of the benefit of the novel material but at a reduced cost.

Use of novel scintillators in the future could lead to a step change in what can be achieved in cluster studies using gamma-ray spectroscopy. For example, Fig. 2.22 shows the results of a simulated study of the $^{12}$C($^{12}$C,$\gamma$) reaction using the PARIS calorimeter. Feeding of individual high-lying states is now readily resolvable. A definitive study of the heavy-ion radiative capture reactions is therefore, perhaps best achieved with a $4\pi$ PARIS. Channel selection would be achieved using calorimetry. Aside from HIRC studies, most of the types of study discussed above would profit from the use of scintillators with high energy resolution.

**Acknowledgements** I would like to acknowledge valuable discussions with Y. Kanada-En'yo and Y. Taniguchi. Sandrine Courtin and Florent Haas should be acknowledged for their careful reading of this manuscript.

## References

1. E. Almqvist et al., Phys. Rev. Lett. **4**, 515 (1960)
2. D.A. Bromley, J.A. Kuehner, E. Almqvist, Phys. Rev. Lett. **4**, 365 (1960)
3. M. Freer, Rep. Prog. Phys. **70**, 2149 (2007)
4. R.R. Betts, A.H. Wuosmaa, Rep. Prog. Phys. **60**, 819 (1996)
5. J.L. Wood et al., Nucl. Phys. A **651**, 323 (1999)
6. E. Farnea et al., Nucl. Instrum. Methods A **621**, 331 (2010)
7. R. Guardiola et al., Nucl. Phys. A **679**, 393 (2001)
8. Y. Yamamoto, T. Togashi, K. Kato, Prog. Theor. Phys. **124**, 315 (2010)
9. R.B. Wiringa, S.C. Pieper, J. Carlson, V.R. Pandharipande, Phys. Rev. C **62**, 014001 (2000)
10. K. Langanke, C. Rolfs, Phys. Rev. C **33**, 790 (1986)
11. K. Langanke, C. Rolfs, Z. Phys. A **324**, 307 (1986)
12. V.M. Datar, S. Kumar, D.R. Chakrabarty, V. Nanal, E.T. Mirgule, A. Mitra, H.H. Oza, Phys. Rev. Lett. **94**, 122502 (2005)

13. F. Hoyle, Astrophys. J. Suppl. Ser. **1**, 121 (1954)
14. C.W. Cook et al., Phys. Rev. **107**, 508 (1957)
15. E. Epelbaum, H. Krebs, D. Lee, U. Meissner, Phys. Rev. Lett. **106**, 192501 (2011)
16. M. Freer et al., Phys. Rev. C **80**, 041303 (2009)
17. B. Buck, C.B. Dover, J.P. Vary, Phys. Rev. C **11**, 1803 (1975)
18. M. Chernykh et al., Phys. Rev. Lett. **105**, 022501 (2010)
19. T. Yamada et al., J. Phys. Conf. Ser. **111**, 012008 (2008)
20. E. Vogt, H. McManus, Phys. Rev. Lett. **4**, 518 (1960)
21. D. Baye, P. Descouvemont, Nucl. Phys. A **419**, 397 (1984)
22. K. Langanke, O.S. van Roosmalen, Phys. Rev. C **29**, 1358 (1984)
23. R.L. McGrath, D. Abriola, J. Karp, T. Renner, S.Y. Zhu, Phys. Rev. C **24**, 2374 (1981)
24. F. Haas et al., Nuovo Cimento A **110**, 989 (1997)
25. A.M. Sandorfi, in *Treatise on Heavy Ion Science*, ed. by D.A. Bromley (Plenum, New York, 1985). Vol. 2, Sect. III and references therein
26. A.M. Nathan, A.M. Sandorfi, T.J. Bowles, Phys. Rev. C **24**, 932 (1981)
27. A.M. Sandorfi, L.R. Kilius, H.W. Lee, A.E. Litherland, Phys. Rev. Lett. **40**, 1248 (1978)
28. A.M. Sandorfi, J.R. Calarco, R.E. Rand, H.A. Schwettman, Phys. Rev. Lett. **45**, 1615 (1980)
29. B.R. Fulton et al., Phys. Lett. B **267**, 325 (1991)
30. B.R. Fulton et al., J. Phys. G **20**, 151 (1994)
31. N. Curtis et al., Phys. Rev. C **51**, 1554 (1995)
32. M.T. Collins, A.M. Sandorfi, D.H. Hoffmann, M.K. Salomaa, Phys. Rev. Lett. **49**, 1553 (1982)
33. D.G. Jenkins et al., Phys. Rev. C **71**, 041301 (2005)
34. D.G. Jenkins et al., Phys. Rev. C **76**, 044310 (2007)
35. D.A. Hutcheon et al., Nucl. Instrum. Methods Phys. Res. A **498**, 190 (2003)
36. S. Bishop et al., Phys. Rev. Lett. **90**, 162501 (2003)
37. P. Marley et al., Phys. Rev. C **84**, 044332 (2011)
38. C.L. Jiang et al., Nucl. Instrum. Methods A **554**, 500 (2005)
39. D. Branford, N. Gardner, I.F. Wright, Phys. Lett. B **36**, 456 (1971)
40. K. Kato, H. Bando, Prog. Theor. Phys. **62**, 644 (1979)
41. P.A. Butler, W. Nazarewicz, Rev. Mod. Phys. **68**, 349 (1996)
42. R.E. Tribble, G.T. Garvey, J.R. Comfort, Phys. Lett. B **44**, 366 (1973)
43. H. Chandra, U. Mosel, Nucl. Phys. A **298**, 151 (1978)
44. S. Courtin et al., Acta Phys. Pol. B **42**, 757 (2011)
45. D. Lebhertz et al., AIP Conf. Proc. **1165**, 331 (2009)
46. P.J. Nolan, P.J. Twin, Annu. Rev. Nucl. Part. Sci. **38**, 533 (1988)
47. C.E. Svensson et al., Phys. Rev. Lett. **85**, 2693 (2000)
48. E. Ideguchi et al., Phys. Rev. Lett. **87**, 222501 (2001)
49. R. Middleton, J.D. Garrett, H.T. Fortune, Phys. Lett. B **39**, 339 (1972)
50. Y. Taniguchi, M. Kimura, Y. Kanada-En'yo, H. Horiuchi, Phys. Rev. C **76**, 044317 (2007)
51. M. Kimura, H. Horiuchi, Phys. Rev. C **69**, 051304 (2004)
52. Y. Taniguchi, Y. Kanada-En'yo, M. Kimura, Phys. Rev. C **80**, 044316 (2009)
53. S. Kubono et al., Nucl. Phys. A **457**, 461 (1986)
54. S. Kubono et al., Phys. Rev. C **33**, 1524 (1986)
55. J. Brenneisen et al., Z. Phys. A **352**, 149 (1995)
56. J. Brenneisen et al., Z. Phys. A **352**, 279 (1995)
57. J. Brenneisen et al., Z. Phys. A **352**, 403 (1995)

# Chapter 3
# “Tomography” of the Cluster Structure of Light Nuclei via Relativistic Dissociation

**P.I. Zarubin**

## 3.1 Introduction

Collective degrees of freedom, in which groups of few nucleons behave as composing clusters, are a key aspect of nuclear structure. The fundamental “building blocks” elements of clustering are the lightest nuclei having no excited states—first of all, the $^4$He nucleus ($\alpha$ particles) as well as the deuteron ($d$), the triton ($t$) and the $^3$He nucleus ($h$, helion). This feature is clearly seen in light nuclei, where the number of possible cluster configurations is small (Fig. 3.1). In particular, the cluster separation thresholds in the nuclei of $^7$Be, $^{6,7}$Li, $^{11,10}$B, $^{11,12}$C and $^{16}$O are below the nucleon separation thresholds. The stable $^9$Be, and unbound $^8$Be and $^9$B nuclei have a clearly pronounced cluster nature. In turn, the cluster nuclei $^7$Be, $^7$Li, and $^8$Be serve as cores in the isotopes $^8$B and $^{9-12}$C. Descriptions of the ground states of light nuclei in the shell and cluster models are complementary. In the cluster pattern the light nuclei are represented as superpositions of different cluster and nucleon configurations. The interest in such states is associated with the prediction of their molecular-like properties [1, 2]. Nuclear clustering is traditionally regarded as the prerogative of the physics of nuclear reactions at low energies [3]. The purpose of these lecture notes is to present the potential of one of the sections of high-energy physics—relativistic nuclear physics—for the development of the concepts of nuclear clustering.

In the last decade, the concepts of ultracold dilute nuclear matter based on the condensation of nucleons in the lightest nuclei have been developed [4–7]. An $\alpha$-particle Bose-Einstein condensate ($\alpha$BEC) is considered as an analogue of atomic quantum gases [5, 7]. These developments put forward the problem of studying a variety of cluster ensembles and unbound nuclei as fundamental components of novel quantum matter. In a macroscopic scale coherent ensembles of clusters may play an

---

P.I. Zarubin (✉)
V.I. Veksler and A.M. Baldin Laboratory of High Energy Physics, Joint Institute for Nuclear Research, Dubna, Russia
e-mail: zarubin@lhe.jinr.ru

C. Beck (ed.), *Clusters in Nuclei, Volume 3*, Lecture Notes in Physics 875,
DOI 10.1007/978-3-319-01077-9_3,

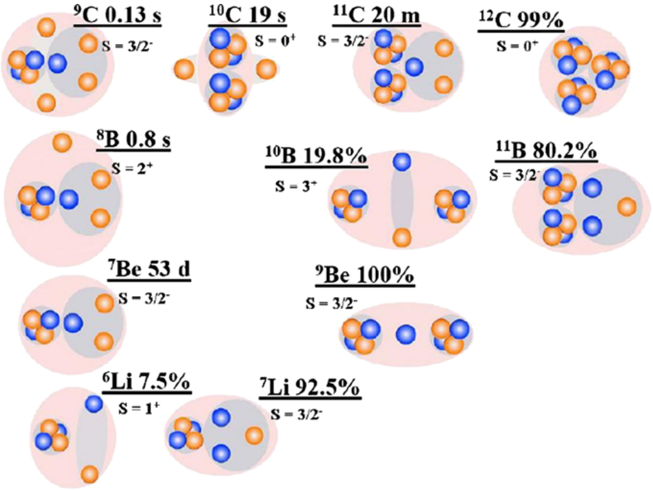

**Fig. 3.1** Diagram of cluster degrees of freedom in stable and neutron-deficient nuclei; abundances or lifetimes of isotopes, their spins and parities are indicated; *orange circles* correspond to protons and *blue ones*—to neutrons; clusters are marked as *dark background*

intermediate role in nucleosynthesis, which makes the study of nuclear clustering more important and going beyond the scope of the problems of nuclear structure. At first glance, the studies of nuclear many-body systems seem to be impossible in laboratory conditions. Nevertheless, they can be studied indirectly in nuclear disintegration processes when the excitation is slightly above the appropriate thresholds. The configuration overlap of the ground state of a fragmenting nucleus with the final cluster states is fully manifested in interactions at the periphery of the target nucleus when the introduced perturbation is minimal. It appears that the phenomenon of peripheral dissociation of relativistic nuclei can serve as an alternative "laboratory" for studying an unprecedented diversity of cluster ensembles.

This idea is based on the following facts. At collisions of nuclei of the energy above 1 *A* GeV, the kinematical regions of fragmentation of the projectile and target nuclei are clearly separated, and the momentum spectra of fragments come to asymptotic behavior. Thus, the regime of the limiting fragmentation of nuclei is reached, which also means that the isotopic composition of the fragments remains constant with increasing collision energy. Of particular value for the cluster physics are the events of peripheral dissociation of the incident nucleus with preservation of the number of nucleons in the region of its fragmentation. At a projectile energy above 1 *A* GeV the probability of such dissociation reaches a few percent. Definition of interactions as peripheral ones is facilitated by increasing collimation of fragments. Thresholds of detection of relativistic fragments are absent, and their energy losses in the detectors are minimal. All these factors are essential for experimental studies.

The cluster ensembles produced in fragmentation of relativistic nuclei are best observed in nuclear track emulsion (NTE). As an example, Fig. 3.2 shows the macro

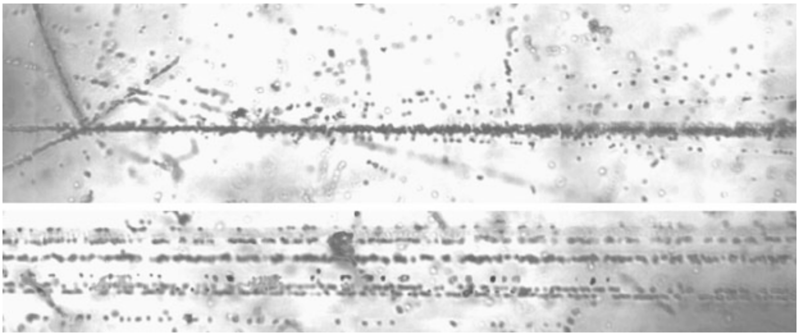

**Fig. 3.2** Fragmentation of a 3.65 $A$ GeV $^{28}$Si nucleus in nuclear track emulsion

photography of interaction in NTE of a 3.65 $A$ GeV $^{28}$Si nucleus. The granularity of the image is about 0.5 μm. Of particular interest is a group of relativistic H and He fragments with the total charge $\sum Z_{fr} = 13$. In the top photo one can see the fragment jet in a narrow cone accompanied by four singly charged relativistic particles in a wide cone and three fragments of the target nucleus. Moving in the direction of the jet fragments (bottom photo) allows three H and five He fragments to be distinguished. An intense “track” on the bottom photo (third from top) splits into a pair of tracks with $Z_{fr} = 2$ and the opening angle of about $2 \times 10^{-3}$ rad, which corresponds to the $^{8}$Be nucleus decay. Such narrow decays are frequently observed in the fragmentation of relativistic nuclei. They testify to the completeness of observations across the spectrum of cluster excitations.

According to NTE observations, the degree of dissociation of light nuclei as well as of the heaviest ones can reach a total destruction into the lightest nuclei and nucleons. Until now, information about this phenomenon has been fragmentary, and its interpretation has not been offered. Light nuclei are sources for the generation of the simplest configurations of the lightest clusters and nucleons. Being interesting by itself, their study provides a basis for understanding the dynamics of multiple fragmentations of heavy nuclei. The nuclear track emulsion exposed to relativistic radioactive nuclei makes it possible to diversify qualitatively the “tomography” of nuclear structure.

The study of cluster structure by relativistic dissociation has both fundamental and practical importance. First of all, the probabilities with which the cluster states are shown in dissociation are related to the fundamental parameters of the ground and excited states of light nuclei. The knowledge of probabilities allows one to determine possible initial configurations of nuclear clusters, which is important for the analysis of the whole variety of nuclear reactions. Clustering is the basis of the underlying processes accompanying the phenomenon of the physics of nuclear isobars, hypernuclei and quark degrees of freedom. The ideas about nuclear clustering obtained in high-energy physics are important for applications in nuclear astrophysics, cosmic ray physics, nuclear medicine, and perhaps even nuclear geology. In particular, the probability distributions of the final cluster states may suggest new ways of multiple particle nuclear fusion, as inverse processes to their dissociation.

At the JINR Nuclotron in 2002, the newly formed BECQUEREL collaboration launched a program of irradiation of NTE stacks in the beams of relativistic isotopes of beryllium, boron, carbon and nitrogen, including radioactive ones (Fig. 3.1). Coinciding with the name of the famous scientist, the project acronym indicates its key tasks—**Be**ryllium (**B**oron) **C**lustering **Que**st in **Rel**ativistic Multifragmentation [8]. The physical design of the program consisted in a systematic verification of the assumption that in the dissociation of light relativistic nuclei it is possible to study the characteristics of their cluster structure. This idea is not obvious, and its implementation by means others than NTE face objective difficulties. Analysis of NTE exposures can best explore the structure and kinematical characteristics of a variety of ensembles of relativistic clusters. The ultimate goal of NTE application is the most complete identification and metrology of unusual configurations of clusters. Detailed information about the structure of dissociation will be very useful for the feasibility studies of electronic experiments with high statistics of events.

Earlier observations among those discussed below were made in NTE exposures with the nuclei $^{12}$C [9], $^{16}$O [10], $^{22}$Ne [11], $^{6}$Li [12] and $^{7}$Li [13] and were carried out at the JINR Synchrotron in the 70–90s. Within the BECQUEREL project the peripheral interactions were analyzed in NTE (Fig. 3.2) exposed to the following set of nuclei: $^{6}$He [14], $^{10}$B [15], $^{7}$Be [16], $^{14}$N [17], $^{9}$Be [18, 19], $^{11}$B [20], $^{8}$B [21], $^{9}$C [22], $^{10}$C, and $^{12}$N [23–27]. These experimental results allow us to present a comprehensive picture of clustering for a family of nuclei at the beginning of the isotope table.

The references to works cited in these lecture notes cover mainly the experimental results on the fragmentation of relativistic nuclei obtained with the NTE technique. It is recognized that this list cannot claim to be complete. Our goal is limited by the desire to give the initial presentation and generate interest in self-immersion in an exciting and promising topic of fragmentation of relativistic nuclei. Some of the unique materials on the subject were not published sufficiently in the 70–90s due to circumstances beyond the authors' control, which makes their formal quoting difficult. Their preprints in Russian are stored on the BECQUEREL site [8]. We referred to them as to physical "folklore" when writing these notes.

## 3.2 Physics of Relativistic Nuclei

The BECQUEREL program owes its existence to a glorious era of research that deserves at least a brief reminder. The discovery of radioactivity by A.H. BECQUEREL at the same time made him the founder of the photographic method of its detection. Since then the searches for new phenomena in microphysics have been raising more and more new waves of interest in the use of nuclear photographs. Despite the known limitations in the statistics of the analyzed events, the classical method gives an objective topology of tracks in the full geometry, which allows one to see the prospects for technically advanced experiments. Events of multiple fragmentation of relativistic nuclei were observed as early as the 40s in NTE exposed to cosmic rays in the stratosphere [28]. Their photographs presented in the classic book by C.H. Powell, P.H. Fowler and D.H. Perkins [29], among other fundamental observations can serve as a model of clarity in our time. Our research is implemented in keeping with this tradition.

Beams of light nuclei of several $A$ GeV were produced at the JINR Synchrophasotron in Dubna and at the BEVALAC of the Lawrence Berkeley Laboratory in the early 70s. Thus, prerequisites appeared for the application of the concepts and methods of high-energy physics for the development of the relativistic theory of atomic nuclei. At the same time experimental studies with the use of the NTE technique began at spectrometers and bubble chambers. Their main thrust was the search for the universal laws that describe the collisions of relativistic composite systems. Transition of spectra of nuclear fragments in the regime of limiting fragmentation and scale-invariant behavior was established. In the case of an uncorrelated formation of groups of relativistic fragments the description of their spectra could be reduced to the superposition of universal functions. However, meeting the generalizing principles the physics of relativistic fragmentation appears to be richer and deeper.

A.M. Baldin proposed to classify multiple particle production in nuclear collisions based on the relativistic-invariant description [30]. The particles are considered in the four-velocity space

$$u_i = P_i/m_i, \tag{3.1}$$

where $P_i$ are 4-momenta of particles participating in the reaction, and $m_i$ are their masses. Experimental data are presented in dimensionless invariant variables

$$b_{ik} = -(P_i/m_i - P_k/m_k)^2 = -(u_i - u_k)^2 = 2\big[(u_i u_k) - 1\big] \tag{3.2}$$

The variables $b_{ik}$ are directly related to the Lorentz factor of the relative motion of particles $\gamma_{ik} = (u_i u_k)$. In the range of relative velocities $b_{ik} \gg 1$, the hadrons involved in the process lose the role of quasiparticles, since the interaction of their constituents is so weakened that they can be considered within the framework of perturbative QCD. In the transition region $0.1 < b_{ik} < 1$, subnucleon degrees of freedom become important in the reconstruction of the structure and interactions of hadrons. The region $b_{ik} < 10^{-2}$, corresponding to the interaction of weakly bound nucleon systems and nuclear clusters near the binding energy, is the domain of classical nuclear physics. It is a characteristic region for the physics of nuclear clustering. Invariant representation of the cluster kinematics can establish a connection with the findings of low-energy physics.

The discovery of exotic nuclei at the BEVALAC accelerator brought the nuclear beams to the forefront of nuclear physics and led to the production of beams of radioactive nuclei in many accelerators. Entirely new phenomena were established in the structure of light radioactive nuclei and in nuclear reactions with their participation. Anomalously large radii of light nuclei, explained on the basis of nuclear structures, which consisted of spatially separated nucleons and nuclear cores, were observed.

The Nuclotron, which replaced the JINR Synchrophasotron in the early 2000s, provides an opportunity to explore nuclear matter in the region $b_{ik} < 10^{-2}$ for the optimal choice of the initial energy and the kinematics of detection. With the development of research in relativistic nuclear physics magneto-optical channels of particle transportation were built at this machine allowing secondary beams of 2 $A$ GeV/$c$ nuclei [31] to be formed. The channel used in our exposures has a length of about 50 m and consists of four bending magnets; its acceptance is about 2–3 %.

The nuclear track emulsion technique at the JINR Synchrophasotron began to be used in the 50s with irradiations by 10 GeV protons [32]. Analysis of inelastic interactions of protons with nuclei of NTE composition pointed to the significant role of peripheral interactions. Often protons produced groups of mesons on Ag and Br nuclei which were visibly not destroyed. Later, these processes called coherent dissociation were studied in NTE irradiated by 70 GeV protons [33]. Similar reactions are possible in nucleus-nucleus interactions when the nucleus acts as a projectile, and the end result of coherent interaction is not the production of new particles, but the dissociation of the projectile nucleus. For the coherent dissociation of a projectile nucleus of the mass $M_0$ into a system of fragments with masses m$_i$ the threshold momentum of the nucleus is estimated as

$$p_{0min} \approx M_0 B^{1/3} \varDelta/\mu \tag{3.3}$$

where $\mu$ is the mass of the $\pi$ meson, $B$ is the mass number of the target nucleus, and $\varDelta = \sum m_i - M_0$ is mass defect with respect to the dissociation channel [9]. In particular, for the coherent dissociation of $^{12}\mathrm{C} \rightarrow 3\alpha$ in the Pb nucleus the estimate $p_{0min}$ is equal to approximately 300 MeV/$c$, and in the case of $^{16}\mathrm{O} \rightarrow 4\alpha$ $p_{0min}$ is roughly twice as much. Thus, the events of coherent dissociation of nuclei characterized by high thresholds should be investigated by experimental methods of high-energy physics.

The establishment in the early 70s of relativistic nuclear physics was supported by the community which had rich experience in NTE applications. The particle accelerators opened a possibility of exploring the interactions of different nuclei of certain values of energy that allowed the spectra of relativistic fragments to be studied by the NTE technique. NTE was irradiated by nuclei that were first accelerated at the JINR Synchrophasotron, at the BEVALAC and later at the accelerators AGS (BNL) and SPS (CERN). The developed stacks of NTE pellicles were transferred for analysis to research centers worldwide in the spirit of traditions of the emulsion collaborations that arose as far back as in the pioneer period of cosmic ray research.

The method received a motivation for further use because of its record-breaking resolution [29, 34]. It still retains uniqueness in the cone of relativistic fragmentation. The spatial resolution of the nuclear emulsion BR-2 (Russia) is 0.5 μm, and its sensitivity ranges from the most highly charged relativistic ions to singly charged relativistic particles. These features can be estimated in the photograph combining the pictures of the interaction of a relativistic sulfur nucleus and a human hair with a thickness of 60 μm (Fig. 3.3). Both images were obtained under identical conditions using a microscope and a digital camera. It can be argued that the nuclear emulsion gives the best projection of the events that occurred on the microcosm scale.

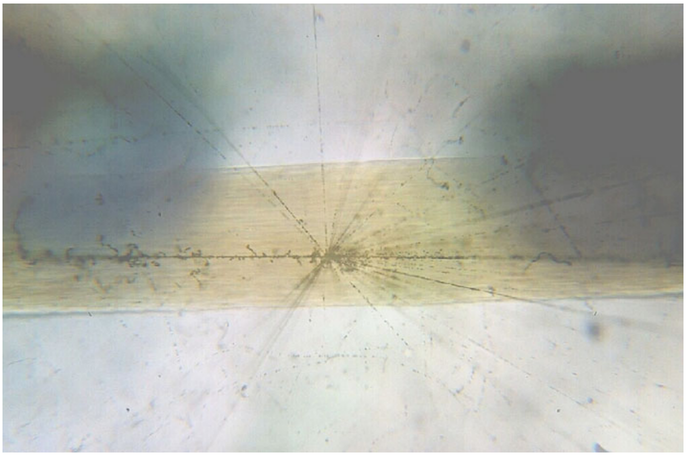

**Fig. 3.3** Superposed photographs of a collision of a relativistic sulphur nucleus and a human hair obtained in the same scale by means of a microscope and a digital camera

Over time, the observation of such beautiful images was considered to be taken for granted. Demonstration of nucleus-nucleus interactions was replaced by the classification of tracks, not obvious to specialists in other techniques. The value of such a classification began to be forgotten with the weakening of interest in NTE caused by complexity of measurements. To make the results available to the perception, conservation of the patterns of peripheral interactions of relativistic nuclei was resumed in our video collection [8].

The emulsion method contributed to the establishment of the fundamental properties that characterize the collision of relativistic composite systems. As a rule, the event search was conducted for the primary tracks without selection providing systematized observations. However, this approach limits the statistics of rare events. Particular attention was given to central collisions as candidates for exotic events. The labor consuming analysis of its many tracks was motivated by searches for nuclear matter at the highest concentration of density and energy—the intranuclear cascade and shock waves in nuclear matter and, to the greatest extent, the quark-gluon plasma. The modern development of this area is widely known.

The results of the 70–90s retain the value in the aspect of relativistic fragmentation. Among the observed interactions of a few percent of events were the peripheral fragmentation of nuclei into the narrow jets of light nuclei, nucleon clusters and nucleons with a total charge close to the initial charge of the nucleus [9–12, 35–45]. Often, the peripheral events were not accompanied by the formation of fragments of the target nuclei, in the case of which there appeared an analogy with the coherent dissociation of protons proceeding at multiple smaller mass differences between the final and initial states. One of the most striking examples is given in Fig. 3.4, which clearly shows the breakdown of ionization as a result of multiple fragmentation of the incident nucleus Au.

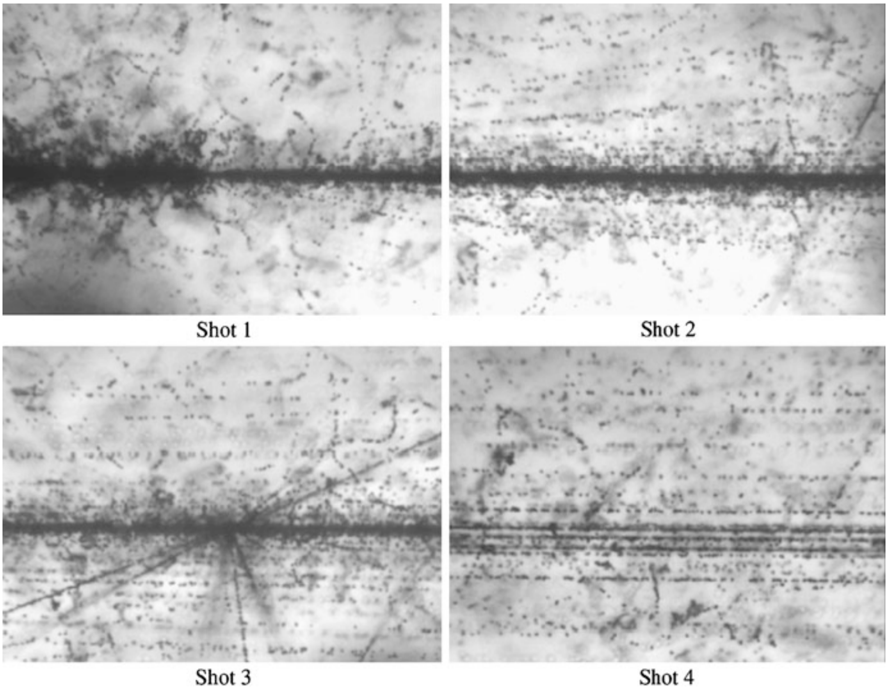
Shot 1
Shot 2
Shot 3
Shot 4

**Fig. 3.4** Consecutively photographed event of the peripheral interaction of a 158 *A* GeV $^{207}$Pb nucleus in nuclear track emulsion: primary nucleus track and interaction vertex followed by projectile fragment jet (Shot 1); jet core with apparent tracks of singly and doubly charged particles (Shot 2); jet core with a secondary interaction star (Shot 3); completely resolved jet core (Shot 4, 3 cm distance from the vertex)

Speaking about the nature of this phenomenon, it is possible to associate the probability of dissociation channels with the spectroscopic factors of the various cluster components of its ground state. These events indicate the disappearance of the Coulomb barrier of the nucleus and the exit of virtual clusters on the mass shell, followed by a rescattering. It is possible that the generation of fragment ensembles occurs not only in the states of the continuous spectrum. In the most “delicate” collisions, population of the excited states above the decay thresholds is possible. In addition, nucleon clusters formed in the peripheral dissociation of relativistic nuclei may have a diffractive scattering. Thus, the peripheral collisions contain unique information about the quantum-mechanical aspects of the formation of the cluster ensembles. This assumption requires verifications with clearly interpretable examples. Positive findings will provide a basis for the development of ideas about the physics of multiple cluster systems.

Despite their hidden aesthetics, peripheral interactions attracted a limited interest. Their study turned out to be in a shadow of “romantic” physics of central collisions. No less important is the fact that, although the possibility of a relativistic approach to the study of nuclear structure was recognized, its application without a complete registration of relativistic fragments appeared to be limited. The apparent simplicity of the fragmentation cone study is deceptive. With respect to such peripheral interactions NTE remains the only means of observation that provide not only unique observation, but also a reasonable statistics. Of course, NTE does not provide momentum analysis. However, due to the development of relativistic physics of few-nucleon systems based on magnetic spectrometers and bubble chambers a variety of data about the fragmentation of relativistic nuclei may be attracted.

Our study is aimed at exploring the coherent dissociation of neutron deficient nuclei, adjacent to the beginning of the table of isotopes (Fig. 3.1), since the NTE technique offers special advantages for this. The following issues were raised:

1. How does relativistic dissociation reflect the $\alpha$-cluster structure of light nuclei?
2. How does $^{2,3}$H and $^{3}$He clustering manifest itself in relativistic dissociation?
3. Is the population of cluster ensembles requiring nucleon rearrangement beyond $\alpha$-clustering is possible in relativistic dissociation?
4. What is the proportion of nuclear diffractive and electromagnetic mechanisms of dissociation on heavy nuclei of NTE composition?

The stages of this study were closely related to the opportunities that arose at the JINR Nuclotron in the 2000s. In the final period of the operation of the JINR Synchrophasotron (1999), first experience of analysis was obtained when NTE was exposed to a mixed secondary beam of $^{6}$He and $^{3}$H nuclei. Construction of the system of slow extraction of accelerated nuclei from the Nuclotron (2002) made it possible to perform irradiation by $^{10}$B nuclei. The $2\alpha + d$ clustering was established for the $^{10}$B dissociation which motivated the irradiation by $^{14}$N nuclei to study the $3\alpha + d$ clustering and later by $^{11}$B nucleus exposure to study the $2\alpha + t$ clustering. The interest in the $^{11}$B nucleus quickened analysis of the $\alpha + t$ clustering in the early $^{7}$Li irradiation. To develop ideas about $^{3}$He-based clustering, irradiation was carried out in the secondary beam of $^{7}$Be nuclei formed in charge-exchange reactions of primary $^{7}$Li nuclei (2004–2005). The acceleration of the $^{10}$B nuclei allowed secondary beams of $^{9}$Be and $^{8}$B isotopes to be created. The results of these exposures gave grounds for exposures in the beams of $^{9,10}$C and $^{12}$N isotopes formed in the fragmentation of primary $^{12}$C nuclei (2005–2006). The resumption of the use of nuclear emulsion has led to the survival of the NTE technology, to the preservation of the experience in data analysis, and to the involvement of young researchers.

The next section presents the approaches taken to analyze the interactions of relativistic nuclei in emulsion and the key facts on the peripheral dissociation of light stable nuclei. Their combined use became the basis for the proposal of the BECQUEREL experiment for the study of radioactive nuclei.

**Fig. 3.5** Photograph of an NTE pellicle on a glass substrate and of a microscope with an installed photo camera

## 3.3 Dissociation of Relativistic Nuclei

### *3.3.1 Advantages of the NTE Technique*

An emulsion chamber is assembled as a stack of pellicles 550 μm thick and $10 \times 20$ cm$^2$ in size (Fig. 3.5). The factors in obtaining large event statistics are thickness reaching 80 g/cm$^2$ along the long side and complete efficiency of charged particle detection. NTE contain Ag and Br nuclei as well as H nuclei in similar concentrations. By the density of hydrogen NTE is close to a liquid hydrogen target. This feature allows one to compare in the same conditions the disintegrations of projectile nuclei in nuclear diffractive and electromagnetic dissociation on heavy target nuclei as well as in collision with protons.

The fragments of the relativistic nuclei are concentrated in a cone limited by the angle

$$\theta_{fr} \approx p_{fr}/p_0 \tag{3.4}$$

where $p_{fr} = 0.2$ GeV$/c$ is a quantity characterizing the Fermi momentum of nucleons, and $p_0$ is the momentum per nucleon of projectile nucleus. If the beam is directed parallel to the pellicles, the tracks of all relativistic fragments can stay long enough in a single pellicle for 3-dimensional reconstruction. The distribution of events over the interaction channels with different composition of charged fragments (or the charged topology) is a direct feature of the fragmentation of relativistic nuclei. The results on charge topology of coherent dissociation for the relativistic nuclei $^{16}$O, $^{22}$Ne, $^{24}$Mg, $^{28}$Si and $^{32}$S are summarized in [46].

In NTE the angular resolution for the tracks of relativistic fragments is of the order of $10^{-5}$ rad. Measurements of the polar angles $\theta$ of fragment emission are not sufficient for comparison of data for different values of the initial energy of nuclei.

More generic is a comparison by the values of the transverse momentum $P_T$ of fragments with the mass number $A_{fr}$ according to the approximation of

$$P_T \approx A_{fr} P_0 \sin\theta \tag{3.5}$$

which corresponds to conservation by the fragments of the velocity of the primary nucleus (or momentum $P_0$ per nucleon). Obviously, the most important is the $\theta$ angle resolution, since the $\theta$ distributions are “pressed against” zero. For $\alpha$-cluster nuclei the assumption about the correspondence of a relativistic fragment with the charge $Z_{fr} = 2$ to the $^4$He isotope is well justified. Separation of the isotopes $^3$He and $^4$He is required for neutron-deficient nuclei.

In the fragmentation of the NTE nuclei, strongly ionizing target fragments (Fig. 3.2) can be observed including $\alpha$ particles, protons with energy below 26 MeV energy and light nuclei—$n_b$ (b-particles), as well as non-relativistic protons above 26 MeV—$n_g$ (g-particles). In addition, the reactions are characterized by a multiplicity of mesons produced outside the cone of fragmentation—$n_s$ (s-particles). Using these parameters, conclusions can be drawn about the nature of the interaction.

In coherent dissociation events there are no fragments of the target nuclei ($n_b = 0$, $n_g = 0$) and charged mesons ($n_s = 0$). Events of this type were informally named as “white” stars due to the absence of tracks of strongly ionizing particles $n_h$ ($n_h = n_b + n_g$). “White” stars are produced by nuclear diffraction and electromagnetic interactions on heavy target nuclei. Their share in the total number of inelastic events is a few percent. The name “white” stars aptly reflects the “breakdown” of ionization in the transition from the primary nucleus track to a narrow cone of the secondary tracks down to $Z_{pr}$ times. This feature constitutes the main difficulty for electronic techniques, since the greater the degree of dissociation at the event, the harder it is to register. In nuclear track emulsions the situation is quite opposite.

The practical task of determining charge topology is identification of fragment charges $Z_{fr}$. Due to 4-fold difference in ionization, the charges of relativistic fragments $Z_{fr} = 1$ and 2 are determined already by visual search. The values of fragment charges $Z_{fr} \geq 3$ are determined by the density of gaps on tracks or by the density of $\delta$-electrons $N_\delta$ depending on charges as $Z_{fr}^2$. A valuable condition is the conservation by relativistic fragments of the charge of the beam nuclei $Z_{pr}$, i.e. $Z_{pr} = \sum Z_{fr}$ for the interpretation of “white” stars in NTE exposed to mixed secondary beams. It allows one to separate in the beam the contribution of lighter nuclei with a similar charge to mass ratio. This criterion is fundamentally important for NTE exposures in beams with complex composition. An example of charge separation of the beam nuclei and secondary fragments in the mixed-beam exposure to $^7$Be, $^{10}$C and $^{12}$N for events $\sum Z_{fr} = 6$ and 7 is shown in Fig. 3.6 [25–27]. In cases of light neutron-deficient nuclei the determination of charges allows one to determine their mass numbers.

Relativistic H and He isotopes are identified by their values $p\beta c$, where $p$ is fragment momentum and $\beta c$ is its velocity. Due to “quantization” of fragment momenta their mass numbers $A_{fr}$ are defined as $p_{fr}\beta_{fr}c/(p_0\beta_0 c)$. The $p\beta c$ value is determined

**Fig. 3.6** Distribution of the beam particle tracks $N_{ev}$ (*solid line*) and secondary fragments (*dashed line*) with respect to the mean number of $\delta$-electrons $N_\delta$, over 1 mm of the track length in nuclear track emulsion exposed to a mixed beam of $^7$Be, $^{10}$C and $^{12}$N nuclei

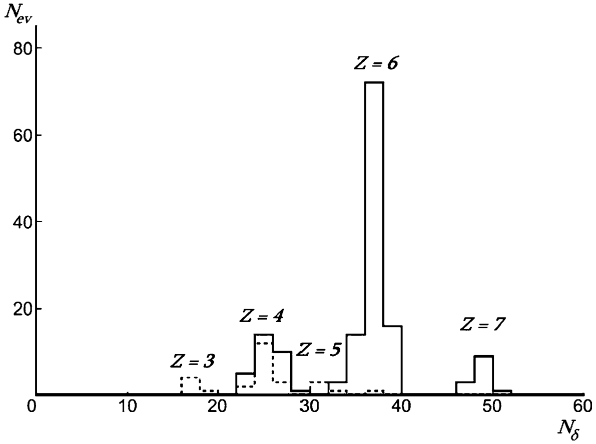

by the average angle of multiple Coulomb scattering estimated via the track offsets $|D|$ on 2–5 cm track sections. It is necessary to measure $|D|$ not less than in 100 points in order to achieve 20–30 % accuracy of $p\beta c$ determination comparable to the difference $A_{fr}$ for $^3$He and $^4$He. This labor-intensive method is not a routine procedure, and its use is justified in fundamentally important cases for limited number of fragment tracks.

In particular, this method was applied in the analysis of NTE exposure [22] to 2 $A$ GeV/$c$ $^9$C nuclei in a situation when the $^3$He nuclei having the same magnetic rigidity as the $^9$C were predominant in the beam. The average value $\langle p\beta c\rangle_{^3\mathrm{He}}$ for the beam $^3$He nuclei was (5.1 ± 0.1) GeV with RMS of 0.8 GeV, which is close to the expected value of 5.4 GeV (for $^4$He—7.2 GeV) and is acceptable for separation of the isotopes $^3$He and $^4$He. The "white" stars with fragments of $Z_{fr} = 5$ and 4 and with the beam particle charges $Z_{pr} = 6$ found in this exposure were interpreted as $^9\mathrm{C} \to {}^8\mathrm{B} + p$ and $^7\mathrm{Be} + 2p$. Indeed, the distribution of particles $Z_{fr} = 1$ has $\langle p\beta c\rangle_\mathrm{H} = (1.5 \pm 0.1)$ GeV and RMS of 0.4 GeV, which corresponds to protons.

The states of 3$^3$He became a central subject of study of the coherent dissociation of $^9$C. Only for 22 He tracks in 16 found "white" stars C → 3He it was possible to perform $p\beta c_{^3\mathrm{He}}$ value measurements (Fig. 3.7). The average value is $\langle p\beta c_{^3\mathrm{He}}\rangle =$ (4.9 ± 0.3) GeV for RMS of 0.9 GeV and corresponds to the calibration of the $^3$He beam nuclei. Only for three $^3$He "white" stars the determination of $p\beta c$ was possible for all of the fragments allowing these events to be identified as 3$^3$He most reliably.

The values $p\beta c_{^4\mathrm{He}}$ were measured for H and He tracks of 16 "white" stars $^{10}\mathrm{C} \to 2\mathrm{He} + 2\mathrm{H}$ in the NTE exposed to a mixed beam of isotopes $^7$Be, $^{10}$C and $^{12}$N [25–27] with the same momentum per nucleon as in the case of $^9$C. The dominance of $^1$H and $^4$He isotopes confirms the separation of $^{10}$C (Fig. 3.7). In the case of He nuclei, 23 tracks were taken from the $^8\mathrm{Be}_{g.s.}$ decays. For all He tracks measured in the exposure to $^9$C (including $^3$He calibration) the average value is $\langle p\beta c_{^3\mathrm{He}}\rangle = (5.0 \pm 0.1)$ GeV at RMS of 0.8 GeV, and in the of $^{10}$C it is $\langle p\beta c_{^4\mathrm{He}}\rangle = (7.9 \pm 0.2)$ GeV at RMS of 0.8 GeV. Thus, two groups of measurements clearly correspond to different He isotopes. Figure 3.7 shows the distribution of the measured values of $p\beta c$ for

**Fig. 3.7** Distribution of the measured values $p\beta c$ for fragments from “white” stars $^{10}C \to 2He + 2H$ (*solid line*—He, *shaded histogram*—H) and $^{9}C \to 3He$ (*dashed line*)

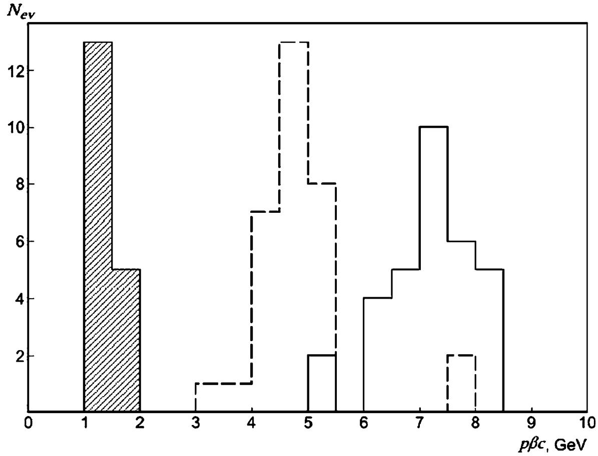

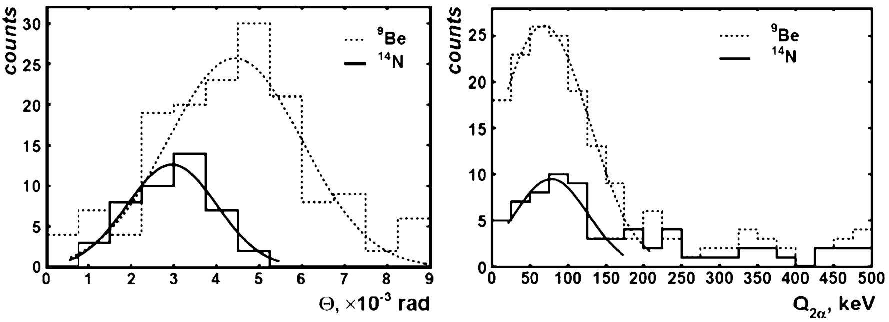

**Fig. 3.8** Distribution of the opening angles $\Theta$ in $\alpha$-particle pairs (*left*) and energy $Q_{2\alpha}$ (*right*) for fragmentation events $^{9}Be \to {}^{8}Be_{g.s.}(0^{+})$ at 2 $A$ GeV/$c$ and $^{14}N \to {}^{8}Be_{g.s.}(0^{+})$ at 2.9 $A$ GeV/$c$

He fragments of the events $^{9}C \to 3^{3}He$ [22]. $^{3}$He and $^{4}$He fragments are clearly separated by $p\beta c$.

The excitation energy of a fragment system $Q$ is defined as the difference between the invariant mass of the fragmenting system $M^{*}$ and the mass of the primary nucleus $M$, i.e. $Q = M^{*} - M$. $M^{*}$ is the sum of all products of the fragment 4-momenta $P_{i,k}M^{*2} = \sum(P_i \cdot P_k)$. 4-momenta $P_{i,k}$ are determined in the approximation of conservation of the initial momentum per nucleon by fragments. The opening angle distributions of $\alpha$-particle pairs $\Theta$ are superposed in Fig. 3.8 for the dissociation $^{9}Be \to {}^{8}Be_{g.s.}$ at 2 $A$ GeV/$c$ [18, 19] and for $^{14}N \to {}^{8}Be_{g.s.}$ at 2.9 $A$ GeV/$c$ [17]. Their average values differ significantly: $(4.4 \pm 0.2) \times 10^{-3}$ rad and $(3.0 \pm 0.2) \times 10^{-3}$ rad, which points to the sensitivity of the measurements to the reduction of the decay cone with increasing momentum. Overlaying when transformed to the $Q_{2\alpha}$ (Fig. 3.8) points to on the identity of the source of narrow $\alpha$ pairs in both cases to $^{8}Be_{g.s.}(0^{+})$ decays with the average energy $\langle Q_{2\alpha}\rangle = (68 \pm 14)$ keV for $^{9}$Be and $(78 \pm 14)$ keV for $^{14}$N. Thus, the observation of the ground state de-

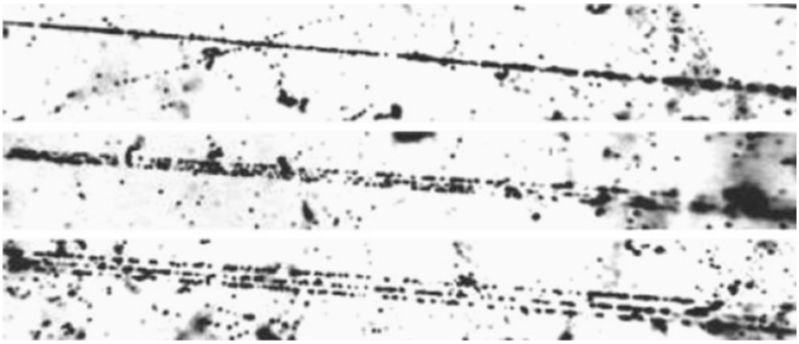

**Fig. 3.9** Coherent dissociation $^{12}C \to 3He$ at 4.5 *A* GeV/*c*; *upper photo*: an interaction vertex and a fragment jet; *middle* and *lower photo*: shifting from the vertex along the fragment jet allows three tracks of doubly charged fragments to be distinguished

**Table 3.1** Charge topology of the fragments of the coherent dissociation of 4.5 *A* GeV/*c* $^{16}O$ nuclei

| N + H | C + He | C + 2H | B + 3H | B + He + H | Be + He | Be + He + H | 4He | 3He + 2H |
|---|---|---|---|---|---|---|---|---|
| 18 | 21 | 7 | 2 | 10 | 1 | 1 | 9 | 3 |

cay of the $^8$Be nucleus shows a fine resolution of angle measurements as well as convenience of invariant representation.

### 3.3.2 Coherent Dissociation of Relativistic $^{12}$C and $^{16}$O Nuclei

At the JINR Synchrophasotron in the early 70s, NTE was exposed to 4.5 *A* GeV/*c* $^{12}$C nuclei (energy of 3.65 *A* GeV). The statistics of 2468 interactions found along a 338 m scanned path of primary tracks included 28 “white” stars. The only option for these stars was the cluster breakup $^{12}C \to 3\alpha$ (threshold $E_{th} = 7.3$ MeV) limited in the cone $\theta < 3°$ (example in Fig. 3.9). Later the NTE was enriched with lead to enhance the electromagnetic dissociation [9]. The search for events was carried out in an accelerated manner over the NTE pellicle area. As a result, the statistics had already 72 “white” stars $^{12}C \to 3\alpha$. A key observation became relativistic $^8$Be decays that constituted at least 20 %.

The same approach was extended to the $^{16}$O nucleus. Table 3.1 shows an increased variety of channels. This distribution leads to a probability distribution. The channels C + He ($E_{th} = 7.2$ MeV, example in Fig. 3.10) and N + H ($E_{th} = 12.1$ MeV) are leading. The statistics of “white” stars $^{16}O \to 4\alpha$ (example in Fig. 3.11) that were found in an accelerated search reached 641 events [10], demonstrating in NTE the possibility of studying processes with the cross-section $10^{-2}$–$10^{-3}$ of the inelastic cross-section. The probabilities of cascading channels

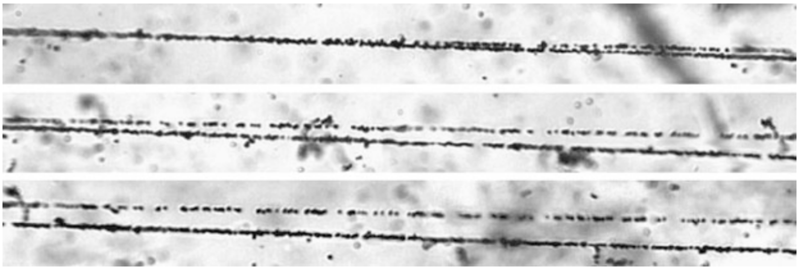

**Fig. 3.10** Coherent dissociation $^{16}$O $\rightarrow$ C + He at 4.5 $A$ GeV/$c$

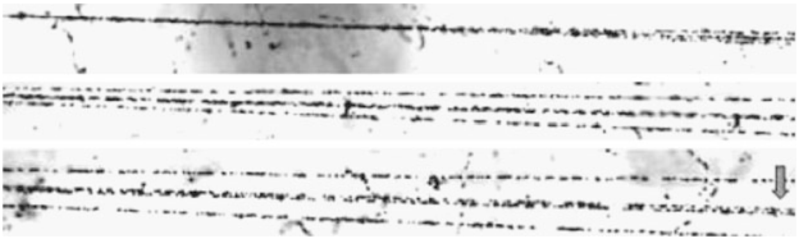

**Fig. 3.11** Coherent dissociation $^{16}$O $\rightarrow$ 2He + $^{8}$Be$_{g.s.}$ at 4.5 $A$ GeV/$c$; arrow points to tracks of the decay $^{8}$Be$_{g.s.} \rightarrow 2\alpha$

defined by simulation were ≈25 % for the $^{8}$Be + 2$\alpha$ and ≈20 % for 2$^{8}$Be. Thus, the relativistic 4$\alpha$-system proved to be strongly correlated.

### *3.3.3 Features of the Dissociation of Heavier Nuclei*

The progress in the development of the JINR Synchrophasotron as a source of relativistic nuclei achieved in the 80s has made it possible to perform exposures with the $^{22}$Ne, $^{24}$Mg, $^{28}$Si and $^{32}$S nuclei. The information received at that time about the peripheral fragmentation of nuclei retains its uniqueness and provides motivation for future experiments. We illustrate this statement, basing on the measurements of interactions of 3.22 $A$ GeV $^{22}$Ne nuclei. The statistics of events is traced in Table 3.2 for the channels $\sum Z_{fr} = 10$ with multiplicities of the target fragments $n_b$ and $n_g$. There are channels present, starting from the separation of single fragments $Z_{fr} = 1$ and 2 down to the destruction into the lightest nuclei (example in Fig. 3.12). An obvious feature is the dominance of “white” stars. Such distributions for relativistic Mg, Si and S nuclei have similar pattern.

A nuclear state analogous to the dilute Bose-Einstein condensate (BEC) can manifest itself in the formation of N$\alpha$-particle ensembles with a narrow velocity distribution in the center of mass. However, the c.m.s. definition is difficult enough, while the analysis of jets in the 4-velocity space $b_{ik}$ can represent N$\alpha$-systems in a universal way. Events $^{22}$Ne $\rightarrow$ N$\alpha$ were selected, satisfying the criterion of $b_{ik} < 10^{-2}$

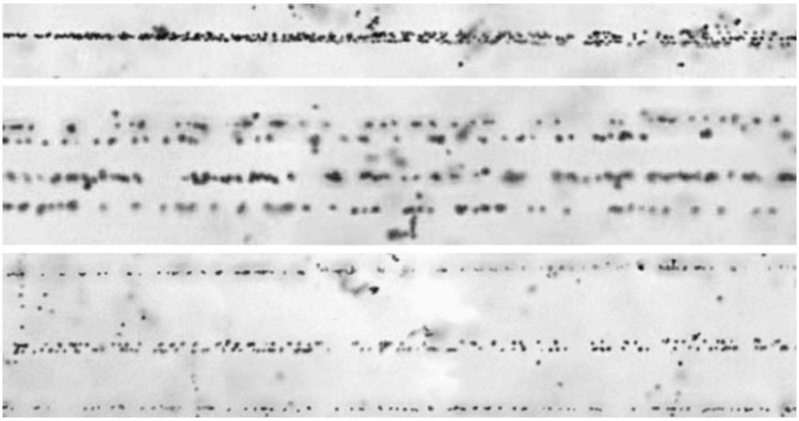

**Fig. 3.12** Coherent dissociation $^{20}\mathrm{Ne} \to 3\mathrm{He} + {}^{8}\mathrm{Be}_{g.s.}(0^{+})$ at 4.5 *A* GeV/*c*

**Table 3.2** The distribution of the peripheral interactions of 3.22 *A* GeV $^{22}$Ne nuclei over multiplicity of target fragments $n_b$ and $n_g$ ($n_s = 0$); in parenthesis is share in %

| $n_b$ | 0 | 0 | 1 | 2 | 3 | >3 |
|---|---|---|---|---|---|---|
| $n_g$ | 0 | 1 | 0 | 0 | 0 | 0 |
| F + H | 26(19.5) | 9(15.0) | 13(44.8) | 2 | – | 1 |
| O + He | 54(40.6) | 19(31.7) | 2(6.9) | – | 1 | 1 |
| O + 2H | 12(9.0) | 7(11.7) | – | – | – | – |
| N + He + H | 12(9.0) | 7(11.7) | 4(13.8) | 1 | – | – |
| N + 3H | 3(2.3) | 3(5.0) | – | – | – | – |
| C + 2He | 5(3.8) | 3(5.0) | 3(10.3) | 1 | – | – |
| C + 2He + 2H | 5(3.8) | 3(5.0) | 3(10.3) | – | – | – |
| C + 4H | 2(1.0) | – | – | – | – | – |
| B + Li + H | 1(0.8) | – | – | – | – | – |
| B + 2He + H | 2(1.5) | 1(1.7) | – | – | – | – |
| B + He + H | 2(1.5) | 1(1.7) | – | – | – | – |
| B + 5H | 1(0.8) | – | 1(3.4) | – | – | – |
| 2Be + 2H | – | 1(1.7) | – | – | 1 | – |
| Be + Li + 3H | 1(0.8) | – | – | – | – | – |
| Be + 3H | 2(1.5) | – | – | – | – | – |
| Be + He + 4H | 1(0.8) | – | – | – | – | – |
| Li + 3He + H | – | 1(1.7) | – | – | – | – |
| 5He | 3(2.3) | – | 1(3.4) | 2 | 1 | – |
| 4He + 2H | 1(0.8) | 5(8.3) | 2(6.9) | – | – | – |

for each $\alpha$-pair for $\mathrm{N}_\alpha = 3$, 4 and 5. Figure 3.13 shows the distribution of normalized excitation energy $Q' = Q/(4\mathrm{N}\alpha)$. Despite the increase in multiplicity, N$\alpha$-jets remain similar. Three "white" stars were found among the events of $^{22}\mathrm{Ne} \to 5\alpha$. Of these there were two "golden" events containing all $\alpha$-particles within the 1°

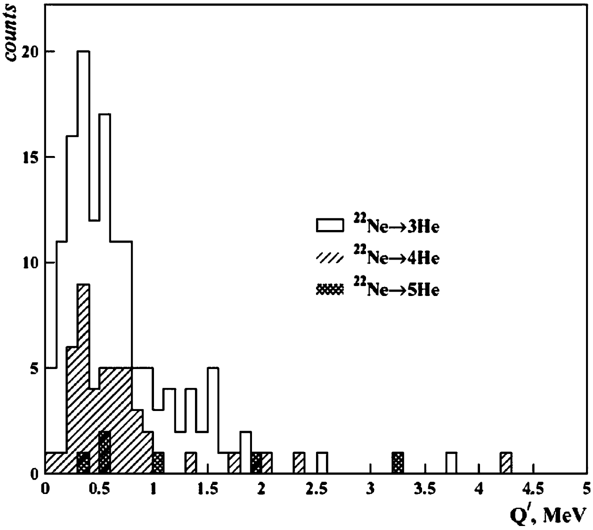

**Fig. 3.13** Distribution of $\alpha$-particle pairs produced in the fragmentation $^{22}\mathrm{Ne} \to \mathrm{N}\alpha$ over energy $Q'$ (per nucleon of a fragment)

cone. For these two events, the values $Q'$ are very small—400 keV and 600 keV per nucleon. The detection of these 5$\alpha$-states is an argument in favor of searching for $\alpha$-particle Bose-Einstein condensate in relativistic fragmentation.

### 3.3.4 Cluster Structure of $^6$Li and $^7$Li Nuclei

The data on the interactions of 4.5 $A$ GeV/$c$ $^6$Li nuclei [12] attracted our attention to the NTE technique for addressing the issues of cluster structure. The $^6$Li nucleus is the only among stable nuclei except the deuteron that are attributable to nuclei with exotic structure. Due to increased sizes and weak nucleon coupling the exotic nuclei are characterized by enhanced interaction cross-sections and narrowed momentum distributions of their cores in fragmentation. These properties of the $^6$Li nucleus are manifested in the relativistic fragmentation in NTE.

The free path with respect to inelastic interactions, which happened to be about 3 cm shorter than the one calculated by the Bradt-Peters formula ($\approx$17 cm) [28], suggests an anomalously large radius of the $^6$Li nucleus. In the model of the geometric overlap of nuclear densities its value is equal to $(2.7 \pm 0.1)$ Fermi which is consistent with the data on the radius of the $^6$Li nucleus. A feature of the isotopic composition of $^6$Li fragments was an unusually high yield of deuterons nearly equal to the yield of protons, which was not observed in the fragmentation of the $^4$He, $^{12}$C, $^{22}$Ne, and $^{28}$Si nuclei. For the fragmentation $^6\mathrm{Li} \to \alpha$ the value of the mean transverse momentum of $\alpha$ particles turned out to be reduced—$\langle P_{T_\alpha} \rangle = (0.13 \pm 0.01)$ GeV/$c$, while for the interactions of $^{12}$C nuclei this value was $\langle P_{T_\alpha} \rangle = (0.01 \pm 0.24)$ GeV/$c$. 31 "white" stars in which fragments were completely identified can be regarded as "golden" events (example in Fig. 3.14). Among them there are 23 events corresponding to the dissociation channel $\alpha + d$ ($E_{th} = 1.47$ MeV), and there are 4 events

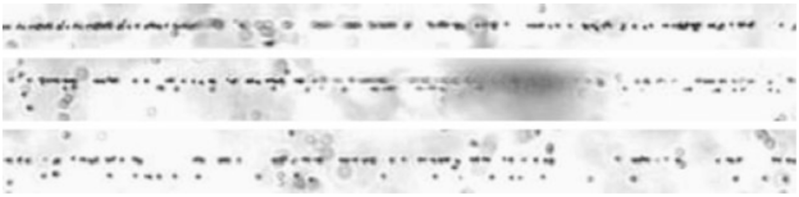

**Fig. 3.14** Coherent dissociation $^6$Li → He + H at 4.5 *A* GeV/*c*

**Fig. 3.15** Differential cross-section of the coherent dissociation $^7\text{Li} \to {}^4\text{He} + {}^3\text{H}$ at 4.5 *A* GeV/*c* over the total transverse momentum $Q$ [47]; experimental data and theoretical dependences of Coulomb (C) and nuclear diffractive (N) interactions

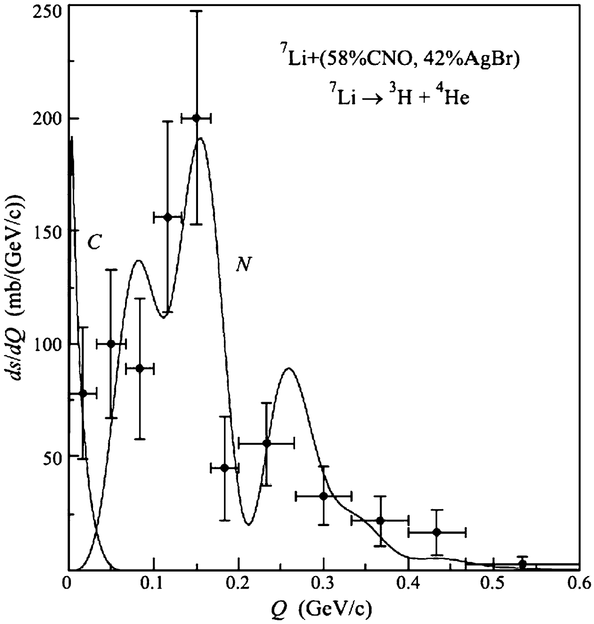

in the channels $^3\text{He} + t$ ($E_{th} = 15.8$ MeV) and $t + d + p$ ($E_{th} = 21.2$ MeV). Thus, the $\alpha + d$ cluster structure is clearly manifested.

The question of the triton as a cluster was resolved based on an analysis of the "white" stars $^7\text{Li} \to \text{He} + \text{H}$ [12]. Determination of the masses of the relativistic fragments showed that 50 % of these events represent the channel $\alpha + t$ ($E_{th} =$ 2.5 MeV), while the channel $\alpha + d + n$ constitued 30 % ($E_{th} = 6.1$ MeV) and $\alpha + p + 2n$ ($E_{th} = 7$ MeV)—20 %. These findings stimulated the analysis of the relationship of nuclear and electromagnetic diffraction mechanisms of cluster dissociation on a mixture of NTE nuclei [47]. The first type of interaction for the $\alpha + t$ channel covers the total momentum range $50 < P_T < 500$ MeV/$c$, and the second—considerably narrower—$P_T < 50$ MeV/$c$ (Fig. 3.15).

### *3.3.5 Exposure in a Mixed Beam of $^6$He and $^3$H Isotopes*

Before the beginning of exposures under the BECQUEREL project experience was gained in the analysis of nuclear emulsion exposed to the beam "cocktail" of a mixture of $^6$He and $^3$H nuclei [14, 29]. An extracted beam of 2.67 $A$ GeV/$c$ $^6$Li nuclei was directed to a plexiglass target located at the focal point of the beam transport channel. The $^6$He nucleus beam was formed by using the selection of products of the charge-exchange process $^6$Li $\rightarrow$ $^6$He. The secondary particles produced almost at a zero angle were seized by the channel tuned to the selection of particles with charge to mass number $Z_{pr}/A_{pr} = 1/3$. The percentage of $^6$He nuclei was about 1 %, and $^3$H nuclei were dominant.

A few "white" stars with a noticeable change in the direction of doubly charged tracks in which the $^6$He nucleus lost a neutron pair and emitted $\alpha$ particles were found in this exposure. The average transverse momentum of these $\alpha$ particles is $\langle P_{T_\alpha} \rangle \approx 35$ MeV/$c$. Thus, an indication for a drastically narrower distribution $P_{T_\alpha}$ for the coherent dissociation of $^6$He was obtained, in which the neutron halo is exhibited as a structural feature of this nucleus. However, the value of the $^6$He mean free path, including the registered coherent interactions, was $16.3 \pm 3.1$ cm, being significantly greater than for $^6$Li. It can be assumed that excessive mean range for $^6$He is due to lack of efficiency of observations of the coherent dissociation $^6$He $\rightarrow$ $^4$He + 2$n$ (no more than 50 %). This assumption means that the contribution of coherent interactions is not less than 20 %. This experiment indicated the importance of selecting "white" stars together with neutrons to determine the characteristics of the cluster structure. It should be recognized that in the case of neutron-rich nuclei per nucleon electronic experiments in the energy range of a few tens of $A$ GeV with the detection of neutrons by hadron calorimeters have the best prospects.

## 3.4 First Exposures at the JINR Nuclotron

### *3.4.1 Dissociation of the $^{10}$B Nucleus*

The $\alpha + d$ clustering of the $^6$Li nucleus, which was demonstrated with remarkable detail [12], led to an idea to identify a more complicated clustering—$2\alpha + d$—in the next odd-odd nucleus—$^{10}$B [15]. The thresholds of separation of nucleons and lightest nuclei are close for this nucleus—$E_{th}(^6\text{Li} + \alpha) = 4.5$ MeV, $E_{th}(^8\text{Be} + d) = 6.0$ MeV, $E_{th}(^9\text{Be} + p) = 6.6$ MeV. It was found that in approximately 65 % of peripheral interactions ($\sum Z_{fr} = 5, n_s = 0$) of 1 $A$ GeV $^{10}$B nuclei occur via the 2He + H channel (example in Fig. 3.16). A singly charged particle in ≈40 % of these events is the deuteron. The abundant deuteron yield is comparable with the $^6$Li case and points to the deuteron clustering in the $^{10}$B nucleus. Events in the He + 3H channel constitute 15 %. 10 % of the events contain both Li and He fragments. The presence (or absence) of fragments of the target nucleus has practically no effect on the charge topology of the projectile nucleus fragmentation.

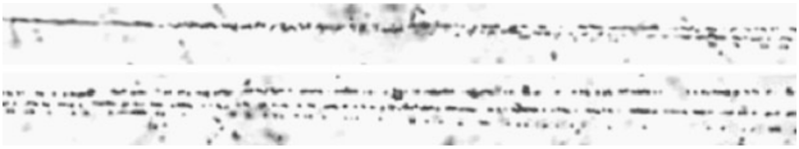

**Fig. 3.16** Coherent dissociation $^{10}$B $\rightarrow$ 2He + H at 1.8 $A$ GeV/$c$

Just 2 % of the events contain fragments with charges $Z_{fr} = 4$ and 1, i.e. the $^{9}$Be nucleus and the proton. This "negative" observation merits attention because it serves as a test of the relation of the shell and cluster description of the $^{10}$B nucleus. Indeed, the spin of this nucleus is equal to 3, which explains the $p$-shell filling order. Removal of a proton from the p-shell leads to the formation of the $^{9}$Be nucleus with spin $3/2$. Thus, the separation of the proton does not require the transfer of the angular momentum. However, this channel is suppressed, which indirectly favors the leading role of the $2\alpha + d$ structure in the $^{10}$B ground state.

A valuable finding of the exposure is an event of the coherent dissociation $^{10}$B $\rightarrow$ 3He. Associated with the rearrangement of nucleons in $\alpha$ clusters, the process $^{10}$B $\rightarrow$ 2$^{3}$He + $^{4}$He could proceed via the charge-exchange reaction $^{10}$B $\rightarrow$ $^{6}$Li + $^{4}$He $\rightarrow$ $^{3}$H + $^{3}$He + $^{4}$He $\rightarrow$ 2$^{3}$He + $^{4}$He ($E_{th} = 20$ MeV). By the charge composition this event is almost certainly identified as $^{10}$B $\rightarrow$ 2$^{3}$He + $^{4}$He, since the threshold of breakup of the second $\alpha$ cluster $^{10}$B $\rightarrow$ 3$^{3}$He + $n$ is even 16 MeV higher. The measurements of multiple scattering of the He tracks have confirmed this interpretation.

### 3.4.2 Dissociation of the $^{11}$B Nucleus

The determining role of the $^{3}$H cluster in the fragmentation of $^{7}$Li motivated a study of the triton cluster in the breakups of 2.75 $A$ GeV $^{11}$B nuclei [20]. The experiment was aimed at the channels with low thresholds of cluster separation—$E_{th}(^{7}\mathrm{Li}+\alpha) =$ 8.7 MeV, $E_{th}(2\alpha + t) = 11.2$ MeV and $E_{th}(^{10}\mathrm{Be} + p) = 11.2$ MeV. A leading channel, 2He + H, was also established for the $^{11}$B nucleus. Similarly to the case of $^{10}$B, a large proportion of tritons in the $^{11}$B "white" stars favor its existence as a cluster. However, the increasing excess of neutrons that require (as in the case of $^{7}$Li) an increasing volume of measurements of multiple scattering leads to a decrease in the effectiveness of our approach.

Eight "white" stars of the charge-exchange reaction $^{11}$B $\rightarrow$ $^{11}$C$^{*}$ $\rightarrow$ $^{7}$Be + $^{4}$He have been found. Charge exchange events through other channels were not observed. This fact demonstrates that while a three-body channel leads in $^{10}$B and $^{11}$B breakups, the two-body leads in the $^{11}$C case. These observations motivate a direct study of $^{11}$C dissociation through the channels $^{7}$Be + $\alpha$ ($E_{th} = 7.6$ MeV), $^{10}$B + $p$ ($E_{th} = 8.7$ MeV) and $^{3}$He + 2$\alpha$ ($E_{th} = 9.2$ MeV).

One should note the practical value of information about the $^{11}$C structure for nuclear medicine. In contrast to the $^{12}$C nucleus there should also be a significant

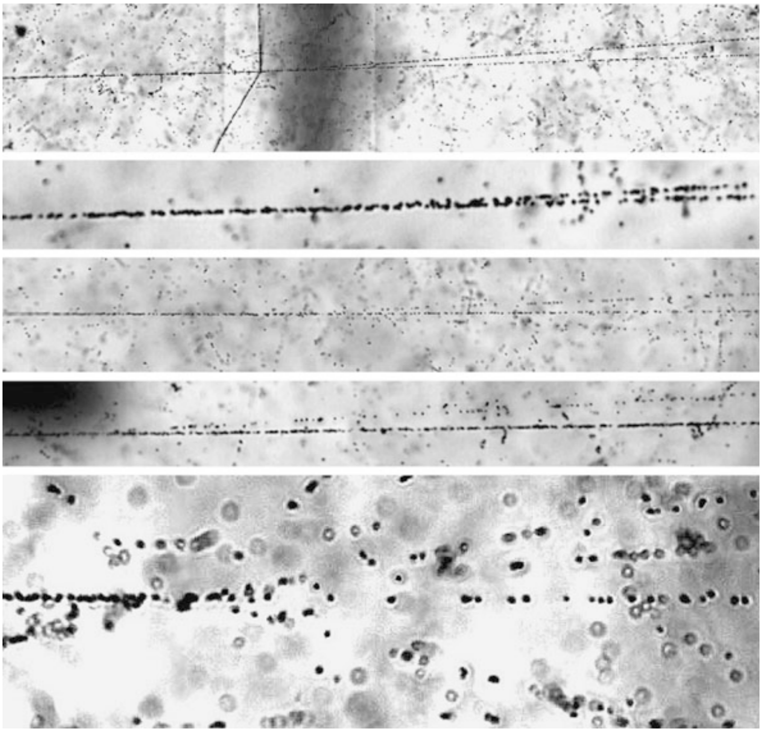

**Fig. 3.17** Examples of events of the peripheral dissociation of $^7$Be nuclei at 2 $A$ GeV/$c$; *top* photo: splitting on two He fragments with production of a pair of target nucleus fragments; *below*: “white” stars 2He, He + 2H, Li + H and 4H

contribution of the $^7$Be nucleus in the final states of $^{11}$C fragmentation. This circumstance leads to less “spreading” of ionization from $^{11}$C fragmentation products.

### 3.4.3 Dissociation of the $^7$Be nucleus

The next stage was peripheral interactions of the $^7$Be nuclei obtained in charge-exchange reactions of 1.2 $A$ GeV $^7$Li nuclei [16, 29]. The numbers of events in various channels of $^7$Be fragmentation with the charge topology $\sum Z_{fr} = 4$ are presented in Table 3.3 (examples in Fig. 3.17). Statistics of 94 coherent $N_{ws}$ ($n_h = 0$) and 55 non-coherent events $N_{tf}$ ($n_h > 0$) is presented. Dissociation thresholds for the given channels $E_{th}$ are indicated (MeV).

Approximately 50 % of the dissociation events occur without neutron emission, i.e., when $\sum A_{fr} = 7$. In general, the coherent dissociation $\sum Z_{fr} = 4$ and $\sum A_{fr} = 7$ is determined by the configuration of $^4$He + $^3$He in the $^7$Be structure. The channels with a high threshold, in which there is no $^4$He cluster play a noticeable role. The statistics of the channels with He clusters shows a weak dependence on the values

**Table 3.3** Distribution of $^7$Be interactions over identified fragmentation channels $\sum Z_{fr} = 4$

| Channel | $^4$He + $^3$He | $^3$He + $^3$He | $^4$He + 2$p$ | $^4$He + $d$ + $p$ | $^3$He + 2$p$ | $^3$He + $d$ + $p$ | $^3$He + 2$d$ | $^3$He + $t$ + $p$ | 3$p$ + $d$ | $^6$Li + $p$ |
|---|---|---|---|---|---|---|---|---|---|---|
| $E_{th}$, MeV | (1.6) | (22.2) | (6.9) | (12.9) | (29.9) | (29.5) | (25.3) | (21.2) | (35.4) | (5.6) |
| $N_{ws}$ | 30 | 11 | 13 | 10 | 9 | 8 | 1 | 1 | 2 | 9 |
| (%) | (31) | (12) | (14) | (11) | (10) | (9) | (1) | (1) | (2) | (10) |
| $N_{tf}$ | 11 | 7 | 9 | 5 | 9 | 10 | | | 1 | 3 |
| (%) | (20) | (12) | (16) | (9) | (16) | (19) | | | (2) | (6) |

of dissociation thresholds. Apparently, the role of the $^3$He cluster in the $^7$Be nucleus goes beyond the $^4$He + $^3$He bond. Table 3.3 gives suggestions for the probabilities of possible configurations in the $^7$Be ground state including unobserved neutrons.

## 3.5 Fragmentation of the $^9$Be Nucleus

The $^9$Be nucleus having the properties of the loosely bound system $2\alpha + n$ is the "cornerstone" of cluster physics. Due to its low neutron separation threshold, dissociation of $^9$Be can be a source of unstable $^8$Be nuclei. The $^8$Be isotope is known as the only nucleus whose ground state is characterized as the $\alpha$-particle Bose condensate. Investigation of the $^9$Be nucleus fragmentation in $\alpha$-particle pairs seems to be an obvious starting point towards more complicated N$\alpha$-systems. However, there is a practical obstacle on the way of studying this stable nucleus. Beryllium is a toxic element which makes immediate acceleration of $^9$Be nuclei impossible. Therefore, a secondary beam of relativistic $^9$Be nuclei was obtained in the fragmentation reaction $^{10}$B → $^9$Be [18, 19, 29]. The share of $^9$Be nuclei was approximately $2/3$, while $1/3$ fell on He and Li isotopes.

In the two-body model used for the calculation of the magnetic moment [48, 49] of the $^9$Be nucleus, the latter is represented as a bound state of the neutron and $^8$Be core in the $0^+$ (g.s.) and $2^+$ states with neutron separation thresholds being $\mathrm{E}_{th} = 1.67$ and 4.71 MeV. The weights of these states are 0.535 and 0.465. Therefore, in the $^9$Be dissociation it is possible to observe the $^8$Be $0^+$ and $2^+$ states with a similar intensity and in the simplest terms. In the $^8$Be nucleus there is a clear separation in energy $E_{ex}$ and width $\Gamma$ of the ground $0^+$ ($E_{ex} = 92$ keV, $\Gamma = 5.6$ eV), the first $2^+$ ($E_{ex} = 3.1$ MeV, $\Gamma = 1.5$ MeV) and second excited $4^+$ ($E_{ex} = 11.4$ MeV, $\Gamma = 3.5$ MeV) states. Observation of these states can serve as a test of NTE spectroscopic capabilities. The excitation structure of $^9$Be itself is much more complicated—there are 10 levels from the threshold to 12 MeV. There is uncertainty about the contribution of the $^5$He state.

An accelerated search for $^9$Be → 2He events was carried out "along the strips". Focusing on a simple topology allowed bypassing the complicated problem of the identification of the secondary beam nuclei. As a result of scanning, 500 $\alpha$-particle pairs were found in the projectile fragmentation cone. Measurements of immersing angles and angles in the emulsion plane were performed for all $\alpha$-pair tracks which made it possible to determine the pair opening angles $\Theta$. A peculiarity of the resulting $\Theta$ distribution is the formation of two peaks. About 81 % of the events formed two roughly equal groups—"narrow" $\alpha$-pairs in the interval $0 < \Theta_{n(arrow)} < 10.5$ mrad and "wide" ones—$15.0 < \Theta_{w(ide)} < 45.0$ mrad. The remaining 19 % of the events are classified as "intermediate" pairs $10.5 < \Theta_{m(ediuum)} < 15.0$ mrad and "wider" pairs—$45.0 < \Theta_{v(ery)w(ide)} < 114.0$ mrad.

The physical meaning of this observation is explicitly manifested in the distribution of the $\alpha$-pair energy $Q_{2\alpha}$ (Fig. 3.18). $(75 \pm 10)$ % of events with "narrow" opening angles $\Theta_n$ are characterized by mean $\langle Q_{2\alpha} \rangle = (86 \pm 4)$ keV with a standard

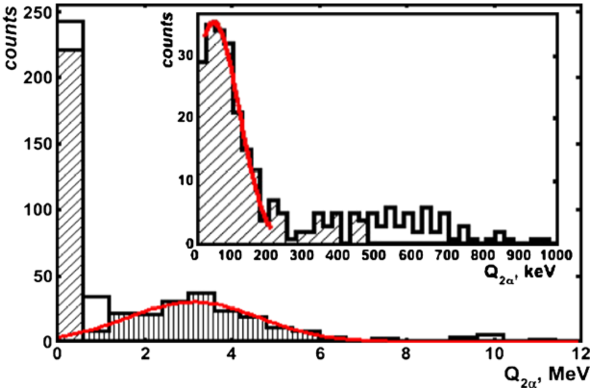

**Fig. 3.18** Distribution of events of the peripheral fragmentation $^{9}$Be → $2\alpha$ at 2 $A$ GeV/$c$ over energy $Q_{2\alpha}$; obliquely shaded histogram—events with opening angles $\Theta_n$; *vertically shaded histogram*—events with opening angles $\Theta_w$; *solid line*—total distribution of opening angles $\Theta$; on insertion—magnified distribution $Q_{2\alpha}$ for angular region $\Theta_n$

deviation $\sigma(Q_{2\alpha}) = (48 \pm 2)$ keV. This value $\langle Q_{2\alpha}\rangle$ corresponds to the $^{8}\mathrm{Be}_{g.s.}$ $0^+$ state decay. The value $\sigma(Q_{2\alpha})$ can serve as an estimate of resolution. For events with "wide" opening angles $\Theta_w$ the value $\langle Q_{2\alpha}\rangle$ is equal to $(3.1 \pm 0.11)$ MeV with $\sigma(Q_{2\alpha}) = (1.30 \pm 0.08)$ MeV. In this case $\langle Q_{2\alpha}\rangle$ and $\sigma(Q_{2\alpha})$ correspond to the $^{8}$Be $2^+$ state. Events with "intermediate" opening angles $\Theta_m$, may be associated with the formation of $^{5}$He, and $\Theta_{vw}$—with the decay of the $^{8}$Be $4^+$ state. For events $\Theta_{vw}$ an important factor is the accuracy of the determination of energy and of identification of He isotopes. Thus, the formation of $\Theta_n$ pairs is matched to decays of the $^{8}$Be $0^+$ ground state and $\Theta_w$ pairs—of the first excited $2^+$ state. The shares of the events $\Theta_n$ and $\Theta_w$ constitute $0.56 \pm 0.04$ and $0.44 \pm 0.04$, respectively. These values demonstrate the compliance with the weights of the $^{8}$Be $0^+$ and $2^+$ states adopted in [48, 49] and point to the presence of these states as components of the $^{9}$Be ground state.

In two important cases the events can be attributed to the target nucleus that participated in the interaction. First, these are "white" stars ($n_b + n_g = 0$) due to interactions on the heavy target nuclei Ag and Br. Second, these are events with single g-particles accompanying interactions with the H nuclei. Approximately 80 % of the "white" stars $^{9}$Be → $2\alpha$ are characterized by the Rayleigh distribution parameter $\sigma_{\mathrm{AgBr}}(P_{Tsum}) = (77 \pm 7)$ MeV/$c$. This value is explainable within the framework of the statistical model for the fragment with mass number $A = 8$ and the outer neutron in $^{9}$Be. When the radius of the $^{9}$Be nucleus is 2.5 Fermi the corresponding value of the dispersion of the neutron momentum distribution should be equal to $\sigma_0 = 81.4$ MeV/$c$. The remaining 20 % of the Ag–Br events are associated with a large angle scattering of "narrow" $\alpha$-particle pairs ($^{8}\mathrm{Be}_{g.s.}$) with $\sigma_{\mathrm{AgBr}}(P_{Tsum}) = (267 \pm 45)$ MeV/$c$. The $P_{Tsum}$ distribution of 88 % events for the H group is characterized by $\sigma_H(P_{Tsum}) = (126 \pm 23)$ MeV/$c$. This value indicates that the breakup $^{9}$Be → $2\alpha$ on protons corresponds to a harder interaction (less peripheral) than in the case of Ag and Br nuclei.

Significant statistics of "white" stars allow checking whether there is a correlation between the $\alpha$-pair momentum transfer $P_{Tsum}$ and the emergence of the $^{8}$Be nucleus in the ground and excited states. Samples from the intervals $\Theta_n$ and $\Theta_m + \Theta_w + \Theta_{vw}$ are described by the Rayleigh distribution with parameters

$\sigma_{\mathrm{AgBr}}(P_{Tsum}) = (75 \pm 9)$ MeV/$c$ and $(80 \pm 10)$ MeV/$c$. Thus, there is no significant difference of the $P_{Tsum}$ distributions for coherent dissociation events via the $0^+$ and $2^+$ states of the $^8$Be nucleus. In general, the data can be viewed as evidence that the nuclear structure of $^9$Be has with high probability a core in the form of the two states of the $^8$Be nucleus and an outer neutron. These results are consistent with the descriptions of the $^9$Be nucleus structure suggesting the presence of the $0^+$ and $2^+$ states of the $^8$Be nucleus with approximately equal weights.

## 3.6 Peripheral Interactions of $^{14}$N Nuclei

The $^{14}$N nucleus is of interest as intermediate between the cluster nucleus $^{12}$C and the doubly magic nucleus $^{16}$O. The study of $^{14}$N nuclei can expand understanding of the evolution of increasingly complex structures beyond the $\alpha$-clustering. The information about the structure of $^{14}$N has an applied value. As a major component of the Earth's atmosphere the $^{14}$N nucleus can be a source of the light rare earth elements Li, Be and B, as well as of deuterium. Generation of these elements occurs as a result of bombardment of the atmosphere during its lifetime by high-energy cosmic particles. Therefore, the cluster features of the $^{14}$N fragmentation can determine the abundances of lighter isotopes. Beams of $^{14}$N nuclei can be used in radiation therapy, which also gives a practical interest in obtaining detailed data about the characteristics of the $^{14}$N fragmentation.

For the first time the fragmentation of relativistic $^{14}$N nuclei was studied in NTE exposed at the Bevatron in the 70s [35]. Limitations in measurement of angles and fragment identification [35] motivated a study of the dissociation of 2.9 $A$ GeV/$c$ $^{14}$N nuclei in NTE exposed at the JINR Nuclotron [17]. The starting task was to reveal the role of external nucleon clustering in the form of a deuteron. This type of clusterization is expected for odd-odd light stable nuclei, whose number is small.

Events were selected in which the total charge of the fragments $\sum Z_{fr}$ was equal to the projectile nucleus charge $Z_{pr} = 7$ and there were no produced mesons (see Table 3.4). The main contribution is provided by the channels C + H, 3He + H, and 2He + 3H (77 %). The share of events C + H ($E_{th} = 7.6$ MeV) is sufficiently significant—25 %. The share of B+He events ($E_{th} = 20.7$ MeV) turned out to be small—only 8 %. A significant reduction in the proportion of deuterons relative to protons in comparison with $^6$Li and $^{10}$B nuclei was demonstrated. A leading role both for "white" stars and events with the formation of target fragments is taken by the multiple channel $^{14}\mathrm{N} \rightarrow 3\mathrm{He} + \mathrm{H}$ ($E_{th} = 15$ MeV) having a probability of about 35 %. Thus, the $^{14}$N nucleus manifests itself as an effective source of 3$\alpha$-systems. It was found that 80 % of the 3$\alpha$ ensembles correspond to the excitations of the $^{12}$C nucleus from the breakup threshold to 14 MeV. $^{14}$N produces fragments in the channel 3He + H via the formation of $^8$Be with approximately 20 % probability. Events $^{11}\mathrm{C} + {}^3\mathrm{H}$, $^6\mathrm{He} + {}^4\mathrm{He} + {}^3\mathrm{He} + p$, $^4\mathrm{He} + 2{}^3\mathrm{He} + d$ have been identified; for these partial rearrangement of the $\alpha$-structure is necessary.

**Table 3.4** Distribution of the peripheral interactions of $^{14}$N nuclei over the configurations $\sum Z_{fr} = 7$ including "white " stars $N_{ws}$ and events $N_{tf}$ with target fragments

| Channel | C + H | B + He | B + 2H | Be + He + H | Li + 4H | Li + He + 2H | 2He + 3H | 3He + H | He + 5H |
|---|---|---|---|---|---|---|---|---|---|
| $N_{ws}$ | 16 | 5 | 5 | 2 | 1 | | 6 | 21 | 5 |
| $N_{tf}$ | 24 | 4 | 3 | 5 | 2 | 3 | 21 | 35 | 3 |

**Table 3.5** Distribution of the peripheral interactions of $^8$B nuclei over the configurations $\sum Z_{fr} = 5$

| Channel<br>$E_{th}$, MeV | B | Be + H<br>(0.138) | 2He + H<br>(1.72) | He + 3H<br>(6.9) |
|---|---|---|---|---|
| $N_{ws}$ (%) | 1 (2) | 25 (48) | 14 (27) | 12 (23) |
| $N_{tf}$ (%) | 11 (19) | 8 (14) | 17 (29) | 22 (38) |

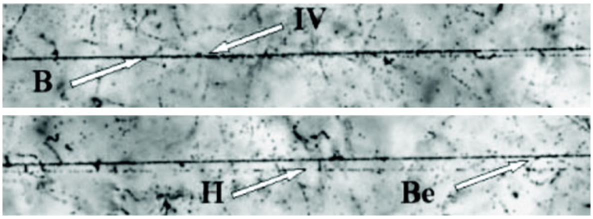

**Fig. 3.19** Coherent dissociation $^8\text{B} \to {}^7\text{Be} + p$ at 2 *A* GeV/*c* (IV is interaction vertex)

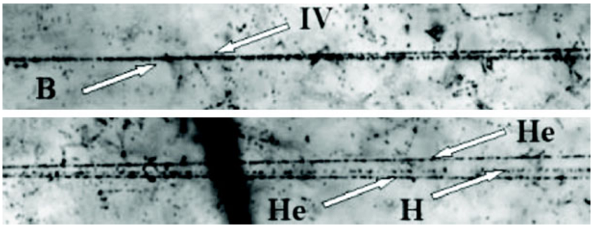

**Fig. 3.20** Coherent dissociation $^8\text{B} \to 2\text{He} + \text{H}$ at 2 *A* GeV/*c*

## 3.7 Coherent Dissociation of $^8$B Nuclei

$^8$B fragments produced by 1.2 *A* GeV $^{10}$B nuclei were selected for exposure of NTE [21, 29]. The charge composition of the relativistic fragments for the events $\sum Z_{fr} = 5$ accompanied by target nucleus fragments and (or) produced mesons $N_{tf}$ and "white" stars $N_{ws}$ (examples in Figs. 3.19 and 3.20) show a qualitative difference (Table 3.5). The main conclusion is that the contribution of the dissociation $^8\text{B} \to {}^7\text{Be} + p$ is leading among "white" stars. This situation is qualitatively different from the dissociation of the $^{10}$B isotope. Data on $N_{ws}$ may be useful as estimates of the probabilities of few body configurations in the $^8$B ground state.

Due to the record low binding energy of the external proton ($E_{th} = 138$ keV), the $^8$B nucleus is the most sensitive probe of the electromagnetic interaction with the target nucleus. In the center of mass of the system $^7\text{Be} + p$ the average transverse momenta of the particles is $\langle P_T^* \rangle = (62 \pm 11)$ MeV/*c* at RMS of 54 MeV/*c*. This small value indicates a weak bond of the proton and the core. The distribution of the total transverse momenta of the pairs in the "white" stars has an average value of $\langle P_T(^8\mathrm{B}^*)\rangle = (95 \pm 15)$ MeV/$c$ at RMS of 73 MeV/$c$, and a significantly greater one for events with target nucleus fragments or produced mesons $\langle P_T(^8\mathrm{B}^*)\rangle = (251 \pm 29)$ MeV/$c$ at RMS of 112 MeV/$c$.

Analysis of angular correlations allowed establishing the criteria of the electromagnetic dissociation events by the total transverse momentum $P_T(^8\mathrm{B}^*) < 150$ MeV/$c$, energy $Q_{p\mathrm{Be}} < 5$ MeV and by the azimuth angle $\varepsilon_{p\mathrm{Be}} > \pi/2$ between the fragments. Because of $Z^2$ dependence of the electromagnetic cross-section on a nucleus target charge species, the proportional contribution can be assumed from Ag and Br nuclei. Then the obtained cross-sections comprise $\sigma_{\mathrm{Ag}} = (81 \pm 21)$ mb and $\sigma_{\mathrm{Br}} = (44 \pm 12)$ mb. Analysis of the ratio of the Coulomb and nuclear dissociation and stripping in the dissociation of $^8\mathrm{B} \rightarrow {}^7\mathrm{Be} + p$ for the Pb target up to the energy of $\approx 2$ $A$ GeV was carried out in [50]. Extrapolation $\sigma_{\mathrm{Ag}}$ to the Pb nucleus leads to the value $\sigma_{\mathrm{Pb}} = (230 \pm 60)$ mb, which is close to the theoretical value of $\approx$210 mb [50].

## 3.8 Coherent Dissociation of $^9$C Nuclei

The $^9$C nucleus became the next studied object on the proton border of nuclear stability. The coherent dissociation of $^9$C can proceed through the channels $^8\mathrm{B}+p$ ($E_{th} = 1.3$ MeV) and $^7\mathrm{Be}+2p$ ($E_{th} = 1.4$ MeV) as well as the $^7$Be core breakups ($E_{th} > 3$ MeV). Besides, the population of the $3^3$He system, which has a relatively low formation threshold (about 16 MeV), is possible by means of neutron rearrangement from the $^4$He cluster to $^3$He cluster being formed. Probability of the transition $^9\mathrm{C} \rightarrow 3^3\mathrm{He}$ can point to the $3^3$He component weight in the $^9$C ground state and may be important in calculating the characteristics of the $^9$C nucleus based on the cluster wave functions taking into account such a deeply bound state. Being a nontrivial cluster excitation, the $3^3$He state may be important for the development of nuclear astrophysics scenario with one more initial state of the fusion reaction similar to the $3\alpha$-process. An intriguing problem is to find a resonant $2^3$He state in the $^9\mathrm{C} \rightarrow 3^3\mathrm{He}$ dissociation similar to the dissociation $^{12}\mathrm{C} \rightarrow {}^4\mathrm{He}^8\mathrm{Be}$.

In the study of $^9$C interactions there is a need to overcome two practical problems. First, the $^3$He nuclei, having the same ratio of the charge $Z_{pr}$ to the mass number $A_{pr}$, are dominant in the generated beam. Thus, it was important to avoid NTE overexposure to $^3$He nuclei. Second, it was necessary to ensure the $^9$C dominance over the contributions of the $^{10,11}$C isotopes. A comparative analysis of the coherent dissociation of the studied neighboring isotopes helped this problem to be solved.

$^{12}\mathrm{C}^{6+}$ ions, created by a laser source, were accelerated to 1.2 $A$ GeV and extracted to the production target. Further, the secondary beam tuned for selection of $^9$C nuclei was guided on the emulsion stack [22, 29]. With dominance of C nuclei, the beam contained an insignificant admixture of $^6$Li, $^7$Be and $^8$B.

**Table 3.6** Distribution of "white" stars $N_{ws}$ of $^9$C nuclei over the configurations $\sum Z_{fr} = 6$

| Channel | B + H | Be + 2H | 3He | 2He + 2H | He + 4H | 6H |
|---|---|---|---|---|---|---|
| $N_{ws}$ | 15 | 16 | 16 | 24 | 28 | 6 |

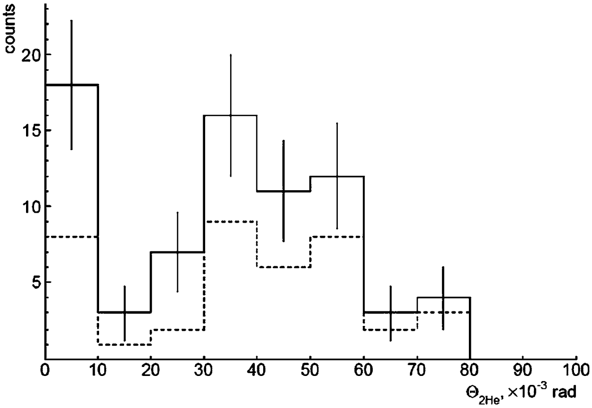

**Fig. 3.21** Total distribution of opening angles $\Theta_{2\mathrm{He}}$ between the relativistic He fragments in the "white" stars $^9\mathrm{C} \to 3^3\mathrm{He}$ and in the events $^8\mathrm{B} \to 2\mathrm{He} + \mathrm{H}$ with the formation of target nucleus fragments or mesons; *dotted line* indicates the contribution of "white" stars $^9\mathrm{C} \to 3^3\mathrm{He}$

The main branch of the coherent dissociation is represented by events $\sum Z_{fr} = 6$, which is to be expected due to the dominance of C nuclei in the beam. The most valuable is the analysis of the channels corresponding to the $^9$C nucleus dissociation with the lowest thresholds $^8\mathrm{B} + p$ and $^7\mathrm{Be} + 2p$, as well as the 3He channel. The events in the last channel could be eligible for the coherent dissociation $^9\mathrm{C} \to 3^3\mathrm{He}$. The events $Z_{pr} = 6$ and $Z_{fr} = 5$ and 4 are interpreted as $^9\mathrm{C} \to {}^8\mathrm{B} + p$ and $^7\mathrm{Be} + 2p$. The events 2He + 2H and He + 4H are dominant (Table 3.6). In the case of $^9$C, events in these channels occur with approximately equal probability as expected due to the dissociation of the $^7$Be core [16]. This ratio does not correspond to the isotope $^{10}$C, for which the probability of the 2He + 2H channel is approximately by an order of magnitude higher than for the He + 4H channel [25, 27]. Besides, "white" stars $^6\mathrm{Li} + 3p$ and 6H produced as a result the dissociation of the $^7$Be core were observed.

The $3^3$He states are the central subject of the current study. The dissociation probability via this channel (≈14 %) is comparable to the nucleon separation channels. The significant probability of the coherent dissociation channel $^9\mathrm{C} \to 3^3\mathrm{He}$ makes it an effective source for the search for a resonant $2^3$He state near the threshold analogous to the $^8$Be ground state. The opening angle distribution $\Theta_{2\mathrm{He}}$ of the fragment pairs in the "white" stars $^9\mathrm{C} \to 3^3\mathrm{He}$ is shown in Fig. 3.21. The main part corresponding to 30 pairs of 2He is described by a Gaussian distribution with parameters $\langle \Theta_{2\mathrm{He}} \rangle = (46 \pm 3) \times 10^{-3}$ rad at RMS of $16 \times 10^{-3}$ rad. The corresponding energy distribution is limited to the region $Q(2^3\mathrm{He}) < 20$ MeV.

Eight narrow 2He pairs with opening angles limited to $\Theta_{2\mathrm{He}} < 10^{-2}$ rad are reliably observed thanks to the NTE resolution. They are allocated in a special group with an average of $\langle \Theta(2^3\mathrm{He}) \rangle = (6 \pm 1) \times 10^{-3}$ rad at RMS of $3 \times 10^{-3}$ rad. The energy distribution has a mean value $\langle Q(2^3\mathrm{He}) \rangle = (142 \pm 35)$ keV at RMS of 100 keV. Thus, despite the low statistics, this distribution points to an intriguing possibility of the existence of a resonant $2^3$He state slightly above the mass threshold of $2^3$He [51].

To test a possible $2^3$He resonance (conventionally called “dihelion”), an analysis of data on the $^8$B nucleus [21] was carried out. Events $^8\mathrm{B} \to 2\mathrm{He} + \mathrm{H}$ accompanied by target nucleus fragments or mesons were selected in order to enhance the effect. This condition provides an effective selection of interactions with neutron knocking out from the $^4$He cluster in the $^8$B nucleus. Thus, the distribution $\Theta(2^3\mathrm{He})$ takes the same view as in Fig. 3.4 and also includes a separate group of narrow pairs with $\langle\Theta(2^3\mathrm{He})\rangle = (4.5 \pm 0.5) \times 10^{-3}$ rad (RMS $1.5 \times 10^{-3}$ rad), corresponding to the case of the “white” stars $^9\mathrm{C} \to 3^3\mathrm{He}$. The total distribution of the opening angles $\Theta_{2\mathrm{He}}$ between the relativistic He fragments in the “white” stars $^9\mathrm{C} \to 3^3\mathrm{He}$ and in the events $^8\mathrm{B} \to 2\mathrm{He} + \mathrm{H}$ with the formation of target nucleus fragments or mesons shown in Fig. 3.21 enhances evidence for the existence of a near-threshold $2^3$He resonance. Moreover, the question arises about the nature of a broad peak with maximum near $\Theta(2^3\mathrm{He}) \approx (40\text{–}50) \times 10^{-3}$ rad. Possibly in this $\Theta$ region the decays $2^3$He are similar to the decay of the $^8$Be $2^+$ state [23, 24].

Of course, this finding is worth studying and testing with much higher statistics. One of its more technically simple options may be the dissociation of $^7\mathrm{Be} \to 2^3\mathrm{He}$ with a neutron knock out and the formation of fragments of target nuclei or mesons. However, it is possible that the “dihelion” formation is associated with the presence of a $2^3$He component in the $^9$C and $^8$B structures. In the $^7$Be nucleus such a component can be suppressed, which means the suppression of “dihelion” formation in the fragmentation of this nucleus. Therefore it is important to implement a search for the $2^3$He resonance with larger statistics using fragmentation of low-energy $^9$C and $^8$B nuclei. Pointing to the existence of“dihelion”, this observation motivates the search for a mirror state of the $^3$H pair—“ditriton”.

## 3.9 Coherent Dissociation of $^{10}$C and $^{12}$N Nuclei

### 3.9.1 Exposure to a Mixed Beam of $^{12}$N, $^{10}$C and $^7$Be Nuclei

A secondary beam containing $^{12}$N, $^{10}$C and $^7$Be nuclei can be formed by selection of products of charge-exchange and fragmentation reactions of relativistic $^{12}$C nuclei. Such a composition is not so much desirable but unavoidable since the $Z_{pr}/A_{pr}$ ratios of these nuclei differ by only 3 %. Separation of these nuclei is not possible in a channel with the momentum acceptance of 2–3 %, and they are simultaneously present in the beam, forming the so-called “beam cocktail”. The contribution of $^{12}$N nuclei is small relative to $^{10}$C and $^7$Be nuclei in accordance with the charge-exchange and fragmentation cross-sections. Because of the momentum spread, $^3$He nuclei can penetrate into the channel. For the neighboring nuclei $^8$B, $^9$C and $^{11}$C the difference of $Z_{pr}/A_{pr}$ from $^{12}$N is about 10 %, which causes their suppression in the secondary beam. An event-by-event identification of $^{12}$N in the exposed NTE is possible for “white” stars by fragment topologies and beam nucleus charges determined by $\delta$-electron counting on the beam tracks. In the case of dominant $^{10}$C nuclei it is sufficient to make sure that the contribution of the neighboring C isotopes by the overall pattern of the composition of “white” stars is small.

Based on these considerations it was suggested to expose NTE to a mixed beam of 2 $A$ GeV/$c$ $^{12}$N, $^{10}$C and $^{7}$Be nuclei [25, 29]. The amplitude spectrum from a scintillation counter installed in the location of NTE irradiation pointed to the dominance of He, Be, C isotopes and to a small admixture of N nuclei in the substantial absence of $^{8}$B nuclei. A stack of 15 NTE layers was exposed to a secondary beam with such a composition. The initial stage of analysis was to search for beam tracks with charges $Z_{pr} = 1, 2$ and $Z_{pr} > 2$. The ratio of beam tracks $Z_{pr} = 1, 2$ and $Z_{pr} > 2$ was $\approx$1:3:18. Thus, the contribution of $^{3}$He nuclei decreased dramatically in this exposure as compared with the $^{9}$C case.

The analysis presented below is based on the search for events along the tracks of primary particles with charges visually valued as $Z_{pr} > 2$ over a length of about 1088 m. As a result, 7241 inelastic interactions were found, including 608 “white” stars containing only relativistic particle tracks in the angular cone $\theta_{fr} < 11^\circ$. In the “white” stars, which might be created by $^{12}$N nuclei, the average densities of $\delta$-electrons $N_\delta$ were measured on the tracks of the beam nuclei and secondary fragments with charges $Z_{fr} > 2$. As was shown in the study of the nuclei $^{8}$B [21] and $^{9}$C [22], the application of this method allows one to eliminate the contribution from the charge-exchange reactions with production of mesons of accompanying lighter nuclei. The dominance of C nuclei in this irradiation has made such selection particularly relevant and has justified the use of a cumbersome procedure of $\delta$-electron counting.

### 3.9.2 Dissociation of $^{10}$C Nuclei

The $^{10}$C nucleus is the only example of a stable 4-body structure in which the removal of any of the constituent clusters or nucleons leads to an unbound state condition. The breakup threshold of the $^{10}\mathrm{C} \to 2\alpha + 2p$ process is $E_{th} = 3.73$ MeV. The next threshold via $^{8}\mathrm{Be}_{g.s.} + 2p$ is slightly higher—$E_{th} = 3.82$ MeV. Knocking out one of the protons ($E_{th} = 4.01$ MeV) leads to the formation of an unstable $^{9}$B nucleus, which decays into a proton and a $^{8}$Be nucleus. By way of $\alpha$-cluster separation ($E_{th} = 5.10$ MeV) a $^{6}$Be resonance can be formed, its decay energy being 1.37 MeV. The decay of $^{6}$Be via the $^{5}$Li resonance is impossible, because the threshold for the formation of $^{5}\mathrm{Li}_{g.s.} + p$ is 0.35 MeV higher than the $^{6}$Be ground state. In addition, the channel $^{5}\mathrm{Li}_{g.s.} + \alpha$ is closed since this threshold is 1.5 MeV higher than the $^{9}$B ground state. Therefore, in the $^{10}$C dissociation the resonances $^{6}\mathrm{Be}_{g.s.}$ and $^{5}\mathrm{Li}_{g.s.}$ can only be produced directly and not in cascade decays of $^{9}$B.

Events $\sum Z_{fr} = 6$ were selected among the found peripheral interactions [25, 27]. Their distribution on the charge topology is presented in Table 3.7. The subject of the analysis was a sample consisting of 227 “white” stars $N_{ws}$. A peculiarity

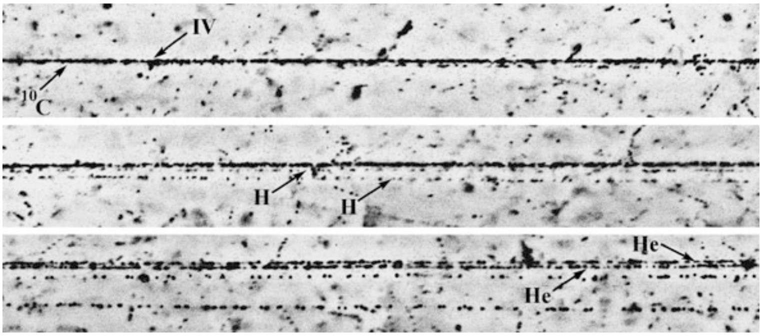

**Fig. 3.22** Coherent dissociation $^{10}\text{C} \to p + {}^{9}\text{B}_{g.s.}$ at 2 $A$ GeV/$c$

**Table 3.7** Distribution over the charge configurations of relativistic fragments $\sum Z_{fr} = 6$ of $^{10}$C fragmentation events for "white" stars $N_{ws}$ and collisions with produced mesons, target fragments or recoil protons $N_{tf}$

| | 2He + 2H | He + 4H | 3He | 6H | Be + He | B + H | Li + 3H | C + n |
|---|---|---|---|---|---|---|---|---|
| $N_{ws}$ | 186 | 12 | 12 | 9 | 6 | 1 | 1 | |
| (%) | (81.9) | (5.3) | (5.3) | (4.0) | (2.6) | (0.4) | (0.4) | |
| $N_{tf}$ | 361 | 160 | 15 | 30 | 17 | 12 | 2 | 30 |
| (%) | (57.6) | (25.5) | (2.4) | (4.8) | (2.7) | (1.9) | (0.3) | (4.8) |

of this class of events is the dominance of the channel 2He + 2H, which is indeed the most expected one for the $^{10}$C isotope. The channels $N_{ws}$ requiring destruction of $\alpha$-clustering in $^{10}$C nuclei and having substantially higher thresholds are manifested with much lower probabilities. The macro photography of a typical event is shown in Fig. 3.22. The interaction vertex in which a group of fragments formed is marked in the top photo. Further, one can distinguish two H (middle photo) and two He fragments (bottom photo). The most remote track originated in the dissociation $^{10}\text{C} \to {}^{9}\text{B}_{g.s.} + p$. The other tracks correspond to the decay of the unbound $^{9}$B nucleus. The pair of the He tracks corresponds to the following decay of another unbound $^{8}$Be nucleus.

Comparison of the $N_{ws}$ topology distribution with the version for the 627 $^{10}$C $N_{tf}$ events accompanied by the production of mesons, fragments of target nuclei or recoil protons, points to the "turning on" of the He + 4H channel in the latter case (Table 3.7). First of all, a much smaller perturbation of the $^{10}$C cluster structure in the "white" stars with the respect to the $N_{tf}$ case is confirmed. In addition, the comparison shows that the probabilities of the fragmentation channels beyond the "pure" clustering $2\alpha - 2p$ do not differ too much in the cases $N_{ws}$ and $N_{tf}$ (Table 3.7). This fact indicates the existence in the $^{10}$C structure of a small admixture of virtual states with participation of deeply bound cluster-nucleon configurations.

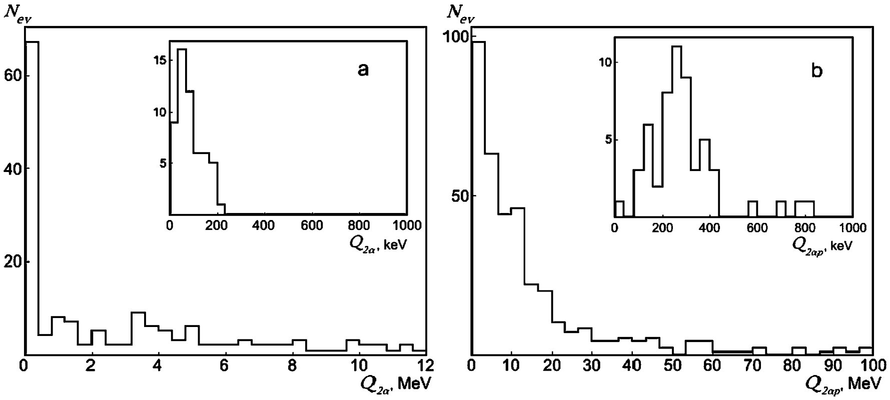

**Fig. 3.23** Distributions of the “white” stars $^{10}$C → $2\alpha + 2p$ over energy $Q_{2\alpha}$ of pairs $2\alpha$ (**a**) and over $Q_{2\alpha p}$ of triples $2\alpha + p$ (**b**); on insertions—magnified distributions $Q_{2\alpha}$ and $Q_{2\alpha p}$

Angular measurements were carried out for the tracks of the “white” stars 2He + 2H. The Rayleigh distribution parameters which describe the statistics of the angles of fragment emission are equal to $\sigma_{\theta_{\rm H}} = (51 \pm 3) \times 10^{-3}$ rad and $\sigma_{\theta_{\rm He}} = (17 \pm 1) \times 10^{-3}$ rad. These values are consistent with those of the statistical model [52, 53] $\sigma_{\theta_p} \approx 47 \times 10^{-3}$ rad and $\sigma_{\theta_\alpha} \approx 19 \times 10^{-3}$ rad for $^1$H and $^4$He fragments. Measurements of the angles allow the transverse momenta of the fragments and their ensembles to be estimated. The distribution of the “white” stars 2He + 2H for the full transverse momentum $P_T$ is described by the Rayleigh distribution with parameter $\sigma_{P_T}(2\alpha + 2p) = (161 \pm 13)$ MeV/$c$. Such a value is expected for the diffraction dissociation [47].

The distribution of these events over the energy $Q_{2\alpha}$ of the $2\alpha$ pairs and $Q_{2\alpha p}$ of the $2\alpha + p$ triples is shown in Fig. 3.23. In 68 of them $2\alpha$ pairs with emission angles not exceeding $10^{-2}$ rad are observed. The distribution $Q_{2\alpha}$ of these $2\alpha$ pairs with an average $\langle Q_{2\alpha} \rangle = (63 \pm 30)$ keV at RMS of 83 keV allows concluding that the formation of $^8$Be$_{g.s.}$ is observed in these events. In turn, the distribution $Q_{2\alpha p}$ indicates that the dissociation $^{10}$C → $2\alpha + 2p$ is accompanied by the formation of unbound $^9$B nuclei. The average value $\langle Q_{2\alpha p} \rangle = (254 \pm 18)$ keV at RMS of 96 keV corresponds to the energy and width of the decay $^9$B$_{g.s.}$ → $^8$Be$_{g.s.}$ + $p$. A clear correlation between $Q_{2\alpha}$ and $Q_{2\alpha p}$ points to the cascade process $^{10}$C → $^9$B → $^8$Be. The contribution of these decays allows concluding that the $^9$B nucleus manifests itself with a probability of (30 ± 4) % in the $^{10}$C structure. Earlier, the $^9$B nuclei from the fragmentation of $^{12}$C were reconstructed in an experiment with transverse orientation of NTE pellicles [54].

For 40 events $^{10}$C → $^9$B (73 %) the Rayleigh parameter $\sigma_{P_T}(^9\mathrm{B})$ of the distribution over the total transverse momentum $P_{T2\alpha p}$ of the $2\alpha + p$ triples is (92 ± 15) MeV/$c$. It corresponds to the value of 93 MeV/$c$ expected in the statistical model. Within this model the radius of the region emission of an outer proton by the $^{10}$C nucleus is $R_p = (2.3 \pm 0.4)$ Fermi which does not contradict to the value derived from the geometric overlap model [28] based on measurements of inelastic

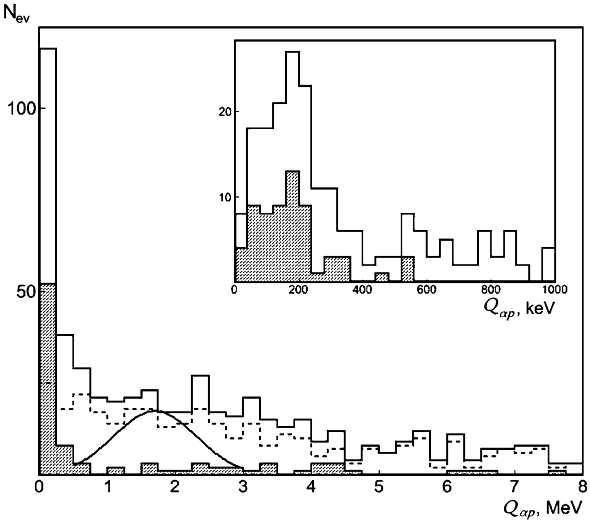

**Fig. 3.24** Distribution over energy $Q_{\alpha p}$ of $\alpha p$ pairs in "white" stars $^{10}C \to 2\alpha + 2p$; *solid line*—histogram of all combinations $Q_{\alpha p}$; *shaded histogram*—$Q_{\alpha p}$ with $^{9}B$ and $^{8}Be$ production; *dashed histogram*—$Q_{\alpha p}$ without $^{9}B$ and $^{8}Be$ production; the *curve* indicates the expected position of the $^{5}Li$ resonance; on *insertion*—magnified distribution $Q_{\alpha p}$

cross-sections. The $^{9}B$ decays unaccounted herein belong to $^{9}B$ scatterings at large angles as compared to the angular decay cone.

The $\sigma_{P_T{}^9B}$ and $R_p$ values can be compared with the data on the fragmentation $^{10}C \to {}^{9}C$. These events are classified as interactions in which target nucleus fragments or mesons are generated, while a heavy relativistic fragment retains the primary nucleus charge (Table 3.7). In 21 interactions of this type no more than one b- or g-particle was observed, which allows them to be attributed to neutron knockouts The distribution of the transverse momentum $P_{T^9C}$ values of $^{9}C$ nuclei is described by the Rayleigh parameter $\sigma_{P_{T^9C}} = (224 \pm 49)$ MeV$/c$. Thus, the $P_{T^9C}$ spectrum appears to be much harder than the $P_{T2\alpha p}$ spectrum of $^{9}B$. This fact is associated with the knocking out of neutrons that are bound much more strongly than the outer protons. On the other hand, the knockout of a neutron by a proton is, generally speaking, not a peripheral process, but rather a "probing" of the overall density of a projectile nucleus. The radius of a neutron knockout region is $(1.0 \pm 0.2)$ Fermi by the statistical model. Of course, this is a naive estimate. Nevertheless, it points to a more compact "package" of neutrons than protons in the $^{10}C$ nucleus.

The distribution of opening angles $\Theta_{\alpha p}$ for 736 $\alpha p$ pairs allows the resonance decay contribution $^{5}Li_{g.s.} \to \alpha p$ to be estimated (Fig. 3.24). The features of $\Theta_{\alpha p}$, which are a narrow peak and a broad maximum, are clarified in the $Q_{\alpha p}$ energy distribution of $\alpha p$ pairs. The peak, pinned to zero, reflects $^{9}B$ decays. The $\alpha p$ pairs of the region $20 \times 10^{-3} < \Theta_{\alpha p} < 45 \times 10^{-3}$ rad are grouped in $Q_{\alpha p}$, corresponding to $^{5}Li_{g.s.}$ decays. Their distribution is described by a Gaussian with a mean value of $(1.9 \pm 0.1)$ MeV with $\sigma$ of 1.0 MeV, which is consistent with the decay energy (1.7 MeV) and the width (1.0 MeV) of the $^{5}Li_{g.s.}$ resonance. About 110 pairs of $\alpha p$ can be attributed to the $^{5}Li_{g.s.}$ decays. There is a small contribution from the $^{6}Be$ resonance decays at the intermediate values of $Q_{\alpha p}$ which are lower than those of the $^{5}Li_{g.s.}$ decay.

Among the "white" stars (Table 3.7) the events Be + He and $^3$He are observed having thresholds $E_{th} = 15$ MeV and 17 MeV for the $^{10}$C nucleus. Identification of the He fragments by the $p\beta c$ parameter confirms their interpretation as $^7\mathrm{Be} + {}^3\mathrm{He}$ and $2^3\mathrm{He} + {}^4\mathrm{He}$ and does not contradict the assumption that it was exactly the $^{10}$C nuclei that were dissociated. The population of these states requires a rearrangement of the neutrons from one of the $\alpha$-particle clusters to a $^3$He cluster to be produced. Another interpretation points to the presence in the $^{10}$C ground state of deeply bound cluster states $^7\mathrm{Be} + {}^3\mathrm{He}$ and $2^3\mathrm{He} + {}^4\mathrm{He}$ with a weight of 8 %.

An inverse "packaging" $2^3\mathrm{He}^4\mathrm{He} \to {}^7\mathrm{Be}^3\mathrm{He} \to 2p2^4\mathrm{He} \to {}^{10}\mathrm{C}$ will result in a powerful release of energy. Replacing of one more $^3$He nucleus by $^4$He gives a state close to the $^{11}$C ground state. The formation of $^{10,11}$C isotopes in astrophysical $^3$He–$^4$He mediums leads one to $^{10,11}$B isotopes. Their abundance in cosmic rays can be indicative of nucleosynthesis in $^3$He and $^4$He mixtures. Such an assertion is not commonly accepted. Boron isotopes are believed to be generated in the bombardment of carbon stars by high-energy particles or in the splitting of heavier nuclei of cosmic rays. Nevertheless, the studies of $^3$He states with various isotopic compositions can add new information to the already known scenarios of nucleosynthesis.

### *3.9.3 Coherent Dissociation of $^{12}$N Nuclei*

Clustering of the insufficiently explored $^{12}$N nucleus is the next goal in the further development of the $^7$Be, $^8$B and $^{9,10,11}$C studies in the relativistic dissociation approach. In an astrophysical aspect its existence provides an alternative scenario for the synthesis of the $^{12}$C isotope via the fusion $^{11}\mathrm{C} + p$. For $^{12}$N "white" stars, the channels $^{11}\mathrm{C} + p$ ($E_{th} = 0.6$ MeV), $^8\mathrm{B} + {}^4\mathrm{He}$ ($\mathrm{E}_{th} = 8$ MeV) and $p + {}^7\mathrm{Be} + {}^4\mathrm{He}$ ($E_{th} = 7.7$ MeV) and the channels associated with the dissociation of the $^7$Be core are expected to play a leading role. The threshold of the channel $^3\mathrm{He} + {}^9\mathrm{B}_{g.s.}$ is located at $E_{th} = 10$ MeV. A small difference in the binding energy compared with the channels containing fragments $Z_{fr} > 2$ suggests a possible duality of the $^{12}$N nucleus. On the one hand, its basis can be represented by the bound $^7$Be and $^8$B nuclei, on the other hand by the unbound $^8$Be and $^9$B nuclei. Therefore, a particular feature of the coherent $^{12}$N dissociation could be a competing contribution of $^8$Be and $^9$B decays.

Measurements of the charges of the beam nuclei $\mathrm{Z}_{pr}$ and relativistic fragments $Z_{fr} > 2$ in the candidate events of the $^{12}$N dissociation made it possible to select 72 "white" stars which satisfy the condition $Z_{pr} = 7$ and $\sum Z_{fr} = 7$ [25, 26]. The charge topology distribution of these stars is shown in Table 3.8. Accidentally, the mass numbers $A_{fr}$ become definite for isotopes $Z_{fr} > 2$. According to the "white" star statistics, the share of $^{12}$N nuclei in the beam is estimated to be 14 %, while those of $^{10}$C and $^7$Be nuclei are about 43 % each (excluding H and He nuclei). These values do not reflect the ratio of the cross-sections of the charge exchange and fragmentation reactions and have a technical importance. The significant contribution to the beam of charge-exchange products $^{12}\mathrm{C} \to {}^{12}\mathrm{N}$ compared

**Table 3.8** Distribution of the $^{12}$N "white" stars; *middle row*—selection with the condition $\theta_{fr} < 11°$, *bottom row*—$\theta_{fr} < 6°$

| He + 5H | 2He + 3H | 3He + H | $^{7}$Be + 3H | $^{7}$Be + He + H | $^{8}$B + 2H | $^{8}$B + He | C + H |
|---|---|---|---|---|---|---|---|
| 9 | 24 | 2 | 10 | 9 | 11 | 3 | 4 |
| 2 | 12 | 2 | 5 | 8 | 9 | 3 | 4 |

with $^{10}$C and $^{7}$Be fragments of $^{12}$C is explained by the fact that the beam was tuned to the ratio $Z_{pr}/A_{pr} = 5/12$ of $^{12}$N, which is slightly different from the values for $^{10}$C and $^{7}$Be.

For a further selection of events containing specifically $^{12}$N fragments (not "participants"), the condition on the angular cone of coherent dissociation was enhanced to $\theta_{fr} < 6°$, which is determined by a "soft" constraint on the nucleon Fermi momentum. In the distribution of 45 selected events (Table 3.8) the share of the channels with heavy fragments $Z_{fr} > 2$ reaches approximately 2/3, and the contribution of the channels containing only He and H fragments is quite significant. A noticeable contribution of a very "fragile" $^{8}$B points to a "cold" fragmentation with minimal perturbation of the $^{12}$N structure. As judged by the facts of approximate equality of the probabilities of the channels 2He and He + 2H in the dissociation of the $^{7}$Be nucleus [16], $^{7}$Be core of $^{8}$B [21] and $^{9}$C [22], one would expect that for the $^{12}$N nucleus the probabilities of the channels 2He + 3H and 3He + H are nearly equal. In contrast, the statistics in the 2He + 3H channel turned out to be unexpectedly large.

Angular measurements were used to study the contribution of $^{8}$Be decays. Only two candidates for $^{8}$Be$_{g.s.}$ decays were found in the distribution on the opening angle $\Theta_{2\mathrm{He}}$ for the "white" stars 2He + 3H and 3He + H. Thus, the contribution of $^{8}$Be$_{g.s.}$ to the $^{12}$N structure is estimated to be only $4 \pm 2$ %. For the neighboring nuclei $^{12}$C [8], $^{10}$C [25, 27], $^{10}$B [15] and $^{14}$N [17] it amounted to about 20 %. The data on $\Theta_{2\mathrm{He}}$ for $^{12}$N do not exclude a possibility of dissociation via $^{8}$Be $2^{+}$ state decays. The latter question requires statistics at a new level.

When searching for an analogy between $^{9}$C and $^{12}$N nuclei by replacing one of the outer protons in the system $2p + {}^{7}$Be by an $\alpha$ cluster, there arises the following difficulty. The probability of channels, which require the splitting of the outer $\alpha$ cluster in the $^{12}$N nucleus, roughly coincides with the values for channels that can be associated with the separation of only $\alpha$ cluster. A "simple" picture of the $^{12}$N nucleus as a $p + {}^{7}\mathrm{Be} + {}^{4}\mathrm{He}$ structure appears to be insufficient. It is most likely that the cluster structure of the $^{12}$N ground state constitute a complex mixture of the $^{7}$Be core states and all possible configurations of H and He nuclei.

## 3.10 Stopped Radioactive Nuclei

Studies of nuclei along the neutron stability border formed an area of research—the physics of nuclei with exotic structure (Fig. 3.25). New phenomena in the structure of such nuclei and in nuclear reactions with their participation have been discovered.

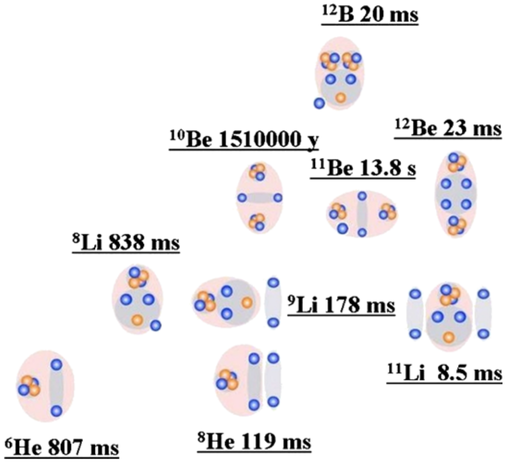

**Fig. 3.25** Diagram of cluster degrees of freedom in stable and neutron-deficient nuclei; lifetimes of isotopes are indicated

Great progress has been made in studying the structure of the nuclei $^6$He, $^8$He, $^{11}$Li and $^{14}$Be [55]. Small values of the binding energy allow the structure of exotic nuclei to be determined as molecule-like. Evidences for their abnormally large radii which are interpreted as the formation of spatially separated clusters and nucleons have been received.

The exotic nature of the structure has been established in the measurement of interaction cross-sections of relativistic nuclei with neutron excess that were found to be enhanced in comparison with the geometric type dependence. However, the relativistic energy range turned out to be inconvenient for deeper investigations of these nuclei. For an increasingly greater neutron excess in the study of relativistic nuclei it would be required to accelerate increasingly heavier nuclei with large intensities. Therefore, research with moving neutron-rich nuclei shifted to low-energy accelerators, where advantages exist for magnetic analysis and neutron detection.

In the energy range of nuclei several MeV per nucleon, there is a possibility of implantation of radioactive nuclei into detector material. Of course, in this approach daughter nuclei are investigated rather than the nuclei themselves. In this respect it is worth mentioning the known, although somewhat forgotten, possibilities of NTE for the detection of slow radioactive nuclei. More than half a century ago, “hammer” tracks from the decay of $^8$Be nuclei through the first excited state $2^+$ of about 2.0 MeV were observed in NTE. They occurred in the $\alpha$ decays of stopped $^8$Li and $^8$B fragments, which in turn were produced by high-energy particles [29]. Another example is the first observation of the $^9$C nucleus from the decay $2\alpha + p$ [56]. When used with sufficiently pure secondary beams, NTE appears to be an effective means for a systematic study of the decay of light nuclei with an excess of both neutrons and protons. In NTE the directions and ranges of the beam nuclei and slow products of their decay can be measured, which provides a basis for $\alpha$ spectrometry. A question of major importance is to supplement the $3\alpha$ spectroscopy of $^{12}$N and $^{12}$B decays [57–59] with data on $3\alpha$ angular correlations.

In March 2012 NTE was exposed at the Flerov Laboratory of Nuclear Reactions (JINR) at the ACCULINNA spectrometer [60, 61]. The beam in use was enriched

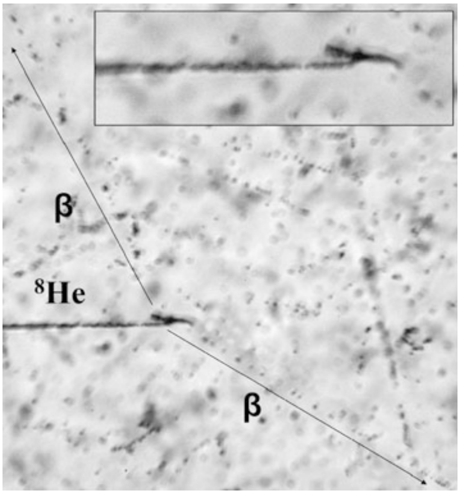

**Fig. 3.26** Decay of a stopped $^8$He nucleus; *arrows* indicate directions of emission of relativistic electrons; on insertion—magnified decay vertex with a pair of $\alpha$-particle tracks (ranges of about 5 μm)

by 7 *A* MeV $^8$He nuclei. A 107 μm thick NTE pellicle was oriented at a 10° angle during irradiation, which provided approximately a five-fold effective thickness increase. Figure 3.26 shows a decay of the $^8$He nucleus stopped in NTE. For ten minutes of irradiation, statistics of about two thousand of such decays was obtained. It is pleasant to note that the used NTE have been recently reproduced by the enterprises “Slavich” (Pereslavl-Zalessky, Russia) [62].

The use of automated microscopes in searching for and measuring such decays will open the possibility of an unprecedented level of detail and statistics. One of such microscopes is PAVICOM-2 (Fig. 3.27) of FIAN (Moscow). The PAVICOM complex [63] was originally designed for handling NTE exposed to Pb nuclei at the SPS accelerator (CERN). Currently, almost all types of solid-state track detectors (emulsions, x-ray films, mylar, plastic, crystals) are handled at the PAVICOM. Automatic analysis of nuclear decays appears to be an exciting prospect for application of the PAVICOM team experience. In this way a synergy can be achieved from the classical technique culture combined with modern technology.

## 3.11 High-Energy Frontier

The presented studies of light nuclei are only the first step toward complex cluster-nucleon ensembles He–H–*n* produced in the dissociation of heavy nuclei. The question that has to be answered is what kind of physics underlies the “catastrophic” destruction shown in Fig. 3.4? Events of dissociation of relativistic nuclei down to a complete destruction into the lightest nuclei and nucleons without visible excitation of target nuclei were reliably observed in NTE for Au and Pb and even U projectile nuclei [36]. The existence of this phenomenon is certain. It is possible that it confirms the essential role of the long-range quantum electrodynamics interaction. The

**Fig. 3.27** Automated microscope PAVICOM-2 (FIAN, Moscow)

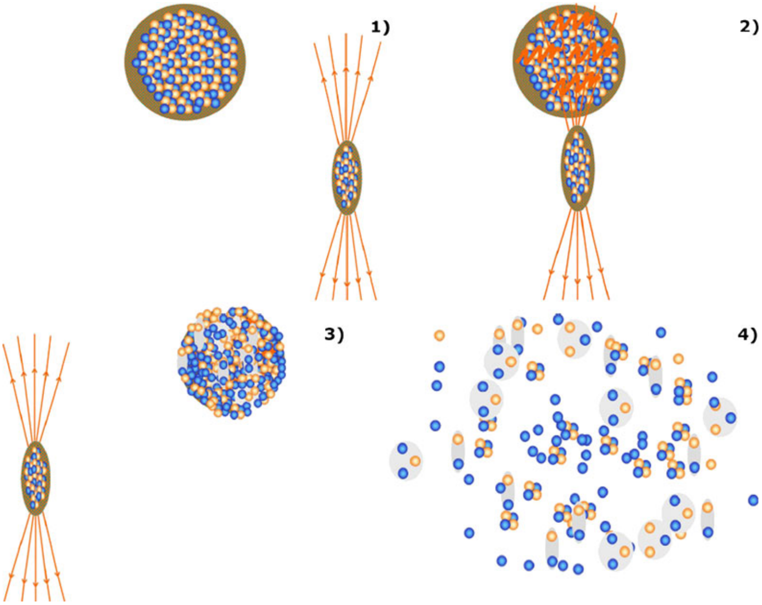

**Fig. 3.28** Scenario of coherent dissociation of a heavy nucleus in the electromagnetic field of a heavy target nucleus. The nuclei approach each other with an impact parameter larger than their radii (**1**). The intersection of electromagnetic field of the target nucleus leads to absorption of several virtual photons and to excitation of the projectile nucleus (**2**). The projectile nucleus turns into an ensemble of lightest fragments and nucleons (**3**). The ensemble breaks down (**4**)

charges of relativistic heavy nuclei make possible multiphoton exchanges and transitions in many-particle states (Fig. 3.28), which are almost impossible to observe in electron-nucleus interactions.

The predicted dependence of these processes on the target nucleus charge has the form $Z^{2n}$, where $n$ is the number of virtual photons in the interaction [64]. Experimentally, such a phenomenon can be established by an enhanced cross-section dependence on the target nucleus charge using the hadron calorimeter method. An alternative scenario of coherent dissociation consists in virtual meson exchanges. In any case the excitation of multiple nuclear giant resonances can give rise to unexpected and even exotic configurations of nucleons and clusters in the final states of decays of these resonances.

The phenomenon of electromagnetic dissociation of relativistic nuclei was discovered in Berkeley in the 70s, when the fragmentation of $^{12}$C and $^{16}$O nuclei in a variety of isotopes was studied at 1.05 $A$ and 2.1 $A$ GeV [65]. A sharp rise of the cross-sections was observed as compared with the overlap dependence of colliding nuclei. The observed effect was explained by the $Z^2$ dependence on the target charge and was described by the equivalent photon method using the data on the cross-sections of photon-nucleus interactions. For the $^{18}$O nucleus at 1.7 $A$ GeV, the fragmentation cross-sections with separation of one or two nucleons were obtained in interactions with nuclei from Be to U [66]. Despite a relatively high threshold for nucleon separation (above 12 MeV), an increase of Coulomb-type ($Z^2$) cross-section was also observed. Channels with lower thresholds remained unreachable (for instance, $^{18}\mathrm{O}(\gamma,\alpha)^{14}\mathrm{C}$ with $E_{th} = 6$ MeV). However, the electromagnetic nature of the effect was revealed in an obvious way.

Observations of coherent dissociation in nuclear emulsion and fragmentation in magnetic spectrometers stimulate ideas of experiments with neutron-rich nuclei at energies above 10 $A$ GeV, when an effective identification of relativistic nuclei and neutrons becomes possible in segmented hadron calorimeters. Identification of the dissociation channels $^6\mathrm{Li} \to {}^3\mathrm{He} + t$, $^9\mathrm{C} \to 3^3\mathrm{He}$ and $^{10}\mathrm{C} \to 2^3\mathrm{He} + \alpha$ raises the problem of search for mirror transitions with replacement of helions ($^3$He) with tritons. The probabilities of the coherent dissociation channels $^6\mathrm{He} \to 2t$, $^9\mathrm{Li} \to 3t$ and $^{10}\mathrm{Be} \to 2t + \alpha$ will allow establishing the role of deeply bound configurations with triton participation. On the other hand, the triton is a long-lived nucleus. The generation and subsequent fusion of tritons in astrophysical processes can lead to new branches of the synthesis of neutron-rich nuclei. For the study of cluster ensembles with participation of tritons the calorimetric method provides an alternative to low-energy nuclear physics approaches.

The possibility of the existence of a cluster of four neutrons or a tetraneutron $^4n$ is under discussion [67–73]. Even being unstable, the $^4n$ state can be manifested as a resonance. A calorimeter-based experiment on the photodisintegration of $^8$He nuclei above 10 $A$ GeV produced in fragmentation of relativistic $^{12}$C nuclei [74] will allow a search for the tetraneutron to be accomplished.

## 3.12 Conclusions

Thanks to its record spatial resolution and sensitivity, the method of nuclear track emulsions allowed carrying out a "tomography" for a whole family of light nuclei, including neutron deficient ones. In the case of peripheral interactions a relativistic scale of collisions of nuclei not only does not impede investigation of the cluster aspects of nuclear structure, but also offers advantages for studying few-particle ensembles. The facts collected in "mosaic" in these notes can serve as experimental "lighthouses" for developing theoretical concepts of nuclear clustering as well as for planning new experimental studies with relativistic nuclei.

In the $^{10}$B and $^{11}$B dissociation the three-body channels 2He + H are dominant (about 75 %). For the $^{10}$B nucleus an enhanced deuteron yield is observed, which is comparable with the $^{6}$Li nucleus case and points to the deuteron clustering in $^{10}$B. A large share of tritons in the dissociation of the $^{7}$Li and $^{11}$B nuclei points to the triton clustering in these nuclei. Observation of the $^{11}$B coherent charge exchange only for the two-body channel $^{7}\mathrm{Be} + {}^{4}\mathrm{He}({}^{11}\mathrm{C}^{*})$ points to a sensitivity of the dissociation to the peculiarities of the mirror nuclei.

In the coherent dissociation of $^{6}$He nuclei, an average transverse momentum of $\alpha$ particles is about 35 MeV/$c$. Its value, which is noticeably smaller than in the inclusive $^{6}$He fragmentation, shows that it is desirable to use most peripheral interactions in studies of the neutron halo in nuclei.

The share of $^{3}$He fragments in the $^{7}$Be dissociation, which is twice exceeds the content of $^{4}$He fragments, points to clustering based on the helion ($^{3}$He nucleus). It is most clearly manifested in the leading role of the coherent dissociation $^{4}\mathrm{He} + {}^{3}\mathrm{He}$. At the same time the role of the $^{3}$He cluster is beyond partnership in the bond $^{4}\mathrm{He} + {}^{3}\mathrm{He}$, and the presence of more complex configurations involving $^{3}$He in the $^{7}$Be structure is possible.

The fragmentation $^{9}\mathrm{Be} \to 2\alpha$ occurs mainly (80 %) via the $0^{+}$ and $2^{+}$states of the $^{8}$Be nucleus with close probabilities. There is no difference between the total transverse momentum distributions of $\alpha$ pairs for the coherent dissociation via these states. These facts support the $^{9}$Be concept suggesting the presence of superposition of the $^{8}$Be $0^{+}$ and $2^{+}$ states with close probabilities in its ground state.

In the peripheral fragmentation of $^{14}$N nuclei the channel $^{14}\mathrm{N} \to 3\mathrm{He} + \mathrm{H}$ is dominant (50 %) and manifests itself as an effective source of $3\alpha$ ensembles. The formation of 80 % of $3\alpha$ triples corresponds to $^{12}$C excitations from the threshold up to 14 MeV. With a probability of about 20 % the $^{14}$N nucleus forms fragments via the $^{8}$Be nucleus.

The contribution of $^{7}\mathrm{Be} + p$ in the coherent dissociation of $^{8}$B is dominant. The contribution of few-body configurations consisting of He and H nuclei in the $^{8}$B structure is estimated to be 50 %. In electromagnetic dissociation of $^{8}$B nuclei a limiting value of the total transverse momentum of pairs $^{7}\mathrm{Be} + p$ does not exceed 150 MeV/$c$.

A particular feature for the $^{9}$C nucleus is events of coherent dissociation into three $^{3}$He nuclei, the probability of which is approximately equal to the values for the channels with the separation of one or a pair of protons (about 14 %). This observation points to a considerable contribution of $3^{3}$He component to the $^{9}$C ground state. In the channel $^{9}\mathrm{C} \to 3^{3}\mathrm{He}$ pairs of $^{3}$He nuclei with opening angles less than $10^{-2}$ rad are observed, which indicates the possibility for the existence of a resonant state $2^{3}$He ("dihelion") with a decay energy of $(142 \pm 35)$ keV.

For the $^{10}$C nucleus the share of the coherent dissociation events $2\alpha + 2p$ is about 80 %. About 30 % of them belong to the channel $^{9}\mathrm{B}_{g.s.} + p$ with a subsequent decay $^{8}\mathrm{Be} + p$.

There are no obviously leading channels in the coherent dissociation of $^{12}$N nuclei. At the same time there is an intensive formation of $^{7}$Be and $^{8}$B fragments. Most probably, the role of the $^{12}$N core can be attributed to the $^{7}$Be nucleus.

Further advance to heavier neutron-deficient isotopes by means of the emulsion method remains promising, although it is getting more difficult. In this way, a further increase of the diversity of the ensembles $p{-}^{3}\mathrm{He}{-}\alpha$ under study is possible.

In general, the presented results confirm the hypothesis that the known features of light nuclei define the pattern of their relativistic dissociation. The probability distributions of the final configuration of fragments allow their contributions to the structure of the investigated nuclei to be evaluated. These distributions have an individual character for each of the presented nuclei appearing as their original "autograph". The nuclei themselves are presented as various superpositions of light nuclei-cores, the lightest nuclei-clusters and nucleons. Therefore, the selection of any single or even a pair of configurations would be a simplification determined by the intention to understand the major aspects of nuclear reactions and nuclear properties rather than the real situation. The data presented are intended to help estimate the degree and effects of such simplifications.

The approach based on the dissociation of relativistic nuclei, opens new horizons in the study of the cluster structure of nuclei and unbound cluster systems. At present only first steps which nevertheless are quite necessary have been made. Dissociation of relativistic nuclei leads to the appearance of multiple particle combinations with kinematical characteristics that are of interest in nuclear astrophysics and that cannot be formed in other laboratory conditions. On the other hand, in multiple dissociations of neutron-rich nuclei into light fragments the presence of a significant neutron component becomes unavoidable which is caused by a symmetrical composition of light nuclei. Thus, there is a prospect of exploration of polyneutron states. Besides, an applied interest appears here too.

Thus, producing new knowledge, nuclear photography awakens "nuclear imagination". One cannot exclude that the completeness of the observations provided by the nuclear track emulsion may remain unattainable for the electronic detection methods. In this case, conclusions of emulsion studies will allow one to recognize their limitations and give confidence to "rich" experiments with a great variety of detectors.

**Acknowledgements** The author considers it his pleasant duty to extend appreciation to his colleagues for the BECQUEREL project. Drawing attention to the cited publications appears to be a suitable form for such an acknowledgement. Nevertheless, the support given by Prof. A.I. Malakhov (JINR) deserves special thanks. It was under his leadership that the beam extraction system from the superconducting Nuclotron was put into operation, making possible our exposures.

The author is sincerely grateful to Prof. C. Beck (University of Strasbourg) for his invitation to write this review. My senior friend Prof. S.P. Kharlamov (Lebedev Physical Institute, Moscow) gave a critical analysis of the initial version. I.G. Zarubina (JINR) made the first proof-text version and prepared illustrations. D.O. Krivenkov (JINR) performed makeups of these notes and of the quoted publications. I.S. Baldina and O.K. Kronshtadtov (JINR) edited the English version.

The preparation of the review was supported by Grant 12-02-00067 from the Russian Foundation for Basic Research and by grants from the Plenipotentiaries of Bulgaria and Romania to JINR.

## References

1. M. Freer, Rep. Prog. Phys. **70**, 2149 (2007)
2. W. von Oertzen, M. Freer, Y. Kanada-En'yo, Phys. Rep. **432**, 43 (2006)
3. C. Beck, P. Papka, Lect. Notes Phys. **848**, 229 (2012)
4. C.J. Horowitz, M.A. Perez-Garcia, D.K. Berry, J. Piekarewicz, Phys. Rev. C **72**, 035801 (2005)
5. S. Shlomo, G. Ropke, J.B. Natowitz, L. Qin, K. Hagel, R. Wada, A. Bonasera, Phys. Rev. C **79**, 034604 (2009)
6. T. Yamada, Y. Funaki, H. Horiuchi, G. Roepke, P. Schuck, A. Tohsaki, Lect. Notes Phys. **848**, 109 (2012)
7. W. von Oertzen, Lect. Notes Phys. **848**, 109 (2012)
8. The BECQUEREL Project, http://BECQUEREL.jinr.ru
9. V.V. Belaga et al., Phys. At. Nucl. **58**, 1905 (1995). arXiv:1109.0817
10. N.P. Andreeva et al., Phys. At. Nucl. **59**, 102 (1996). arXiv:1109.3007
11. A. El-Naghy et al., J. Phys. G **14**, 1125 (1988)
12. M.I. Adamovich et al., Phys. At. Nucl. **62**, 1378 (1999). arXiv:1109.6422
13. M.I. Adamovich et al., J. Phys. G **30**, 1479 (2004)
14. M.I. Adamovich et al., Phys. Part. Nucl. Lett. **110**, 29 (2002). nucl-ex/0206013
15. M.I. Adamovich et al., Phys. At. Nucl. **67**, 514 (2004). arXiv:nucl-ex/0301003
16. N.G. Peresadko et al., Phys. At. Nucl. **70**, 1266 (2007). nucl-ex/0605014
17. T.V. Shchedrina et al., Phys. At. Nucl. **70**, 1230 (2007). arXiv:nucl-ex/0605022
18. D.A. Artemenkov et al., Phys. At. Nucl. **70**, 1226 (2007). nucl-ex/0605018
19. D.A. Artemenkov et al., Few-Body Syst. **44**, 273 (2008)
20. M. Karabova et al., Phys. At. Nucl. **72**, 300 (2009). arXiv:nucl-ex/0610023
21. R. Stanoeva et al., Phys. At. Nucl. **72**, 690 (2009). arXiv:0906.4220
22. D.O. Krivenkov et al., Phys. At. Nucl. **73**, 2103 (2010). arXiv:1104.2439
23. D.A. Artemenkov et al., Few-Body Syst. **50**, 259 (2011). arXiv:1105.2374
24. D.A. Artemenkov et al., Int. J. Mod. Phys. E **20**, 993 (2011). arXiv:1106.1749
25. R.R. Kattabekov, K.Z. Mamatkulov et al., Phys. At. Nucl. **73**, 2110 (2010). arXiv:1104.5320
26. R.R. Kattabekov et al., Phys. At. Nucl. **76** (in press)
27. K.Z. Mamatkulov et al., Phys. At. Nucl. **76** (in press)
28. H.L. Bradt, B. Peters, Phys. Rev. **77**, 54 (1950)
29. C.F. Powell, P.H. Fowler, D.H. Perkins, *The Study of Elementary Particles by the Photographic Method* (Pergamon, Elmsford, 1959)
30. A.M. Baldin, L.A. Didenko, Fortschr. Phys. **38**, 261 (1990)
31. P.A. Rukoyatkin et al., Eur. Phys. J. Spec. Top. **162**, 267 (2008). arXiv:1210.1540
32. V.S. Barashenkov et al., Nucl. Phys. **9**, 77 (1958/1959)
33. M.G. Antonova et al., Phys. Lett. B **39**, 285 (1972)
34. W.H. Barkas, *Nuclear Research Emulsions* (Academic Press, San Diego, 1963)
35. H.H. Heckman, D.E. Greiner, P.J. Lindstrom, H. Shwe, Phys. Rev. C **17**, 173 (1978)
36. E.M. Friedlander, H.H. Heckman, Y.J. Karant, Phys. Rev. C **27**, 2436 (1983)
37. P.L. Jain et al., Phys. Rev. **52**, 1763 (1984)
38. G. Singh et al., Phys. Rev. C **41**, 999 (1990)
39. G. Singh, P.L. Jain, Z. Phys. A **344**, 73 (1992)
40. G. Baroni et al., Nucl. Phys. A **516**, 673 (1990)

41. G. Baroni et al., Nucl. Phys. A **540**, 646 (1992)
42. M.I. Adamovich et al., Nucl. Phys. A **351**, 311 (1995)
43. M.I. Adamovich et al., Z. Phys. A **359**, 277 (1997)
44. M.I. Cherry et al., Eur. Phys. J. C **5**, 641 (1998)
45. M.I. Adamovich et al., Eur. Phys. J. A **5**, 429 (1999)
46. N.P. Andreeva et al., Phys. At. Nucl. **68**, 455 (2005). arXiv:nucl-ex/0605015
47. N.G. Peresadko, V.N. Fetisov et al., JETP Lett. **88**, 75 (2008). arXiv:1110.2881
48. Y.L. Parfenova, Ch. Leclercq-Willain, Phys. Rev. C **72**, 054304 (2005)
49. Y.L. Parfenova, Ch. Leclercq-Willain, Phys. Rev. C **72**, 024312 (2005)
50. H. Esbensen, K. Hencken, Phys. Rev. C **61**, 054606 (2000)
51. D.A. Artemenkov et al., J. Phys. Conf. Ser. **337**, 012019 (2012)
52. H. Feshbach, K. Huang, Phys. Lett. B **47**, 300 (1973)
53. A.S. Goldhaber, Phys. Lett. B **53**, 306 (1974)
54. T. Toshito et al., Phys. Rev. C **78**, 067602 (2008)
55. T. Aumann, Eur. Phys. J. A **26**, 441 (2005)
56. M.S. Swami, J. Schneps, W.F. Fry, Phys. Rev. **103**, 1134 (1956)
57. S. Hyldegaard et al., Phys. Lett. B **678**, 459 (2009)
58. S. Hyldegaard et al., Phys. Rev. C **80**, 044304 (2009)
59. S. Hyldegaard et al., Phys. Rev. C **81**, 024303 (2010)
60. A.M. Rodin et al., Nucl. Instrum. Methods Phys. Res., Sect. B, Beam Interact. Mater. Atoms **204**, 114 (2003)
61. The ACCULINNA Project, http://aculina.jinr.ru/
62. TD Slavich, www.slavich.ru
63. A.B. Aleksandrov et al., Nucl. Instrum. Methods Phys. Res., Sect. A, Accel. Spectrom. Detect. Assoc. Equip. **535**, 542 (2004)
64. W.J. Llope, P. Braun-Munzinger, Phys. Rev. C **45**, 799 (1992)
65. H.H. Heckman, P.J. Lindstrom, Phys. Rev. Lett. **37**, 5 (1976)
66. D.L. Olson et al., Phys. Rev. C **24**, 1529 (1981)
67. F.M. Marques et al., Phys. Rev. C **65**, 044006 (2002)
68. A.V. Nesterov, V.S. Vasilevsky, O.F. Chernov, arXiv:nucl-th/0006001
69. N.K. Timofeyuk, arXiv:nucl-th/0203003
70. N.K. Timofeyuk, arXiv:nucl-th/0301020
71. I.V. Simenog, B.E. Grinyuk, Yu.M. Bidasyuk, arXiv:nucl-th/0511006
72. C.A. Bertulani, V. Zelevinsky, J. Phys. G **29**, 2431 (2003)
73. N. Orr, F.M. Marques, arXiv:nucl-th/0303005
74. L. Anderson et al., Phys. Rev. C **28**, 1224 (1983)

# Chapter 4
# From Light to Hyper-heavy Molecules and Neutron-Star Crusts in a Dynamical Mean-Field Approach

**Cédric Simenel**

## 4.1 Introduction

Clustering in atomic nuclei is a general concept which includes a large variety of phenomena. Most of them have been covered in the volumes of "Clusters in Nuclei". These include, for instance, $\alpha$-clustering [1–5] and molecules formed by two light [6–8], intermediate/heavy [9] or very heavy [3, 10] fragments.

These cluster configurations are usually considered as specific structures of the total systems. However, except for light nuclei such as some beryllium isotopes [1, 3, 11], and eventually some heavier nuclei subject to cluster radioactivity [3, 12], they are barely found in nuclear ground-state but rather in (sometimes highly) excited states. The question of the formation of these systems in nuclear reactions comes then naturally. However, the large variety of structures and reactions to investigate makes it very challenging to develop a unique model able to describe both dynamical and static properties of these systems.

One possibility to describe clustering structures and dynamics is to assume *a priori* the presence of clusters in the state of the system. This is done, for instance, to describe $\alpha$-condensates in Ref. [5] and di-nuclear systems in Ref. [9]. Combining microscopic and macroscopic degrees of freedom is also possible within the two-center shell model [10, 12] and the generator coordinate method (GCM) [4].

Nevertheless, purely microscopic approaches describing the state of each nucleon can be used assuming specific forms of the many-body wave functions. In the anti-symmetrised molecular dynamics (AMD) model, for instance, Gaussian single-particle wave-functions are considered [1, 11]. Another example of purely micro-

---

C. Simenel (✉)
CEA, Centre de Saclay, IRFU/Service de Physique Nucléaire, 91191 Gif-sur-Yvette, France
e-mail: cedric.simenel@anu.edu.au

C. Simenel
Department of Nuclear Physics, RSPE, Australian National University, Canberra, ACT 0200, Australia

C. Beck (ed.), *Clusters in Nuclei, Volume 3*, Lecture Notes in Physics 875,
DOI 10.1007/978-3-319-01077-9_4,

scopic approach is the time-dependent Hartree-Fock (TDHF) theory (see Ref. [13] for a recent review), which will be thoroughly used in the present chapter.

An attracting feature of the TDHF approach is that it uses the same energy density functional for both the structure of the collision partners and their dynamics during the reaction. Also, the same functional is used over the nuclear chart, allowing for both descriptions of structures and reaction mechanisms with a limiting number of parameters. In particular, only nuclear structure inputs are used in the fitting procedure of the functional.

These aspects of the TDHF theory make it a promising tool to investigate various interplays between nuclear dynamics and (at least some) clustering effects. Few early TDHF codes have been used to study some cluster states and molecular structures. For instance, $\alpha$-clustering were investigated [14], as well as light [15] and hyper-heavy [16, 17] molecules.

More recently, the dynamics of di-nuclear states formed in heavy-ion collisions were analysed with modern three-dimensional TDHF codes. For instance, the path to fusion and nucleus-nucleus potentials have been studied in Refs. [7, 13, 18–48]. The transfer of one or many-nucleons and the isospin equilibration between the fragments in contact have also been investigated in Refs. [13, 19, 27–29, 44, 47–61]. In addition to heavy-ion collisions, the TDHF approach has been used to describe neutron star crust dynamics [62, 63].

First, formal and practical aspects of TDHF calculations are presented in Sect. 4.2. Then, the formation of light molecules and the dynamics of $\alpha$-cluster states are discussed in Secs. 4.3 and 4.4, respectively. Quasi-elastic transfer is the subject of Sect. 4.5, followed by the study of more damped collisions, namely deep inelastic collisions in Sect. 4.6 and quasi-fission reactions in Sect. 4.7. Calculations of hyper-heavy molecules dynamics in reactions between actinides are presented in Sect. 4.8. Finally, recent TDHF studies of neutron star crust dynamics are discussed in Sect. 4.9.

## 4.2 The Time-Dependent Hartree-Fock Theory

The TDHF theory has been developed by Dirac in 1930 [64]. This is an extension of the mean-field approach to the ground-state of many-fermion systems introduced by Hartree [65] and Fock [66].

### 4.2.1 *The Mean-Field Approximation*

The TDHF theory determines the dynamics of a many-fermion system out of equilibrium under the approximation that the state of the system can be described by an independent-particle state at any time. The spatial correlations between the particles are obtained from the self-consistent mean-field. It is then assumed that each particle evolves independently in the mean-field generated by all the others.

The TDHF approach is naturally well adapted to many-body systems in weak interactions. Indeed, when the interactions are strong, the system is expected to develop correlations which make the independent particle picture fail on a relatively short time scale. One may then wonder why the TDHF approach has been so successful in describing low-energy nuclear dynamics (see Refs. [13, 67] for reviews).

In fact, at low energy, the Pauli principle prevents collisions between nucleons in such a way that the mean-free path of a nucleon in the nucleus is of the order of the size of the nucleus. This means that the wave-functions of the nucleons are essentially sensitive to the mean-field directly determined by the density. As a result, a nucleus in its ground state, where all the single-particle states below the Fermi level are almost entirely occupied, can be described with an independent particle state in a first approximation. Hartree-Fock calculations based on energy density functionals (EDF) are indeed able to reproduce quite well the binding energies and ground-state deformations along the nuclear chart (see Ref. [68] for a review).

Similarly, low-energy heavy-ion collisions can be treated at the mean-field level. Indeed, at energies around the fusion barrier, the motion of the nuclei is slow enough to prevent nucleon-nucleon collisions thanks to the Pauli principle during the first few zeptoseconds (zs) of the reaction. However, the mean-field approximation is expected to fail at higher energies (e.g., in the Fermi regime), or for longer times. For instance, only the first steps of the fusion process can be described with TDHF, while beyond mean-field correlations are needed to form an equilibrated compound nucleus (CN) on a longer time scale.

### 4.2.2 Formalism

The time-dependent Hartree-Fock equation reads [64]

$$i\hbar\frac{d}{dt}\rho(t) = \big[h\big[\rho(t)\big],\rho(t)\big], \tag{4.1}$$

where $\rho(t)$ is the one-body density matrix with matrix elements

$$\rho_{\alpha\beta} = \langle\Phi|\hat{a}^\dagger_\beta\hat{a}_\alpha|\Phi\rangle. \tag{4.2}$$

As the system is described by an independent particle-state, the state $|\Phi\rangle$ is a Slater determinant of the form

$$|\Phi\rangle = \left(\prod_{i=1}^{A}\hat{a}^\dagger_i\right)|-\rangle, \tag{4.3}$$

where $A$ is the number of particles, $\hat{a}^\dagger_i$ creates an occupied single-particle state $|\varphi_i\rangle = \hat{a}^\dagger_i|-\rangle$, and $|-\rangle$ is the vacuum. The one-body density matrix associated to such a state is a projector onto the subspace of occupied single-particle states with the property $\rho^2 = \rho$. It is associated to the single-particle operator

$$\hat{\rho} = \sum_{i=1}^{A}|\varphi_i\rangle\langle\varphi_i|. \tag{4.4}$$

The Hartree-Fock single-particle Hamiltonian $h[\rho]$ entering the TDHF equation (4.1) is obtained from the first derivative of the expectation value of the many-body Hamiltonian $\hat{H}$ according to the one-body density matrix. Its matrix elements read

$$h[\rho]_{\alpha\beta} = \frac{\delta\langle\Phi|\hat{H}|\Phi\rangle}{\delta\rho_{\beta\alpha}}. \tag{4.5}$$

In nuclear physics, however, the hard-core of the nucleon-nucleon interaction leads to a divergence of $\langle\Phi|\hat{H}|\Phi\rangle$ when evaluated on an independent-particle state. The effect of the hard-core can be renormalised in such a way that the energy does not diverge without affecting the low-energy properties of the system. In practical HF and TDHF calculations, the expectation value of $\hat{H}$ is replaced by an energy density functional $E[\rho]$ determined, for instance, from the Skyrme [69] or Gogny [70] phenomenological effective interaction. The HF Hamiltonian then reads

$$h[\rho]_{\alpha\beta} = \frac{\delta E[\rho]}{\delta\rho_{\beta\alpha}}. \tag{4.6}$$

### *4.2.3 The Skyrme Energy Density Functional*

The Skyrme energy density functional is obtained from a zero-range effective interaction with gradient terms [69]. Numerical calculations are greatly helped by the zero-range nature of the interaction which simplifies the expression of the mean-field.

The interaction between two nucleons in the medium reads

$$\begin{aligned}\hat{v}(1,2) = {} & t_0(1+x_0\hat{P}_\sigma)\hat{\delta} \\ & + \frac{1}{2}t_1(1+x_1\hat{P}_\sigma)\big(\hat{\mathbf{k}}'^2\hat{\delta}+\hat{\delta}\hat{\mathbf{k}}^2\big) \\ & + t_2(1+x_2\hat{P}_\sigma)\big(\hat{\mathbf{k}}'\cdot\hat{\delta}\hat{\mathbf{k}}\big) \\ & + \frac{1}{6}t_3(1+x_3\hat{P}_\sigma)\rho^\alpha(\hat{\mathbf{R}})\hat{\delta} \\ & + iW_0\hat{\boldsymbol{\sigma}}\cdot\big(\hat{\mathbf{k}}'\times\hat{\delta}\hat{\mathbf{k}}\big)\end{aligned} \tag{4.7}$$

where $\hat{\delta} = \delta(\hat{\mathbf{r}}(1) - \hat{\mathbf{r}}(2))$, $\hat{\mathbf{k}} = \frac{1}{2i}(\nabla(1) - \nabla(2))$ (relative momentum), $\hat{\mathbf{k}}'$ is the complex conjugated of $\hat{\mathbf{k}}$ acting on the left, and $\hat{\mathbf{R}} = (\hat{\mathbf{r}}(1) + \hat{\mathbf{r}}(2))/2$. The operators $\hat{\boldsymbol{\sigma}} = \hat{\boldsymbol{\sigma}}(1) + \hat{\boldsymbol{\sigma}}(2)$, with $\hat{\boldsymbol{\sigma}}(i) = \hat{\sigma}_x(i)\mathbf{e}_x + \hat{\sigma}_y(i)\mathbf{e}_y + \hat{\sigma}_z(i)\mathbf{e}_z$, are expressed in terms of the Pauli matrices $\hat{\sigma}_{x/y/z}(i)$ acting on the spin of the particle $i$. $\hat{P}_\sigma = [1 + \hat{\boldsymbol{\sigma}}(1)\cdot\hat{\boldsymbol{\sigma}}(2)]/2$ corresponds to the exchange of the spins. The particle density in $\mathbf{r}$ is noted $\rho(\mathbf{r}) \equiv \sum_{sq}\rho(\mathbf{r}sq, \mathbf{r}sq)$ where $\rho$ is the one-body density matrix, $s$ the spin and $q$ the isospin. The "$t_1$" and "$t_2$" terms are non-local in space and simulate the short range part of the interaction. Finally the last term accounts for the spin-orbit interaction.

The EDF describes how the energy of the system depends on its density. It is standard to introduce a local energy density $\mathscr{H}(\mathbf{r})$ such that

$$E = \int d\mathbf{r}\mathscr{H}(\mathbf{r}). \tag{4.8}$$

This energy density can be expressed as [71]

$$\begin{aligned}\mathscr{H}(\mathbf{r}) = {} & \frac{\hbar^2}{2m}\tau + B_1\rho^2 + B_2\sum_q \rho_q^2 \\ & + B_3\big(\rho\tau - \mathbf{j}^2\big) + B_4\sum_q\big(\rho_q\tau_q - \mathbf{j}_q^2\big) \\ & + B_5\rho\Delta\rho + B_6\sum_q \rho_q\Delta\rho_q + B_7\rho^{2+\alpha} + B_8\rho^\alpha\sum_q\rho_q^2 \\ & + B_9\Big(\rho\boldsymbol{\nabla}\cdot\mathbf{J} + \mathbf{j}\cdot\nabla\times\mathbf{S} + \sum_q\rho_q\boldsymbol{\nabla}\cdot\mathbf{J}_q + \mathbf{j}_q\cdot\nabla\times\mathbf{S}_q\Big) \\ & + B_{10}\mathbf{S}^2 + B_{11}\sum_q\mathbf{S}_q^2 + B_{12}\rho^\alpha\mathbf{S}^2 + B_{13}\rho^\alpha\sum_q\mathbf{S}_q^2.\end{aligned} \tag{4.9}$$

The densities entering Eq. (4.9) are the local density

$$\rho(\mathbf{r}) = \sum_{is}\varphi_i^*(\mathbf{r}s)\varphi_i(\mathbf{r}s), \tag{4.10}$$

where $s$ denotes the spin, and $\varphi_i$ are occupied single-particle states, the kinetic energy density

$$\tau(\mathbf{r}) = \sum_{is}\big|\boldsymbol{\nabla}\varphi_i(\mathbf{r}s)\big|^2, \tag{4.11}$$

the current density

$$\mathbf{j}(\mathbf{r}) = \frac{1}{2i}\sum_{is}\varphi_i^*(\mathbf{r}s)\boldsymbol{\nabla}\varphi_i(\mathbf{r}s) + c.c., \tag{4.12}$$

where *c.c.* means “complex conjugated”, the gradient of the spin-orbit density

$$\boldsymbol{\nabla}.\mathbf{J}(\mathbf{r}) = -i\sum_{iss'}\boldsymbol{\nabla}\varphi_i^*(\mathbf{r}s)\times\boldsymbol{\nabla}\varphi_i\big(\mathbf{r}s'\big)\cdot\langle s|\boldsymbol{\sigma}\big|s'\big\rangle, \tag{4.13}$$

and the spin density

$$\mathbf{S}(\mathbf{r}) = \sum_{is}\varphi_i^*(\mathbf{r}s)\varphi_i\big(\mathbf{r}s'\big)\langle s|\boldsymbol{\sigma}\big|s'\big\rangle. \tag{4.14}$$

In the above expressions, it is assumed that the one-body density-matrix $\rho$ is diagonal in isospin. The isospin is then omitted to simplify the notation. The $\mathbf{j}$ and $\mathbf{S}$ densities are time-odd and vanish in time-reversal invariant systems. They are, however, important in time-dependent calculations to ensure Galilean invariance [72].

Note that the general Skyrme EDF includes other terms which are neglected in Eq. (4.9). These additional terms are of the form $\mathbf{S} \cdot \Delta \mathbf{S}$ and with other densities, i.e., the spin-current pseudo-tensor $\overset{\leftrightarrow}{J}$ and the spin-kinetic energy density $\mathbf{T}$ [22, 72]. They are sometimes included in TDHF calculations [21, 22, 73]. In Eq. (4.9), only the anti-symmetric part of $\overset{\leftrightarrow}{J}$, which is the spin-orbit density $\mathbf{J}$, is included. The spin-orbit energy is indeed expected to be more important (by about one order of magnitude) than the other spin-gradient terms [74].

The coefficients $B_i$ in Eq. (4.9) are related to the parameters of the Skyrme effective interactions $\{t_{0-3}, x_{0-3}, \alpha, W_0\}$ as

$$\begin{aligned}
B_1 &= \frac{t_0}{2}\left(1+\frac{x_0}{2}\right) \\
B_2 &= -\frac{t_0}{2}\left(x_0+\frac{1}{2}\right) \\
B_3 &= \frac{1}{4}\left[t_1\left(1+\frac{x_1}{2}\right)+t_2\left(1+\frac{x_2}{2}\right)\right] \\
B_4 &= -\frac{1}{4}\left[t_1\left(x_1+\frac{1}{2}\right)-t_2\left(x_2+\frac{1}{2}\right)\right] \\
B_5 &= -\frac{1}{16}\left[3t_1\left(1+\frac{x_1}{2}\right)-t_2\left(1+\frac{x_2}{2}\right)\right] \\
B_6 &= \frac{1}{16}\left[3t_1\left(x_1+\frac{1}{2}\right)+t_2\left(x_2+\frac{1}{2}\right)\right] \\
B_7 &= \frac{t_3}{12}\left(1+\frac{x_3}{2}\right) \\
B_8 &= -\frac{t_3}{12}\left(x_3+\frac{1}{2}\right) \\
B_9 &= -\frac{1}{2}W_0 \\
B_{10} &= \frac{t_0 x_0}{4} \\
B_{11} &= -\frac{t_0}{4} \\
B_{12} &= \frac{t_3 x_3}{24} \\
B_{13} &= -\frac{t_3}{24}.
\end{aligned} \tag{4.15}$$

The Skyrme-HF mean-field is derived from Eq. (4.6). Its action on single-particle wave functions is then given by [71]

$$\begin{aligned}
&\big(h[\rho]\varphi_i\big)(\mathbf{r},s) \\
&\quad = \sum_{s'}\left[\left(-\boldsymbol{\nabla}\frac{\hbar^2}{2m^*_{q_i}(\mathbf{r})}\boldsymbol{\nabla}+U_{q_i}(\mathbf{r})+i\mathbf{C}_{q_i}(\mathbf{r})\cdot\boldsymbol{\nabla}\right)\delta_{ss'}\right.
\end{aligned}$$

$$+\mathbf{V}_{q_i}(\mathbf{r})\cdot\langle s|\boldsymbol{\sigma}|s'\rangle + i\mathbf{W}_{q_i}(\mathbf{r})\cdot\big(\langle s|\boldsymbol{\sigma}|s'\rangle\times\nabla\big)\Big]\varphi_i\big(\mathbf{r},s'\big), \tag{4.16}$$

where $q_i$ is the isospin of the state $|\varphi_i\rangle$. The derivatives act on each term sitting on their right, including the wave function. The fields (functions of $\mathbf{r}$) read

$$\frac{\hbar^2}{2m_q^*} = \frac{\hbar^2}{2m} + B_3\rho + B_4\rho_q \tag{4.17}$$

$$\begin{aligned} U_q =\, & 2B_1\rho + 2B_2\rho_q + B_3(\tau + i\nabla\cdot\mathbf{j}) + B_4(\tau_q + i\nabla\cdot\mathbf{j}_q) \\ & + 2B_5\Delta\rho + 2B_6\Delta\rho_q + (2+\alpha)B_7\rho^{1+\alpha} \\ & + B_8\left[\alpha\rho^{\alpha-1}\sum_q \rho_q^2 + 2\rho^\alpha\rho_q\right] + B_9(\nabla\cdot\mathbf{J} + \nabla\cdot\mathbf{J}_q) \\ & + \alpha\rho^{\alpha-1}\left(B_{12}\mathbf{S}^2 + B_{13}\sum_q \mathbf{S}_q^2\right) \end{aligned} \tag{4.18}$$

$$\begin{aligned} \mathbf{V}_q =\, & B_9\nabla\times(\mathbf{j}+\mathbf{j}_q) + 2B_{10}\mathbf{S} + 2B_{11}\mathbf{S}_q \\ & + 2\rho^\alpha(B_{12}\mathbf{S} + B_{13}\mathbf{S}_q) \end{aligned} \tag{4.19}$$

$$\mathbf{W}_q = -B_9\nabla(\rho+\rho_q) \tag{4.20}$$

$$\mathbf{C}_q = 2B_3\mathbf{j} + 2B_4\mathbf{j}_q - B_9\nabla\times(\mathbf{S}+\mathbf{S}_q), \tag{4.21}$$

where the derivatives act on the first term sitting on their right only. The label $q$ denotes the isospin. The effective mass $m_q^*$ of nucleons with isospin $q$ is introduced in [Eq. (4.17)]. It originates from the non-local terms of the effective interaction in Eq. (4.7).

The parameters of the Skyrme EDF are fitted on few quantities (see, e.g., Ref. [74]). These include the density $\rho_0 \simeq 0.16$ fm$^{-3}$ and energy per nucleon $E/A \simeq -16$ MeV of the infinite symmetric nuclear matter at saturation as well as its compressibility. Depending on the parametrisation, the equation of state of the infinite neutron matter [75], the enhancement factor of the Thomas-Reiche-Kuhn sum rule, the symmetry energy, and the radii and binding energies of few doubly-magic nuclei may be included as constraints into the fitting procedure as well.

It is interesting to note that no input on nuclear reaction mechanism, such as fusion barriers or cross-sections, are included in the fit. Nevertheless, as we will see in this chapter, the description of collision dynamics with TDHF is very realistic, and agreements with experimental observables are sometimes impressive.

Finally, the Coulomb interaction between the protons is added to the Skyrme mean-field. The direct part of the Coulomb energy reads

$$E_c^{dir} = \frac{e^2}{2}\int d^3r \int d^3r' \frac{\rho_p(\mathbf{r})\rho_p(\mathbf{r}')}{|\mathbf{r}-\mathbf{r}'|}. \tag{4.22}$$

The latter is usually computed by solving, first, the Poisson equation to get the Coulomb potential $V_c(\mathbf{r})$, and, then, by evaluating the integral $\frac{1}{2}\int d^3r\rho_p V_c$. The exchange part of the Coulomb energy is usually determined within the Slater approximation as

$$E_c^{ex} = \frac{-3e^2}{4}\left(\frac{3}{\pi}\right)^{\frac{1}{3}} \int d^3r \rho_p(\mathbf{r})^{\frac{4}{3}}. \tag{4.23}$$

As a result, the contribution of the Coulomb interaction to the proton mean-field reads

$$U_c = V_c - e^2\left(\frac{3\rho_p}{\pi}\right)^{\frac{1}{3}}. \tag{4.24}$$

### 4.2.4 Numerical Implementation

The TDHF equation is never implemented with its Liouville-von Neumann form given in Eq. (4.1). Instead, a set of non-linear Schrödinger-like equations for single-particle motion is used. Indeed, Eq. (4.1) can be expressed in a fully equivalent way as

$$i\hbar\frac{d}{dt}\big|\varphi_i(t)\big\rangle = \hat{h}\big[\rho(t)\big]\big|\varphi_i(t)\big\rangle, \quad 1 \le i \le A. \tag{4.25}$$

The numerical advantage of using Eqs. (4.25) instead of Eq. (4.1) is obvious in terms of computer memory. Indeed, for a basis of $N$ single-particle states (e.g., the number of points of a Cartesian grid), the storage of $\rho$ requires a $N \times N$ array, while the wave-functions in Eq. (4.25) require a $N \times A$ array. As $A$ is usually much smaller than $N$, one clearly realises the advantage of solving Eqs. (4.25) instead of Eq. (4.1).

Equations (4.25) are coupled by the self-consistency of the HF Hamiltonian as it depends on the total density of the system. As a result, the HF Hamiltonian is time-dependent and one needs to solve Eqs. (4.25) iteratively in time. The sates at time $t + \Delta t$ are determined from the states at time $t$ assuming that $\hat{h}$ is constant between $t$ and $t + \Delta t$. This implies that $\Delta t$ has to be chosen small enough for this condition to be valid. Typical time step increments $\Delta t$ in nuclear physics range from $\sim 5 \times 10^{-25}$ s [76, 77] to $\sim 1.5 \times 10^{-24}$ s [18, 78].

In addition, to conserve energy and particle number, the algorithm has to be symmetric under time-reversal transformation. This implies that the HF Hamiltonian has to be evaluated at $t + \frac{\Delta t}{2}$ [79]. The evolution operator then reads

$$\big|\varphi_i(t + \Delta t)\big\rangle \simeq e^{-i\hat{h}(t+\frac{\Delta t}{2})/\hbar}\big|\varphi_i(t)\big\rangle. \tag{4.26}$$

A truncated Taylor development of the exponential is usually considered. The evolution operator then breaks unitarity and one should check the orthonormalisation of the wave-functions during the time evolution.

A possible algorithm to perform the time evolution in Eq. (4.26) is described below:

$$\begin{tikzcd}
\left\{\left|\varphi_1^{(n)}\right\rangle \cdots \left|\varphi_A^{(n)}\right\rangle\right\} \arrow[r, Rightarrow] & \rho^{(n)} \arrow[d, Rightarrow] \\
\left|\varphi_i^{(n+1)}\right\rangle = e^{-i\frac{\Delta t}{\hbar}\hat{h}^{(n+\frac{1}{2})}}\left|\varphi_i^{(n)}\right\rangle \arrow[u, Rightarrow] & \hat{h}^{(n)} \equiv \hat{h}\left[\rho^{(n)}\right] \arrow[d, Rightarrow] \\
\hat{h}^{(n+\frac{1}{2})} \equiv \hat{h}\left[\rho^{(n+\frac{1}{2})}\right] \arrow[u, Rightarrow] & \left|\tilde{\varphi}_i^{(n+1)}\right\rangle = e^{-i\frac{\Delta t}{\hbar}\hat{h}^{(n)}}\left|\varphi_i^{(n)}\right\rangle \arrow[d, Rightarrow] \\
\rho^{(n+\frac{1}{2})} = \frac{\rho^{(n)}+\tilde{\rho}^{(n+1)}}{2} \arrow[u, Rightarrow] & \tilde{\rho}^{(n+1)} \arrow[l, Rightarrow]
\end{tikzcd} \tag{4.27}$$

where $|\varphi_i^{(n)}\rangle$ is an approximation of $|\varphi_i(t_n = n\Delta t)\rangle$. A first evolution over $\Delta t$ is performed to estimate the density at $t + \Delta t$. The latter is used, together with the density at $t$, to determine the density, and then the HF Hamiltonian, at $t + \frac{\Delta t}{2}$. This Hamiltonian is finally used to evolve the wave-function from $t$ to $t + \Delta t$.

Possible single-particle bases to solve the TDHF equation numerically are the harmonic-oscillator basis [80], basis-spline collocation method [81], wavelets [62], adaptive networks [76], or regular Cartesian grids [18, 82]. Typical regular mesh spacing with $\Delta x \simeq 0.6$ fm [77], 0.8 fm [18] and 1.0 fm [78, 82] are used.

The initial condition of a TDHF calculation of heavy-ion collisions usually assumes that the nuclei are at some finite distance in their HF ground state. HF calculations of the collision partners then need to be performed prior to the TDHF evolution. This is done with the same EDF as in the TDHF calculation to ensure full self-consistency between structure and dynamics. Large initial distances between the centers-of-mass should be used to enable a proper treatment of the Coulomb excitation in the entrance channel. Typical distances of the order of ∼40 fm are considered as a good compromise to limit computational time. It is also usually assumed that the nuclei followed a Rutherford trajectory prior to this initial condition. It determines the initial momenta $\hbar\mathbf{k}$ to be applied to the nucleons using Galilean boosts of the form

$$\left|\varphi_i(t=0)\right\rangle = e^{i\mathbf{k}\cdot\hat{\mathbf{r}}}\left|\varphi_i^{HF}\right\rangle, \tag{4.28}$$

where $|\varphi_i^{HF}\rangle$ are the HF single particle states.

More details on numerical implementations of the TDHF equation can be found in Refs. [13, 83].

### 4.2.5 Beyond the TDHF Approach

The independent-particle approximation can be considered as a zeroth order approximation to the many-body problem. In fact, the exact evolution of the one-body density-matrix reads

$$i\hbar\frac{\partial}{\partial t}\rho_1 = [t_1, \rho_1] + \frac{1}{2}\,\mathrm{Tr}_2[\bar{v}_{12}, \rho_{12}], \tag{4.29}$$

where $\bar{v}_{12}$ is the antisymmetrised two-body interaction and $\rho_1$ and $\rho_{12}$ are the one- and two-body density-matrices, respectively. Solving Eq. (4.29) requires the knowledge of $\rho_{12}(t)$. The latter obeys an evolution equation which depends on the three-body density-matrix. In fact, Eq. (4.29) is the first equation of the BBGKY hierarchy [84–86] providing a set of coupled equations for $\rho_1$, $\rho_{12}$, $\rho_{123} \ldots$

We see that the TDHF equation is obtained by neglecting the last term in Eq. (4.29). It is important to know what is the physical meaning of this term. It contains the so-called two-body correlations which develop because of the residual interaction, i.e., the difference between the exact and mean-field Hamiltonians. Three main types of correlations can be identified:

- pairing correlations,
- correlations induced by a collision term,
- and long-range dynamical fluctuations.

Pairing correlations are important for a proper description of mid-shell nuclei, as well as to describe pair-transfer reactions, as we will see in Sect. 4.5.2. They can be included using a "generalised" mean-field approximation. In this case, the state of the system is described as a quasi-particle vacuum [87]. This leads to the BCS model for pairing between time-reversed states, or, more generally, to the Hartree-Fock-Bogoliubov approximation. Nuclear dynamics in presence of pairing has been investigated recently with the TD-BCS approach [88, 89], and at the TDHFB level [80, 90, 91]. The linearised version of TDHFB is the quasi-particle random-phase approximation (QRPA) which has been widely applied to study nuclear vibrations [92–95]. Applications of the TDHFB formalism to study pairing vibrations are presented in Sect. 4.5.3.

The collision term is important at high energy, and to describe long-term dynamics such as the thermalisation of the compound nucleus. It can be added to the TDHF equation in what becomes the Extended-TDHF formalism [96–101]. A more general approach including pairing and a collision term is given by the time-dependent density-matrix (TDDM) formalism [102, 103] which has been applied to heavy-ion collisions [104, 105]. However, to describe reaction mechanisms at intermediate energy such as multi-fragmentation, quantum effect can be neglected in a first approximation. Semi-classical versions of the mean-field theory including collision terms, such as the Landau-Vlasov formalism, have then been widely used to describe reaction mechanisms at intermediate energy [106–108].

Long-range dynamical fluctuations may play an important role even at low energy. For instance, they are crucial to determine fluctuations of one-body operators, such as the fragment mass and charge distribution widths in heavy-ion collisions. In the limit where fluctuations around the TDHF path are small, then a good description of these distributions is obtained within the time-dependent RPA (TDRPA) formalism. The latter can be obtained from the Balian-Vénéroni variational principle [109, 110]. Numerical applications to describe fragment mass and charge distributions in deep-inelastic collisions have been recently performed and compared to experiment in Ref. [59]. Alternatively, such fluctuations could also be obtained from the stochastic mean-field (SMF) approach [50, 111], or from the time-dependent generator coordinate method (TDGCM) [112, 113].

Realistic calculations with these approaches beyond TDHF are often very demanding from a numerical point of view and systematic applications are usually prohibitive even with modern high-performance computing facilities. In this chapter, we then focus on TDHF applications, paying attention to the limitations and possible improvements in the future. However, recent numerical calculations with the TDHFB and TDRPA approaches are also presented.

## 4.3 Formation of Light Molecules

Nuclear molecules made of light nuclei such as $^{12}$C and $^{16}$O are formed and studied thanks to nuclear collisions. The dynamics of the formation of such di-nuclear systems is the purpose of the present section.

### 4.3.1 *Structures in Fusion Cross-Sections*

Structures in fusion cross-sections are possible experimental signatures of nuclear molecules [7, 114]. However, structures in fusion excitation functions may also appear in light systems which are not necessarily due to the formation of nuclear molecules. Such structures or oscillations appear clearly in cross-sections for the fusion of $^{12}\mathrm{C}+{}^{12}\mathrm{C}$ [115], $^{12}\mathrm{C}+{}^{16}\mathrm{O}$ [116], and $^{16}\mathrm{O}+{}^{16}\mathrm{O}$ [117–119]. In particular, the discrete nature of angular momentum may reveal itself in fusion excitation functions as peaks associated to barriers for specific angular momenta [120–122].

The fusion cross-section is written as

$$\sigma_{fus.}(E_{c.m.}) = \frac{\pi\hbar^2}{2\mu E_{c.m.}}\sum_{L=0}^{\infty}(2L+1)P_{fus.}(L,E_{c.m.}) \tag{4.30}$$

where $\mu$ is the reduced mass of the system. $P_{fus.}(L,E_{c.m.})$ is the fusion probability for the partial wave with orbital angular momentum $L$ at the center-of-mass energy $E_{c.m.}$.

TDHF calculations do not include tunnelling of the many-body wave-function, i.e., $P_{fus.}^{\mathrm{TDHF}}=0$ or 1. As a result, the fusion cross-section can be estimated with the quantum sharp cut-off formula [123]

$$\begin{aligned}\sigma_{fus.}(E_{c.m.}) &= \frac{\pi\hbar^2}{2\mu E_{c.m.}}\sum_{L=0}^{L_{max}(E_{c.m.})}(2L+1)\\ &= \frac{\pi\hbar^2}{2\mu E_{c.m.}}\left[L_{max}(E_{c.m.})+1\right]^2,\end{aligned} \tag{4.31}$$

where $L_{max}(E_{c.m.})$ is the maximum angular momentum at which fusion occurs at $E_{c.m.}$. For fusion of symmetric systems with $0^+$ ground-states, fusion can only occur

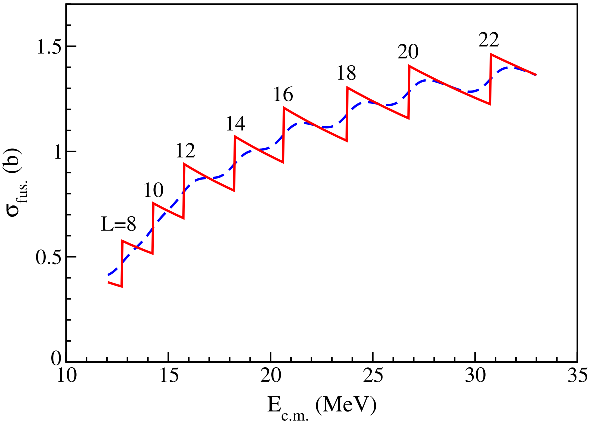

**Fig. 4.1** Fusion cross-section as a function of center-of-mass energy in $^{16}O + {}^{16}O$ obtained with TDHF calculations. The cross-sections are computed with the sharp cut-off formula (*solid line*) and using Eq. (4.33) for the barrier penetration probabilities (*dashed line*). The *numbers* indicate the position of the barriers $B(L)$

for even values of the angular momentum. The cross-section with the sharp cut-off formula then reads

$$\sigma_{fus.}(E_{c.m.}) = \frac{\pi\hbar^2}{2\mu E_{c.m.}}\big[L_{max}(L_{max}+3)+2\big]. \tag{4.32}$$

An example of fusion cross-section in $^{16}O + {}^{16}O$ as function of energy obtained with the TDHF3D code with the SLy4*d* Skyrme EDF [18] and Eq. (4.32) is shown in Fig. 4.1 with solid line. The sharp increases of the fusion cross-sections at the positions of the angular momentum dependent barriers $B(L)$ are due to the fact that fusion penetration probabilities are either 0 or 1 at the TDHF level.

These peaks are highly smoothen when tunnelling is taken into account. As a first approximation, one can estimate the barrier penetration probability according to the Hill-Wheeler formula [124] with a Fermi function

$$P_{fus.}(L, E_{c.m.}) \simeq \frac{e^{x_L}}{1+e^{x_L}}, \tag{4.33}$$

with $x_L = [E - B(L)]/\varepsilon$. Choosing the decay constant $\varepsilon = 0.4$ [122], one gets the fusion cross-sections represented by a dashed line in Fig. 4.1. Oscillations for $E_{c.m.} > 16$ MeV are clearly visible and due to $L$-dependent barriers with $L \geq 12\hbar$. Note that these oscillations are less visible for asymmetric systems due to the fact that all integer values of $L$ are possible. In addition, the observation of these oscillations is limited to light systems up to, e.g., $^{28}Si + {}^{28}Si$ [122, 125]. For heavier systems, the oscillations are indeed expected to be smeared out as the coupling to many reaction channels sets in [122].

To conclude, structures due to oscillations of the fusion cross-sections generated by the discrete nature of the angular momentum are expected to occur in light systems, in particular for symmetric collisions. As a result, one should be careful in the search for resonances associated to molecular states in these systems. In particular, the observation of a peak in the fusion cross-sections may not be sufficient to assign such a structure to a resonance state. One should, in addition, search for this resonance in other channels, and investigate its decay properties [7].

**Fig. 4.2** Distance between the centers-of-mass of the fragments as a function of time in $^{12}$C + $^{16}$O at $E_{c.m.} = 8.8$ MeV for $L = 3\hbar$, $4\hbar$ and $5\hbar$

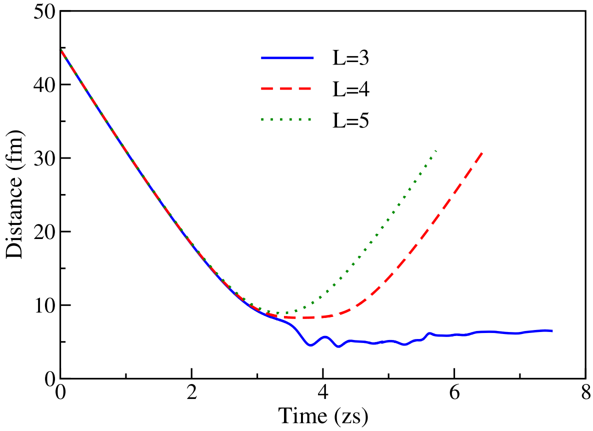

### 4.3.2 Contact Times Around the Barrier in $^{12}$C + $^{16}$O

Resonances at and below the barrier may strongly affect the reaction outcome. For instance, narrow resonances have been observed in the radiative capture $^{12}$C($^{16}$O, $\gamma$)$^{28}$Si close to the Coulomb barrier [7]. In particular, tentative spins of $4\hbar$, $5\hbar$ and $6\hbar$ have been assigned in the collision energy range $E_{c.m.} \simeq 8.5 - 9$ MeV [7, 114, 126].

To try to better understand in a dynamical way the presence of resonances and the contribution of relatively large spins at energies close to the Coulomb barrier, TDHF calculations have been performed on the $^{12}$C + $^{16}$O system [7]. For this system, the Coulomb barrier obtained with the TDHF3D code and the SLy4*d* Skyrme functional [18] is $B = 7.85 \pm 0.05$ MeV.

Figure 4.2 shows the distance between the centers-of-mass of the fragments as a function of time at $E_{c.m.} = 8.8$ MeV for different values of the angular momentum. Fusion occurs at $L \leq 3\hbar$ and re-separation at $L \geq 4\hbar$. Without the presence of molecular states at $4\hbar$, $5\hbar$ and $6\hbar$, the system would undergo a fast re-separation within ∼1–2 zs. This indicates that these spins are populated by a direct transition toward resonant states of the compound nucleus.

In the collision, the system may spend some time in a di-nuclear configuration, which presents some analogies with a molecular state. The excitation of the latter is then expected to increase with the lifetime of the di-nuclear system. The definition chosen here for the existence of a di-nucleus is the following: the nuclear density at the neck should be between 0.004 and 0.14 fm$^{-3}$, i.e., lower than the saturation density of 0.16 fm$^{-3}$. These nuclear densities correspond to distances between $^{12}$C and $^{16}$O from 5.98 to 10.43 fm.

The di-nuclear lifetime is shown as a function of the average angular momentum $\langle L\rangle$ in Fig. 4.3. Peaks are observed at the critical mean angular momentum $\langle L\rangle_c$ for fusion. We get $\langle L\rangle_c \simeq 3.2\hbar$, $3.9\hbar$, and $4.4\hbar$ for $E_{c.m.} = 8.5$, 8.8, and 9 MeV, respectively. Below $\langle L\rangle_c$, this time increases with $\langle L\rangle$ because the fusion process is slowed down by the centrifugal repulsion. In contrast, for $\langle L\rangle$ greater than $\langle L\rangle_c$, the

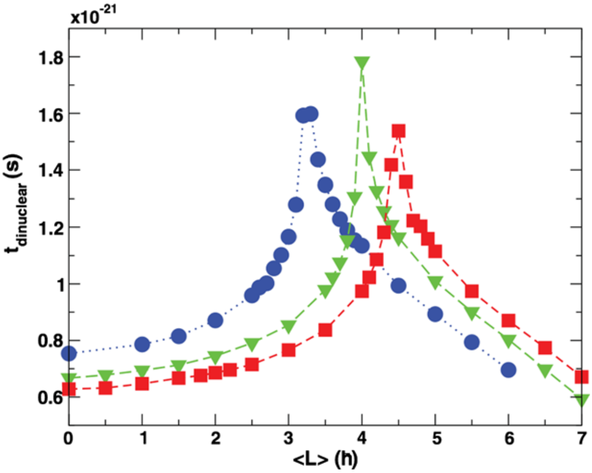

**Fig. 4.3** Di-nuclear lifetimes (see text) as a function of the mean angular momentum at $E_{c.m.} = 8.5$ MeV (*blue circles*), 8.8 MeV (*green triangles*), and 9 MeV (*red squares*). Adapted from Ref. [7]

fragments re-separate and the time of contact decreases for more peripheral collisions.

With the present definition of the di-nuclear system lifetime, we see that such a system exists at relatively high angular momenta of $5\hbar$ and $6\hbar$ during $\sim$0.7–1.2 zs depending on the energy. The corresponding lifetimes are shorter than the lifetimes of typical resonances at the Coulomb barrier, which are $\sim$2.6 zs [126, 127]. However, they may be sufficient to enable a direct excitation of a resonant or molecular state of the compound nucleus with a similar structure. In particular, we see that, for $\langle L\rangle = 5\hbar$ and $6\hbar$ (above the critical angular momenta), the lifetime increases with energy. Similarly, the probability for the population of a molecular state is also expected to increase. This may explain why the experimental cross-section for radiative capture is observed to increase with energy for these spins [7].

### 4.3.3 The $J^\pi = 36^+$ Resonance in $^{24}$Mg + $^{24}$Mg

The $^{24}$Mg + $^{24}$Mg system presents a resonance with high spin ($36\hbar$ to $38\hbar$) at twice the Coulomb barrier, corresponding to an excitation energy $E^* \simeq 60$ MeV in the $^{48}$Cr. At this energy, many decay channels are open and it is necessary, from an experimental point of view, to investigate as many of these channels as possible. For instance, the $J^\pi = 36^+$ resonance in $^{24}$Mg + $^{24}$Mg is observed at $E_{c.m.} = 45.7$ MeV essentially in inelastic scattering [128] with a lifetime $\tau = \frac{\hbar}{\Gamma} \simeq 3.9$ zs. The decay of this resonance has been recently investigated in both inelastic and fusion-evaporation channels [8].

One particularity of the $^{24}$Mg is its strong prolate deformation. Indeed, HF calculations with the EV8 code [129] and the SLy4*d* Skyrme functional [18] of the Skyrme EDF [69] give a quadrupole deformation parameter $\beta_2 \simeq 0.4$ [20]. As mentioned in Sect. 4.2, one advantage of the TDHF theory is that it describes the structure and the reaction mechanisms on the same footing. It is then well suited to

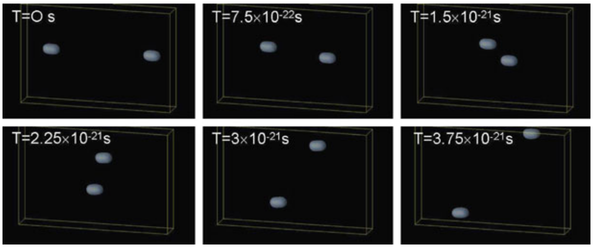

**Fig. 4.4** TDHF calculation of the reaction $^{24}\mathrm{Mg} + {}^{24}\mathrm{Mg}$ at $L = 36\hbar$ and $E_{c.m.} = 45.7$ MeV. The isodensity is plotted at half the saturation density, i.e., $\rho_0/2 = 0.08\ \mathrm{fm}^{-3}$. The deformation axes are aligned with the $x$-axis at the initial time of the collision

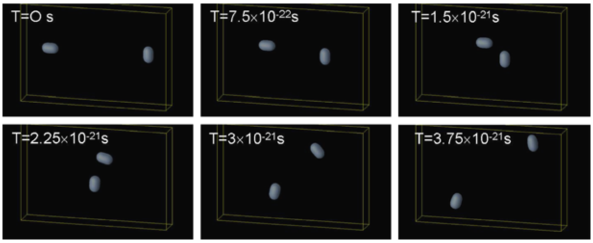

**Fig. 4.5** Same as Fig. 4.4 with the deformation axis of the right nucleus aligned with the $y$-axis at initial time

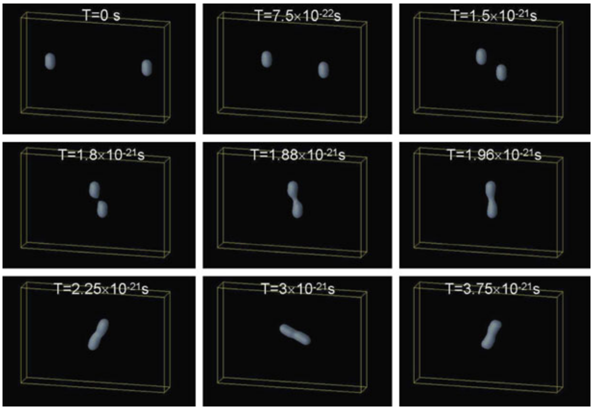

**Fig. 4.6** Same as Fig. 4.4 with both deformation axes aligned with the $y$-axis at initial time

investigate the role of the orientation of deformed nuclei on reaction mechanisms [20, 24, 29, 31, 52, 53].

In the present case, we can then investigate the role of the orientation of the $^{24}$Mg fragments at contact on the outcome of the reaction at $L = 36\hbar$ and $E_{c.m.} = 45.7$ MeV, that is, where the $36^+$ resonance is expected. In particular, we can determine which relative orientations (e.g., tip-tip, tip-side, side-side) lead to the formation of a di-nuclear system.

Figures 4.4, 4.5 and 4.6 present density evolutions of the $^{24}\mathrm{Mg} + {}^{24}\mathrm{Mg}$ system at $L = 36\hbar$ and $E_{c.m.} = 45.7$ MeV for different initial orientations of the nuclei computed with the TDHF3D code using the SLy4$d$ Skyrme functional [18]. We observe that the contact time between the fragments, if any, is extremely short as compared to the lifetime of the resonance, except when the contact occurs by the tip of the deformed collision partners, as it can be seen in Fig. 4.6. In the latter case, a di-nuclear system is formed with a lifetime similar or greater than the one of the resonance. As a result, it is likely to populate the resonance. This resonance could then be associated to a molecular state with the two fragments linked by a neck between their tips. In particular, it corresponds to a hyper-deformed nucleus as we can see in Fig. 4.6.

To sum up, TDHF calculations provide an insight into the formation of the $36^+$ resonance in $^{24}$Mg + $^{24}$Mg. In particular, this resonance may be associated to a highly deformed state of the $^{48}$Cr formed by the two aligned $^{24}$Mg in contact by their tips.

## 4.4 $\alpha$-Clustering

$\alpha$-clusters play an important role in nuclear structure, both for ground- and excited states, due to the high binding energy of $^4$He [1–5, 130–133]. They may also affect reactions. For instance, large cross-sections for the $^7\text{Li} + ^{208}\text{Pb} \rightarrow 2\alpha + ^{207}\text{Tl}$ were recently measured [134], whereas this channel has a large negative Q-value. $\alpha$-clustering in the entrance and/or exit channel is also believed to enhance $\alpha$-transfer in heavy-ion collisions. One recent illustration is the formation of $\alpha$-cluster states in $^{212}$Po with the reaction $^{208}$Pb($^{18}$O, $^{14}$C) [135]. $\alpha$-clustering is also playing an important role in astrophysical processes such as helium burning in stars [136].

In this section, we present examples of reactions to illustrate the role of $\alpha$-clusters in nuclear reactions. We first investigate the $^4$He + $^8$Be reaction of astrophysical interests, and, then, we study the survival of an $\alpha$-cluster in its fusion with a $^{208}$Pb nucleus.

### 4.4.1 *Three-$\alpha$ Cluster Configurations in* $^4$He + $^8$Be

The $^8$Be ground-state exhibits a 2-$\alpha$-cluster configuration [1, 3]. This can be seen in Fig. 4.7 which shows the density profile of $^8$Be obtained from a HF calculation. In fact, the $^8$Be is unbound and decays by the emission of $2\alpha$ with a lifetime of the order of $\sim 10^{-16}$ s. This lifetime, however, is long enough to allow the $^4$He + $^8$Be fusion by radiative capture to occur in stars. This reaction is considered as the main source of $^{12}$C production in the universe [136].

In this reaction, the $^{12}$C is formed in the $0_2^+$ state at $E^* = 7.654$ MeV of excitation energy, i.e., just above the 3-$\alpha$ separation threshold. This state, also known as the Hoyle state [137], is believed to have a strong 3-$\alpha$ cluster configuration [1, 4, 5]. The exact configuration of the $\alpha$-clusters in the Hoyle state is still under debate. In particular, it has been suggested that 3-$\alpha$ linear chains may contribute [138, 139].

Recently, Umar and collaborators have investigated the dynamics of 3-$\alpha$ linear chains formed in the $^4$He + $^8$Be reaction using the TDHF formalism [38]. A 3-$\alpha$ linear chain is formed by the capture of a $^4$He by the tip of the $^8$Be in low-energy central collisions. Density profiles illustrating different stages of the dynamics of a

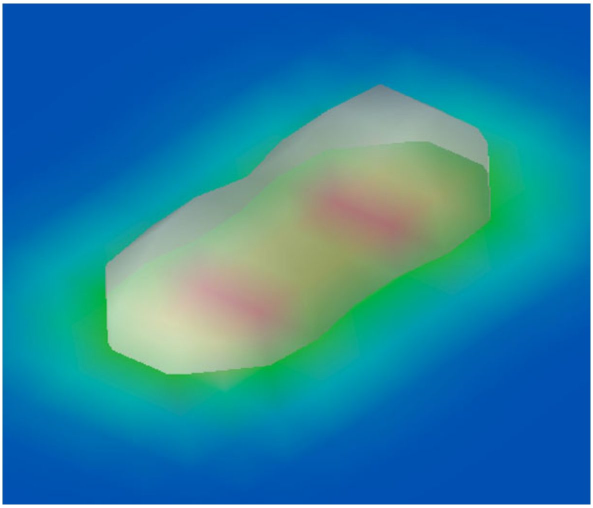

**Fig. 4.7** HF ground-state density of $^8$Be obtained with the SLy4*d* parametrisation [18] of the Skyrme EDF

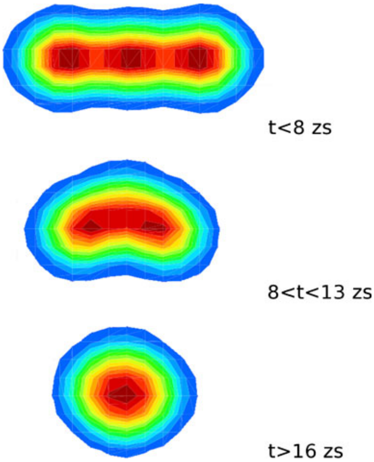

**Fig. 4.8** Density snapshots of a $^4\text{He} + ^8\text{Be}$ reaction at $E_{c.m.} = 2$ MeV leading to a 3-$\alpha$ linear chain (*top*) and evolving toward a triangular shape (*middle*) and then toward a more compact shape (*bottom*). Adapted from Ref. [38]

3-$\alpha$ linear chain formed in such a central collision are shown in Fig. 4.8. The linear chain (top of Fig. 4.8) is present during a long time (up to 8 zs). During this time, the $\alpha$-clusters present a longitudinal vibrational mode [38]. It is interesting to note that the clusters remain for such a long time, while the underlying formalism is a mean-field model of independent particles, i.e., without imposing the presence of such clusters in the wave-function.

For longer times, the chain becomes unstable due to the appearance of a bending motion favouring the formation of triangular shapes (middle of Fig. 4.8). The clusters still encounter some vibrations in this mode, with the center cluster oscillating perpendicular to the left and right clusters. This vibration mode last for another $\sim 4$ zs with almost no damping before a more compact shape is formed (bottom of Fig. 4.8).

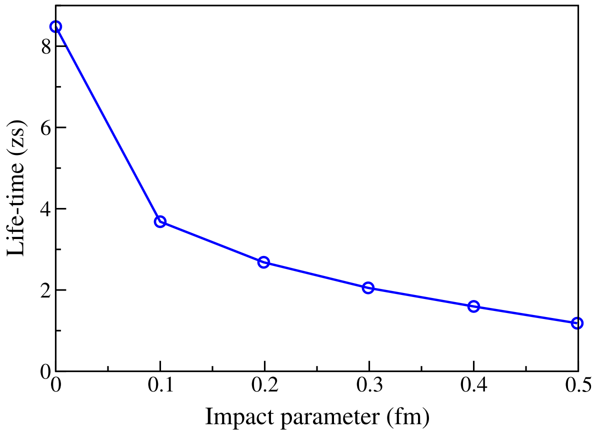

**Fig. 4.9** Lifetime of the 3-$\alpha$ chain as a function of the impact parameter for the $^{4}$He + $^{8}$Be reaction at $E_{c.m.} = 2$ MeV. Adapted from Ref. [38]

The role of impact parameter has also been studied by Umar et al. in Ref. [38]. A decrease of the lifetime of the linear chain with the impact parameter was observed, as reported in Fig. 4.9. We note that, although non-central collisions do not favour long lifetime of linear chains, they are stable enough to survive more than 1 zs as long as the collision occurs with the tip of $^{8}$Be and for impact parameters not exceeding 0.5 fm. These times are of the same order of magnitude, if not larger, than typical lifetimes of di-nuclear systems formed in near-barrier heavy-ion collisions.

To conclude, relatively long lifetimes of few zs are observed for linear chains of 3-$\alpha$ clusters formed in $^{4}$He + $^{8}$Be within the TDHF approach which does not assume *a priori* cluster components in the wave-function. The dynamics of these structures exhibit complex vibrational modes based on oscillations of the $\alpha$-cores. In fact, similar vibrational modes have been found with the fermionic molecular dynamics approach by Furuta and collaborators [131]. In particular, possible strong effects on the vibrational response functions of light nuclei have been noticed.

### *4.4.2 Survival of α-Clusters in* $^{4}$He + $^{208}$Pb *Near-Barrier Fusion*

The previous section emphasises the survival of $\alpha$-clustering after a capture process in a light system. $\alpha$-clustering is not limited, however, to light nuclei. Indeed, the well-known $\alpha$-radioactivity, which occurs essentially in heavy nuclei, is another form of $\alpha$-clustering. In addition, the reverse process of capture of an $\alpha$ by a heavy nucleus in a transfer or a fusion reaction may form excited states interpreted as nucleus + $\alpha$ molecules. For instance, new excited states have been recently observed in $^{212}$Po that are interpreted as $\alpha$+$^{208}$Pb configurations [135].

The dynamics of the $\alpha$ + $^{208}$Pb system after capture of the $\alpha$ by the heavy partner has been investigated with an early TDHF code in Ref. [14]. However, these calculations were performed with a simplified Skyrme functional. In particular, they did not include the spin-orbit interaction which is known to be crucial for a proper description of nuclear reactions [21, 22, 140]. In fact, the spin-orbit interaction and the difference between proton and neutron mean-fields may induce a “dissolution” of an $\alpha$-particle entering the mean-field of a collision partner [141].

To test this idea, three-dimensional TDHF calculations with the TDHF3D code and the SLy4$d$ Skyrme functional [18] including spin-orbit terms have been performed. The $^{4}$He + $^{208}$Pb central collision at $E_{c.m.} = 19.8$ MeV, i.e., slightly above the Coulomb barrier, is considered. The evolution of the density associated to the single-particle wave-functions initially forming the $^{4}$He projectile is shown with green contours in Fig. 4.10. A clear dissolution of the $\alpha$-particle in at least two components is observed as soon as it enters the mean-field of the heavy partner, represented by a single isodensity at half the saturation density (white solid line in Fig. 4.10).

To conclude, the correlations responsible for the survival of $\alpha$-clustering in the previous study of the $^{4}$He + $^{8}$Be system are not strong enough, at the mean-field level, to enable similar effects in a $^{4}$He + $^{208}$Pb central collision at the barrier. Indeed, the $2p$-$2n$ spatial correlations in the $^{4}$He fragment are lost in the mean-field of the heavy partner. The experimentally observed $\alpha$-cluster states in the $^{212}$Po nucleus [135] may either be due to beyond-mean-field correlations, or to an $\alpha$-cluster located at the surface and orbiting around the heavy core. To test the latter idea, the present calculations should be repeated above the barrier and around the grazing angle to investigate possible long-lived $\alpha$-cluster configurations.

## 4.5 Transfer in Heavy-Ion Collisions

Transfer reactions are highly sensitive to cluster effects. This is illustrated in the $\alpha$-transfer experiment of Ref. [135] discussed above. Other types of clusters may also be transferred in heavy-ion collisions, such as pairs of protons and neutrons [142]. These types of multi-nucleon transfer reactions are in competition with the sequential transfer, i.e., a transfer of independent nucleons.

Theoretically, transfer probabilities in microscopic approaches are obtained from a particle number projection technique. First, this technique is described. It is then applied at the TDHF level to estimate sequential transfer probabilities in the $^{16}$O + $^{208}$Pb system. The latter are used as a reference to interpret experimental data in terms of cluster transfer. Finally, pairing vibrations, which may be excited in pair transfer reactions, are studied with the TDHFB approach.

### *4.5.1 Particle Number Projection Technique*

Transfer probabilities have been extracted at the TDHF level [56, 143] thanks to a projection onto a good particle number technique. This technique is standard in beyond-mean-field models for nuclear structure subject to pairing correlations [87,

**Fig. 4.10** Snapshots of the density profile in the $^{4}$He + $^{208}$Pb central collision at $E_{c.m.} = 19.8$ MeV. Wave-functions initially belonging to the $^{4}$He are shown with green contours. A single isodensity at half the saturation density (*white solid line*) is shown for the wave-functions initially belonging to the $^{208}$Pb fragment

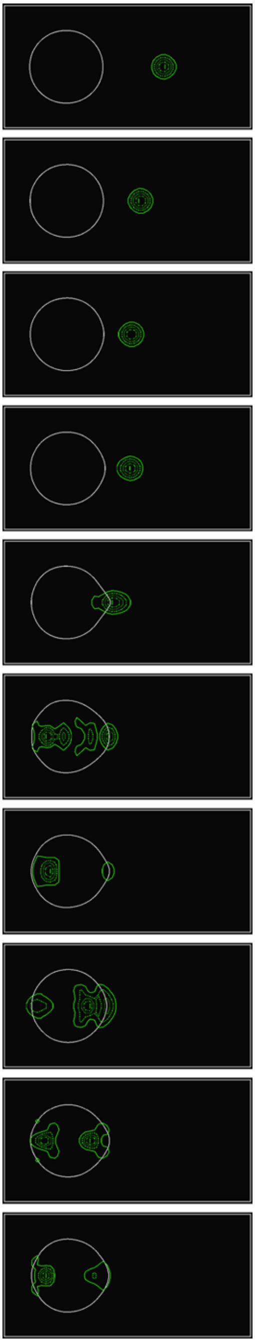

144]. Here, it is applied on the outgoing fragments to determine their proton and neutron number probabilities.

It is possible to extract the component of the wave function associated to a specific transfer channel using a particle number projector onto $N$ protons or neutrons in the $x > 0$ region where one fragment is located at the final time, the other one being in the $x < 0$ region. Such a projector is written [56]

$$\hat{P}_R(N) = \frac{1}{2\pi}\int_0^{2\pi} \mathrm{d}\theta e^{i\theta(\hat{N}_R - N)}, \tag{4.34}$$

where

$$\hat{N}_R = \sum_s \int \mathrm{d}\mathbf{r}\hat{a}^\dagger(\mathbf{r}s)\hat{a}(\mathbf{r}s)\Theta(x) \tag{4.35}$$

counts the number of particles in the $x > 0$ region ($\Theta(x) = 1$ if $x > 0$ and $\Theta(x) = 0$ elsewhere). Isospin is omitted to simplify the notation.

The projector defined in Eq. (4.34) can be used to compute the probability to find $N$ nucleons in $x > 0$ in the final state $|\phi\rangle$,

$$\left|\hat{P}_R(N)|\phi\rangle\right|^2 = \frac{1}{2\pi}\int_0^{2\pi} \mathrm{d}\theta e^{-i\theta N}\big\langle\phi\big|\phi_R(\theta)\big\rangle, \tag{4.36}$$

where $|\phi_R(\theta)\rangle = e^{i\theta\hat{N}_R}|\phi\rangle$ represents a rotation of $|\phi\rangle$ by a gauge angle $\theta$ in the gauge space associated to the particle number degree of freedom in $x > 0$. Note that $|\phi_R(\theta)\rangle$ is an independent particle state. The last term in Eq. (4.36) is then the determinant of the matrix of the occupied single particle state overlaps [56]:

$$\big\langle\phi \mid \phi_R(\theta)\big\rangle = \det(F) \tag{4.37}$$

with

$$F_{ij} = \sum_s \int \mathrm{d}\mathbf{r}\varphi_i^{s*}(\mathbf{r})\varphi_j^s(\mathbf{r})e^{i\theta\Theta(x)}. \tag{4.38}$$

The integral in Eq. (4.36) is discretised using $\theta_n = 2\pi n/M$ with the integer $n = 1\cdots M$. Choosing $M = 300$ ensures numerical convergence for the $^{16}\mathrm{O} + {}^{208}\mathrm{Pb}$ system.

### *4.5.2 Sub-barrier Transfer in* $^{16}\mathrm{O} + {}^{208}\mathrm{Pb}$

We mentioned in Sect. 4.4 the $\alpha$-transfer reaction $^{208}$Pb($^{18}$O,$^{14}$C) populating $\alpha$-cluster states in $^{212}$Po [135]. One could expect a similar $\alpha$-transfer mechanism to dominate the $^{208}$Pb($^{16}$O, $^{A}$C) reaction channels below and around the barrier [145–147]. Indeed, $^{16}$O is a good candidate for $\alpha$-clustering, and $\alpha$-condensates [148] as well as linear $\alpha$-chains [132] have been predicted. Experimental indications of $\alpha$-clustering in $^{16}$O have also been reported [149, 150]. Recent experimental data [57]

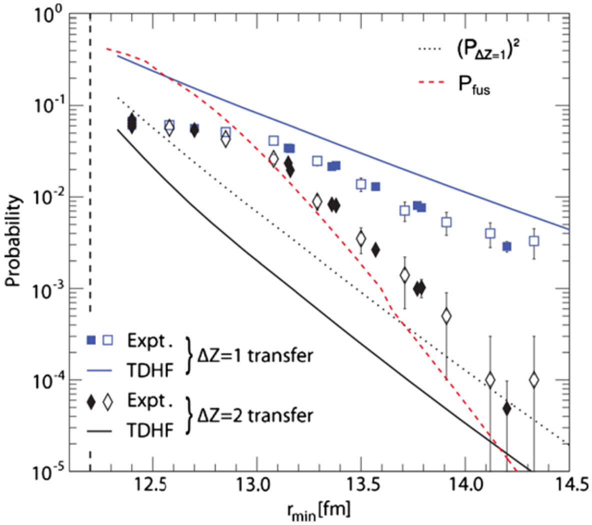

**Fig. 4.11** Charge transfer probability in $^{16}O + ^{208}Pb$. TDHF calculations of the $\Delta Z = 1$ ($1p$ stripping) and $\Delta Z = 2$ ($2p$ stripping) transfer probabilities as a function of the distance of closest approach $r_{min}$ are shown by the *full curves*. Experimental data are shown for $\Delta Z = 1$ (*squares*) and $\Delta Z = 2$ (*diamonds*). The *vertical dashed line* indicates the average barrier radius. The *dotted curve* shows the square of the TDHF $\Delta Z = 1$ transfer probabilities. The *red dashed curve* shows the sub-barrier fusion probability as calculated with the coupled-channels code CCFULL. From Ref. [57]

showed, however, that the most probable carbon isotope formed in $^{16}O + ^{208}Pb$ is $^{14}C$, indicating a dominance of two-proton transfer against $\alpha$-transfer.

TDHF calculations [56] have been performed with the TDHF3D code and the SLy4$d$ Skyrme functional [18] to estimate the probability for production of nitrogen ($\Delta Z = 1$) and carbon ($\Delta Z = 2$) in $^{16}O + ^{208}Pb$. The results are shown in Fig. 4.11 (solid lines) as a function of the distance of closest approach for Coulomb trajectories

$$r_{min} = \frac{Z_1 Z_2 e^2}{2E_{c.m.}}\left(1 + \text{cosec}\frac{\theta_{c.m.}}{2}\right). \tag{4.39}$$

We observe that these probabilities decrease exponentially with increasing $r_{min}$, as expected for quasi-elastic transfer [151].

Due to the independent particle approximation, the TDHF approach is only able to describe sequential multi-nucleon transfer, i.e., neglecting cluster correlations. The probability for sequential transfer of two nucleons is sometimes approximated by the square of the one-nucleon transfer probability. This leads, however, to an overestimation of the two-proton sequential transfer in $^{16}O + ^{208}Pb$, as can be seen in Fig. 4.11 (compare dotted and solid black lines). In fact, the above approximation is valid when a large number of particles are available for transfer toward states with large degeneracies. In general, this criterion is not fulfilled due essentially to the relatively small number of single-particle states around the Fermi level. Indeed, the latter have the smallest binding energies, and, then, the largest transfer probabilities. In the $^{16}$O case, for instance, transfer is dominated by the $1p_{1/2}$ single particle states. Quantum microscopic approaches such as the TDHF theory are then needed to estimate correct sequential multi-nucleon transfer probabilities.

Comparison with experimental data in Fig. 4.11 indicates that to assume pure sequential transfer, as in TDHF calculations, leads to an overestimation of one-proton transfer probabilities by a factor $\sim 2$, and to an underestimation of two-proton transfer probabilities by approximatively one-order of magnitude. This is interpreted as a strong cluster effect in $^{16}\mathrm{O} + {}^{208}\mathrm{Pb}$ charge-transfer [56, 57]. Indeed, correlations such as proton pairing or $\alpha$-clustering favour the transfer of two protons, while they reduce the probability for transferring only one proton. In fact, it is shown in Ref. [57] that pairing correlations dominate the $\Delta Z = 2$ channel over $\alpha$-clustering.

It is interesting to note that at large distances of closest approach, i.e., $r_{min} > 13$ fm, the sum of the $\Delta Z = 1$ and 2 channels is rather well reproduced by the TDHF calculations [56]. Closer to the barrier, however, sub-barrier fusion dominates, as shown by the coupled-channels calculations with the CCFULL code [152]. As a result, the experimental transfer probabilities are reduced at the barrier, inducing a deviation from the exponential dependence observed at larger distances. One drawback of the TDHF approach is that it does not enable tunnelling of the many-body wave-function. Thus, sub-barrier fusion is not included in TDHF calculations, inducing an overestimation of the total transfer probabilities close to (but below) the barrier.

To sum up, the TDHF approach provides a good estimate of sequential transfer probabilities well below the barrier. These sequential transfer probabilities can be used as a benchmark to compare with experimental data in order to emphasise the role of cluster correlations on the transfer mechanism.

### *4.5.3 Pairing Vibrations*

It is possible to include pairing correlations in the mean-field dynamics by considering quasiparticle vacua instead of independent particle states. This leads to the TD-BCS model when only pairs between time-reversed single-particle states are considered, or, more generally, to the time-dependent Hartree-Fock-Bogoliubov (TDHFB) formalism [153]. Numerical applications are now possible thanks to the recent development of TD-BCS [88, 89] and TDHFB [80, 90, 91] codes.

A proper description of pairing dynamics is crucial to investigate the evolution of nuclei produced by a pair transfer mechanism [142, 154–158]. Indeed, pair transfer reactions are a good tool to excite the so-called “pairing vibrations” [87, 142, 154, 159, 160]. Pairing correlations are then expected to induce a collectivity which manifests itself as an increase of transition amplitude toward these states.

Recent studies of pairing vibrations have been performed at the QRPA level [155, 156], that is, in the linearised version of TDHFB [87, 153]. Here, we discuss a similar study with a real-time description of pairing vibrations excited in

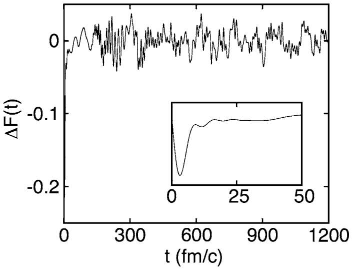

**Fig. 4.12** Evolution of $\langle F\rangle(t)$ after a pair transfer type excitation on $^{44}$Ca. The *inset* shows the same quantity at early times. Adapted from Ref. [163]

two-neutron transfer reactions in $^{44}$Ca with a fully self-consistent TDHFB code [90, 161, 162]. Applications to other systems including oxygen, calcium, and tin isotopes can be found in Refs. [90, 162, 163].

Starting with an even-even nucleus ground-state with $A$ nucleons and spin-parity $0^+$, and assuming a $\Delta L = 0$ direct pair transfer reaction, pair vibration states with $J^\pi = 0^+$ are populated in the $A+2$ (pair addition) and/or $A-2$ (pair removal) nuclei. The transfer process is simulated by an initial excitation generated by a boost with a Hermitean pair-transfer operator [160]

$$\hat{F} = \int d\mathbf{r}\, f(r)\big(\hat{a}^\dagger_{\mathbf{r},\downarrow}\hat{a}^\dagger_{\mathbf{r},\uparrow} + \hat{a}_{\mathbf{r},\uparrow}\hat{a}_{\mathbf{r},\downarrow}\big), \tag{4.40}$$

where the arrows label the spin of the single-particles (we omit the isospin to simplify the notation). In the present application, $f(r)$ is a Fermi-Dirac spatial distribution containing the nucleus and cutting at 4 fm outside the nucleus. Its role is to remove unphysical high energy modes associated to pair creation outside the nucleus.

The evolution of the system after the boost is obtained with the TDHFBRAD code [90]. This code solves the TDHFB equation in spherical symmetry with a full Skyrme EDF and density-dependent pairing effective interaction. The linear response of $\langle\hat{F}\rangle(t)$ after a boost excitation is shown in Fig. 4.12 for a $^{44}$Ca initial ground-state. The SLy4 parametrisation of the Skyrme EDF is used [74], together with a "volume" pairing effective interaction of the form $\tilde{t}_0\delta(\hat{\mathbf{r}}_1 - \hat{\mathbf{r}}_2)$ with $\tilde{t}_0 = -187$ MeV fm$^{-3}$ and a cut-off energy of 80 MeV in the quasi-particle spectrum to avoid ultra-violet divergence. See Refs. [162–164] for a discussion on the role of the form of the pairing functional on the excitation of pairing vibrations.

The apparent chaotic behaviour of $\langle\hat{F}\rangle(t)$ in Fig. 4.12 is due to the simultaneous excitation of several states. A simple Fourier analysis can be used to extract the energy and relative contributions of these states to the time evolution of $\langle\hat{F}\rangle(t)$. The resulting strength function is plotted in Fig. 4.13 with a solid line. Both pair additional and pair removal (indicated by the arrows) modes are present. The unperturbed strength function (dashed line) obtained by removing the self-consistency of the generalised mean-field is also shown. Overall, an increase of the strength is observed due to the dynamical pairing residual interaction present in TDHFB, but neglected in the unperturbed response. This increase of the strength is a signature for collective motion, indicating that several quasi-particles participate to the vibrational modes. In addition, this residual interaction lowers the transition energies due

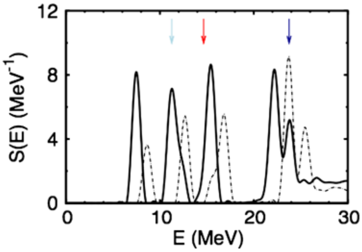

**Fig. 4.13** TDHFB strength function (*solid line*) associated to the evolution of $\langle F \rangle(t)$ in Fig. 4.12. The unperturbed spectrum (*dotted line*) is also shown. The *arrows* indicate pair removal transitions from deep hole states. Adapted from Ref. [163]

to its attractive nature. These characteristics of pairing vibrations are in agreement with previous observations with the QRPA model [155].

To conclude, collective pairing vibrations may be excited in pair-transfer reactions. These reactions are then a unique probe to investigate the dynamics of pairs of nucleons in nuclei, in particular their vibrational modes. Pairing vibrations have been studied at the TDHFB level with spherical symmetry. The recent development of a three-dimensional TDHFB code [91] might enable similar studies in deformed nuclei and for $L \neq 0$ modes. The complete description of pairing vibration excitations in heavy-ion collisions might also be possible with such a code.

## 4.6 Deep-Inelastic Collisions

Deep-inelastic collisions (DIC) have been widely studied in the past [165–169]. They are characterised by a strong damping of the relative kinetic energy and an orbiting of the di-nuclear system before re-separation of the two fragments. In particular, large widths of the fragment mass and charge distributions are usually observed.

DIC have been used to investigate isospin equilibration in damped collisions [170–173], and to produce nuclei and study their structure (see for example Refs. [174, 175]). Upcoming radioactive beams will be used to further investigate transport properties of isospin asymmetric nuclear matter [176].

The characteristics of DIC provide stringent tests to nuclear transport models [177–179]. For instance, it has been shown that standard TDHF calculations usually fail to reproduce the large widths of mass and charge distributions [143, 177]. This is due to the fact that the many-body wave-function is constrained to be a single Slater determinant at all time [180]. Fluctuations are then computed with beyond TDHF approaches such as the TDRPA [110] and stochastic mean-field [111] formalisms.

We first discuss briefly the calculation of fluctuations at the TDRPA level. Then, we present applications to the $^{40}$Ca + $^{40}$Ca reaction well above the barrier.

### 4.6.1 Fluctuations of One-Body Observables

Balian and Vénéroni (BV) have introduced a variational principle in which the TDHF theory turns out to be optimised to the expectation value of one-body observables [109]. It could then fail to reproduce quantities like two-body observables and fluctuations of one-body observables.

Balian and Vénéroni also used their variational principle to derive a prescription for fluctuations and correlations between one-body observables [110, 181] (a detailed derivation can also be found in Ref. [13]). This prescription is, in fact, fully equivalent to the TDRPA approach where small fluctuations around the mean-field evolution are considered.

The BV variational principle can then be used to determine an optimum prediction for correlations $\sigma_{XY}$ and fluctuations $\sigma_{XX}$ of one-body operators assuming small fluctuations around the mean-field path [110, 181]. Correlations are obtained from the general expression

$$\sigma_{XY}^2 = \left|\frac{1}{2}\big(\langle\hat{X}\hat{Y}\rangle + \langle\hat{Y}\hat{X}\rangle\big) - \langle\hat{X}\rangle\langle\hat{Y}\rangle\right|, \tag{4.41}$$

where $\sigma_{XY}$ has the sign of the term between the absolute value bars. The $X$ and $Y$ distributions are correlated (resp. anti-correlated) for $\sigma_{XY} > 0$ (resp. $\sigma_{XY} < 0$). Fluctuations are obtained by taking $\hat{X} = \hat{Y}$, leading to

$$\sigma_{XX} = \sqrt{\langle\hat{X}^2\rangle - \langle\hat{X}\rangle^2}. \tag{4.42}$$

Assuming independent particle states, the BV variational principle leads to the prescription

$$\sigma_{XY}^2(t_1) = \lim_{\varepsilon\to 0}\frac{1}{2\varepsilon^2}\mathrm{tr}\big\{\big[\rho(t_0) - \rho_X(t_0,\varepsilon)\big]\big[\rho(t_0) - \rho_Y(t_0,\varepsilon)\big]\big\}, \tag{4.43}$$

where tr denotes a trace in the single-particle space. The one-body density matrices $\rho_X(t,\varepsilon)$ obey the TDHF equation (4.1) with the boundary condition at the final time $t_1$

$$\rho_X(t_1,\varepsilon) = e^{i\varepsilon q_X}\rho(t_1)e^{-i\varepsilon q_X}, \tag{4.44}$$

while $\rho(t) = \rho_X(t,0)$ is the standard TDHF solution.

Equation (4.43) has been solved numerically in the past for particle number fluctuations with simple effective interactions and geometry restrictions [182–184]. Modern three-dimensional TDHF codes with full Skyrme functionals are now used for realistic applications of the BV variational principle to determine these fluctuations [13, 59, 185–187] as well as the correlations between the proton and neutron number distributions [59, 187]. See Ref. [13] for numerical details of the implementation of Eq. (4.43).

### 4.6.2 *The* $^{40}$Ca + $^{40}$Ca *Reaction Well Above the Barrier*

The $^{40}$Ca + $^{40}$Ca reaction has been investigated at $E_{c.m.} = 128$ MeV (~2.4 times the barrier) [59] with the TDHF3D code and its TDRPA extension using the SLy4*d*

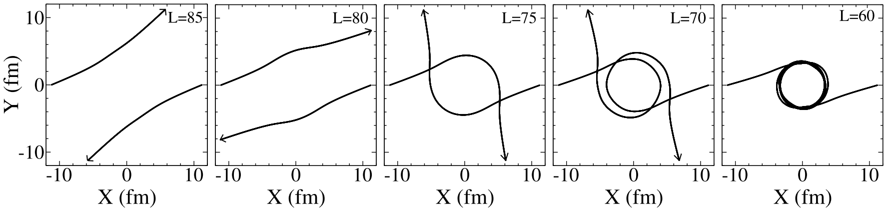

**Fig. 4.14** Trajectories of the fragment centers-of-mass in $^{40}$Ca + $^{40}$Ca at $E_{c.m.} = 128$ MeV and different angular momenta $L$ in units of $\hbar$

**Fig. 4.15** Total kinetic energy loss of the fragments in $^{40}$Ca + $^{40}$Ca at $E_{c.m.} = 128$ MeV as a function of the angular momentum $L$ in units of $\hbar$. Adapted from Ref. [59]

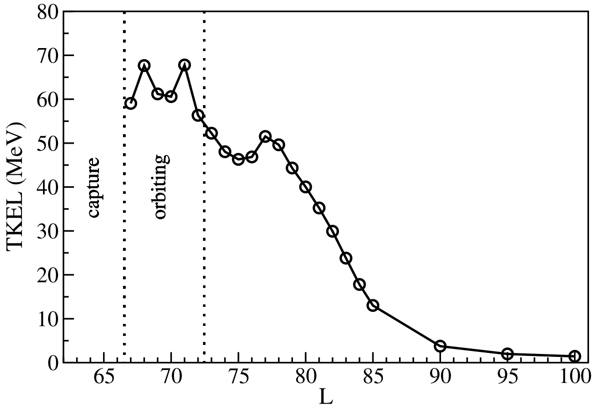

Skyrme functional [18]. Figure 4.14 provides some examples of trajectories obtained at different angular momenta. The TDHF calculations for this reaction predict that fusion occurs at $L \leq 66\hbar$ [59]. We see in Fig. 4.14 that orbiting followed by re-separation is predicted at $L = 70\hbar$. Partial orbiting at $L = 75\hbar$ and smaller nuclear deflections at larger $L$ are also observed.

It is interesting to note that different angular momenta may lead to similar scattering angles. This is the case, for instance, with $L = 70\hbar$ and $L = 75\hbar$ which are associated to different orbiting trajectories (see Fig. 4.14). In fact, the amount of orbiting changes very rapidly with $L$ for DIC. Comparisons with experimental data imply then to perform calculations with a small angular momentum step in the orbiting region [59].

As mentioned before, DIC are not only characterised by a large orbiting of the di-nuclear system. They are also associated to a large damping of the initial relative kinetic energy. This is quantified by the total kinetic energy loss $TKEL = E_{c.m.} - E_1 - E_2$, where $E_{1,2}$ are the asymptotic kinetic energies of the fragments in the exit channel. The $TKEL$ in $^{40}$Ca + $^{40}$Ca at $E_{c.m.} = 128$ MeV are shown in Fig. 4.15 as a function of the initial angular momentum. The maximum $TKEL$ of ~60–70 MeV are obtained close to the critical angular momentum for fusion. These $TKEL$ have to be compared with the Viola systematics for fission fragments [188]. The latter gives an expected $TKEL$ in symmetric fission of ~76 MeV. This indicates that the DIC around $L \simeq 70\hbar$ are almost fully damped. Note that this result is obtained

**Fig. 4.16** Fragment charge fluctuation $\sigma_{ZZ}$ with TDHF (*dashed line*) and TDRPA (*filled circles*) as a function of the angular momentum $L$ in units of $\hbar$. The fluctuations $\sigma_{NN}$ of the neutron number distributions, not shown, are very close to the proton ones. Correlations $\sigma_{NZ}$ between proton and neutron numbers distributions obtained with TDRPA calculations are shown with *open triangles*. Adapted from Ref. [59]

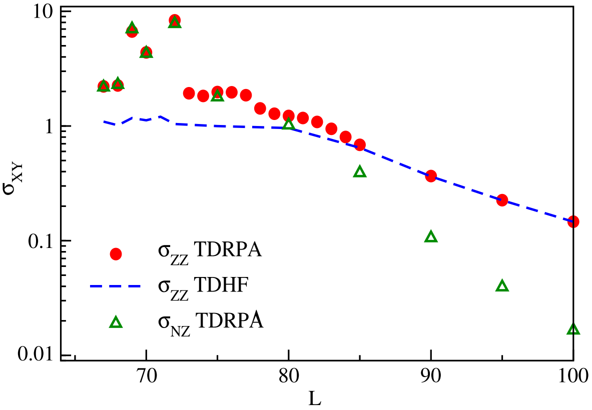

with TDHF calculations which contain one-body dissipation only. As a result, the damping of relative kinetic energy in DIC is essentially of one-body nature.

Another characteristic of DIC is the large width of the fragment mass and charge distributions. Independent particle descriptions such as the TDHF theory usually strongly underestimate these widths [59, 143, 177]. It is then necessary to include beyond TDHF fluctuations with the TDRPA [110] or with the stochastic mean-field (SMF) approach [111]. Calculations with the TDRPA [59, 182–187] and with the SMF approach [50, 58] indeed predict larger fluctuations than the TDHF theory.

This is illustrated in Fig. 4.16 where the fragment charge fluctuations obtained from TDHF (dashed line) and TDRPA (filled circles) are reported as a function of the angular momentum for the $^{40}$Ca $+$ $^{40}$Ca reaction at $E_{c.m.} = 128$ MeV [59]. We see that, for large angular momenta $L \geq 90\hbar$, both approaches predict similar fluctuations. These reactions are very peripheral and associated to small *TKEL* of few MeV (see Fig. 4.15). Collisions at $L \geq 90\hbar$ are then dominated by quasi-elastic scattering. This shows that the TDHF approach may be used safely to compute quasi-elastic transfer (see also Sect. 4.5) as it provides similar fluctuations than the TDRPA for these quasi-elastic events.

On the other hand, we observe in Fig. 4.16 that fluctuations with the TDRPA are much larger than with the TDHF approach for more central collisions, in particular in the DIC region at $L \sim 70\hbar$. A comparison of these fluctuations with the experimental data of Roynette and collaborators [165] has been performed in Ref. [59]. The results are reported in Fig. 4.17 for a selection of events with $TKEL > 30$ MeV. Although the TDRPA results still underestimate experimental data, they provide both a better qualitative and quantitative agreement than the TDHF calculations. In fact, the plateau observed at large angles contains a contribution from fusion-fission events [165]. The latter are not treated in the calculations and may be the origin of the remaining difference between the TDRPA calculations and the experimental data [59].

Correlations between proton and neutron numbers distributions have also been computed recently with the TDRPA approach for $^{40}$Ca $+$ $^{40}$Ca collisions at $E_{c.m.} =$ 128 MeV [59]. In standard TDHF calculations, these correlations are strictly zero.

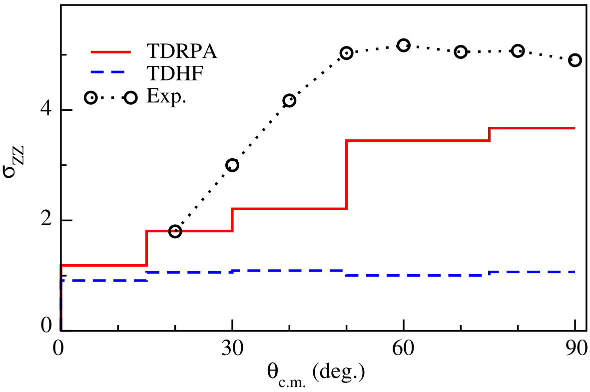

**Fig. 4.17** Fluctuations $\sigma_{ZZ}$ of the proton number distributions obtained with TDHF (*dashed line*) and TDRPA (*solid line*) calculations are plotted as function of the center-of-mass scattering angle $\theta_{c.m.}$. Experimental data (*open circles*) from Ref. [165] are also indicated. Adapted from Ref. [59]

In the TDRPA, however, they become important in the DIC region, as shown in Fig. 4.16 (open triangles). Although they are negligible for quasi-elastic scattering ($L \geq 90\hbar$), they are similar to the charge fluctuations for the most damped events. This indicates that, e.g., an addition of several protons in one fragment is likely to be accompanied by an addition of neutrons as well. This is a manifestation of the symmetry energy which favours $N = Z$ fragments.

Finally, combining neutron and proton fluctuations with their correlations, one can estimate the distribution of nuclei produced in the reaction. Let us assume a Gaussian probability distribution of the form

$$\mathscr{P}(n,z) = \mathscr{P}(0,0)\exp\left[-\frac{1}{1-\rho^2}\left(\frac{n^2}{\sigma_N^2}+\frac{z^2}{\sigma_Z^2}-\frac{2\rho nz}{\sigma_N\sigma_Z}\right)\right], \tag{4.45}$$

where $n$ and $z$ are the number of transferred neutrons and protons, respectively. The probability for the inelastic channels reads

$$\mathscr{P}(0,0) = \left(2\pi\sigma_N\sigma_Z\sqrt{1-\rho^2}\right)^{-1}.$$

The dimensionless quantity

$$\rho = \text{sign}(\sigma_{NZ})\frac{\sigma_{NZ}^2}{\sigma_N\sigma_Z} = \frac{\langle nz\rangle}{\sqrt{\langle n^2\rangle\langle z^2\rangle}} \tag{4.46}$$

quantifies the correlations and obeys $|\rho| < 1$. The case $\rho = 0$ corresponds to independent distributions of the form $\mathscr{P}(n,z) = \mathscr{P}(n)\mathscr{P}(z)$. On the other side, fully (anti-)correlated distributions are found in the limit $\rho \to \pm 1$.

Iso-probabilities corresponding to $\mathscr{P}(n,z) = \mathscr{P}(0,0)/2$ are plotted in Fig. 4.18 for different angular momenta. Independent proton and neutron distributions would produce ellipses with the principal axis parallel to the abscissa or to the ordinate. This is not what is observed, particularly for the smallest angular momenta corresponding to the most violent collisions. We see that not only the fluctuations are important to determine distributions of DIC, but the correlations play a significant role as well.

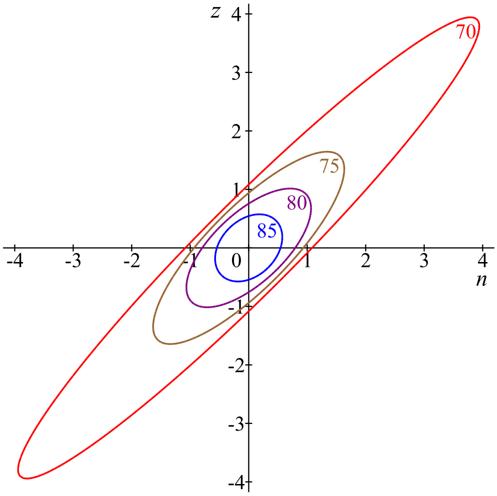

**Fig. 4.18** TDRPA calculations of iso-probabilities $\mathscr{P}(n,z)=\mathscr{P}(0,0)/2$ for $n$ neutrons and $z$ protons transfered in $^{40}$Ca + $^{40}$Ca at $E_{c.m.}=128$ MeV. The *numbers on the curves* indicate the angular momentum in units of $\hbar$

To conclude, the TDHF theory is a good tool to compute transfer probabilities in quasi-elastic scattering. However, beyond TDHF fluctuations are mandatory to describe fragment mass and charge distributions in more violent reactions such as deep-inelastic collisions. Calculations based on the TDRPA indeed provide a better agreement with experimental data than standard TDHF codes. The correlations are also shown to be important in DIC with these TDRPA calculations. They should be sensitive to the symmetry energy and might be used in the future to test this part of the functional, in particular with exotic beams.

## 4.7 The Quasi-fission Process

When two nuclei collide with an energy above the Coulomb barrier and a small enough impact parameter, a capture of the two fragments is expected to occur, i.e., a di-nuclear system is formed after dissipation of the relative kinetic energy [9]. The outcome of such a di-nuclear system is either (i) fusion, i.e., the formation of a unique system where two centers cannot be identified anymore in the density distribution, or (ii) a re-separation after a possible multi-nucleon transfer between the fragments.

In light and medium mass systems, fusion is usually enabled by a close contact between the fragments. For heavy systems with typical charge products greater than $\sim$1600–1800, however, the second process is often dominant around the Coulomb barrier, leading to a fusion hindrance in these systems [189]. Instead of fusing, the di-nuclear system encounters a re-separation in two fragments after a possible exchange of a large number of nucleons. This process is called quasi-fission as the characteristics of the fragments may exhibit some strong similarities with those emitted in statistical fission of the compound nucleus formed by fusion [190–192].

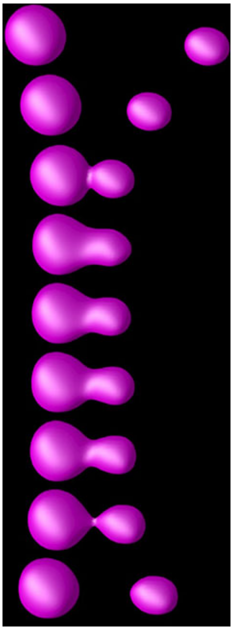

**Fig. 4.19** Snapshots of the density for a $^{56}\text{Fe} + ^{208}\text{Pb}$ central collision at $E_{c.m.} = 240$ MeV. The isodensity is plotted at half the saturation density, i.e., at $\rho_0/2 = 0.08\ \text{fm}^{-3}$. Snapshots are shown every 0.75 zs. Time runs from *top* to *bottom*

Note that, although much less probable than fusion, quasi-fission may also occur in lighter systems [193–195].

Firstly, we present some TDHF calculations of fusion hindrance in several heavy systems. Then, we investigate the effect of some structure properties of the collision partners, in particular their deformation, on the quasi-fission process.

### *4.7.1 Fusion Hindrance in Heavy Systems*

Let us illustrate the phenomenon of fusion hindrance with TDHF calculations of heavy systems using the TDHF3D code with the SLy4*d* Skyrme functional [18]. Figure 4.19 shows the density evolution of a $^{56}\text{Fe} + ^{208}\text{Pb}$ ($Z_1 Z_2 = 2132$) central collision at $E_{c.m.} = 240$ MeV. This energy is well above the Coulomb barrier. Indeed, the barrier computed with the proximity model [196] is $B_{prox.} \simeq 224$ MeV. However, this collision does not lead to fusion. Indeed, despite the formation of a rather compact di-nuclear system, the latter end up in quasi-fission. The lifetime of the di-nuclear system is $\sim$3 zs, which is too short to enable a full mass equilibration [190–192, 197] which would be signed by a symmetric exit channel.

Fusion may eventually occur in some collisions if enough energy above the Coulomb barrier is brought into the system. This additional energy, sometimes called "extra-push" energy, may be computed with phenomenological approaches such as the extra-push model of Swiatecki [198]. Modern TDHF calculations are also able to determine such fusion thresholds without any parameter adjusted on reaction mechanism [13, 47, 199].

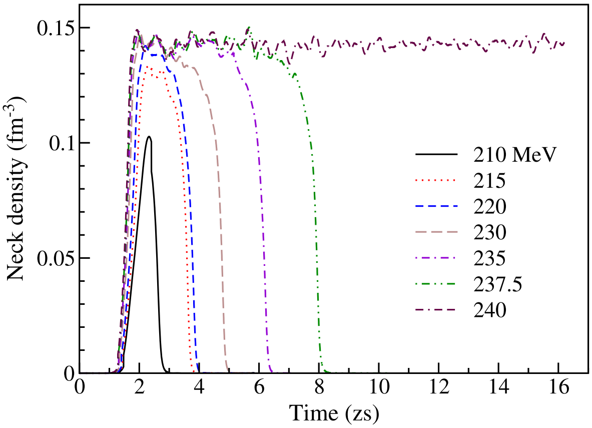

**Fig. 4.20** Neck density in $^{90}$Zr + $^{124}$Sn central collisions as function of time [200]. The center-of-mass energies are indicated in the *legend*

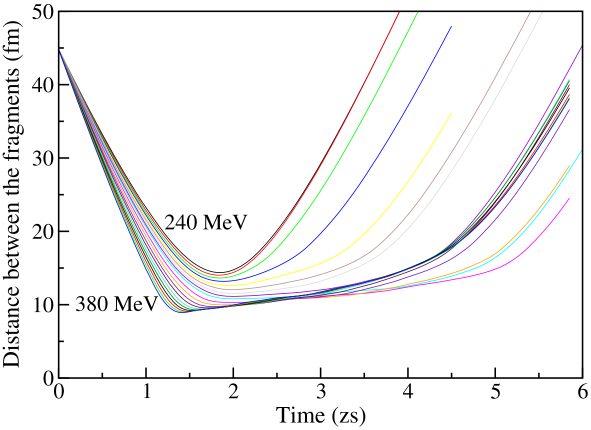

**Fig. 4.21** Distance between the centers-of-mass of the fragments in $^{70}$Zn + $^{208}$Pb central collisions as a function of time for center-of-mass energies between 240 MeV and 380 MeV [200]

An example is provided in Fig. 4.20 where the neck density is plotted as a function of time for $^{90}$Zr + $^{124}$Sn ($Z_1Z_2 = 2000$) central collisions at several energies. This system has a proximity barrier $B_{prox.} \simeq 215$ MeV. Densities exceeding 0.13 fm$^{-3}$ are observed at this energy and above. However, re-separation occurs for energies smaller than 240 MeV. Increasing contact times with energy are observed below 240 MeV. At $E_{c.m.} = 240$ MeV, however, the neck survives more than 14 zs, which may be interpreted as a fusion process. An extra-push energy of 22 to 25 MeV above the proximity barrier is then needed for the $^{90}$Zr + $^{124}$Sn system to fuse.

Increasing the collision energy does not guarantee to reach such a fusion threshold in all systems. For instance, TDHF calculations predict that fusion is not possible in the $^{70}$Zn+$^{208}$Pb ($Z_1Z_2 = 2460$) system [48]. This is illustrated in Fig. 4.21 where the distance between the centers-of-mass of the fragments is plotted as a function of time at different center-of-mass energies ranging from 240 MeV to 380 MeV. The proximity barrier for this system is $B_{prox.} \simeq 252$ MeV. We see that, at an energy of more than 100 MeV above this barrier, the system is still not fusing. In fact, we

**Fig. 4.22** Contact time between the fragments arbitrarily defined as the time the systems spend at a distance between their centers-of-mass smaller than 15 fm. Adapted from Ref. [48]. The *arrow* indicates a lower limit

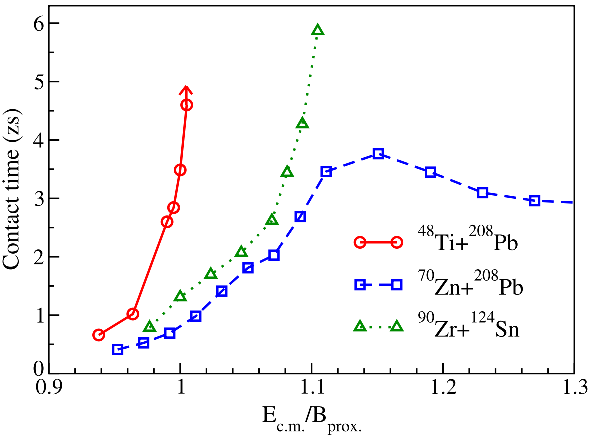

observe a rise and fall of the contact time in this system with increasing energy in Fig. 4.22. This indicates that no fusion is expected in this system.

To conclude, the fusion hindrance in heavy systems which hinders the formation of very heavy elements by fusion is described in the TDHF approach. When not fusing, the di-nuclear systems encounter quasi-fission within several zeptoseconds. Fusion may occur in some systems with an additional extra-push energy. However, others, with larger charge products are never found to fuse whatever the energy.

### *4.7.2 Effects of the Structure of the Collision Partners*

The previous section shows the importance of quasi-fission in the outcome of heavy di-nuclear systems. Realistic descriptions of quasi-fission are challenging because many degrees of freedom are at play. In addition, the shape of the di-nuclear system and its mass and isospin repartition evolves dynamically on different time scales.

The equilibration of the isospin degree of freedom has been studied with the TDHF approach in several works [19, 27, 28, 44, 51, 54, 55, 59–61, 201]. It has been shown to occur on a typical time scale smaller than 2 zs [61]. This time scale is smaller than standard quasi-fission times. Quasi-fission fragments are then expected to have a similar $N/Z$ ratio than the compound nucleus.

Shell effects of the collision partners have also been shown to play an important role in the competition between fusion and quasi-fission [61, 202, 203]. In particular, fusion might be eased by the magicity as less dissipation is expected in the fusion valley of magic nuclei [204, 205]. As a result, more compact di-nuclear systems can be formed [203, 206–208]. This may explain the success of super-heavy element synthesis with the doubly-magic $^{48}$Ca projectile [209, 210]. However, these effects remain to be investigated with quantum microscopic approaches such as the TDHF formalism.

The role of deformation and orientation on quasi-fission has been investigated in several experiments [193, 211–216]. These studies led to the general conclusion

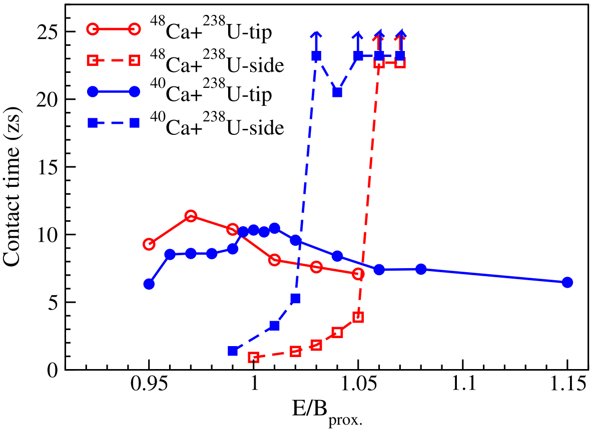

**Fig. 4.23** Contact time between the fragments as function of center-of-mass energy normalised by the proximity barrier [196] in $^{40,48}$Ca + $^{238}$U central collisions. Here, contact times are defined as the time during which the neck density exceeds half the saturation density $\rho_0/2 = 0.08$ fm$^{-3}$. Collisions with the tip (*solid line*) and the side (*dashed line*) of $^{238}$U are considered. The *arrows* indicate lower limits

that quasi-fission in collisions with the tip of a deformed heavy target (e.g., in the actinide region) is dominant. On the other side, collisions with the side lead to more compact shapes which favour long lifetimes of the di-nuclear systems and then increase the fusion probability.

The effect of deformation and orientation on quasi-fission has been investigated recently with TDHF calculations [13, 47, 48, 217] of the $^{40}$Ca + $^{238}$U system. In particular, it has been shown that collisions with the tip of $^{238}$U do not lead to fusion, but to quasi-fission with a contact time of ∼10 zs and a partial mass equilibration almost independent with energy. On the contrary, contact with the side of $^{238}$U leads to long di-nuclear lifetimes above the barrier which may induce the formation of a compound nucleus.

In Ref. [61], it was shown that $^{40}$Ca and $^{48}$Ca behave differently as far as the interplay between quasi-fission and fusion is concerned when colliding with a $^{208}$Pb target. In particular, the hindrance of quasi-fission due to shell effects is observed only with $^{48}$Ca, despite the fact that $^{40}$Ca is also doubly magic. This is interpreted as an effect of isospin asymmetry which, in the case of $^{40}$Ca, induces a fast $N/Z$ equilibration breaking the magicity of the fragments in the di-nuclear system [61].

It is interesting to see if differences in the quasi-fission process between the two calcium isotopes are also observed in collision with a heavy deformed nucleus. Contact times, defined, here, as the time during which the neck density exceeds $\rho_0/2 = 0.08$ fm$^{-3}$, have been computed in $^{48}$Ca + $^{238}$U central collisions with the TDHF3D code and the SLy4*d* Skyrme functional [18]. The evolution of these contact times as a function of energy is plotted in Fig. 4.23 for collisions with the tip (solid line) and with the side (dashed line) of $^{238}$U. The behaviours of the contact times present similarities between the two isotopes. For instance, quasi-fission times for collisions with the tip are of the order of 10 zs for both $^{40}$Ca and $^{48}$Ca. Collisions with the side also present a sharp increase of the contact time above the barrier in both cases, with long contact times (more than 20 zs) at high energy which could lead to fusion. However, long contact times for collisions with the side are reached at higher energies with $^{48}$Ca than with $^{40}$Ca. This might be attributed to shell effects in the $^{48}$Ca-like fragment which are absent in the $^{40}$Ca-like fragment due to $N/Z$ equilibration [61]. This effect needs further investigations.

To sum up, the competition between quasi-fission and fusion is affected by the structure of the collision partners. In particular, the deformation and the orientation is crucial. Recent TDHF calculations confirm that collisions with the tip lead essentially to quasi-fission, while long contact times possibly leading to fusion may be reached above the barrier for collisions with the side producing more compact shapes. More investigations with quantum microscopic approaches are needed to gain a deeper understanding on how the various structure characteristics, such as, e.g., shell effects and isospin, affect quasi-fission.

## 4.8 Actinide Collisions

Collisions of actinides form “hyper-heavy molecules” with $\sim$500 nucleons in interaction during short times of few zeptoseconds [10]. The description of their dynamics is of course a great challenge for theorists. These reactions may be an alternative way to produce more neutron-rich heavy and super-heavy nuclei than those formed by fusion [53, 187, 218, 219]. This is possible thanks to the fact that actinides have large neutron to proton ratio, of the order of $N/Z \sim 1.5$.

Another interest of actinide collisions is the possibility to make the QED vacuum unstable due to the strong electric field [220–222]. As a result, a spontaneous decay of the vacuum by the emission of a $e^+e^-$ pair is expected. The lifetime of the hyper-heavy molecule is a crucial parameter which determines if this QED vacuum decay may be observed experimentally.

These applications of actinide collisions require a precise description of the reaction mechanisms. The dynamics of actinide collisions has been investigated with various theoretical approaches, including macroscopic models [219, 223, 224], semi-classical microscopic approaches [225, 226], and the TDHF theory [16, 17, 52, 53].

In the following we describe, first, the role of the relative orientation of the nuclei on the reaction mechanisms. Then, we look for the optimal conditions for the observation of spontaneous $e^+e^-$ emission.

### *4.8.1 Role of the Initial Orientation*

Di-nuclear systems formed in actinide collisions are too heavy to fuse. They always encounter quasi-fission. As in quasi-fission with lighter projectiles, the deformation and orientation of the nuclei play a crucial role in the outcome of the collision [10]. This has been confirmed with recent TDHF calculations of the $^{238}$U + $^{238}$U [52] and $^{232}$Th + $^{250}$Cf [53] systems with the TDHF3D code and the SLy4$d$ Skyrme functional [18].

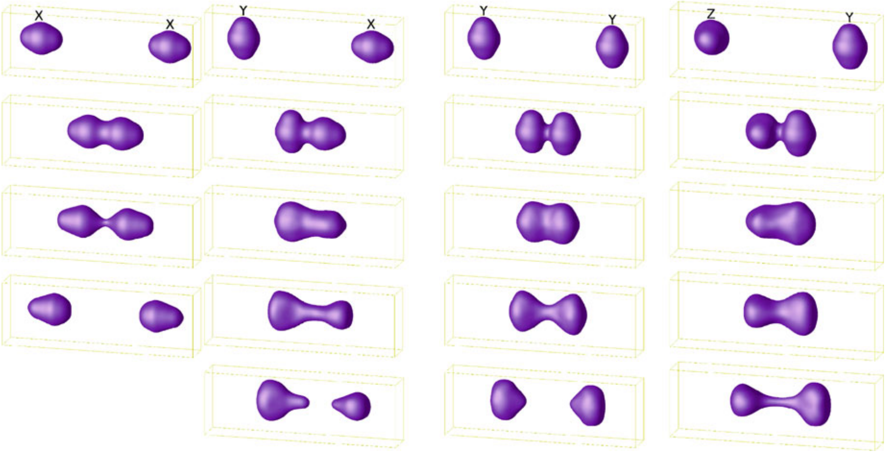

**Fig. 4.24** Isodensities at half the saturation density, i.e., $\rho_0/2 = 0.08$ fm$^{-3}$, in $^{238}$U + $^{238}$U central collisions at a center-of-mass energy $E_{c.m.} = 1200$ MeV. Evolutions associated to the four initial configurations $XX$, $YX$, $YY$, and $ZY$ are plotted in columns (time runs from *top* to *bottom*). Consecutive snapshots are separated by 1.125 zs. Adapted from Ref. [187]

As an example, Fig. 4.24 shows snapshots of the density in $^{238}$U + $^{238}$U central collisions at $E_{c.m.} = 1200$ MeV. Different shape evolutions are observed depending on the initial orientations of the actinides. In particular, a collision of the tips ($XX$ configuration) leads to a rapid neck formation, but to a faster re-separation of the fragments than with the other orientations. The most compact configurations are obtained for side on side collisions ($YY$ and $ZY$ configurations). In particular, the $ZY$ configuration leads to the longest contact times as it has less Coulomb repulsion than the $YY$ orientation.

These orientations exhibit also differences as far as the mass flow between the di-nuclear fragments is concerned. In fact, no net transfer is observed due to symmetry reasons, except when a tip collide with a side ($YX$ configuration). Indeed, in this case, no spatial symmetry prevents a net mass transfer to occur between the fragments. In fact, TDHF calculations predict that a large amount of nucleons are transferred from the tip to the side, allowing for the production of neutron-rich fragments in the fermium ($Z = 100$) region in the $^{238}$U + $^{238}$U reaction at energies around the Coulomb barrier [52]. This phenomenon has also been investigated with the $^{232}$Th + $^{250}$Cf system using the TDHF approach. In particular, it is shown that when the tip of the $^{232}$Th collides with a side of the $^{250}$Cf, the latter increases its mass, producing new neutron-rich transfermium nuclei [53, 187]. This phenomenon is called "inverse quasi-fission" as the exit channel is more mass asymmetric than the colliding partners. Note that inverse quasi-fission is also expected from shell effects in the $^{208}$Pb region, as shown by calculations based on the Langevin equation [219] (see Chap. 7 of *Clusters in nuclei vol. 1* [10]).

Let us now investigate in more details the role of the orientation on collision times. Figure 4.25 gives the evolution of the contact time between the fragments in

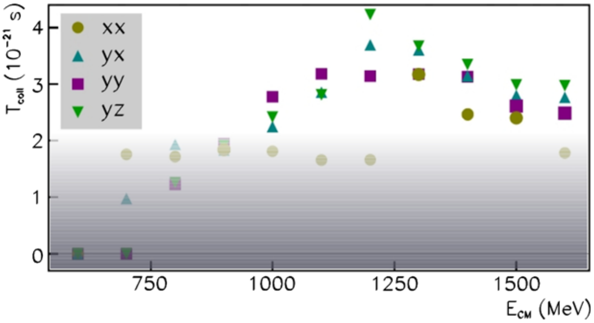

**Fig. 4.25** Collision times for each orientation as a function of the center-of-mass energy. Here, these times are defined as the time during which the neck density exceeds $\rho_0/10 = 0.016$ fm$^{-3}$. The *shaded area* indicates the limit of 2 zs above which vacuum decay is expected to be observable in central collisions. Adapted from Ref. [52]

**Fig. 4.26** Maximal density in the neck as a function of the center-of-mass energy in $^{232}$Th + $^{250}$Cf central collisions with different orientations (see text). The *dashed line* represents the saturation density at $\rho_0 = 0.16$ fm$^{-3}$. Adapted from Ref. [53]

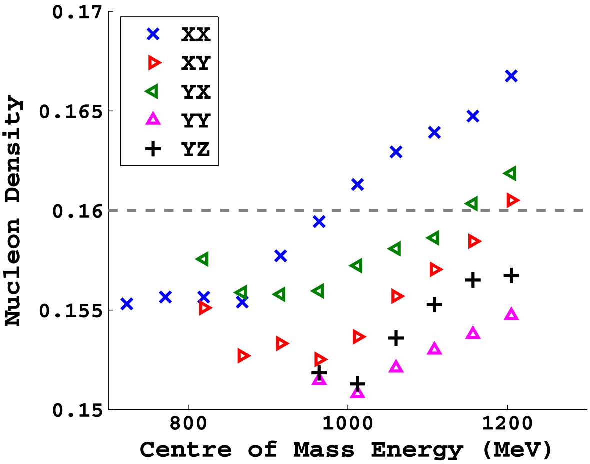

$^{238}$U + $^{238}$U central collisions as a function of energy and for the different orientations represented in the top of Fig. 4.24. A saturation of the contact time to 2 zs is observed for tip on tip collisions ($XX$) up to $E_{c.m.} \simeq 1200$ MeV. (Above this energy, $XX$ contact times increase due to ternary quasi-fission [52].) This saturation is interpreted as a repulsive force generated by large densities in the neck when the tips overlap. A similar effect is observed in $^{232}$Th + $^{250}$Cf [53]. The maximal density in the neck region for this system is reported in Fig. 4.26. We observe that the $XX$ configuration leads to large densities above the saturation density.

These large densities in the neck are also responsible, in some cases, for a re-separation of the system in three fragments [52]. This is illustrated in Fig. 4.27 for the $^{238}$U + $^{238}$U central tip on tip collision at $E_{c.m.} = 900$ MeV. A small fragment is observed at rest in the exit channel. A similar phenomenon is discussed in Ref. [10]. The formation of this third fragment is interpreted as due to an excess of density in the neck region. To illustrate this argument, Fig. 4.28 shows the internal density at

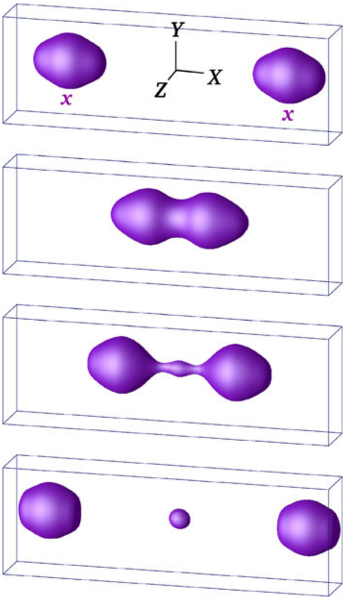

**Fig. 4.27** Zeptosecond snapshots of $^{238}$U + $^{238}$U at $E_{c.m.} = 900$ MeV for a tip on tip central collision. Adapted from Ref. [52]

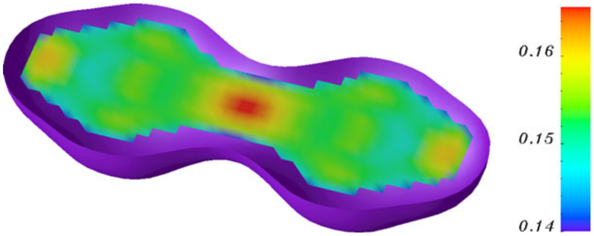

**Fig. 4.28** Nucleon density (in fm$^{-3}$) in the collision plane is plotted when the density in the neck reaches its maximum in the $XX$ configuration at $E_{c.m.} = 900$ MeV. The half cut surface is an isodensity at half the saturation density, i.e. $\rho_0/2 = 0.08$ fm$^{-3}$. Adapted from Ref. [52]

the distance of closest approach. Densities above the saturation density are indeed observed in the neck region. In fact, instead of breaking in the middle of the neck, the system breaks in both sides of this over saturation density region, producing a third small fragment at rest [52].

To conclude, the dynamics of actinide collisions has been studied with the TDHF approach. These systems encounter quasi-fission with typical di-nuclear system lifetimes of 2 to 4 zs, depending on the initial orientation of the nuclei. The mass transfer also strongly depends on the relative orientation at contact. In particular, collisions where the tip of a nucleus is in contact with the side of its collision partner lead to important mass transfer. These multi-nucleon transfer reactions may be used in the future for the production of neutron-rich transfermium nuclei. Finally, it is shown that the complex neck dynamics may lead to the production of a third fragment at rest.

### *4.8.2 Lifetime and Spontaneous $e^+e^-$ Emission*

It is predicted that nuclear systems with more than $\sim$173 protons generate super-critical Coulomb fields [10, 220–222], i.e., with the lowest quasi-molecular electronic state in the Dirac sea. This is illustrated in Fig. 4.29 in the case of a collision of two bare uranium. Without Coulomb field, the lowest energy of an electron is $E = m_e c^2$ for an electron at rest. In the top of Fig. 4.29, we see that when the two uranium are at a distance $D_{U-U} \simeq 300$ fm, the lowest quasi-molecular state available for an electron has an energy $E \simeq 0$ [220]. At this distance, the system is still sub-critical as the state is above the Dirac sea.

A super-critical state is obtained at $D_{U-U} \simeq 36$ fm when the quasi-molecular state crosses the Dirac sea at $E = -m_e c^2$ (middle panel in Fig. 4.29). At this distance the nuclei are not yet in contact. The latter occurs at $D_{U-U} \simeq 16$ fm. At this distance, the quasi-molecular state has an energy $E \simeq -1.5 m_e c^2$.

If the super-critical state is not or partially occupied, then it induces a hole in the Dirac sea. According to QED, such a state is unstable, i.e., it is a resonance with a finite lifetime depending on the depth of the energy level. This resonance is predicted to decay by producing a $e^+e^-$ pair (see bottom panel in Fig. 4.29). In this case, the $e^-$ occupies the state with negative energy $E$, while the positron is emitted in the continuum with an energy $-E$.

The Dirac equation has been solved to predict the lifetime of the resonance in Ref. [222]. Figure 4.30 shows the resulting positron spectra for different hypotheses about the contact time $T$ between the actinides. The positrons emitted in the case $T = 0$ (solid red line) are due to standard $e^+e^-$ pair creation when electric charges are accelerated in a strong Coulomb field. For finite contact times, additional positrons are produced from the decay of the vacuum. These additional positrons form a peak around $E = 1.5 - 2 m_e c^2$ which can be observed for contact times greater than 2 zs.

To enable the observation of the QED vacuum decay via $e^+e^-$ pair emission, it is then crucial to have contact times between the actinides as large as possible. Predictive calculations of the nuclear dynamics, in particular of the contact times between the nuclei are then mandatory. We see in Fig. 4.25 that contact times greater than 2 zs are obtained for central collisions at $E_{c.m.} \geq 1000$ MeV. In particular, the largest contact times of 3–4 zs obtained at $E_{c.m.} \simeq 1200$ MeV might enable the observation of spontaneous QED vacuum decay. Similar conclusions have been reached with quantum molecular dynamics calculations [225]. Note that these energies are greater than the previous experimental search for spontaneous $e^+e^-$ emissions. Indeed, these experiments were using beams around the Coulomb barrier at 700–800 MeV (see Ref. [227] and references therein).

To sum up, a possible signature of the QED vacuum decay would be the observation of a peak in the spectra of positrons produced in actinide collisions. Microscopic calculations predict optimum center-of-mass energies at more than 1 GeV. These energies are much larger than the energies considered in early experiments.

**Fig. 4.29** Coulomb potential energy (*blue solid lines*) generated by two fully stripped uranium nuclei at distances $D_{U-U} = 299$, 31 and 16 fm. The *horizontal purple* and *red lines* indicate the lowest quasi-molecular electronic state [220]

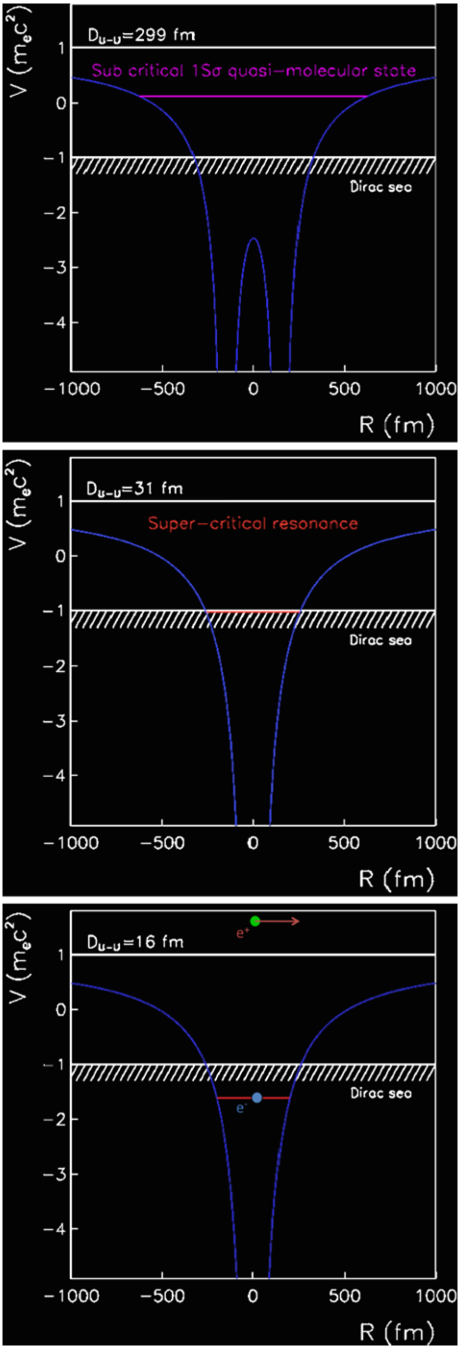

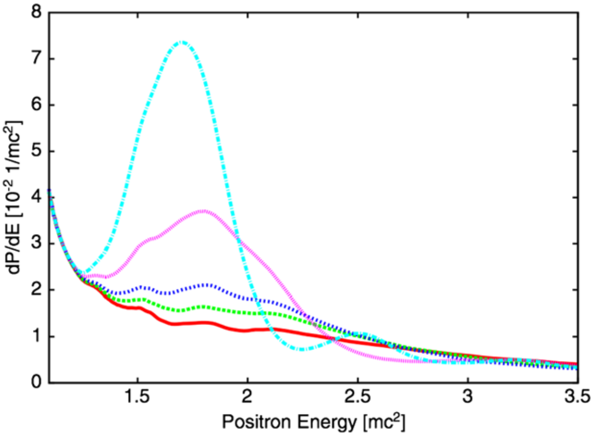

**Fig. 4.30** Total differential positron spectrum $dP/dE$ for the U–U system at $E_{c.m.} = 740$ MeV, for different nuclear sticking times calculated using the time-dependent Dirac equation. The *solid red curve* is for $T = 0$ zs, the *long-dashed green curve* for $T = 1$ zs, the *short-dashed blue curve* for $T = 2$ zs, the *dotted magenta curve* for $T = 5$ zs, and the *dash-dotted cyan curve* for $T = 10$ zs. Adapted from Ref. [222]

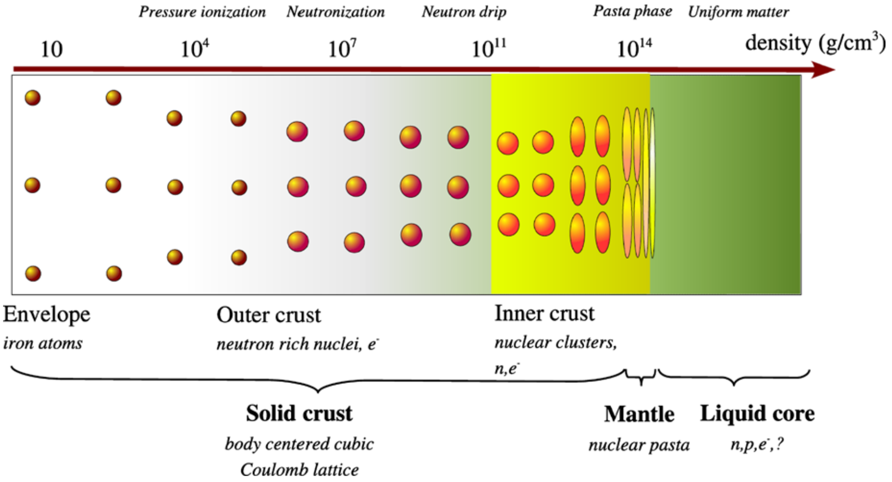

**Fig. 4.31** Schematic picture of the structure of a neutron star as a function of density. From Ref. [233]

## 4.9 Dynamics of Neutron Star Crust

Although the description of supernova explosion mechanisms is not yet complete [228], it is well known that “neutron stars” are a possible residue of such explosions. These dense baryonic objects have drawn lots of interests in the past [229]. However, their structure, which is intimately linked to the nuclear phase diagram, is still actively discussed nowadays. For instance, the order of the crust-core phase transition is under debate [230, 231]. In addition, the structure of the inner core may be affected by possible phase transitions involving strangeness [232].

The outer layers of neutron stars are also expected to exhibit exotic structures involving different geometrical organisations of the nuclear species [234]. Figure 4.31

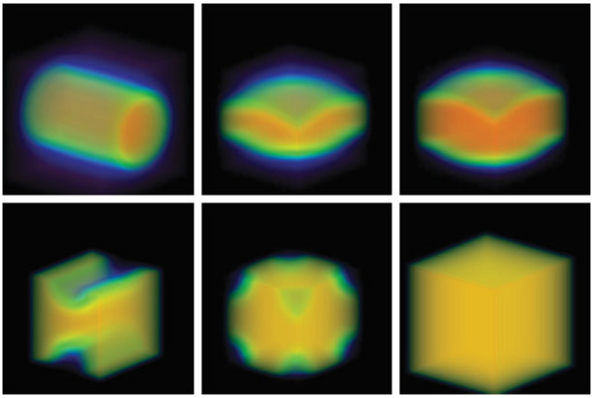

**Fig. 4.32** Neutron density profiles at a temperature $T = 2.5$ MeV, a proton fraction $x_p = 0.3$, and baryon densities of 0.04 fm$^{-3}$ (*top left*), 0.06 fm$^{-3}$ (*top middle*), 0.08 fm$^{-3}$ (*top right*), 0.09 fm$^{-3}$ (*bottom left*), 0.10 fm$^{-3}$ (*bottom middle*), and 0.11 fm$^{-3}$ (*bottom right*). The lowest neutron densities are in *dark* (*blue*) *colors*, while the highest are in *gray* (*red*). From Ref. [239]

provides a schematic picture of neutron stars [233]. The outer crust is expected to exhibit a lattice of droplets in a sea of nuclear matter [235–237]. In this picture, the inner crust is composed of nuclear clusters which may be unstable to quadrupole deformations, forming prolate nuclei. The latter would eventually join up to form stringlike structures in the so-called “nuclear pasta phase” [238].

The total energy is shared between bulk, surface, and Coulomb contributions. Inside nuclei, the density is approximatively constant. As a result, only the surface and Coulomb terms depend on nuclear shapes. The details of the diagram in Fig. 4.31 are then sensitive to a subtle competition between the surface tension, which makes nuclei spherical, versus the Coulomb force, which tends to deform them.

Static Hartree-Fock calculations based on Skyrme functionals have been performed to investigate these structures in more details in Refs. [239–241]. As an example, Fig. 4.32 represents neutron densities for different total baryon densities from 0.04 to 0.11 fm$^{-3}$ computed by Newton and Stone [239]. Except at the highest density, where an homogeneous distribution is obtained, various pasta phases can be observed.

The formation of these structures has been also investigated within microscopic theories [62, 63, 242, 243]. For instance, the quantum molecular dynamics (QMD) semi-classical model has been used by Watanabe and collaborators to show that pasta phase could be formed dynamically [242, 243].

In addition, using a quantum microscopic framework based on the TDHF equation (called the DYWAN model), Sébille and collaborators have investigated the stability of some lattice structures [62, 63]. As an example, the evolution of an initially perturbed face-centered oxygen lattice with proton fraction $x_p = 0.5$ and mean neutron density $\langle\rho\rangle = 0.058$ fm$^{-3}$ toward a cylinder is shown in Fig. 4.33. The initial perturbation consists of a random displacement of the oxygen centers in order to break the mean-field symmetry.

The role of proton fraction, lattice geometry, and nuclear species on the lattice sites have also been considered in Ref. [63]. Different shapes of the pasta phase have then been obtained, depending on the mean neutron density $\langle\rho\rangle$ and on the threshold density $\rho_t$ used to represent the isodensities. An example of distributions

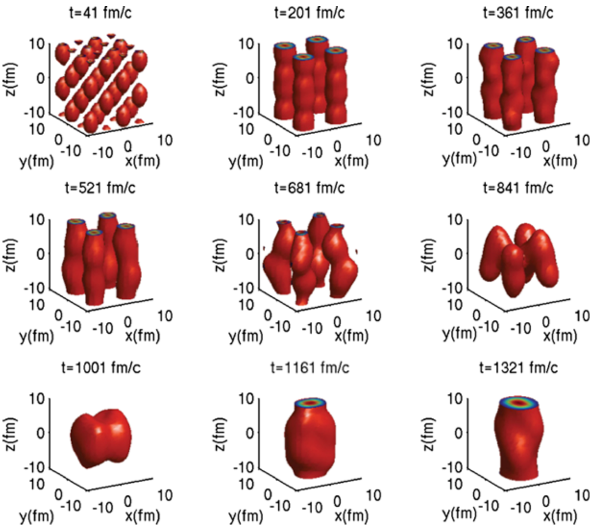

**Fig. 4.33** Snapshots of the density profiles of a perturbed supercell of oxygen isotopes in a face-centered cubic lattice. The mean neutron density is $\langle\rho\rangle = 0.058\ \text{fm}^{-3}$, and a proton fraction $x_p = 0.5$ is considered. From Ref. [63]

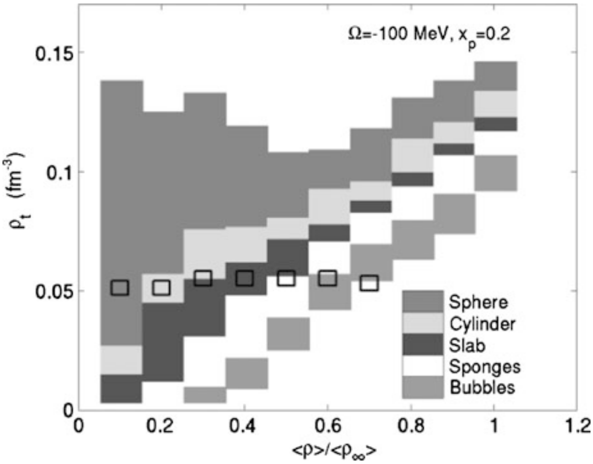

**Fig. 4.34** Neutron structure distributions as a function of the threshold density $\rho_t$ at which isodensities are plotted and of the neutron mean density $\langle\rho\rangle$ normalised to $\rho_\infty = 0.145\ \text{fm}^{-3}$ for a proton fraction $x_p = 0.2$. Initial simple cubic lattices of oxygen isotopes are used. From Ref. [63]

of structures as a function of these quantities is shown in Fig. 4.34. We see that the TDHF mean-field dynamics is able to reproduce the different types of structures expected in pasta phases.

To conclude, the dynamics of nuclear cluster aggregation and pasta phase formation from regular lattice of nuclei can be studied at the TDHF level. It should be noted, however, that these dynamics may be sensitive to the energy-density functional, and, in particular, to its isospin and density dependences [244]. In addition, the neutron structure distributions could be different if non-local effective forces were used [245, 246]. Finally, the role of beyond mean-field correlations remains to be investigated.

## 4.10 Selected Conclusions and Perspectives

The TDHF approach provides a mean-field description of nuclear dynamics in the presence of some clustering and molecular effects. The same formalism is used to investigate light systems exhibiting $\alpha$-clustering, heavy-ion collisions in a wide energy and mass range, and instabilities of lattice of nuclei in neutron star crusts.

Non-trivial dynamics are observed depending on the initial conditions. For instance, $\alpha$-clusters, which are shown to survive and vibrate several zeptoseconds in light systems such as $^{4}\mathrm{He}+{}^{8}\mathrm{Be}\rightarrow{}^{12}\mathrm{C}$, quickly dissolve when entering the mean-field of a heavy nucleus. Another example is the formation of di-nuclear systems in collisions of atomic nuclei. These systems are possible doorways to the formation of molecular states of the compound system.

The dynamics of di-nuclear systems is crucial as it determines the outcome of the reaction, i.e., a re-separation of the fragments or their fusion in a compound nucleus. Although they exhibit some common features across the nuclear chart, such as lifetimes of the order of few zeptoseconds, the evolution of di-nuclear systems may strongly depend on the entrance channel properties. For instance, fusion probabilities are much larger in light systems, while the heaviest ones formed in actinide collisions always encounter quasi-fission. It is also shown that deformation and orientation are playing an important role in the dynamics.

In terms of theoretical description of the proton-neutron composition of the final fragments, the TDHF approach can be safely used for the less violent collisions, such as quasi-elastic transfer reactions, although one should keep in mind that only sequential transfer is included, i.e., transfer of clusters of nucleons is neglected. However, damped reactions, such as deep-inelastic collisions and quasi-fission, usually involve a large transfer of nucleons between the fragments which may be underestimated at the mean-field level. In fact, experimental charge and mass distributions in damped collisions are usually wider than TDHF predictions. This drawback is overcame thanks to the inclusion of fluctuations at the TDRPA level. In addition, not only particle number fluctuations are important in damped collisions, but also correlations between proton and neutron distributions are shown to be large. These correlations, which can be computed within the TDRPA approach, are crucial for a good description of fragment distributions in damped collisions.

The transfer of correlated nucleons (paired nucleons, $\alpha$-clusters…) is one of the main challenges for microscopic approaches. For instance, the inclusion of pairing correlations at the TDHFB level will help to describe pair transfer reactions. In particular, a possible Josephson effect similar to what is observed in superconductors could be observed.

A good understanding of radiative capture between light nuclei at deep sub-barrier energies is crucial to describe stellar nucleosynthesis. However, the present time-dependent mean-field approaches do not enable a tunneling of the many-body wave-function. Beyond TDHF approaches should then be considered to describe sub-barrier fusions of astrophysical interest. In particular, dynamical long-range fluctuations must be included. Possible candidates are the time-dependent GCM, where the generator coordinate is the distance between the fragments [4], and the imaginary time-dependent Hartree-Fock formalism derived from the Feynman path-integral approach for many-body systems [67].

**Acknowledgements** Long term theoretical collaborations with D. Lacroix, Ph. Chomaz, and B. Avez are acknowledged. Some of the calculations have been performed in collaboration with B. Avez, C. Golabek, D.J. Kedziora, D. Lebhertz, and A. Wakhle. The redaction of this chapter would not have been possible without numerous scientific exchanges with theoreticians and experimentalists. In particular, discussions with E. Ackad, G. Adamian, N. Antonenko, Ch. Beck, M. Bender, K. Bennaceur, S. Courtin, M. Dasgupta, T. Duguet, M. Evers, W. Greiner, F. Gulminelli, F. Haas, D.J. Hinde, D. Jacquet, D.H. Luong, J. Meyer, J.A. Maruhn, M. Morjean, V. de la Mota, M.-G. Porquet, R. du Rietz, N. Rowley, M.-D. Salsac, P. Schuck, F. Sébille, E. Suraud, and S. Umar are acknowledged. E. Ackad, N. Chamel, M. Evers, J.A. Maruhn, V. de la Mota, W. Newton, F. Sébille, and S. Umar are warmly thanked for providing figures of their own works. The calculations with the TDHF3D code were performed on the Centre de Calcul Recherche et Technologie of the Commissariat à l'Énergie Atomique, France, and on the NCI National Facility in Canberra, Australia, which is supported by the Australian Commonwealth Government. Some of the works presented in this chapter were performed with the support from ARC grants DP0879679, DP110102858, DP110102879, and FT120100760.

## References

1. H. Horiuchi, in *Clusters in Nuclei*, ed. by C. Beck. Lecture Notes in Physics, vol. 818 (Springer, Berlin, 2010), pp. 57–108. ISBN 978-3-642-13898-0
2. W. Oertzen, in *Clusters in Nuclei*, ed. by C. Beck. Lecture Notes in Physics, vol. 818 (Springer, Berlin, 2010), pp. 109–128. ISBN 978-3-642-13898-0
3. R. Gupta, in *Clusters in Nuclei*, ed. by C. Beck. Lecture Notes in Physics, vol. 818 (Springer, Berlin, 2010), pp. 223–265. ISBN 978-3-642-13898-0
4. P. Descouvemont, M. Dufour, in *Clusters in Nuclei, vol. 2*, ed. by C. Beck. Lecture Notes in Physics, vol. 848 (Springer, Berlin, 2012), pp. 1–66. ISBN 978-3-642-24706-4
5. T. Yamada, Y. Funaki, H. Horiuchi, G. Röpke, P. Schuck, A. Tohsaki, in *Clusters in Nuclei, vol. 2*, ed. by C. Beck. Lecture Notes in Physics, vol. 848 (Springer, Berlin, 2012), pp. 229–298. ISBN 978-3-642-24706-4
6. P. Papka, C. Beck, in *Clusters in Nuclei*, ed. by C. Beck. Lecture Notes in Physics, vol. 2, vol. 848 (Springer, Berlin, 2012), pp. 299–353. ISBN 978-3-642-24706-4
7. D. Lebhertz, S. Courtin, F. Haas, D.G. Jenkins, C. Simenel, M.D. Salsac, D.A. Hutcheon, C. Beck, J. Cseh, J. Darai et al., Phys. Rev. C **85**, 034333 (2012)
8. M.D. Salsac, F. Haas, S. Courtin, A. Algora, C. Beck, S. Beghini, B. Behera, R. Chapman, L. Corradi, Z. Dombradi et al., Nucl. Phys. A **801**, 1 (2008)
9. G. Adamian, N. Antonenko, W. Scheid, in *Clusters in Nuclei, vol. 2*, ed. by C. Beck. Lecture Notes in Physics, vol. 848 (Springer, Berlin, 2012), pp. 165–227. ISBN 978-3-642-24706-4
10. V. Zagrebaev, W. Greiner, in *Clusters in Nuclei*, ed. by C. Beck. Lecture Notes in Physics, vol. 818 (Springer, Berlin, 2010), pp. 267–315. ISBN 978-3-642-13898-0
11. Y. Kanada-En'yo, M. Kimura, in *Clusters in Nuclei*, ed. by C. Beck. Lecture Notes in Physics, vol. 818 (Springer, Berlin, 2010), pp. 129–164. ISBN 978-3-642-13898-0
12. D. Poenaru, W. Greiner, in *Clusters in Nuclei*, ed. by C. Beck. Lecture Notes in Physics, vol. 818 (Springer, Berlin, 2010), pp. 1–56. ISBN 978-3-642-13898-0
13. C. Simenel, Eur. Phys. J. A **48**, 152 (2012)
14. A. Sandulescu, R. Cusson, W. Greiner, Nuovo Cimento A **36**, 321 (1983)
15. A.S. Umar, M.R. Strayer, R.Y. Cusson, P.G. Reinhard, D.A. Bromley, Phys. Rev. C **32**, 172 (1985)

16. R.Y. Cusson, J.A. Maruhn, H. Stöcker, Z. Phys. A **294**, 257 (1980)
17. M.R. Strayer, R.Y. Cusson, H. Stoecker, J.A. Maruhn, W. Greiner, Phys. Rev. C **28**, 228 (1983)
18. K.H. Kim, T. Otsuka, P. Bonche, J. Phys. G **23**, 1267 (1997)
19. C. Simenel, P. Chomaz, G. de France, Phys. Rev. Lett. **86**, 2971 (2001)
20. C. Simenel, P. Chomaz, G. de France, Phys. Rev. Lett. **93**, 102701 (2004)
21. J.A. Maruhn, P.G. Reinhard, P.D. Stevenson, M.R. Strayer, Phys. Rev. C **74**, 027601 (2006)
22. A.S. Umar, V.E. Oberacker, Phys. Rev. C **73**, 054607 (2006)
23. A.S. Umar, V.E. Oberacker, Phys. Rev. C **74**, 021601 (2006)
24. A.S. Umar, V.E. Oberacker, Phys. Rev. C **74**, 024606 (2006)
25. A.S. Umar, V.E. Oberacker, Phys. Rev. C **74**, 061601 (2006)
26. L. Guo, J.A. Maruhn, P.G. Reinhard, Phys. Rev. C **76**, 014601 (2007)
27. C. Simenel, P. Chomaz, G. de France, Phys. Rev. C **76**, 024609 (2007)
28. A.S. Umar, V.E. Oberacker, Phys. Rev. C **76**, 014614 (2007)
29. C. Simenel, B. Avez, Int. J. Mod. Phys. E **17**, 31 (2008)
30. L. Guo, J.A. Maruhn, P.G. Reinhard, Y. Hashimoto, Phys. Rev. C **77**, 041301 (2008)
31. A.S. Umar, V.E. Oberacker, Phys. Rev. C **77**, 064605 (2008)
32. K. Washiyama, D. Lacroix, Phys. Rev. C **78**, 024610 (2008)
33. A.S. Umar, V.E. Oberacker, J.A. Maruhn, P.G. Reinhard, Phys. Rev. C **80**, 041601 (2009)
34. S. Ayik, K. Washiyama, D. Lacroix, Phys. Rev. C **79**, 054606 (2009)
35. A.S. Umar, V.E. Oberacker, Eur. Phys. J. A **39**, 243 (2009)
36. A.S. Umar, V.E. Oberacker, J. Phys. G **36**, 025101 (2009)
37. K. Washiyama, D. Lacroix, Int. J. Mod. Phys. E **18**, 2114 (2009)
38. A.S. Umar, J.A. Maruhn, N. Itagaki, V.E. Oberacker, Phys. Rev. Lett. **104**, 212503 (2010)
39. A.S. Umar, V.E. Oberacker, J.A. Maruhn, P.G. Reinhard, Phys. Rev. C **81**, 064607 (2010)
40. V.E. Oberacker, A.S. Umar, J.A. Maruhn, P.G. Reinhard, Phys. Rev. C **82**, 034603 (2010)
41. N. Loebl, J.A. Maruhn, P.G. Reinhard, Phys. Rev. C **84**, 034608 (2011)
42. Y. Iwata, J.A. Maruhn, Phys. Rev. C **84**, 014616 (2011)
43. A.S. Umar, V.E. Oberacker, J.A. Maruhn, P.G. Reinhard, Phys. Rev. C **85**, 017602 (2012)
44. V.E. Oberacker, A.S. Umar, J.A. Maruhn, P.G. Reinhard, Phys. Rev. C **85**, 034609 (2012)
45. R. Keser, A.S. Umar, V.E. Oberacker, Phys. Rev. C **85**, 044606 (2012)
46. A.S. Umar, V.E. Oberacker, C.J. Horowitz, Phys. Rev. C **85**, 055801 (2012)
47. C. Simenel, A. Wakhle, B. Avez, J. Phys. Conf. Ser. **420**, 012118 (2013)
48. C. Simenel, A. Wakhle, B. Avez, D.J. Hinde, R. du Rietz, M. Dasgupta, M. Evers, C.J. Lin, D.H. Luong, EPJ Web Conf. **38**, 09001 (2012)
49. A.S. Umar, V.E. Oberacker, J.A. Maruhn, Eur. Phys. J. A **37**, 245 (2008)
50. K. Washiyama, S. Ayik, D. Lacroix, Phys. Rev. C **80**, 031602 (2009)
51. Y. Iwata, T. Otsuka, J.A. Maruhn, N. Itagaki, Eur. Phys. J. A **42**, 613 (2009)
52. C. Golabek, C. Simenel, Phys. Rev. Lett. **103**, 042701 (2009)
53. D.J. Kedziora, C. Simenel, Phys. Rev. C **81**, 044613 (2010)
54. Y. Iwata, T. Otsuka, J.A. Maruhn, N. Itagaki, Phys. Rev. Lett. **104**, 252501 (2010)
55. Y. Iwata, T. Otsuka, J.A. Maruhn, N. Itagaki, Nucl. Phys. A **836**, 108 (2010)
56. C. Simenel, Phys. Rev. Lett. **105**, 192701 (2010)
57. M. Evers, M. Dasgupta, D.J. Hinde, D.H. Luong, R. Rafiei, R. du Rietz, C. Simenel, Phys. Rev. C **84**, 054614 (2011)
58. B. Yilmaz, S. Ayik, D. Lacroix, K. Washiyama, Phys. Rev. C **83**, 064615 (2011)
59. C. Simenel, Phys. Rev. Lett. **106**, 112502 (2011)
60. Y. Iwata, J. Mod. Phys. **3**, 476 (2012)
61. C. Simenel, D.J. Hinde, R. du Rietz, M. Dasgupta, M. Evers, C.J. Lin, D.H. Luong, A. Wakhle, Phys. Lett. B **710**, 607 (2012)
62. F. Sébille, S. Figerou, V. de la Mota, Nucl. Phys. A **822**, 51 (2009)
63. F. Sébille, V. de la Mota, S. Figerou, Phys. Rev. C **84**, 055801 (2011)
64. P.A.M. Dirac, Proc. Camb. Philos. Soc. **26**, 376 (1930)
65. D.R. Hartree, Proc. Camb. Philos. Soc. **24**, 89 (1928)

66. V.A. Fock, Z. Phys. **61**, 126 (1930)
67. J.W. Negele, Rev. Mod. Phys. **54**, 913 (1982)
68. K. Bennaceur, P. Bonche, J. Meyer, C. R. Phys. **4**, 555 (2003)
69. T. Skyrme, Philos. Mag. **1**, 1043 (1956)
70. J. Dechargé, D. Gogny, Phys. Rev. C **21**, 1568 (1980)
71. P. Bonche, H. Flocard, P. Heenen, Nucl. Phys. A **467**, 115 (1987)
72. Y. Engel, D. Brink, K. Goeke, S. Krieger, D. Vautherin, Nucl. Phys. A **249**, 215 (1975)
73. N. Loebl, A.S. Umar, J.A. Maruhn, P.G. Reinhard, P.D. Stevenson, V.E. Oberacker, Phys. Rev. C **86**, 024608 (2012)
74. E. Chabanat, P. Bonche, P. Haensel, J. Meyer, R. Schaeffer, Nucl. Phys. A **635**, 231 (1998)
75. R.B. Wiringa, V. Fiks, A. Fabrocini, Phys. Rev. C **38**, 1010 (1988)
76. T. Nakatsukasa, K. Yabana, Phys. Rev. C **71**, 024301 (2005)
77. C. Simenel, P. Chomaz, Phys. Rev. C **80**, 064309 (2009)
78. A.S. Umar, V.E. Oberacker, Phys. Rev. C **71**, 034314 (2005)
79. P. Bonche, S. Koonin, J.W. Negele, Phys. Rev. C **13**, 1226 (1976)
80. Y. Hashimoto, Eur. Phys. J. A **48**, 1 (2012)
81. A. Umar, M. Strayer, Comput. Phys. Commun. **63**, 179 (1991)
82. J.A. Maruhn, P.G. Reinhard, P.D. Stevenson, J.R. Stone, M.R. Strayer, Phys. Rev. C **71**, 064328 (2005)
83. C. Simenel, D. Lacroix, B. Avez, *Quantum Many-Body Dynamics: Applications to Nuclear Reactions* (VDM Verlag, Sarrebruck, 2010). arXiv:0806.2714
84. N.N. Bogoliubov, J. Phys. (URSS) **10**, 256 (1946)
85. H. Born, H.S. Green, Proc. R. Soc. A, Math. Phys. Eng. Sci. **188**, 10 (1946)
86. J.G. Kirkwood, J. Chem. Phys. **14**, 180 (1946)
87. P. Ring, P. Schuck, *The Nuclear Many-Body Problem* (Springer, Berlin, 1980)
88. S. Ebata, T. Nakatsukasa, T. Inakura, K. Yoshida, Y. Hashimoto, K. Yabana, Phys. Rev. C **82**, 034306 (2010)
89. G. Scamps, D. Lacroix, G. Bertsch, K. Washiyama, Phys. Rev. C **85**, 034328 (2012)
90. B. Avez, C. Simenel, P. Chomaz, Phys. Rev. C **78**, 044318 (2008)
91. I. Stetcu, A. Bulgac, P. Magierski, K.J. Roche, Phys. Rev. C **84**, 051309 (2011)
92. J. Engel, M. Bender, J. Dobaczewski, W. Nazarewicz, R. Surman, Phys. Rev. C **60**, 014302 (1999)
93. E. Khan, N. Sandulescu, M. Grasso, N. Van Giai, Phys. Rev. C **66**, 024309 (2002)
94. S. Fracasso, G. Colò, Phys. Rev. C **72**, 064310 (2005)
95. S. Péru, H. Goutte, Phys. Rev. C **77**, 044313 (2008)
96. C.Y. Wong, H.H.K. Tang, Phys. Rev. Lett. **40**, 1070 (1978)
97. C.Y. Wong, H.H.K. Tang, Phys. Rev. C **20**, 1419 (1979)
98. P. Danielewicz, Ann. Phys. **152**, 305 (1984)
99. W. Botermans, R. Malfliet, Phys. Rep. **198**, 115 (1990)
100. S. Ayik, Z. Phys. A **298**, 83 (1980)
101. D. Lacroix, P. Chomaz, S. Ayik, Nucl. Phys. A **651**, 369 (1999)
102. W. Cassing, U. Mosel, Prog. Part. Nucl. Phys. **25**, 235 (1990)
103. F.V. De Blasio, W. Cassing, M. Tohyama, P.F. Bortignon, R.A. Broglia, Phys. Rev. Lett. **68**, 1663 (1992)
104. M. Tohyama, A.S. Umar, Phys. Rev. C **65**, 037601 (2002)
105. M. Assie, D. Lacroix, Phys. Rev. Lett. **102**, 202501 (2009)
106. C. Grégoire, B. Remaud, F. Sébille, L. Vinet, Y. Raffray, Nucl. Phys. A **465**, 317 (1987)
107. P. Schuck, R. Hasse, J. Jaenicke, C. Grégoire, B. Rémaud, F. Sébille, E. Suraud, Prog. Part. Nucl. Phys. **22**, 181 (1989)
108. V. de la Mota, F. Sebille, M. Farine, B. Remaud, P. Schuck, Phys. Rev. C **46**, 677 (1992)
109. R. Balian, M. Vénéroni, Phys. Rev. Lett. **47**, 1353 (1981)
110. R. Balian, M. Vénéroni, Phys. Lett. B **136**, 301 (1984)
111. S. Ayik, Phys. Lett. B **658**, 174 (2008)
112. P.G. Reinhard, R.Y. Cusson, K. Goeke, Nucl. Phys. A **398**, 141 (1983)

113. H. Goutte, J.F. Berger, P. Casoli, D. Gogny, Phys. Rev. C **71**, 024316 (2005)
114. E.C. Schloemer, M. Gai, J.F. Ennis, M. Ruscev, B. Shivakumar, S.M. Sterbenz, N. Tsoupas, D.A. Bromely, Phys. Rev. Lett. **51**, 881 (1983)
115. P. Sperr, T.H. Braid, Y. Eisen, D.G. Kovar, F.W. Prosser, J.P. Schiffer, S.L. Tabor, S. Vigdor, Phys. Rev. Lett. **37**, 321 (1976)
116. P. Sperr, S. Vigdor, Y. Eisen, W. Henning, D.G. Kovar, T.R. Ophel, B. Zeidman, Phys. Rev. Lett. **36**, 405 (1976)
117. J.J. Kolata, R.C. Fuller, R.M. Freeman, F. Haas, B. Heusch, A. Gallmann, Phys. Rev. C **16**, 891 (1977)
118. I. Tserruya, Y. Eisen, D. Pelte, A. Gavron, H. Oeschler, D. Berndt, H.L. Harney, Phys. Rev. C **18**, 1688 (1978)
119. D.G. Kovar, D.F. Geesaman, T.H. Braid, Y. Eisen, W. Henning, T.R. Ophel, M. Paul, K.E. Rehm, S.J. Sanders, P. Sperr et al., Phys. Rev. C **20**, 1305 (1979)
120. R. Vandenbosch, Phys. Lett. B **87**, 183 (1979)
121. H. Esbensen, Phys. Rev. C **77**, 054608 (2008)
122. H. Esbensen, Phys. Rev. C **85**, 064611 (2012)
123. J.S. Blair, Phys. Rev. **95**, 1218 (1954)
124. D.L. Hill, J.A. Wheeler, Phys. Rev. **89**, 1102 (1953)
125. S. Gary, C. Volant, Phys. Rev. C **25**, 1877 (1982)
126. W. Treu, W. Galster, H. Fröhlich, H. Voit, P. Dück, Phys. Lett. B **72**, 315 (1978)
127. K. Erb, D. Bromley, *Treatise on Heavy Ion Science*, vol. 3 (Plenum, New York, 1985), p. 201, and references therein
128. R. Zurmühle, P. Kutt, R. Betts, S. Saini, F. Haas, O. Hansen, Phys. Lett. B **129**, 384 (1983)
129. P. Bonche, H. Flocard, P.H. Heenen, Comput. Phys. Commun. **171**, 49 (2005)
130. W. von Oertzen, M. Freer, Y. Kanada-En'yo, Phys. Rep. **432**, 43 (2006)
131. T. Furuta, K.H.O. Hasnaoui, F. Gulminelli, C. Leclercq, A. Ono, Phys. Rev. C **82**, 034307 (2010)
132. T. Ichikawa, J.A. Maruhn, N. Itagaki, S. Ohkubo, Phys. Rev. Lett. **107**, 112501 (2011)
133. J.P. Ebran, E. Khan, T. Niksic, D. Vretenar, Nature **487**, 341 (2012)
134. D. Luong, M. Dasgupta, D. Hinde, R. du Rietz, R. Rafiei, C. Lin, M. Evers, A. Diaz-Torres, Phys. Lett. B **695**, 105 (2011)
135. A. Astier, P. Petkov, M.G. Porquet, D.S. Delion, P. Schuck, Phys. Rev. Lett. **104**, 042701 (2010)
136. W.A. Fowler, in *Highlights of Modern Astrophysics. Concepts and Controversies*, ed. by S.L. Shapiro, S.A. Teukolsky (Wiley, New York, 1986)
137. F. Hoyle, Astrophys. J. Suppl. Ser. **1**, 121 (1954)
138. H. Morinaga, Phys. Rev. **101**, 254 (1956)
139. Y. Fujiwara, H. Horiuchi, K. Ikeda, M. Kamimura, K. Katō, Y. Suzuki, E. Uegaki, Prog. Theor. Phys. **68**, 29 (1980)
140. A.S. Umar, M.R. Strayer, P.G. Reinhard, Phys. Rev. Lett. **56**, 2793 (1986)
141. Y. Iwata, N. Itagaki, J.A. Maruhn, T. Otsuka, Int. J. Mod. Phys. E **17**, 1660 (2008)
142. W. von Oertzen, A. Vitturi, Rep. Prog. Phys. **64**, 1247 (2001)
143. S.E. Koonin, K.T.R. Davies, V. Maruhn-Rezwani, H. Feldmeier, S.J. Krieger, J.W. Negele, Phys. Rev. C **15**, 1359 (1977)
144. M. Bender, P.H. Heenen, P.G. Reinhard, Rev. Mod. Phys. **75**, 121 (2003)
145. R.M. DeVries, D. Shapira, W.G. Davies, G.C. Ball, J.S. Forster, W. McLatchie, Phys. Rev. Lett. **35**, 835 (1975)
146. H. Hasan, C. Warke, Nucl. Phys. A **318**, 523 (1979)
147. I. Thompson, M. Nagarajan, J. Lilley, M. Smithson, Nucl. Phys. A **505**, 84 (1989)
148. Y. Funaki, T. Yamada, H. Horiuchi, G. Röpke, P. Schuck, A. Tohsaki, Phys. Rev. Lett. **101**, 082502 (2008)
149. C. Wheldon, N.I. Ashwood, M. Barr, N. Curtis, M. Freer, T. Kokalova, J.D. Malcolm, S.J. Spencer, V.A. Ziman, T. Faestermann et al., Phys. Rev. C **83**, 064324 (2011)

150. M. Abdullah, S. Hossain, M. Sarker, S. Das, A. Tariq, M. Uddin, A. Basak, S. Ali, H. Sen Gupta, F. Malik, Eur. Phys. J. A **18**, 65 (2003)
151. L. Corradi, G. Pollarolo, S. Szilner, J. Phys. G **36**, 113101 (2009)
152. K. Hagino, N. Rowley, A. Kruppa, Comput. Phys. Commun. **123**, 143 (1999)
153. J.P. Blaizot, G. Ripka, *Quantum Theory of Finite Systems* (MIT Press, Cambridge, 1986)
154. G. Ripka, R. Padjen, Nucl. Phys. A **132**, 489 (1969)
155. E. Khan, N. Sandulescu, N. Van Giai, M. Grasso, Phys. Rev. C **69**, 014314 (2004)
156. E. Pllumbi, M. Grasso, D. Beaumel, E. Khan, J. Margueron, J. van de Wiele, Phys. Rev. C **83**, 034613 (2011)
157. H. Shimoyama, M. Matsuo, Phys. Rev. C **84**, 044317 (2011)
158. M. Grasso, D. Lacroix, A. Vitturi, Phys. Rev. C **85**, 034317 (2012)
159. A. Bohr, B. Mottelson, *Nuclear Structure* (Benjamin, Elmsford, 1975), 2 vols.
160. D. Bès, R. Broglia, Nucl. Phys. **80**, 289 (1966)
161. B. Avez, C. Simenel, P. Chomaz, Int. J. Mod. Phys. E **18**, 2103 (2009)
162. B. Avez, P. Chomaz, T. Duguet, C. Simenel, Mod. Phys. Lett. A **25**, 1997 (2010)
163. B. Avez, Ph.D. thesis, University of Paris XI (2009)
164. E. Khan, M. Grasso, J. Margueron, Phys. Rev. C **80**, 044328 (2009)
165. J.C. Roynette, H. Doubre, N. Frascaria, J.C. Jacmart, N. Poffé, M. Riou, Phys. Lett. B **67**, 395 (1977)
166. W.U. Schroder, J.R. Huizenga, Annu. Rev. Nucl. Part. Sci. **27**, 465 (1977)
167. W. Schroder, J. Huizenga, *Treatise on Heavy-Ion Science*, vol. 2 (Plenum, New York, 1984)
168. H. Freiesleben, J. Kratz, Phys. Rev. **106**, 1 (1984)
169. P. Evans, A. Smith, C. Pass, L. Stuttgé, B. Back, R. Betts, B. Dichter, D. Henderson, S. Sanders, F. Videbaek et al., Nucl. Phys. A **526**, 365 (1991)
170. R. Planeta, S.H. Zhou, K. Kwiatkowski, W.G. Wilson, V.E. Viola, H. Breuer, D. Benton, F. Khazaie, R.J. McDonald, A.C. Mignerey et al., Phys. Rev. C **38**, 195 (1988)
171. R. Płaneta, K. Kwiatkowski, S.H. Zhou, V.E. Viola, H. Breuer, M.A. McMahan, W. Kehoe, A.C. Mignerey, Phys. Rev. C **41**, 942 (1990)
172. R.T. de Souza, W.U. Schröder, J.R. Huizenga, R. Planeta, K. Kwiatkowski, V.E. Viola, H. Breuer, Phys. Rev. C **37**, 1783 (1988)
173. R.T. de Souza, W.U. Schröder, J.R. Huizenga, J. Tke, S.S. Datta, J.L. Wile, Phys. Rev. C **39**, 114 (1989)
174. B. Fornal, R. Broda, W. Krolas, T. Pawlat, J. Wrzesinski, P. Daly, P. Bhattacharyya, Z. Grabowski, C. Zhang, D. Bazzacco et al., Eur. Phys. J. A **1**, 355 (1998)
175. G. Lane, R. Broda, B. Fornal, A. Byrne, G. Dracoulis, J. Blomqvist, R. Clark, M. Cromaz, M. Deleplanque, R. Diamond et al., Nucl. Phys. A **682**, 71 (2001)
176. R. Lemmon, A. Chbihi et al., Transport properties of isospin asymmetric nuclear matter. Letter of intent for SPIRAL2 (2012)
177. K.T.R. Davies, V. Maruhn-Rezwani, S.E. Koonin, J.W. Negele, Phys. Rev. Lett. **41**, 632 (1978)
178. J. Randrup, Nucl. Phys. A **383**, 468 (1982)
179. H.A. Weidenmüller, Prog. Part. Nucl. Phys. **3**, 49 (1980)
180. C.H. Dasso, T. Døssing, H.C. Pauli, Z. Phys. A **289**, 395 (1979)
181. R. Balian, M. Vénéroni, Ann. Phys. **216**, 351 (1992)
182. J.B. Marston, S.E. Koonin, Phys. Rev. Lett. **54**, 1139 (1985)
183. P. Bonche, H. Flocard, Nucl. Phys. A **437**, 189 (1985)
184. T. Troudet, D. Vautherin, Phys. Rev. C **31**, 278 (1985)
185. J.M.A. Broomfield, P.D. Stevenson, J. Phys. G **35**, 095102 (2008)
186. J.M.A. Broomfield, Ph.D. thesis, University of Surrey (2009)
187. C. Simenel, C. Golabek, D.J. Kedziora, EPJ Web Conf. **17**, 09002 (2011)
188. V.E. Viola, K. Kwiatkowski, M. Walker, Phys. Rev. C **31**, 1550 (1985)
189. H. Gäggeler, T. Sikkeland, G. Wirth, W. Brüchle, W. Bögl, G. Franz, G. Herrmann, J.V. Kratz, M. Schädel, K. Sümmerer et al., Z. Phys. A **316**, 291 (1984)

190. R. Bock, Y.T. Chu, M. Dakowski, A. Gobbi, E. Grosse, A. Olmi, H. Sann, D. Schwalm, U. Lynen, W. Müller et al., Nucl. Phys. A **388**, 334 (1982)
191. J. Töke, R. Bock, G. Dai, A. Gobbi, S. Gralla, K. Hildenbrand, J. Kuzminski, W. Müller, A. Olmi, H. Stelzer et al., Nucl. Phys. A **440**, 327 (1985)
192. W.Q. Shen, J. Albinski, A. Gobbi, S. Gralla, K.D. Hildenbrand, N. Herrmann, J. Kuzminski, W.F.J. Müller, H. Stelzer, J. Töke et al., Phys. Rev. C **36**, 115 (1987)
193. D.J. Hinde, M. Dasgupta, J.R. Leigh, J.C. Mein, C.R. Morton, J.O. Newton, H. Timmers, Phys. Rev. C **53**, 1290 (1996)
194. I.M. Itkis, E.M. Kozulin, M.G. Itkis, G.N. Knyazheva, A.A. Bogachev, E.V. Chernysheva, L. Krupa, Y.T. Oganessian, V.I. Zagrebaev, A.Y. Rusanov et al., Phys. Rev. C **83**, 064613 (2011)
195. A. Nasirov, A. Muminov, R. Utamuratov, G. Fazio, G. Giardina, F. Hanappe, G. Mandaglio, M. Manganaro, W. Scheid, Eur. Phys. J. A **34**, 325 (2007)
196. J. Błocki, J. Randrup, W. Swiatecki, C. Tsang, Ann. Phys. **105**, 427 (1977)
197. R. du Rietz, D.J. Hinde, M. Dasgupta, R.G. Thomas, L.R. Gasques, M. Evers, N. Lobanov, A. Wakhle, Phys. Rev. Lett. **106**, 052701 (2011)
198. W. Swiatecki, Nucl. Phys. A **376**, 275 (1982)
199. L. Guo, T. Nakatsukasa, EPJ Web Conf. **38**, 09003 (2012)
200. B. Avez, Private communication
201. P. Bonche, N. Ngô, Phys. Lett. B **105**, 17 (1981)
202. C. Stodel, Ph.D. thesis, University of Caen (1998)
203. G. Fazio, G. Giardina, G. Mandaglio, R. Ruggeri, A.I. Muminov, A.K. Nasirov, Y.T. Oganessian, A.G. Popeko, R.N. Sagaidak, A.V. Yeremin et al., Phys. Rev. C **72**, 064614 (2005)
204. D. Hinde, M. Dasgupta, Phys. Lett. B **622**, 23 (2005)
205. P. Armbruster, Annu. Rev. Nucl. Part. Sci. **50**, 411 (2000)
206. A. Sandulescu, R. Gupta, W. Scheid, W. Greiner, Phys. Lett. B **60**, 225 (1976)
207. R.K. Gupta et al., Z. Naturforsch. **32a**, 704 (1977)
208. Y. Aritomo, Nucl. Phys. A **780**, 222 (2006)
209. Y.T. Oganessian, V.K. Utyonkov, Y.V. Lobanov, F.S. Abdullin, A.N. Polyakov, R.N. Sagaidak, I.V. Shirokovsky, Y.S. Tsyganov, A.A. Voinov, G.G. Gulbekian et al., Phys. Rev. C **74**, 044602 (2006)
210. S. Hofmann, D. Ackermann, S. Antalic, H. Burkhard, V. Comas, R. Dressler, Z. Gan, S. Heinz, J. Heredia et al., Eur. Phys. J. A **32**, 251 (2007)
211. D.J. Hinde, M. Dasgupta, J.R. Leigh, J.P. Lestone, J.C. Mein, C.R. Morton, J.O. Newton, H. Timmers, Phys. Rev. Lett. **74**, 1295 (1995)
212. Z. Liu, H. Zhang, J. Xu, Y. Qiao, X. Qian, C. Lin, Phys. Lett. B **353**, 173 (1995)
213. Y.T. Oganessian, V.K. Utyonkov, Y.V. Lobanov, F.S. Abdullin, A.N. Polyakov, I.V. Shirokovsky, Y.S. Tsyganov, G.G. Gulbekian, S.L. Bogomolov, B.N. Gikal et al., Phys. Rev. C **70**, 064609 (2004)
214. G.N. Knyazheva, E.M. Kozulin, R.N. Sagaidak, A.Y. Chizhov, M.G. Itkis, N.A. Kondratiev, V.M. Voskressensky, A.M. Stefanini, B.R. Behera, L. Corradi et al., Phys. Rev. C **75**, 064602 (2007)
215. D.J. Hinde, R.G. Thomas, R. du Rietz, A. Diaz-Torres, M. Dasgupta, M.L. Brown, M. Evers, L.R. Gasques, R. Rafiei, M.D. Rodriguez, Phys. Rev. Lett. **100**, 202701 (2008)
216. K. Nishio, H. Ikezoe, S. Mitsuoka, I. Nishinaka, Y. Nagame, Y. Watanabe, T. Ohtsuki, K. Hirose, S. Hofmann, Phys. Rev. C **77**, 064607 (2008)
217. A. Wakhle, C. Simenel, D.J. Hinde, M. Dasgupta, in preparation
218. V.V. Volkov, Phys. Rep. **44**, 93 (1978)
219. V.I. Zagrebaev, Y.T. Oganessian, M.G. Itkis, W. Greiner, Phys. Rev. C **73**, 031602 (2006)
220. J. Reinhardt, B. Müller, W. Greiner, Phys. Rev. A **24**, 103 (1981)
221. W. Greiner (ed.), *Quantum Electrodynamics of Strong Fields* (Plenum, New York, 1983)
222. E. Ackad, M. Horbatsch, Phys. Rev. A **78**, 062711 (2008)
223. Z.Q. Feng, G.M. Jin, J.Q. Li, Phys. Rev. C **80**, 067601 (2009)

224. V.V. Sargsyan, Z. Kanokov, G.G. Adamian, N.V. Antonenko, W. Scheid, Phys. Rev. C **80**, 047603 (2009)
225. J. Tian, X. Wu, K. Zhao, Y. Zhang, Z. Li, Phys. Rev. C **77**, 064603 (2008)
226. K. Zhao, X. Wu, Z. Li, Phys. Rev. C **80**, 054607 (2009)
227. I. Ahmad, S.M. Austin, B.B. Back, R.R. Betts, F.P. Calaprice, K.C. Chan, A. Chishti, C.M. Conner, R.W. Dunford, J.D. Fox et al., Phys. Rev. C **60**, 064601 (1999)
228. S.A. Colgate, R.H. White, Astrophys. J. **143**, 626 (1966)
229. P. Haensel, A.Y. Potekhin, D.G. Yakovlev, *Neutron Stars 1: Equation of State and Structure*. Astrophysics and Space Science Library, vol. 326 (Springer, New York, 2007)
230. A.R. Raduta, F. Gulminelli, Phys. Rev. C **82**, 065801 (2010)
231. F. Gulminelli, A.R. Raduta, Phys. Rev. C **85**, 025803 (2012)
232. F. Gulminelli, A.R. Raduta, M. Oertel, Phys. Rev. C **86**, 025805 (2012)
233. N. Chamel, P. Haensel, Living Rev. Relativ. **11**, 10 (2008)
234. K. Oyamatsu, Nucl. Phys. A **561**, 431 (1993)
235. G. Baym, H.A. Bethe, C.J. Pethick, Nucl. Phys. A **175**, 225 (1971)
236. D.G. Ravenhall, C.J. Pethick, J.R. Wilson, Phys. Rev. Lett. **50**, 2066 (1983)
237. M. Hashimoto, H. Seki, M. Yamada, Prog. Theor. Phys. **71**, 320 (1984)
238. C.J. Pethick, D.G. Ravenhall, Annu. Rev. Nucl. Part. Sci. **45**, 429 (1995)
239. W.G. Newton, J.R. Stone, Phys. Rev. C **79**, 055801 (2009)
240. P. Magierski, P.H. Heenen, Phys. Rev. C **65**, 045804 (2002)
241. P. Gögelein, H. Müther, Phys. Rev. C **76**, 024312 (2007)
242. G. Watanabe, K. Sato, K. Yasuoka, T. Ebisuzaki, Phys. Rev. C **66**, 012801 (2002)
243. G. Watanabe, H. Sonoda, T. Maruyama, K. Sato, K. Yasuoka, T. Ebisuzaki, Phys. Rev. Lett. **103**, 121101 (2009)
244. J. Margueron, E.v. Dalen, C. Fuchs, Phys. Rev. C **76**, 034309 (2007)
245. F. Chappert, M. Girod, S. Hilaire, Phys. Lett. B **668**, 420 (2008)
246. D.T. Loan, N.H. Tan, D.T. Khoa, J. Margueron, Phys. Rev. C **83**, 065809 (2011)

# Chapter 5
# Covalent Binding on the Femtometer Scale: Nuclear Molecules

**Wolfram von Oertzen and Matko Milin**

## 5.1 Molecular Binding Energy Between Nuclei

In the last decades of the last century a large variety of experimental and theoretical work has been devoted to find evidence for the formation of "quasi-molecular" states mainly for $N = Z$ nuclei involving $\alpha$-clusters and $A = 2N + 2Z$ nuclei (see Ref. [1] for the last survey). Such states are resonances formed in the interaction of two strongly bound clusters. These resonances are mostly connected to the intrinsic excitation of the two interacting clusters and to specific deformed structures observed in the compound states at large deformations. The feature is well known from the early work at Tandem-laboratories, and played an important role in history of nuclear science. There has been a steady activity in the field of clustering in nuclei; see e.g. proceedings of cluster conferences in Bochum [2], College Park [3], Winnipeg [4], Chester [5], Kyoto [6], Strasbourg [7], Rab [8], Nara [9] and Stratford-upon-Avon [10]. The fact that valence neutrons will create covalent binding via their exchange between two nuclear cores has been formulated already in 1970 by von Oertzen in Ref. [11]. At this time the concept was used to describe the parity dependence of nuclear potentials for the scattering of nuclei with neutron excess, and the special phenomena connected to the scattering of nuclei with a small mass difference (*elastic transfer*), namely with a few excess neutrons/protons (e.g. $A = 2N(+xn) + 2Z$). The particularly pronounced effects in the case of the elastic transfer process, has been summarised in Ref. [12], while the Parity dependence of the heavy-ion potential has been discussed in Refs. [13, 14].

---

W. von Oertzen (✉)
Fachbereich Physik and Helmholtz-Zentrum Berlin, Freie Universitaet, 14109 Berlin, Germany
e-mail: oertzen@helmholtz-berlin.de

M. Milin
Faculty of Science, University of Zagreb, 10000 Zagreb, Croatia
e-mail: matko.milin@phy.hr

C. Beck (ed.), *Clusters in Nuclei, Volume 3*, Lecture Notes in Physics 875,
DOI 10.1007/978-3-319-01077-9_5,

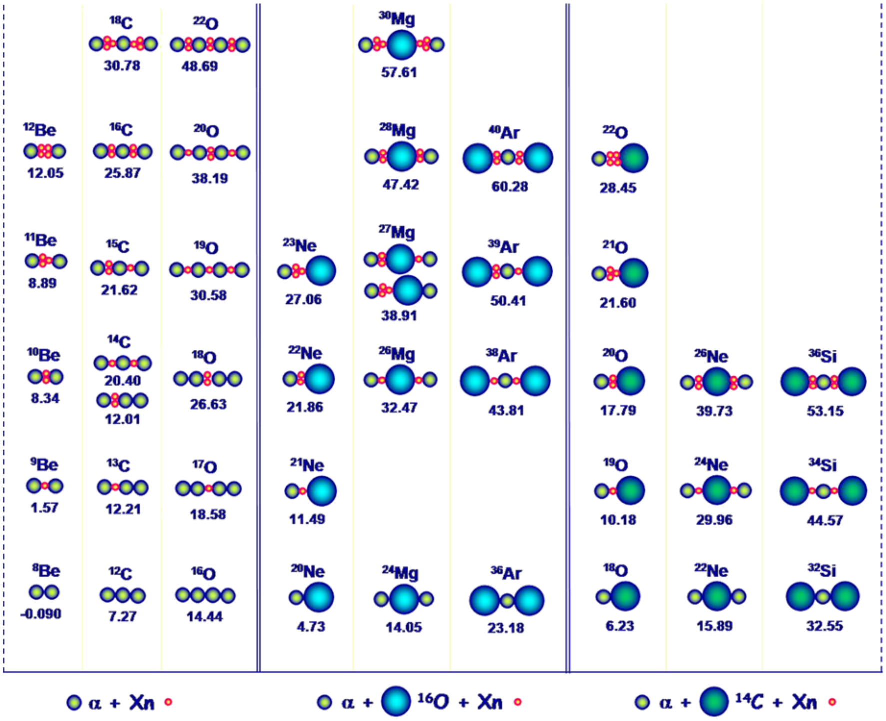

**Fig. 5.1** A scheme of nuclear molecules consisting of two or more clusters bound by *covalent* orbitals of the valence neutrons. The energies for their decay into the shown constituents are also given. The *lowest line* of each configuration corresponds to parts of the original Ikeda diagram. However, because of its deformation, the $^{12}$C nucleus is not included, as it was in the original Ikeda diagram. In contrast, $^{14}$C is suggested as a perfect strongly bound spherical cluster, so molecular configurations based on combinations with this cluster are also shown, on the right side (see Sect. 5.4 and Ref. [20] for detailed discussion)

The molecular orbital approach was developed to describe the scattering states, like in the $^{12}$C + $^{13}$C system [15]. Later in the nineties of the last century the existence of true nuclear molecular bound states, based on two nuclear clusters bound by neutrons in covalent molecular orbitals, has been established [16–18]. Attention in the present article is focused on these nuclear molecular states, namely nuclear structures based on *true* (not *quasi*) molecular cluster structure. This includes also particle stable states, which can decay via $\gamma$-emission. Such states are indeed *femto-scale molecules*, with structure analog to the molecules on the scale of atoms (and bound by electrons), well described by quantum chemistry. The related nuclear molecular structures and their rotational bands are found in a large number of light nuclei [1, 19]. The light nuclei show many cases of *covalent* binding of nuclear clusters by valence neutrons. The strongly bound clusters which play the dominant role (see Fig. 5.1) are $^{4}$He, $^{14}$C and $^{16}$O [20].

For the present discussion, it is quite important that the existence of nuclear clusters and the covalently bound molecular states is well described in model independent theoretical approaches, e.g. the anti-symmetrized molecular dynamics (AMD) with an effective $N$-$N$ force [21]. Within this model Horiuchi, Kanada-En'yo et al. [22–25] explained the ground state properties and a large variety of excited nuclear states in neutron-rich light isotopes, among those many with the molecular structure. The density distributions of the nucleons, the neutrons and the protons which reside inside of the clusters, are obtained and show the persistence of molecular configurations [23, 25].

Independently, in a related method based on a more fundamental basis (with all degrees of freedom in the $N$-$N$ nuclear forces), so-called Fermionic Molecular Dynamics (FMD) by Feldmeier and Neff et al. [26, 27], it has been shown that the $\alpha$-clusters appear as the dominant substructures in light deformed nuclei. This work and a variety of other nuclear models, have established that $\alpha$-clusters play a decisive role in the description of light nuclei and their excited states, in particular for the deformed and weakly bound neutron-rich isotopes.

In the present lecture notes we study mainly structures which can be described as molecular states. Therefore the vast body of nuclear reaction studies of neutron rich (exotic) light nuclei and their analysis is not surveyed here.

### 5.1.1 Molecular Potentials Between Nuclei

The large amount of experimental results and their comparison with theoretical approaches, allow a design of a diagram [19] for covalently bound cluster molecular states, with two or three clusters, which appear close to the thresholds for the decomposition into clusters and valence neutrons. This is in analogy to the well known concept of the Ikeda diagram [28–31], with cluster states around the corresponding particle decay thresholds. The most important ingredient in the concept of the Ikeda-diagram (of $N = Z$ nuclei) is the $\alpha$-particle. The new diagram includes covalently bound states consisting of clusters and valence neutrons and is shown in Fig. 5.1. Binary molecules with two centres, but also clustered states with three and more centres can be predicted, (e.g. linear chains, with the most recent result reported in Ref. [32]).

The most important ingredient to form bound *dimers* is the shape of the local core-core potential ($\alpha$-$\alpha$-potential). As in atomic molecules, the nuclear potentials between the two clusters must have a repulsive core at small distances (in atomic molecules there is the Coulomb repulsion). These properties are actually found in the case of the $\alpha$-$\alpha$-potential, as well as for the $\alpha$-$^{16}$O-potential—these potentials are shown in Fig. 5.2. The nuclear potentials with $\alpha$-particles are deep and non-local if calculated microscopically. However, it has been shown by Baye [33], that a phase equivalent *local* potential can be obtained by super-symmetric transformations from the non-local microscopic potentials. This results in shallow (local) potentials with a repulsive core, see Fig. 5.2 (from Ref. [34]). Actually an empirical (local) potential has been obtained from experiments on $\alpha$-$\alpha$ scattering at low energies by

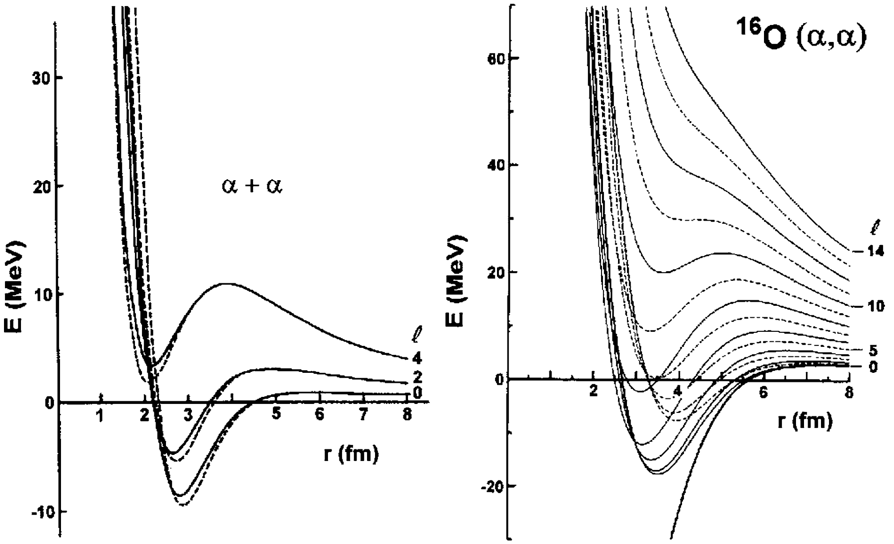

**Fig. 5.2** The equivalent local potentials describing the $\alpha$-$\alpha$ and the $\alpha$-$^{16}$O interaction. The resonant energies in $^{8}$Be and the phase shifts are reproduced. For the $\alpha$-$^{16}$O potential a similar van der Waals type of interaction is obtained. These allow the formation of bound *dimers*: $^{9,10,11}$Be and $^{20,21}$Ne, respectively. The empirical potentials (*full lines*) and the theoretical (*dashed*) are shown, for different angular momenta. Taken from Ref. [33]

Ali and Bodmer [35]. Their result agrees with the local potential obtained by theoretical concepts, see Fig. 5.2. The same procedure produces a "*molecular*" potential for the system $\alpha$-$^{16}$O, which allows the formation of covalently bound isotopes of $^{22,21,20}$Ne. In view of these circumstances, the "*extended*" Ikeda diagram for covalent molecules contains mainly $\alpha$-particles and $^{16}$O, and in view of the structure of $^{14}$C, which has properties very similar to $^{16}$O, the cluster $^{14}$C had to be added recently (see Fig. 5.1). The latter is responsible for the formation of covalent nuclear molecules with rotational as bands found in the isotopes of oxygen $^{16-22}$O; the detailed discussion is given in Sect. 5.4 and Refs. [20, 36, 37].

### *5.1.2 The Simplest Covalent Particle Stable Molecules,* $^{9-12}$Be

Molecular states in beryllium isotopes consist of two clusters. With two $\alpha$-particles the first very fundamental case of bound molecular configurations in nuclear physics [16, 17] are found in $^{9}$Be, and $^{10}$Be. The constituents in $^{9}$Be are $(\alpha + n + \alpha) \rightarrow {}^{5}\text{He} + {}^{4}\text{He}$ [38], with a $p_{3/2}$ neutron resonance in $^{5}$He at an energy of 0.798 MeV. The other ingredient is the unbound $^{8}$Be (i.e. two $\alpha$-particle resonance at 0.092 MeV). The covalent binding in this system is obtained by the creation of two-centre molecular wave functions, in two forms, the $\sigma$ and $\pi$ orbits. With the $\pi$

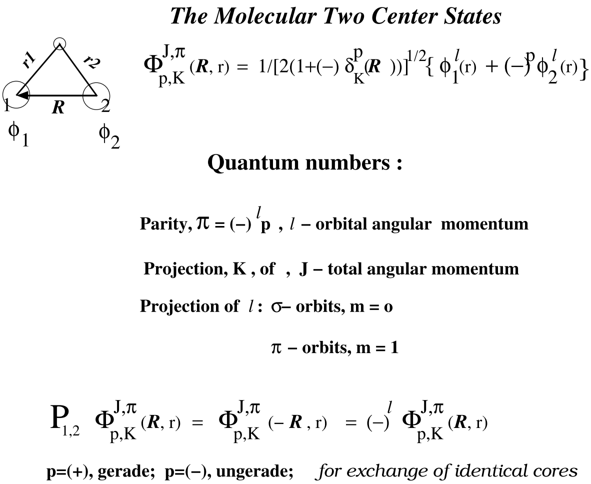

**Fig. 5.3** The two-centre wave functions of the molecular orbitals, forming the molecular basis states of $^9$Be; the $g$ and $u$ symmetry is shown

neutron-orbitals a bound *dimer* is formed, with the binding energy $E_b = 1.57$ MeV, for the ground state of the $^9$Be-nucleus.

Here we have the typical covalent wave functions with the only bound state in $^9$Be being the ground state. These wave functions are obtained by linear combinations of the two single centre basis states, as shown in Fig. 5.3. Plotting the energies of these states as function of distance between the two centres, we obtain the *correlation diagram* shown in Fig. 5.4 for two $\alpha$-particles and valence neutrons. The intrinsic states of the free centres are split in energy into orbitals defined by quantum numbers of molecular symmetries: the projections of the orbital angular momentum on the symmetry axis, the $\sigma$ and $\pi$ orbits, the projection $K$ of the spin, the parity and the specific $g$ and $u$ properties for molecules with identical cores [11]. Neutrons can be placed in these orbitals with two parities (+, −), and two values of the K-quantum numbers, $K = 3/2$, and $K = 1/2$, for $l = 1$, respectively. We use the designations like in atomic molecules: the $\sigma$ and $\pi$ orbits for the neutron orbitals, with quantum numbers $m_l = 0$ ($\sigma$), the projection of the orbital angular momentum, and $\pi$ for $m_l = 1$. These orbitals have very different spacial distributions. The $\pi_{3/2}(g)$ orbital has a density distribution outside of the symmetry axis, its driving potential gains energy towards smaller distances. A weak attraction at larger distances turns there into a repulsion, which adds to the $\alpha$-$\alpha$-potential at a distance of 3.0 fm (as shown in Fig. 5.2), which helps to stabilise the $^9$Be-molecule.

From the correlation diagram we can predict the spin and parity sequence of the states in $^9$Be, i.e. the relative positions in excitation energy of the various states at the distance where the minimum of the potential between the two $\alpha$-particles occurs: the $K = 3/2^-$ state, the ground state of $^9$Be, with a driving potential to small distances. With the $\sigma_{1/2}(g)$-orbital the next state in $^9$Be, is predicted to be the $K = 1/2^+$ state, this results in larger distances between the $\alpha$-particles, and larger moments of inertia $\theta$ for the rotational bands, where a $\sigma$-orbit is involved: the $K = 1/2^+$-band in $^9$Be, the for the second $J = 0^+_2$ band in $^{10}$Be, with a $(\sigma)^2$ configuration. For $^{11}$Be the ground state has the $(K = 3/2^-)^2$-configuration. Another very pronounced

**Fig. 5.4** The correlation diagram for two-centre orbitals as function of $r$, the distance between the centres. The basis states in $^5$He are the two orientations of the $p_{3/2}$ states, leading to the formation of four (4) molecular orbitals with the quantum numbers $K$, parity, and *gerade*/*ungerade* as indicated. In the correlation diagram the positions of the valence neutrons for the $K = 3/2$ band in $^{11}$Be, starting from an excited state are shown. The rotational band of this configuration is shown in Fig. 5.6. With the single centre $p_{3/2}$ configurations the possible molecular orbitals are the $\sigma$ and $\pi$ orbits, with spatial distributions as illustrated in the lower part of the figure

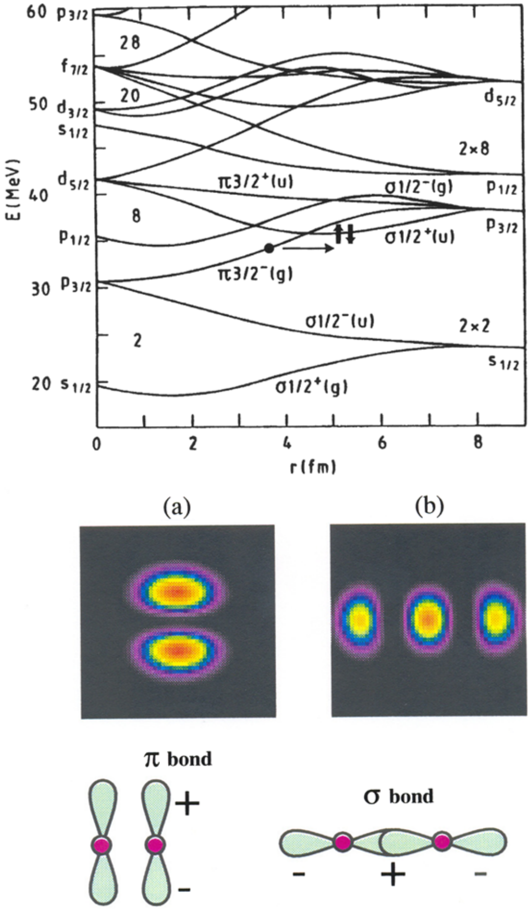

sequence of rotational states with $K = 3/2^-$ are observed experimentally in a two neutron transfer reaction, populating an excited state (Fig. 5.6) in $^{11}$Be with a $\pi \times (\sigma)^2$ configuration (see Fig. 5.4). The $K = 1/2^+$ band in $^{11}$Be again shows a distinct Coriolis decoupling effect (like the $K = 1/2^+$ in $^9$Be). These facts point to the realisation of the molecular $\sigma$-orbitals for the valence neutrons. A similar feature is observed for the $K = 1/2^+$ band in $^{21}$Ne (Fig. 5.26), with one valence neutron.

The excitation energies $E_{ex}(J)$ of the states in the rotational bands (as a function of their spin), including the Coriolis decoupling effect, described with the parameter $(a)$, are given by:

$$E_{ex}(J) = E_0 + \frac{\hbar^2}{2\theta}[J(J+1) + (-)^{J+1/2}a(J+1/2)], \tag{5.1}$$

where $\theta$ is the moment of inertia.

All states in $^9$Be and $^{10}$Be can be explained as covalently bound molecular states or their rotational excitations. This statement about the number of molecular cluster states relative to the number of “*normal*” shell model states (usually spheri-

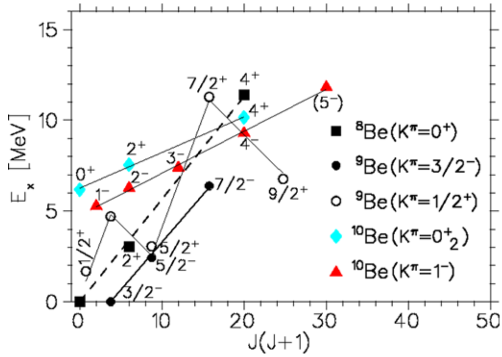

**Fig. 5.5** The rotational bands of the isotopes $^{8,9,10}$Be. For $^9$Be and $^8$Be the same slope is observed, defined by the moment of inertia, $\theta$. Note the strong *zig-zag* dependence for the $K = 1/2^+$ band in $^9$Be. This is due to the Coriolis-decoupling effect, which is observed in $K = 1/2$ bands, in our case it is given by the $\sigma$-configurations of the odd valence neutron

cal or moderately deformed), is an important issue for the concept of a *complete spectroscopy* of light nuclei. This concept has been used in finding the cluster states, e.g. in carbon isotopes, $^{13,14}$C, which can have oblate or prolate deformation [39, 40]. Therefore an important indication for the formation of dimers and other molecular cluster states is the observation of the associated rotational bands and their large moments of inertia.

Recent experimental results [41, 42] have definitely established the existence of molecular rotational bands in $^{10}$Be (alternatively described as $(sd)^2$ states in the shell model picture [43, 44]). The states in the $K = 0_2^+$-band ($0^+$ at $E_x = 6.18$ MeV, $2^+$ at $E_x = 7.54$ MeV and $4^+$ at $E_x = 10.15$ MeV) were found to show extreme deformation, one of the largest among all known states of all nuclei (and much larger than the deformation of the classic cluster example, ground state of $^8$Be). Due to that fact, it would be highly interesting to also identify the rotational bands of the analogue $T = 1$ states in other $A = 10$ nuclei, *i.e.* in $^{10}$B and in $^{10}$C. Some experimental results in that direction have recently been published [45–48], but a clear picture is yet to be found.

The $^{10}$C nucleus, which has been studied by Curtis et al. [49, 50], is a particular case because it has unbound sub-systems. It is Borromean nucleus, however, with a four-body configuration $\alpha + \alpha + p + p$. Several states in $^{10}$C have been seen in different experiments [46, 49, 50], but their properties (spin, parity and decay widths) still has to be established.

For $^{10}$B, results are obtained for different decay modes of the excited states, including proton, deuteron and $\alpha$-particle emission. The $\alpha$-decay is particularly interesting, when it leads to the excited states of $^6$Li, especially the second one (with $S = 0$ and $T = 1$ at $E_x = 3.56$ MeV ($^6$Li$^{**}$)), which is an analogue to the $^6$He ground state. The $^{10}$B states analogue to the two lowest members of the $^{10}$Be molecular band are for long time known to be the ones at $E_x = 7.56$ and 8.89 MeV. The position of the $4^+$ state is crucial for a complete understanding of the molecular configurations in $A = 10$ nuclei, so several experiments have been performed to identify it. Results from the $^{11}$B($^3$He, $^6$Li$^{**}\alpha$)$^4$He measurements [45, 48] suggest that the $4^+$ state is at $E_x \approx 11.5$ MeV. It is clear that further work (*i.e.* clear spin and parity assignments) is definitely needed, especially because the analogue of the 9.56 MeV $2^+$ state in $^{10}$Be is also expected in this energy region.

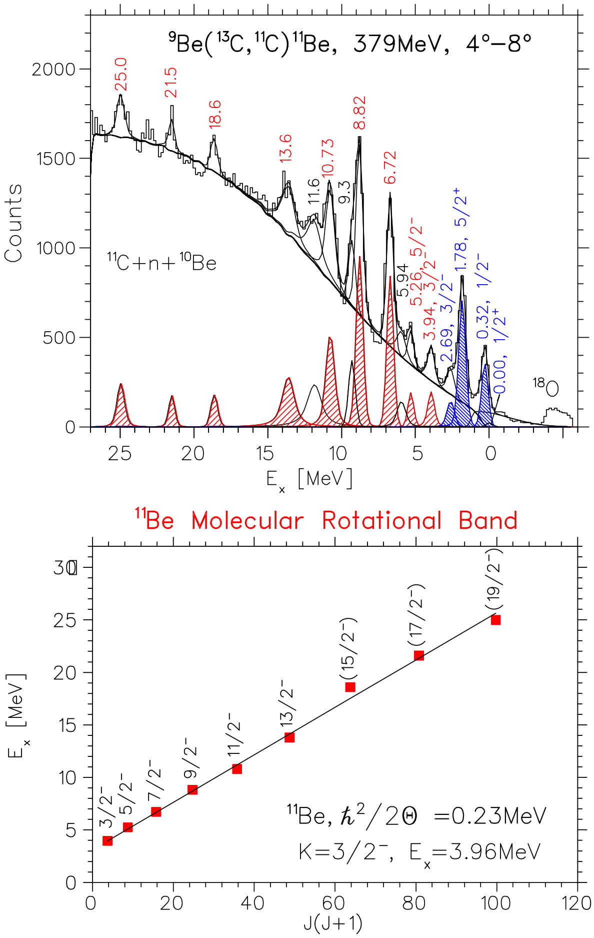

**Fig. 5.6** The $^{11}$Be rotational band with $K = 3/2^-$. For the slope defined by the moment of inertia, $\theta$, we find the same value as for the second $0_2^+$ in $^{10}$Be. Here 2 neutrons are in a $\sigma^2$-configuration (see Fig. 5.4) and one neutron in a $\pi$-orbit. The known $K = 1/2^+$ band has the same strong *zig-zag* dependence as the $K = 1/2^+$ band in $^9$Be, due to the Coriolis-decoupling effect

The structure of $^{11}$Be also reflects our considerations of molecular orbitals. In particular, the gs-state band ($K = 1/2^+$), has *two* neutrons in the lowest orbital, *i.e.* the $\pi$ orbitals with $(K = 3/2^-)^2$ and *one* neutron in the $K = 1/2^+$ orbit. In contrast the pronounced rotational band starting at $E_{ex} = 3.955$ MeV with $K = 3/2^-$, has *two* neutrons in the $(\sigma)^2$ and *one* neutron in the $\pi$ orbitals; the corresponding configuration is shown in the correlation diagram in Fig. 5.4. There we show the configuration for the three neutrons, $K = 3/2^- \times (\sigma)^2$—the corresponding band reaches up to $J = 13/2$ and it has a large moment of inertia due to the $(\sigma)^2$ configuration of the two neutrons that push the two $\alpha$-particles apart (Fig. 5.6). This band is very strongly populated in various 2-neutron transfer reactions on $^9$Be-targets (Refs. [51–53] and recently has also been observed in Ref. [54]). A feature connected to the orbital picture, the Coriolis decoupling effect is illustrated in the cluster model calculations by Descouvement [55], shown in Fig. 5.7. In this work the rotational bands in $^{9-10}$Be are also predicted with the features discussed above.

**Fig. 5.7** The predicted rotational band for the $K = 1/2^+$ in $^{11}$Be, for the configuration with two neutrons in $\pi$-orbitals and one in the $\sigma$-orbital, showing the pronounced Coriolis decoupling effect. Taken from Ref. [55]

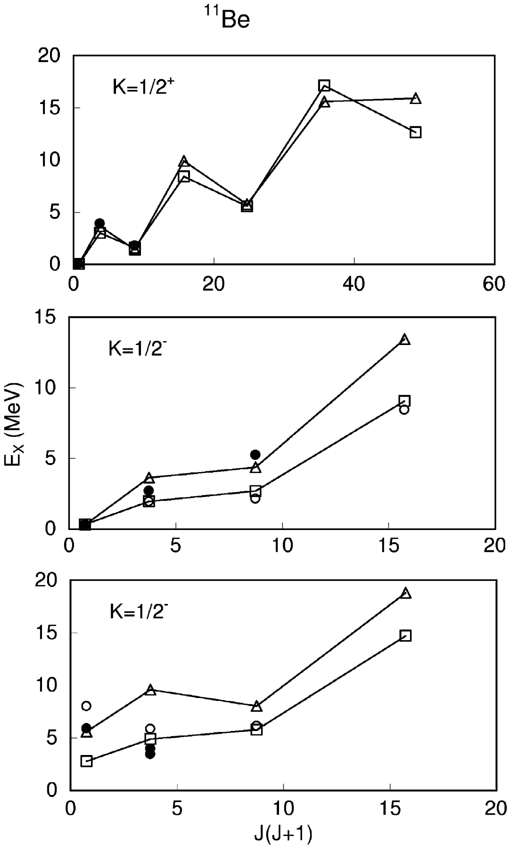

We can summarise our knowledge on the covalent bonds in the Be-isotopes by showing the distance between the $\alpha$-particles as obtained from AMD calculations by Kanada-En'yo [56, 57] (Fig. 5.8). For the two $J = 0^+$ rotational bands in $^{10}$Be, two different moments of inertia are observed, again due the configurations with either $(\sigma)^2$ or $(\pi)^2$ configurations.

The spectroscopy of $^{9-12}$Be is still far from being finished—e.g. different theoretical calculations for $^{10}$Be predict further states of the "atomic" $^6\text{He} + \alpha$ character [58], the $\alpha + t + t$ structure [59], gas-like structures with configurations as $\alpha + \alpha +$ dineutron or $^6\text{He} + \alpha$, having extremely extended shapes with an $\alpha$-clustering [60]. None of these predicted states have been experimentally seen so far, so further efforts are needed to check their existence. For the $^{12}$Be-nucleus (with 4 valence neutrons) neutron transfer reactions have been studied by Bohlen et al. [61] at high beam energies; the $2n$-transfer on $^{10}$Be was compared to the $3n$-transfer on $^9$Be. In the $^{10}$Be($^{14}$N,$^{12}$N) reaction only low lying states are populated, whereas in the $^9$Be($^{12}$C,$^9$C) reaction, states up to 16.7 MeV have been observed. This indicates that the bands in $^{12}$Be do not have a large parentage in the $^{10}$Be-ground state, which is known to have a relatively small deformation.

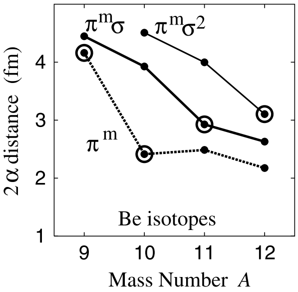

**Fig. 5.8** The distance between the two $\alpha$-clusters in the different molecular bands based on $\sigma$- or $\pi$-orbitals of the valence neutrons in the beryllium isotopes of $^{10-12}$Be, as obtained in the AMD calculations by Kanada-En'yo [57]. For valence neutrons in $\sigma$-orbitals the distances become larger, see Fig. 5.5 for the band with $K = 0_2^+$. For $\sigma$ orbitals the densities of the neutrons are concentrated on the symmetry axis (Fig. 5.4)

Furthermore, we should mention the different studies concerning the isotopes $^{13}$Be (e.g. [62]) and $^{14}$Be (e.g. [63]). Their properties are not directly concerned with molecular orbital structure, their deformation is lower and many states of (deformed) shell model nature appear. The breaking of $N = 8$ magicity is also suggested for $^{13}$Be [64].

### 5.1.3 *The Antisymmetrized Molecular Dynamics (AMD) for the Exotic Light Nuclei*

For many very remarkable results of "*model independent*" calculations in the AMD (Antisymmetrised Molecular Dynamics) framework [25], one should look to the Chap. 4 of Vol. 1 of the Lecture Notes on "Clusters in Nuclei" by Y. Kanada-En'yo and M. Kimura [21]. Their contribution contains the most complete list of references also on the molecular orbital (MO) interpretation. The emphasis in the present lecture is the identification of the covalent structures in the neutron-rich light nuclei. Actually the AMD calculations, which give density distributions of the valence neutrons as well as of the cores, gives strong support of the MO-approach. Thus the work of Horiuchi and Kanada-En'yo supported (Fig. 5.9) already in 1997 the molecular orbital structure [23, 56], proposed for the Be-isotopes by von Oertzen in 1996 [16–18], which at this time has been met with extreme criticism by the referees.

We use the AMD-results as illustrations of the concepts of covalent binding described in the previous section. Reference [21] gives a large number of illustrations (figures with density distributions) which show the wide range of nuclei for which the MO applies. A certain number of nucleons are confined in a volume with a positive kinetic energy, basic concepts like the Schrödinger equation and the Pauli principle are introduced. An effective nucleon-nucleon interaction has to be chosen, at this stage the "case" of a model can be defined by the choice of an effective $N$-$N$

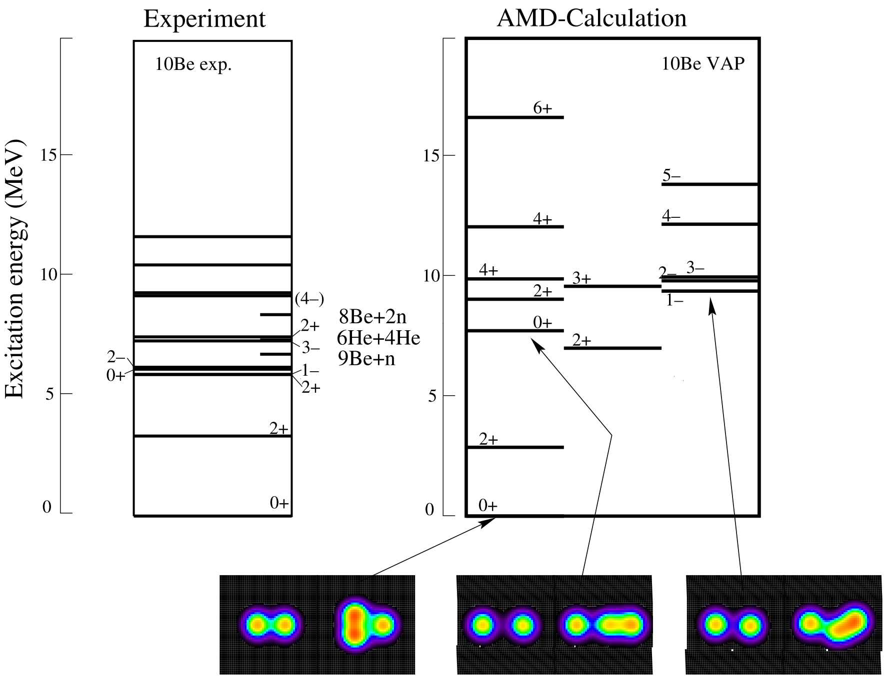

**Fig. 5.9** Scheme of states in $^{10}$Be with the density distributions from AMD-calculations [56]. The excited $0^+$—state is a $\sigma^2$-configuration the ground state, $0^+$, is a $\pi^2$-configuration. For these states the AMD calculation gives the intrinsic densities for the nucleons. In the panels in the *lower part*, both the densities of protons and neutrons are shown separately. The protons, the *left side* in the panels, represent the $\alpha$-particles. The neutrons (including neutrons in the $\alpha$-particles) are shown in the *right side* of the coloured panels. For the $1^-$-state a mixed configuration $\sigma \times \pi$ appears, which causes the distorted density and the $K = 1^-$ rotational band (see Refs. [18, 56])

interaction. A Slater-determinant is obtained from which various states (configurations) can be obtained by projections. In fact in a related method, the Fermionic molecular dynamics (FMD), by Feldmeier, Neff et al. [26, 27], a basic $N$-$N$ interaction is chosen, which contains the non-local and the tensor components, making the calculations quite difficult. In the latter method the well known cluster states in light nuclei are also reproduced, like the second $0^+$ in $^{12}$C ("Hoyle state").

In the AMD model [24] a cooling method is applied and projecting on spin, ground states and excited states of nuclei and their rotational bands are obtained. By repeating this process a large variety of intrinsic nuclear states and their rotational bands can be described. In this AMD approach during the cooling process at first a certain number of states with $\alpha$-clusters are obtained (see also the discussion of $\alpha$-particle condensed states Vol. 1 [65]).

With extra valence neutrons, before the formation of the higher density states, the extra neutrons are automatically placed in molecular orbitals, which correspond to the configurations described in textbooks of quantum chemistry [66]. Finally the

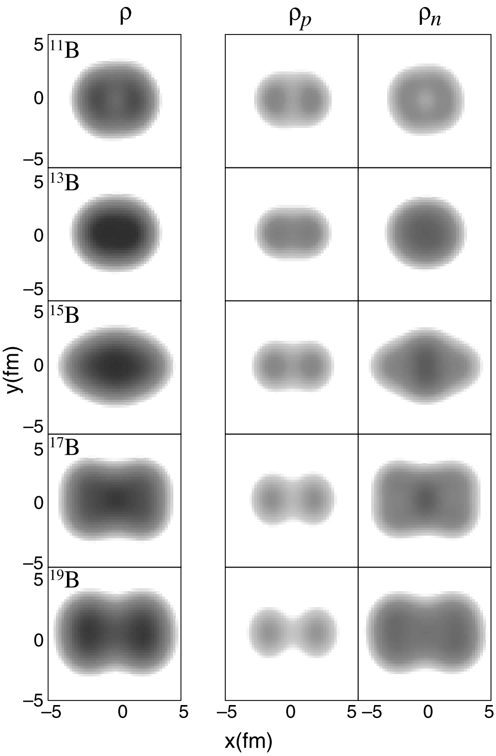

**Fig. 5.10** Densities of isotopes of boron $^{11-19}$B obtained in the AMD calculations (from Ref. [67]). Note the increasing deformation with the increase of the neutron excess

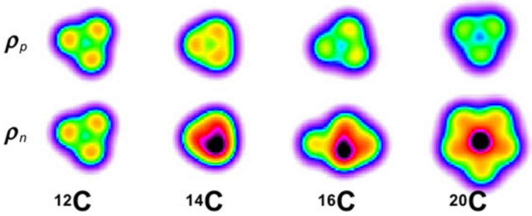

**Fig. 5.11** Intrinsic densities of carbon isotopes $^{12-19}$C obtained in the AMD calculations by Kanada-En'yo et al. [67]

ground states of a variety of nuclei, with different ratios of $N/Z$ [25] can be reproduced.

Results obtained by AMD for the very neutron-rich isotopes of carbon and boron are especially interesting. We take as an example the result of the AMD calculations for Boron isotopes, which are shown in Fig. 5.10. The property of the $N$-$N$ interaction to favour the stronger interactions between neutrons and protons induces large deformations, and clustering with prolate and oblate shapes are predicted. These allow for the maximum of interactions of the excess neutrons with the protons residing in the $\alpha$-particles. This effect can be clearly seen in the nucleon densities in many cases, e.g. also in carbon isotopes obtained with the AMD-calculations, shown in Fig. 5.11.

Quite clear structures to be associated with clusters and valence neutrons are observed in neutron rich isotopes of carbon, some of the shapes remain *oblate*. Examples of intrinsic shapes obtained from AMD calculation [67] are shown in Fig. 5.11. Molecule-like structure with covalent neutrons where also suggested by AMD calculation for fluorine isotopes $^{21}$F and $^{23}$F [68].

## 5.2 Molecular and Cluster States in Carbon Isotopes $^{12-16}$C

### *5.2.1* $^{12}$C *and the Second* $0_2^+$ *State, the Hoyle State*

The $^{12}$C is a very interesting nucleus—since a long time this isotope played an important role in the studies of nuclear resonances in $N = Z$ nuclei [1]. In various cluster models with $\alpha$-clusters and in AMD calculations [25], the ground state and the excited states are well described. Of particular interest is the $0_2^+$ state, which in the AMD calculation appears as a loose assembly with no definite geometry with free $\alpha$-particles. The structure of this state and its possible rotational excitations has been under intensive study (see e.g. Refs. [69–73] for recent results), because it plays a decisive role in the synthesis of $^{12}$C from three $\alpha$'s in stars [74]. Three alpha particles get captured sequentially populating the $0_2^+$ state at 7.65 MeV, which decays through $\gamma$-transitions to the $2^+$ at 4.44 MeV and subsequently to the ground state.

The inelastic electron scattering on a $^{12}$C-target has been studied repeatedly. The form factor for the transition to the excited state at 7.65 MeV, the *Hoyle State*, with $J^\pi = 0^+$ is thus well known, see Refs. [75, 76] and earlier references therein. The question if there is a rotational band based on this state with a sequence of states $0_2^+$, $2_2^+$, $4_2^+$ is quite important, because the moment of inertia underlying such a band can give information on it's internal structure, and its radial extension. Experiments with this issue have been followed over the last ten years by Freer et al. [69, 72, 73]. We will later also refer to this result for the structure of $^{13}$C.

For the heavier carbon isotopes shell model states appear; e.g. those for $^{14}$C are listed in Ref. [40]. The more loosely bound molecular structures to be expected here are stabilised by additional valence neutrons, a large variety of molecular structures with oblate and prolate shapes (also chains) appear, which are connected to $\alpha$-clusters and covalent neutron orbitals [40].

There are extensive studies of inelastic electron and hadron scattering on $^{12}$C, with the population, via an (E0)-transition, of the $0_2^+$ at 7.65 MeV, the (*Hoyle state*), using a large variety of projectiles. The elastic and inelastic $\alpha$-scattering at energies between 104 MeV and 240 MeV has recently been analysed with microscopic transition densities and the double folding approach for the scattering potential [77], and with a diffraction model [78]. The angular distributions exhibit at smaller angles strong diffraction patterns, and partially also a refractive maximum at larger angles.

One feature, the Blair phase rule [76], describes the relative position of the maxima (and minima) in elastic and inelastic scattering in the diffractive patterns at

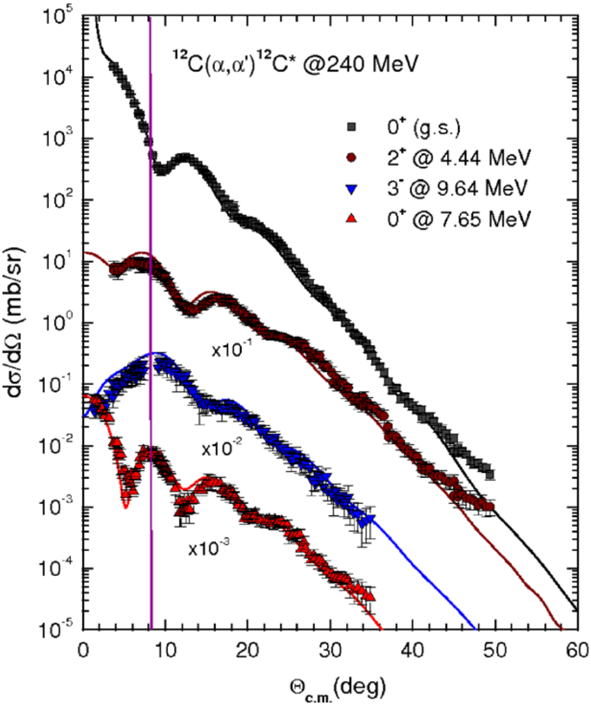

**Fig. 5.12** Inelastic scattering of $\alpha$-particles on $^{12}$C, showing a diffractive scattering pattern. There is a shift from the predicted position of the structures for the second $0_2^+$ due to it's larger radial extension (larger by 10 %)

forward angles. The latter depend on the radial extension. The structures of the elastic scattering, e.g. the minimum in the elastic channel and the maximum (Fig. 5.12) in inelastic scattering for ($L = 0$) transitions are exactly *out of phase if no parity change has occurred*. The position of the diffractive minima depend on the radial extension of the excited states. The result at an incident energy of 240 MeV is shown in Fig. 5.12, the angular distributions show pronounced diffraction structures. Indeed the diffractive pattern for the inelastic excitation to the $2^+$ state at 4.43 MeV is clearly out of phase with that for the ground state. For the $0_2^+$ state at 7.65 MeV the diffractive pattern is more pronounced and is shifted by approximately 2 degrees to forward angles relative to the elastic scattering, indicating a larger radius of the excited state.

The calculations, which were performed with the double folding model for the elastic scattering potential as well as for the transition densities [76], are also shown in Fig. 5.12. The other inelastic transitions have been calculated, and the data are perfectly reproduced due to the choice of the transition densities obtained in the folding model. The analysis with a diffraction model [78] of such data gives the systematics of the diffraction radius over a large energy range. The result gives a 10 % larger radius for the $0_2^+$ state as compared to the ground state. This approach can be used to identify the corresponding excited $0_i^+$ states which have large radial extensions.

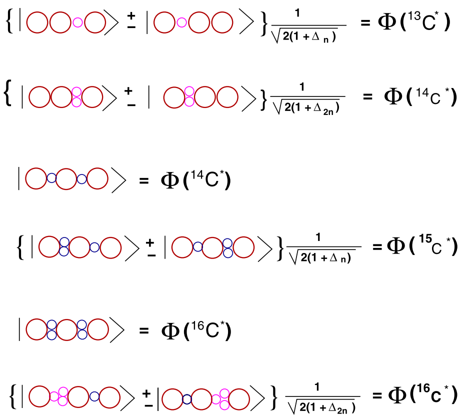

**Fig. 5.13** Intrinsic structures of strongly deformed neutron-rich isotopes of carbon (chains) with their projections on parity. For $^{13}$C only one configuration appears, for $^{14}$C and $^{16}$C symmetric and asymmetric intrinsic shapes are possible

### 5.2.2 *Parity Splitting of Rotational Cluster-Bands in Carbon Isotopes*

With increasing numbers of constituent clusters, larger extensions in molecules are created. There the symmetry properties of the geometrical arrangements of the centres, and cases with different clusters, have to be considered. In the isotopes of carbon $^{13-16}$C oblate and prolate shapes appear (see Fig. 5.13).

For three $\alpha$-particles in a linear arrangement, the neutrons may not be shared with equal amplitude at the different centres. Further for the isotopes of oxygen $^{16-22}$O, the combination of clusters of different size appear: The molecular state and their bands consist of two different clusters, and of different size. For example for $^{18}$O we have as a possible structure: ($^{14}\mathrm{C} \otimes \alpha$). Such intrinsically asymmetric molecular structures usually correspond to nuclei with octupole deformations [79, 80]. These are nuclei with intrinsic shapes of undefined symmetry (parity). The definite parity is obtained by projection of the intrinsic shapes on good parity, which leads to specific properties of the rotational bands. In the book of Herzberg [66], at the very beginning of our knowledge of structures in atomic molecules, the nature of the rotational spectra of asymmetric molecular structures is reviewed (in 1950!).

The most important aspect for an intrinsically asymmetric structure, is the broken intrinsic reflection symmetry. Such systems have no well defined parity. The parity projection, which is obtained from the linear combinations of two reflected states using a positive and a negative sign, respectively, leads to a parity-splitting of the rotational bands. The feature of symmetry breaking has been explored in nuclear physics by Bohr and Mottelson [80], where this phenomenon appears with the odd multipoles of deformation, in particular with the octupole deformation. The various manifestations in nuclear structure have been discussed in numerous reviews [81–83].

For reflection-asymmetric but axial-symmetric systems the signs in the linear combinations correspond to the *signature, r*, defined as the eigenvalues of the *R* operator. $R$ describes a rotation by 180° about an axis perpendicular to the symmetry axis [80, 81]:

$$r = e^{-i\pi J} \tag{5.2}$$

Here $J$ is the spin and $\pi$ the intrinsic parity. For systems with intrinsic octupole-deformed shapes and an even number of nucleons, a parity doublet appears [82] with bands for $r = \pm 1$ and an energy splitting between them:

$$r = +1, \qquad J^\pi = 0^+, 2^+, 4^+, \ldots \tag{5.3}$$

$$r = -1, \qquad J^\pi = 1^-, 3^-, 5^-, \ldots \tag{5.4}$$

This feature allows clear predictions for the states of parity doublets, if the splitting energy is known. Their properties of broken symmetry give rise to the energy splitting of the rotational bands into the "parity inversion doublets".

For spin $J = 0$ in the ground state we must identify for the molecules, formed with two clusters of different size, two rotational bands (the parity inversion doublet) with $K = 0^+$ and $K = 0^-$, which originate from the same intrinsic structure. The latter starts with $J = 1^-$, for clusters with spin zero, like in $^{20}$Ne.

As an example for the $^{14}\mathrm{C} \otimes \alpha$ cluster configuration in $^{18}$O with $\phi_r = |^{14}\mathrm{C} \otimes \alpha\rangle$ ($\alpha$-cluster right), $\phi_l = |\alpha \otimes ^{14}\mathrm{C}\rangle$ ($\alpha$-cluster left), and $N$ as a normalisation factor, the linear combination can be written as follows:

$$\Phi^\pm = N(\phi_r \pm \phi_l)$$

The wave functions $\Phi^+$ and $\Phi^-$

$$\left|\Phi^\pm\right\rangle = \frac{1}{\sqrt{2(1 \pm \langle\phi_r|\phi_l\rangle)}}(|\phi_r\rangle \pm |\phi_l\rangle) \tag{5.5}$$

have eigenvalues

$$E^\pm = \frac{1}{(1 \pm \Delta)} \ (\bar{E} \pm E_\Delta) \tag{5.6}$$

with $\Delta = \langle\phi_r|\phi_l\rangle$ the non-orthogonality, $\bar{E} = 1/2(E_r + E_l)$ and $E_\Delta = \langle\phi_r|H|\phi_l\rangle$. For $\Delta \ll 1$, we have in first order the following energies:

$$E^\pm \approx \bar{E} \pm \delta_E \tag{5.7}$$

with

$$\delta_E = E_\Delta - \bar{E} \cdot \Delta. \tag{5.8}$$

The energy splitting amounts to $E^+ - E^- = 2 \cdot \delta_E$ (see Eq. (5.7)). The value of this energy splitting reflects the intrinsic asymmetric structure, it is the most important parameter, it measures the probability of tunnelling between the two shapes through the central cluster. In heavy nuclei many cases of intrinsic octupoles have been studied [83], with many related parity doublet bands.

In Fig. 5.14 we illustrate the splitting of the known parity doublet bands for the $\alpha$-cluster structures $^{12}\mathrm{C} \otimes \alpha$ of $^{16}$O and for $^{16}\mathrm{O} \otimes \alpha$ of $^{20}$Ne. We will come back to these structures in connection with the discussion of the isotopes of oxygen, $^{16-20}$O in Sect. 5.4.2. For the carbon isotopes we can expect parity inversion doublets with a variety of prolate shapes which are summarised in Fig. 5.13.

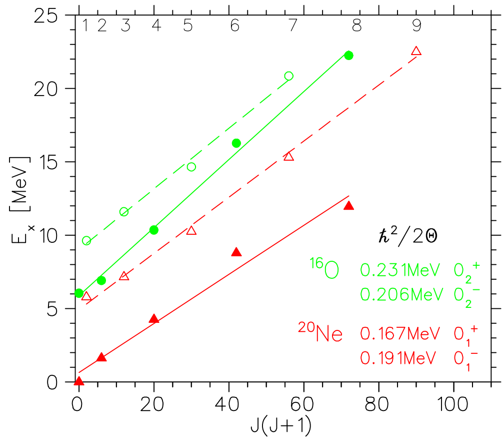

**Fig. 5.14** The $\alpha$-cluster-bands of positive and negative parity in $^{16}$O (*circles*) [84] in comparison with the structure in $^{20}$Ne (*triangles*) [28, 29, 85]

### *5.2.3 Valence Neutrons and the Structures in $^{13-14}$C*

For these isotopes prolate (chains) and oblate (triangular, pancakes) shapes are expected The method of complete spectroscopy has been applied in the case of $^{13}$C. Identifying and "removing" the shell model states [39] we are left with many states, whose spins and parities are only partially known from the literature. These states must be arranged into prolate shapes, which are chain-states as proposed in 1997 by von Oertzen [17]. An important issue, which has been the subject of intensive studies, is the question of the analog of the *Hoyle* state in the isotopes of carbon, $^{13}$C and $^{14}$C.

The inelastic scattering on $^{13}$C has been studied with high energy $\alpha$-particles ($E_{lab}$) by Sasamoto et al. [86], and a high energy resolution with a magnetic spectrometer. It is found that at excitation energies of 10 MeV, two states with $J = 1/2^-$ show a large monopole strength for the excitation from the $J = 1/2^-$ ground state. The large E0-strength points to large radial extension, as in the corresponding state in $^{12}$C. In a study of all states in $^{13}$C states, they found that the states at 8.86 MeV ($J = 1/2^-$) and at 10.96 MeV ($J = 1/2^+$) should be based on the $J = 0_2^+$ at 7.65 MeV *Hoyle*-state (see also [39]).

The carbon isotopes are good examples for the co-existence of different shapes based on the shell model and the cluster-model (e.g. appearance of cluster state in $^{13}$C is discussed within a microscopic model in Ref. [87]). For the latter oblate and prolate configurations (chain states) have been observed. For prolate shapes in $^{14}$C, a structure like $^{10}$Be × $\alpha$ produces parity doublets, due to the intrinsic reflection asymmetry, shown in Fig. 5.17. Simultaneously in $^{14}$C a band based on the intrinsic triangular shape with a band head with spin, parity $3^-$, is observed [40]. For the chain states the various symmetries of the molecules are of great importance. In fact because of these we anticipate for $^{14}$C chain states, which have symmetric shapes and others which will have parity inversion doublets.

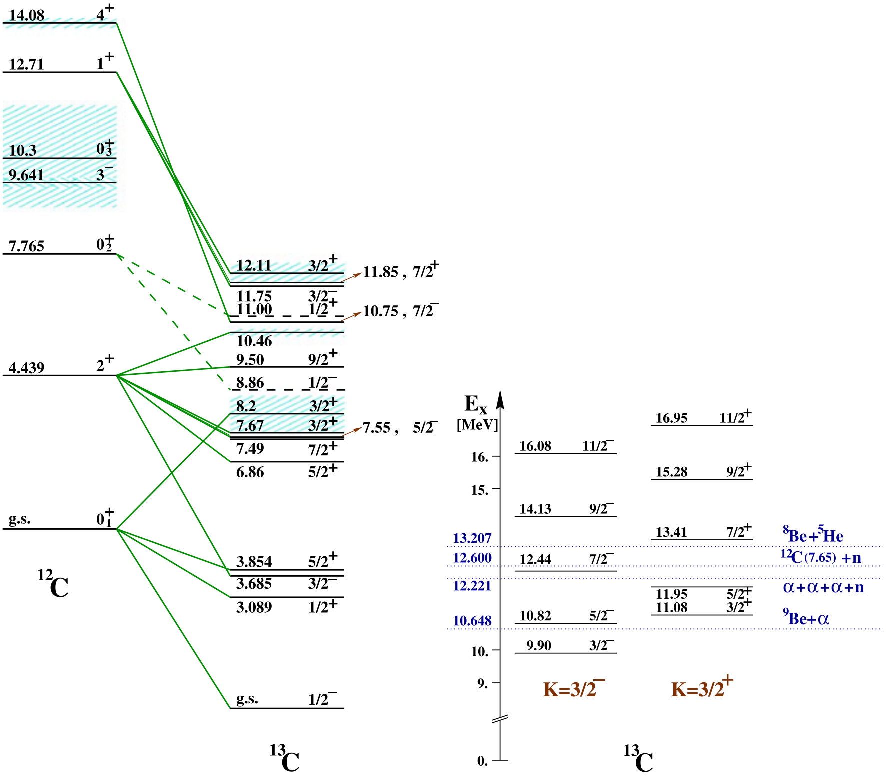

**Fig. 5.15** Illustration of the shell model states in $^{13}$C connected to the $\alpha$-particle clusters and oblate states in $^{13}$C. *Right side*: the states observed as rotational bands with prolate intrinsic shapes. These bands are parity inversion doublets, they start with states with excitation energies in the vicinity of the $\alpha$-particle thresholds. The energies of various thresholds are indicated

Recent experimental studies of the $^{13,14}$C spectroscopy are done either by investigating the decay modes [88, 89], or through the resonant elastic scattering [90]. The latter have been performed for $^{13}$C using the thick-target approach with a $^4$He gas volume and a large-area silicon strip detector; $^9$Be beam energies in the range 12 to 21.4 MeV were used to measure the $^{13}$C excitation energy spectrum between 13.2 and 16.2 MeV. An R-matrix analysis has been performed to characterise the spins and widths of $^{13}$C resonances, some of which agree with the proposed bands in Ref. [39], while some don't. Further experimental work is needed to clarify the issue—in particular, one should try to identify $^{13}$C states decaying to the Hoyle state in $^{12}$C by neutron emission. Such study has been performed for the $^{13}$N nucleus [91] and several states were found to have a significant branching ratio for decay by proton emission to the Hoyle state.

For the oblate shapes the most remarkable structure is the triangular shape (see Fig. 5.16, where the two valence neutrons reside between the three clusters [92]. Such states are also obtained from AMD calculations.

**Fig. 5.16** The density of oblate excited states of the carbon $^{14}$C isotope obtained in the AMD calculations by Itagaki [92]. The rotational bands based on excited states in (e.g. the $^{14}$C $K = 3^-$ band) are shown in Fig. 5.15

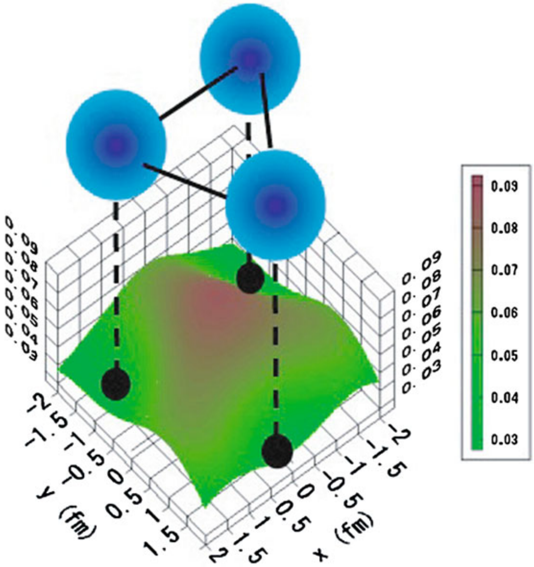

The chain states are among the particular prolate shapes which, however, are found to be unstable against the bending mode [93]. Recent calculations [94] for the $^{16}$C chain states, which are based on a $^{10}$Be-core, show that with the increase of the number of valence neutrons linear chains, which are stable against the bending mode should be found at higher excitation energies. For chain states in the isotopes of carbon with more additional neutrons, a higher stability is expected. Recent calculations using the Hartree-Fock scheme for $^{12}$C, $^{16}$C, and $^{20}$C, have been studied by Maruhn et al. [94, 95]. They show, that with a mean field with Skyrme interactions clustering appears as well without any a priori model assumptions. The chain configuration are stabilised against the bending mode and that life-times of such states can be long enough to allow the observation of resonances (with a width of 100 keV) for decay to oblate states.

Some cluster states in $^{13-14}$C must also appear as parity doublets, see Fig. 5.15. Be-$\alpha$ correlations in the linear-chain structure of carbon isotopes were also studied by Suhara and Kanada-En'yo [96]. In $^{13}$C, linear chain configurations may also be observed with parity inversion effects [97]; such structure has also been studied by Furutachi and Kimura within a microscopic $3\alpha + n$ model [98].

A rather detailed experimental search for high-lying states in $^{16}$C [99] and $^{17}$C [100] has been performed recently up to excitation energies of $\approx$16 MeV, but clear identification of cluster and molecular states would be possible only after spin/parity assignment to those states, as well as studies of their decay paths.

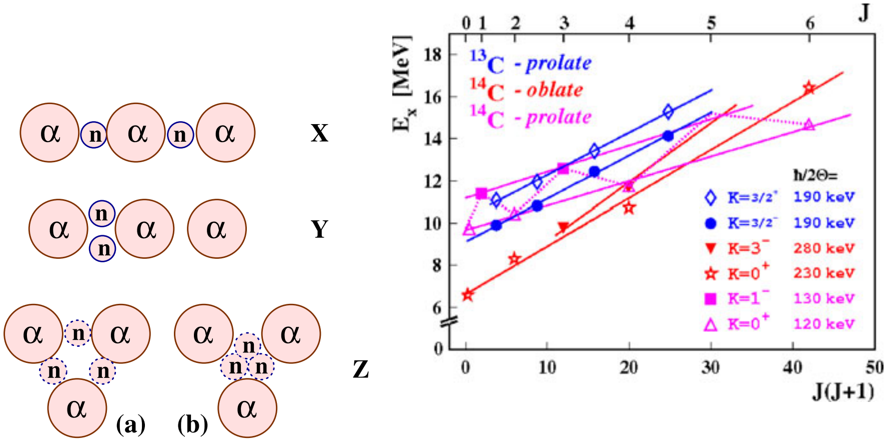

**Fig. 5.17** *Left side*: Schematic illustration of the intrinsic symmetry of states in $^{14}$C connected to $\alpha$ and $^{9-10}$Be substructure. The intrinsic shapes, denoted as $X$, are completely symmetric, for $Y$ with intrinsic asymmetry, a parity doublet must be observed. These bands have distinctly different moments of inertia, as seen on the *right side*. Here the energy systematics of excited states in rotational bands, as extracted from various experiments, are shown as function of their spin $J(J+1)$

## 5.3 Intrinsically Reflection Asymmetric Molecules and Parity Doublets

We have already introduced the concept of intrinsically asymmetric shapes in Sect. 5.2.2, with the structure of the carbon isotopes $^{13,14}$C [39, 40]. The most evident case of a molecular structure with two different clusters are the basic structures of $^{20}$Ne. For $^{20}$Ne the appearance of low lying negative parity states has been a disturbing feature in the shell model approach, because the nucleons should be mainly in $(s,d)$-configurations. Horiuchi and Ikeda [28, 29] have already in 1968 shown, that there are two molecular cluster bands (parity inversion doublets) with opposite parity. In the cluster model this fact is due to the existence of the clusters $^4$He and the $^{16}$O. They are forming the parity inversion doublet, with the quantum numbers $K = 0^+$ (the ground state), we have a band starting with spin $J = 0^+$ and the $K = 0^-$ band starting with a spin value of $J = 1^-$. Odd spin numbers are associated with the latter band, and the even parity bands have even spin values ($J = 0^+$) due to the constituents with spin $0^+$, namely $^{16}$O and $^4$He.

Very pronounced rotational bands with underlying cluster structure can be found in the neutron rich isotopes of oxygen see Refs. [20, 36, 37] for the most recent experiments. In order to visualise the formation of molecular cluster bands we show Fig. 5.18. Although we have a closed shell, with the $^{16}$O-cluster, we find, that excitations of this core with two protons into the sd-shell a $^4$He-cluster can be formed (see middle part of Fig. 5.18). The remaining nucleons form a strongly bound $^{14}$C-cluster. The latter has a well closed shell for neutrons and protons (better then in $^{16}$O!) and the first excited states are found at 6 MeV. This makes the nucleus $^{14}$C an equivalent cluster as the $^{16}$O nucleus, and in the extended Ikeda diagram of von

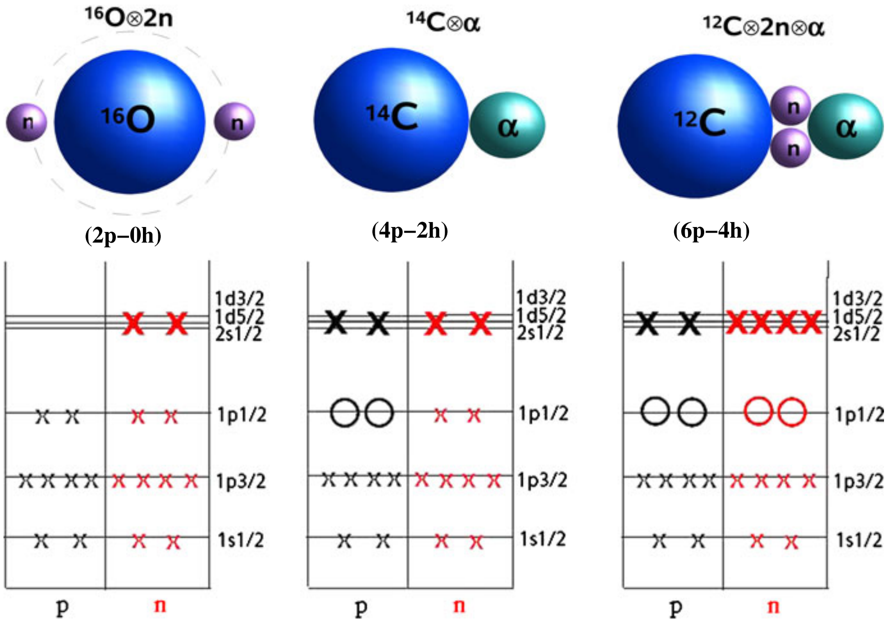

(a) (b) (c)

**Fig. 5.18** Shell model states and structure of the corresponding molecular cluster states in $^{18}$O, connected to the formation of a $^{14}$C cluster [36]. The structure to the *left can* be described by the shell model. The structure in the *middle* would correspond to an additional ($2p$-$2h$) excitation, and a ($^{14}$C + $^{4}$He)-structure is obtained in the cluster model. The structure to the *right side* is the ($6p$-$4h$) excitation in the shell model, and the ($^{14}$C + $^{4}$He) "molecular" configuration with two valence neutrons

Oertzen, the $^{14}$C-nucleus is included in the systematics of the covalently bound cluster molecules. This has been shown in Sect. 1 and with Fig. 5.1.

The different configurations of the $^{18}$O nucleus can be characterised by particle-hole excitations on a shell model basis (see Fig. 5.18). Among these pure shell model states are: (i) $^{16}\mathrm{O} \otimes 2n$, while cluster states are based on the formation of the $^{14}$C-cluster: (ii) $^{14}\mathrm{C} \otimes \alpha$, and the $^{12}$C-cluster: (iii) $^{12}\mathrm{C} \otimes 2n \otimes \alpha$. All these structures can be populated in the $^{12}\mathrm{C}(^{7}\mathrm{Li}, p)^{18}\mathrm{O}$ reaction, which has been used in an recent experiment [36]. In this case we transfer "$^{6}$He" or rather an $\alpha$-particle and 2 neutrons to the $^{12}$C target in an arbitrary sequence. The shell model states with $^{16}\mathrm{O} \otimes [\nu(sd)^2]$ are characterised by 2-**p**article-0-**h**ole ($2p$-$0h$) configurations with even parity. Another possibility is a ($2p$-$2h$) proton excitation of the $^{16}$O-core, which leads to ($4p$-$2h$)-states with $^{14}\mathrm{C} \otimes [\pi(sd)^2 \otimes \nu(sd)^2]$-structures and with a strong parentage to the $^{14}\mathrm{C} \otimes \alpha$ cluster configuration. Furthermore, we expect the molecular $^{12}\mathrm{C} \otimes 2n \otimes \alpha$-structure consisting of a $^{12}$C-core and an $\alpha$-particle, bound by two valence neutrons. In a shell model description this corresponds to a ($6p$-$4h$) configuration with 2 protons and 4 neutrons in the ($sd$) shell corresponding to a $^{12}\mathrm{C} \otimes [\pi(sd)^2 \otimes \nu(sd)^2]_\alpha \otimes \nu(2s1d)^2$ structure. An odd-particle-odd-hole excitation produces odd parity states by excitations from the $(1p)$ shell to the $(2s1d)$ shell, at a high price in excitation energy. The low values of the excitation energy for the negative parity states are due to the underlying cluster structure—they represent the parity inversion partners. The description of other cluster states need higher order $xp$-$yh$-excitations and thus are very difficult to obtain in shell model calculations.

## 5.4 Covalently Bound Molecular States in Oxygen Isotopes

### *5.4.1 $^{18}$O: Coexistence of Shell Model States and Covalently Bound Molecules*

For the $^{18}$O nucleus the literature compilation [101] shows a large variety of reaction studies, which established the level scheme and the main shell model structures. In the shell model framework deformations and rotational bands appear as multi-particle multi-hole excitations ($xp$-$yh$). These are also well known in $^{16}$O, a rotational band with ($4p$-$4h$) is well established starting at 6.05 MeV, a band with $(K = 0_2^+)$. With parity projection, with the clusters structure shown in Fig. 5.18 for $^{18}$O, we obtain inversion doublets, again two bands with quantum numbers $K = 0_2^+$ and $K = 0_2^-$. Quite important are also cluster states with a $(^{12}\text{C} + 2n + \alpha)$-configuration, here molecular orbitals for the valence neutrons appear [102], as also found in the neon isotopes with masses $(A = 21, 22)$. Configurations showing the cluster structure in $^{18}$O have been discussed previously [103, 104], emphasis was on the $(^{14}\text{C} + \alpha)$-structure with intrinsic dipole and octupole moments, and the expectation of E1-$\gamma$-transitions [105, 106]. The intrinsic reflection asymmetry of the underlying cluster structure should give rise to rotational bands as parity doublets, and with E1-$\gamma$-transitions between the two bands. Until now the complete establishment of these parity doublet bands was missing. More recently, pronounced cluster structure of rotational bands in the oxygen isotopes was obtained in the framework of Antisymmetrised Molecular Dynamics by Furutachi et al. [107]. From these calculations for $^{18}$O the bands with quantum numbers $K = 0_2^+$ and $K = 0_2^-$ are well established in their energy positions.

High resolution spectra of the ($^7$Li, $p$) reaction on $^{12}$C,$^{13}$C and $^{14}$C targets have recently been obtained with a Q3D-magnetic spectrometer, see Fig. 5.19 at the Maier-Leibniz Laboratorium at the Technical University and the LM-University in Munich. The incident energy of $^7$Li was 44 MeV, which allowed the population of states with excitation energies up to 21 MeV. Many new states have been identified in $^{18}$O [36], $^{19}$O [20] and $^{20}$O [37]. The spins of the higher lying levels have not been determined, however, the intensity of the lines as well as the ordering of the excitation energies give strong arguments for their classification in parity inversion doublets (Fig. 5.20). Of course, configuration mixing complicates the above simplified picture [108].

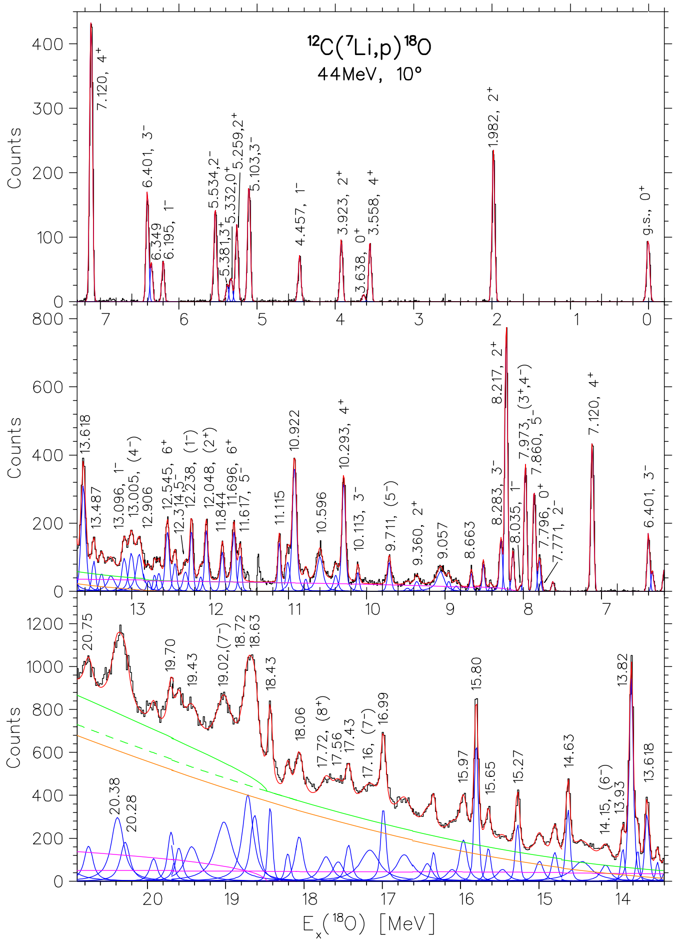

**Fig. 5.19** States in $^{18}$O populated with the $^{12}$C($^{7}$Li, $p$) reaction measured with the Q3D-spectrometer at the Tandem Laboratory in Munich [36]. States up to 21 MeV were populated. Several "molecular" bands, e.g. with two valence neutrons in the cluster model, reach to high excitation energy

### *5.4.2 Covalently Bound Molecular States in $^{19}$O and $^{20}$O*

With the described results on the structure of the $^{18}$O-isotope, we have a good basis to search for cluster bands in the heavier oxygen isotopes, $^{19,20}$O. For the extra neutron in $^{19}$O we can use the weak coupling approach [20]—we expect therefore very similar bands with the same moments of inertia as observed in $^{18}$O. We have studied the $^{13}$C($^{7}$Li, $p$)$^{19}$O reaction on a $^{13}$C-target within the same experiment at the Q3D in Munich [20], as for $^{18}$O; the obtained spectrum is shown in Fig. 5.21. Very narrow lines are again observed in this reaction, even at high excitation energies. We expect very similar intrinsic structures as in $^{18}$O, an additional neutron has to be

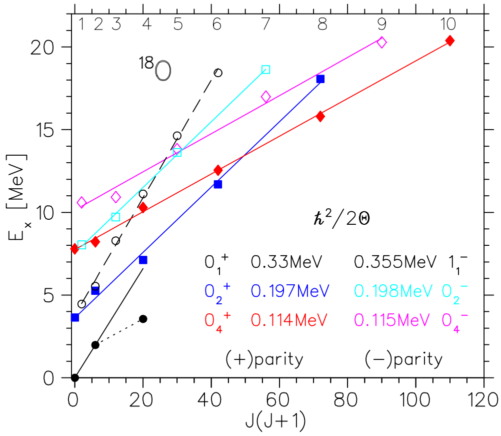

**Fig. 5.20** Overview of all bands observed in $^{18}$O. The curves are drawn to guide the eye for the slopes, which are determined by the moments of inertia $\Theta$. The first doublet of parity split bands reaching up to $8^+$ corresponds to a $^{14}\mathrm{C} \otimes \alpha$ configuration. The second parity split band, with smaller slope, i.e. a larger moment of inertia, is characterised by a $^{12}\mathrm{C} \otimes 2n \otimes \alpha$ configuration

placed in the scheme of Fig. 5.18. With this weak coupling approach bands are constructed for $K = 3/2$, with an extra $d_{3/2}$-neutron (see the case of $^{21}$Ne). The bands are expected to be parallel to the $^{18}$O-bands (Fig. 5.22). Also the energy splitting between the parity inversion partners appears to be the same. In analogy to the case of $^{21}$Ne, see Sect. 5.5.2, there should be also a $K = 1/2$-band with a strong Coriolis coupling, however, due to the lack of knowledge on spins of levels it is impossible to propose a sequence for this band.

For the isotope $^{20}$O configurations similar to $^{18}$O can be anticipated. But also states with a distinct clustering into $^{14}\mathrm{C} \otimes (2n) \otimes \alpha$, which we show in Fig. 5.23, similar to the case of $^{18}$O.

### *5.4.3 Moments of Inertia, Parity Splitting and Binding Energies of Rotational Bands in Oxygen Isotopes*

The parity splitting of the $K = 0_2^+$ band in $^{20}$O turns out to be 5.2 MeV, a value slightly larger than for $^{18}$O. For the negative parity states we have selected mainly broad states, as in the case of $^{18}$O. The experimental values of the moments of inertia $\theta$ for the proposed bands are summarised in Table 5.1.

If we assume the ($^{14}\mathrm{C} \otimes {}^{6}\mathrm{He}$) configuration for the lower lying band (as in Ref. [107]), and take the experimentally determined slope parameter (164 keV, see Table 5.1), the procedure results in a distance between the clusters of $d =$ 3.50 fm. The same procedure for the higher lying proposed rotational band (with the $^{16}\mathrm{C} \otimes {}^{4}\mathrm{He}$ configuration and $\hbar^2/2\theta = 84$ keV) gives $d = 6.35$ fm. Furutachi et al. [107] obtained in their AMD calculations for the $K = 0_2^+$ band a distance of 3.65 fm between the $^{14}$C and $^{6}$He clusters, while in the density plots they have obtained a deformation parameter of $\beta_2 intr = 0.41$. Furthermore, their density plots show also configurations which we can call "ionic" , with $\beta_2 intr = 0.61$. These correspond to a pronounced ($^{16}\mathrm{C} \otimes {}^{4}\mathrm{He}$)-structure, in particular for the negative

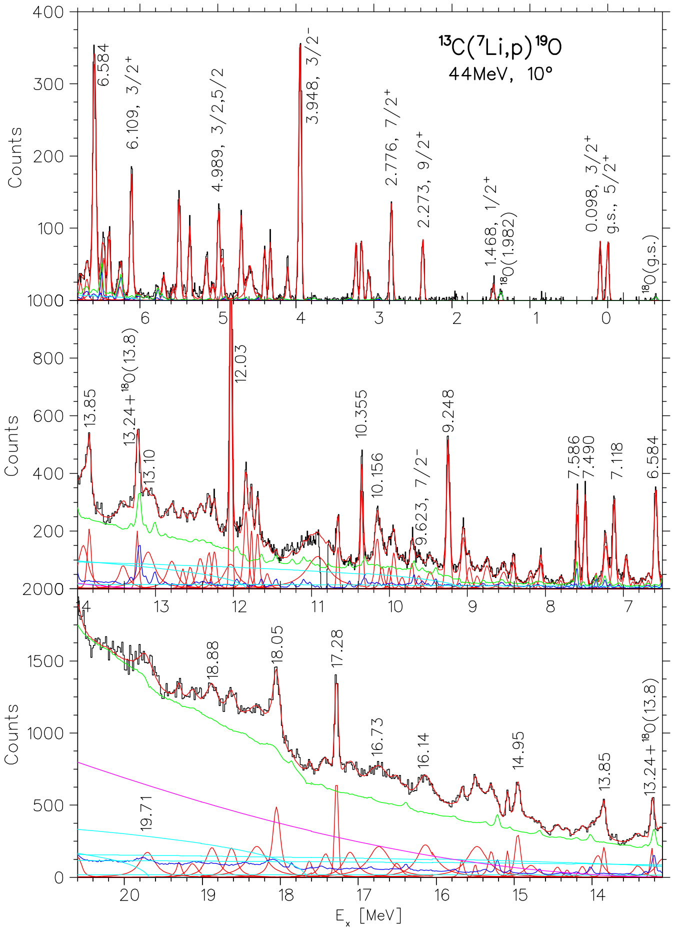

**Fig. 5.21** States in $^{19}$O populated with the $^{13}$C($^7$Li,$p$) reaction measured [20] with the Q3D-spectrometer at the Tandem Laboratory in Munich (as in Fig. 5.19)

parity states. Actually these configurations are expected to be linked to the $\sigma$-configurations for the two neutrons (similar to the case of $^{22}$Ne shown in Fig. 4 in the work of Kimura [109]). The $\pi$-orbitals appear with the band with $\beta = 0.50$ shown in Fig. 8e in Ref. [107]. The parity splitting for this extended configuration is expected to be quite small. Unfortunately the parity projection of these $^{22}$Ne bands has not been done directly—however, we can extract the parity splitting from Fig. 8 of Ref. [109] to be around 1.1 MeV, a value close to our experimental result.

The value for the parity splitting of the $K = 0_4^{\pm}$ bands in our work is 1.7 MeV. This value is even smaller than the corresponding value for the $^{18}$O molecular band built on $0_4^+$ (2.4 MeV, see Table 5.1) indicating that the transition between *direct* and *reflected* configurations is less probable for the case of $^{20}$O—this is probably due to the larger distance between the two major clusters $^{14}$C and $\alpha$. Note that the trend is

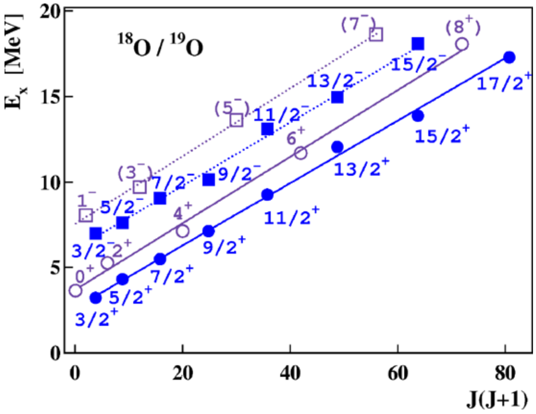

**Fig. 5.22** The $K = 3/2$ parity inversion doublet of $^{19}$O compared to the $K = 0_2^+$ doublet in $^{18}$O. In the weak coupling model the bands in the two cases are assumed to have the same moments of inertia. *Full squares* and *full dots* are used for $^{19}$O, open symbols for $^{18}$O, from Ref. [20]

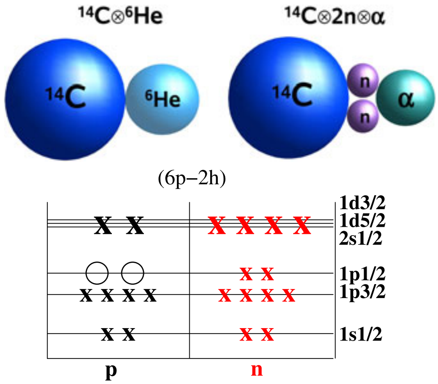

**Fig. 5.23** The cluster model and the shell model structure of states in $^{20}$O. We can expect also a parity inversion doublet for the $^{14}$C × $^6$He clustering, in addition to the covalent molecule with the $^{14}$C × $2n$ × $\alpha$ structure

**Table 5.1** Cluster and molecular rotational bands in some oxygen and neon isotopes. The slope parameters ($\hbar^2/2\theta$) are given for both positive and negative parity bands of a given structure. Last column gives the energy splitting ($2 \cdot \delta_E$) of the parity doublets

| Nuclide | Band-head | $\pi = +\hbar^2/2\theta$ (keV) | $\pi = -\hbar^2/2\theta$ (keV) | Energy splitting (MeV) |
|---|---|---|---|---|
| $^{16}$O | $0_2^+$ | 231 | 205 | 2.9 |
| $^{18}$O | $0_2^+$ | 197 | 198 | 4.0 |
| $^{18}$O | $0_4^+$ | 114 | 115 | 2.4 |
| $^{19}$O | $3/2_2^+$ | 201 | 195 | 3.8 |
| $^{20}$O | $0_2^+$ | 164 | 153 | 5.2 |
| $^{20}$O | $0_4^+$ | 84 | 96 | 1.7 |
| $^{20}$Ne | $0_1^+$ | 167 | 191 | 4.8 |
| $^{22}$Ne | $0_2^+$ | 110 | 105 | 2.0 |
| $^{22}$Ne | $0_3^+$ | 85 | 85 | 1.0 |

different for simple cluster configurations ("ionic")—the energy splitting for such bands increases with the number of nucleons, as is the case in the classic example of $^{16}$O and $^{20}$Ne [110]. This is a consequence of the decreasing distance between the two centres. In molecular configurations with increasing mass number and increasing number of valence neutrons, larger prolate deformations, combined with the higher neutron densities along the symmetry axis, are expected and therefore a smaller energy splitting should be expected. This is the case for the $K = 0_4^{\pm}$ bands proposed in $^{20}$O and $^{18}$O. A similar effect has been seen for the prolate rotational bands in $^{13}$C and $^{14}$C [39, 40].

From Table 5.1 it is evident that in both $^{18}$O and $^{20}$O the bands at higher excitation energies have also higher moments of inertia (i.e. lower slope parameters) and smaller energy splittings. For lighter well-studied systems, $^{10}$Be [111] and $^{12}$Be [112, 113], it was found that their higher-lying bands have more “ionic” character, while the lower-lying bands are of molecular nature (i.e. with shared neutrons between two clusters), because the delocalisation of neutrons reduces significantly the excitation energy. Similar claims were made for $^{22}$Ne [109] and finally for $^{20}$O [107], where the lower-lying band was suggested to have mixed $^{14}\mathrm{C} + {}^{6}\mathrm{He}$ and $^{12}\mathrm{C} + 4n + \alpha$ configurations, while the higher-lying one is suggested to correspond to the $^{16}\mathrm{C} + \alpha$ “ionic” structure. Studies of decay modes of the observed states, (like the one performed for $^{17}$O in Ref. [114]), should be done to give clear answers on this question. Experimental search for exotic decays like $^{6}$He- or $^{9}$Be-emission is also essential.

## 5.5 Covalently Bound Molecular States in the Neon Fluorine Nuclei

### *5.5.1* $^{20}$Ne

As already mentioned in Sect. 5.3, the $^{20}$Ne-nucleus was the first case, where low lying negative parity states have been observed and explained as cluster structure, namely as a parity inversion doublet with $^{16}\mathrm{O} \otimes \alpha$ structure (already in 1968 [28, 29]). Whereas in beryllium isotopes one finds that almost all states are of molecular origin, in heavier nuclei only a few states have such structure. Therefore the coexistence of shell model states and cluster states has been a subject of detailed studies over the decades. The deformed cluster states have in the shell model picture a structure described by multi-particle-multi-hole excitations (e.g. $4p$-$4h$ as for the excited $J = 0^+$ band in $^{16}$O). The aspect of band termination of the ground state band at $J = 8^+$ in $^{20}$Ne has also been a subject of intensive studies. Actually 2 protons and 2 neutrons in the $(sd)$ shell corresponding to a $^{16}\mathrm{O} \otimes [\pi(sd)^2 \otimes \nu(sd)^2]_\alpha$ structure, clearly points to a termination of the band in $^{20}$Ne at value of $J = 8^+$, similar to the band based on the excited state $J = 0_2^+$ (a $K = 0^+$ band) in $^{16}$O.

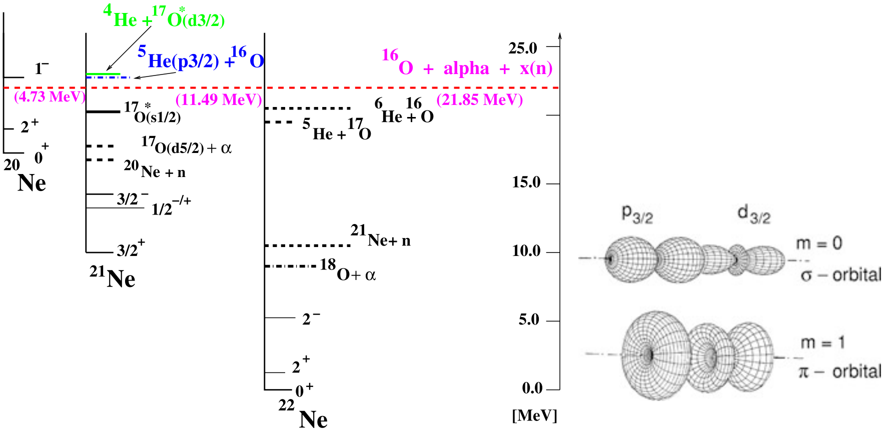

**Fig. 5.24** *Left side*: thresholds for single particle neutron orbitals in $^5$He and $^{17}$O for the formation of a covalently bound state in $^{21}$Ne. The almost degenerate orbitals of the $d_{3/2}$ resonance in $^{17}$O and the $p_{3/2}$ resonance at $^5$He form the $\pi$- and $\sigma$-orbitals, shown at the *right side* (from Ref. [102])

## *5.5.2* $^{21}$Ne

This nucleus, having one valence neutron more than the well studied $^{20}$Ne, appears as a textbook example of an intrinsically reflection asymmetric molecule [102] with one valence neutron. The valence neutron is shared between two different clusters with the structure $^{16}O \otimes 1n \otimes \alpha$. However, the binding energy of the neutron is very different at the two centres, suggesting rather an ionic molecular configuration, which is not possible in nuclear molecules, due to the dominant Coulomb interaction. In order to have equal probabilities at the two centres (covalent binding), we will rather construct the dimer of $^{21}$Ne, with the $p_{3/2}$ resonance in $^5$He and the $d_{3/2}$ resonance in $^{17}$O as shown in Fig. 5.24. The energies of these resonances are very close, within 150 keV (which is much smaller than the width of the $^5$He resonance), and give rise to a resonant exchange of the neutron between the two different cores, $^4$He and $^{16}$O. With this configuration (see Fig. 5.24) we must have two parity inversion doublets with a $K = (3/2)^{+,-}$ rotational bands for the $\pi$ orbitals and the $K = (1/2)^{+,-}$ bands for the $\sigma$ orbitals.

In the last decades of the last century the structure of $^{21}$Ne has been studied extensively, with an emphasis on a complete spectroscopy of states. The authors concentrated mainly on states of positive parity, see references in Ref. [102], because in the shell model the nucleons would reside mainly in the sd-shell. In fact the authors were able to place the observed states in the deformed (Nilsson)-shell model, with some single-particle- single-hole excitations with the p-shell for the negative parity states. However, these were extremely difficult to be placed at lower excitation energy. The authors actually also complain that they have to many states of positive parity. The cluster model solves these problems by the description of the rotational bands as the parity inversion doublets predicted by the scheme presented above.

**Fig. 5.25** A scheme of the parity projections of neon and magnesium isotopes $^{20,21,22}$Ne and $^{26}$Mg, and possible structures with one or two additional $\alpha$-particles

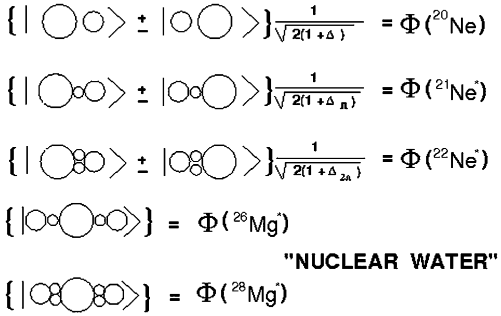

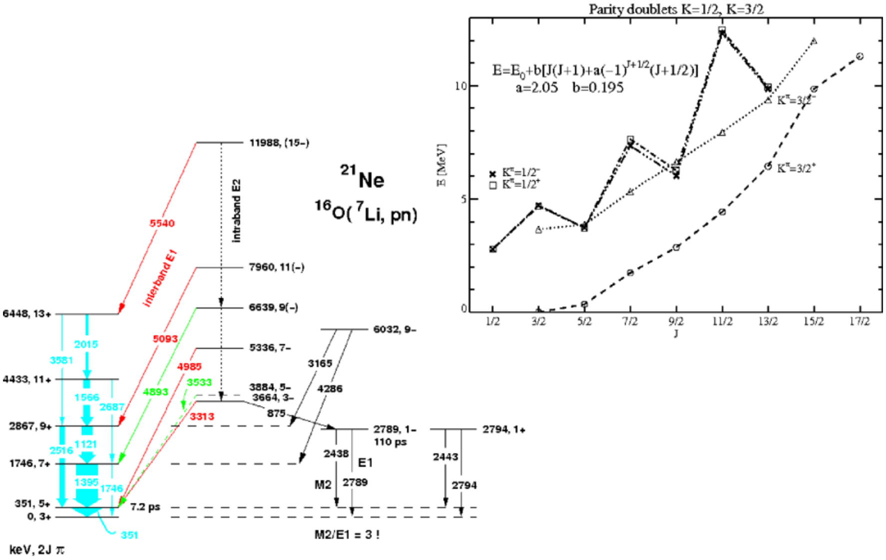

**Fig. 5.26** Gamma transitions in $^{21}$Ne (*left side* from Ref. [116]). The E1-transitions are observed between members of the parity inversion doublet with $K = (3/2)$, which have opposite parity. *Right side*: the molecular rotational bands, doublets starting from the ground state with $K = (3/2)$, and the $K = (1/2)^{+,-}$. The latter doublet has a very small splitting due to the $\sigma$ neutron orbital, blocking the central region on the symmetry axis (see Fig. 5.24)

Actually a weak coupling approach as suggested with the case of $^{19}$O, suggests the existence of parity inversion doublets in $^{21}$Ne based on the $^{20}$Ne.

The intrinsically reflection asymmetric configurations must be used to obtain states with good parity (Fig. 5.25). There we show the structure of the molecular rotational bands of neon isotopes $^{20-22}$Ne, and some other symmetric covalent molecules obtained with two $\alpha$-particles in isotopes of $^{26,28}$Mg. For the $^{21}$Ne nucleus a recent study of gamma-transitions [115, 116], has established the molecular parity inversion doublet structure in this nucleus, see Fig. 5.26. The energy splitting associated with these structures contains essential information on the intrinsic structure. Whereas the $K = (3/2)$ bands show an energy splitting comparable to

**Fig. 5.27** The potential energy relevant for the description of $^{21}$Ne (as $^{16}O \otimes 1n \otimes \alpha$), as a function of the deformation parameter $\beta_3$. The energy splitting is indicated

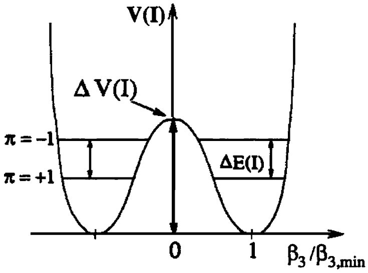

the gs-band of $^{20}$Ne, the two bands associated with $K = (1/2)^{+,-}$ have an almost vanishing energy splitting. The explanation can be found in the intrinsic configurations shown in Fig. 5.24: for the $\pi$ orbitals the overlap of the neutron orbitals occurs outside of the symmetry axis, creating an overlap for the cores similar to the $^{20}$Ne case.

In contrast, the higher lying molecular orbitals of the valence neutron for the $K = (1/2)^{+,-}$ bands, are build by the $\sigma$-orbitals. This band shows the Coriolis decoupling effect with a zig-zag curve for the excitation energy as function of spin. This has been observed also in the $K = 1/2$ band in $^{11}$Be (see Fig. 5.6). For these the density of the valence neutrons are concentrated *on* the symmetry axis. This fact blocks the exchange of nucleons between the two cores, namely the $\alpha$-particle and the $^{16}$O. Thus a unique example of a very small parity splitting is observed (see level scheme in Fig. 5.26). This is related to the molecular orbital structure of the valence neutron. The same situation will occur in $^{22}$Ne, the relevant orbital structure with two neutrons is shown in Fig. 5.28.

Recent work on $^{21}$Ne [116] allows us to determine the intrinsic dipole moment $D_0$. From the study of the $\gamma$-transitions in $^{21}$Ne, in particular for the $K^{\pi} = 3/2^-$ band with the level $I = 9/2^-$, we have determined the mixing of $E1$ to $E2$ transitions. This gives us for the ratio of the intrinsic dipole to quadrupole moments, respectively the value: $(D_0/Q_0)^2 = 4.2 \times 10{-}7\ (\text{fm})^{-2}$. With the independent determination (from the literature) of the intrinsic quadrupole moment $Q_0 = 0.52(5)\ \text{e b} = 52\ \text{e fm}$, we are able to calculate the intrinsic dipole moment, as $D_0 = 0.0373(79)\ \text{e fm}$. This result illustrates the fact that the charge and mass centres of gravity in $^{21}$Ne do not coincide. This is due to the intrinsic cluster structure of $^{20}$Ne consisting of $^{16}O + \alpha$, which persists in $^{21}$Ne. Another approach could be a week coupling of the valence neutron, a situation discussed in the deformed shell-model [117].

As an illustration of the intrinsic deformation, we show in Fig. 5.27 the potential energy as function of the deformation parameter $\beta_3$. With this reflection asymmetric intrinsic deformation (discussed before), we obtain the two parity inversion doublets, with the $K = 3/2$ (ground state, large energy splitting), and the bands with $K = 1/2$. The latter with very small energy splitting, because of the neutron density concentrated *on* the symmetry axis, which inhibits the exchange of $\alpha$-particles.

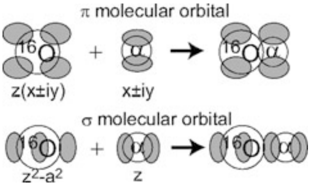

**Fig. 5.28** The molecular two-centre orbital structure in $^{22}$Ne, doublets bands are expected with the $\pi$ orbitals, $K = 3/2^2$, and with the intrinsic structure for the $\sigma$-configurations, $K = (1/2)^2$. The latter is expected at higher excitation energy, the centres have a larger distance

### *5.5.3* $^{22}$Ne

In all cases of the Ne-isotopes, there is a distinct difference between bands of positive and negative parities. For the negative parity states already in $^{20}$Ne the density distributions of the nucleons from the AMD calculations, show more pronounced clustering and a larger distance between the clusters, as compared to the ground state band. The positive parity bands generally show a mixture with shell model configurations, which is less probable for the negative parity states, where the corresponding shells (f,p shells) are placed at higher energies. For this isotope AMD calculations show spectacular formation of molecular structure with $\pi$-orbitals for the two valence neutrons.

The basic molecular structure is similar to $^{22}$Ne: we expect two-centre orbitals with the $\sigma$- and $\pi$-configurations, which are schematically shown in Fig. 5.28. In order to have the parity doublet structure the $(+)$ and $(-)$ signs have to be chosen in the linear combinations (the latter are not shown in the figure). The alpha-clustering and molecular orbitals of $^{22}$Ne has been studied in Ref. [109], within the AMD framework. Di-nuclei and molecular states have been predicted and identified based on the recent experimental results [118–120]; parity splitting of the lower-lying molecular bands has also been observed. The third $0^+$ state is also suggested to be a good candidate for the cluster configuration stabilised by the s$^2$ bond of two neutrons [121]. High spin states in $^{22}$Ne were recently studied experimentally by the $^{14}$C($^{12}$C$, \alpha$) reaction [122].

### *5.5.4* $^{21-23}$F

$^{19}$F is a classic example of an odd nucleus well described by the early cluster model calculations (e.g. [123, 124]). The lowest $^{15}$N $+ \alpha$ doublet ($K^\pi = 1/2^\mp$) is built on the $1/2^-$ state at $E_x = 110$ keV and its parity partner at $E_x \approx 5.3$ MeV—those have a structure in which one proton in p-shell is excited into sd-shell. For heavier isotopes of flour (with even number of neutrons), AMD calculations [68] show that the addition of the sd-shell neutrons to the $^{19}$F cluster states reduces the $\alpha$-clustering of the core and increases the excitation energies, since those neutrons do not favour strong deformation caused by the clustering of the core. Contrary to that, the addition of valence neutrons into $\sigma$ molecular orbitals switches on the clustering on the core—such states have then molecular character and their excitation energies are greatly reduced toward neutron drip-line [68]; this drastic reduction is closely related to the breaking of the neutron magic number $N = 20$. In $^{21}$F, the AMD calculations [68] predict $\alpha$-cluster rotational bands starting with $3/2^+$ at $E_x \approx 7.9$ MeV and the $1/2_2^+$ at $E_x \approx 10.0$ MeV; experimental identification of these states (and their $^{23}$F partners) have not been performed yet.

## 5.6 Cluster Structures in Heavier Nuclei

In several contributions to Vol. 1 of the Lecture Notes 818, on "Clusters in Nuclei", ed. by C. Beck, the problem of cluster formation in heavy nuclei is treated extensively: by R.K. Gupta [125] and by V. Zagrebaev and W. Greiner [126]. The work cited there is mainly based on the liquid drop model and the energy gain for particular nucleon numbers for certain deformations, added to these.

In the previous examples shown in this lecture note and more explicitly in Ref. [1] the connection between molecular structure and deformation effects (within the shell model, or rather the Nilsson model) has been emphasised. The most pronounced molecular structure appears in cases, where the two clusters, representing the cores, have small or negligible overlap (e.g. in the Be-isotopes, or in negative parity states, e.g. in the Ne-isotopes). The nuclei with molecular properties of extreme deformation may be found by inspecting the chart of nuclei with quadrupole deformation as function of nucleon number, established some time ago by Ragnarsson and Sheline [127].

In Fig. 5.29, one can find deep minima (dark blue lakes) for the well known magic numbers of the deformed shell (Nilsson) model. We get further pronounced potential energy effects for larger values of the quadrupole deformation parameters. The potential energy surfaces show a sequence of minima and deep valleys towards larger nucleon numbers and with strong minima up to values of the quadrupole parameter as large as $\varepsilon_2 = 1.0$–$1.2$ ($\beta_2 = 1.6$–$1.7$). Well known are also the clustering effects in fission processes. Clusters with higher yields appear for nuclei with magic nucleon numbers in binary and ternary fission. The enhanced probabilities for certain fission products, is connected to a larger phase space for fission as a statistical decay process. The main effect is here due to the increased Q-values as compared to neighbouring mass partitions. This fact allows higher kinetic energies as well as higher excitation energies (and larger level densities) in the fragments. Both effects give an increase of the phase space for statistical decays.

The cold binary and ternary decays can be studied in the algebraic cluster model see Ref. [128, 129], and typical substructures appear. In the case of the collinear ternary fission observed recently by Pyatkov et al. [130]; in fact the dominant substructure observed in the true ternary fission of $^{252}$Cf is $^{132}$Sn + $^{48}$Ca + $^{72}$Ni, in accordance withe the prediction of Algora et al. [129].

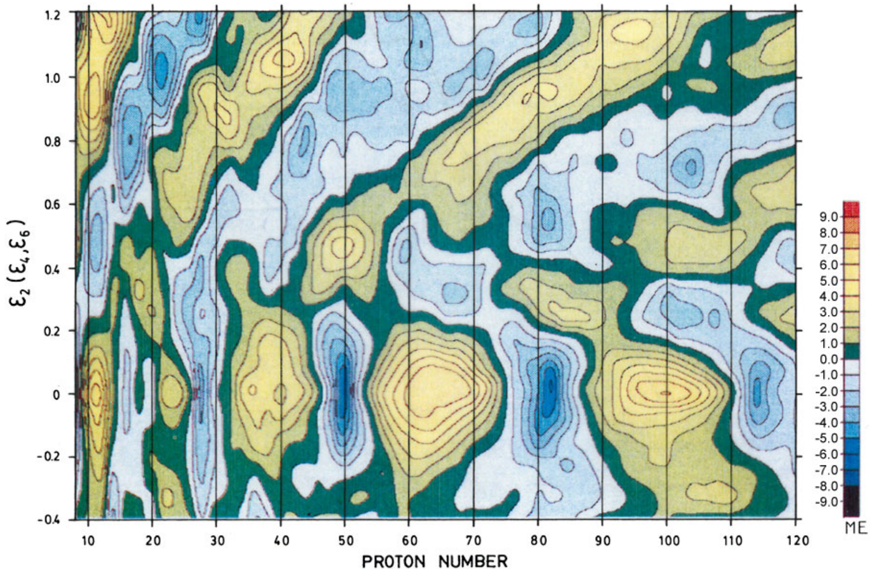

**Fig. 5.29** Chart of the potential energies as function of deformations in nuclei and proton number. The potential energy surface is shown for quadrupole deformations $\varepsilon_2$, minimised for higher components $\varepsilon_{4,6}$

**Acknowledgements** We would like to dedicate this article to H.G. Bohlen (now retired), who has dedicated his work in the last four decades to exceptionally precise and thorough experimental studies of light nuclei structure and reactions.

## References

1. M. Freer, Rep. Prog. Phys. **70**, 2149 (2007)
2. *Proc. Inter. Conf. on Clustering Phenomena in Nuclei*, Bochum (Croatia). Inter. Atomic Energy Agency (1969)
3. D.A. Goldberg, J.B. Marion, S.J. Wallace (eds.), Proc. Second Inter. Conf. on Clustering Phenomena in Nuclei, College Park, Maryland (USA) (U.S. E.R.D.A.), ORO-4856-26
4. W.T.H. Van Oers, J.P. Svenne, J.S.C. McKee, W.R. Falk (eds.), *Proc Inter. Conf. on Clustering Aspects of Nuclear Structure and Reactions, Winnipeg (Canada)* (Am. Inst. of Phys, New York, 1978)
5. J.S. Liley, M.A. Nagarajan (eds.), *Proc. 4th Inter. Conf. on Clustering Aspects of Nuclear Structure and Reactions, Chester (UK)* (Springer, Berlin, 1985)
6. K. Ikeda, K. Katori, Y. Suzuki, *Proc. 5th Inter. Conf. on Clustering Aspects in Nuclear and Subnuclear Systems, Kyoto (Japan)* (Phys. Society of Japan, Tokyo, 1989)
7. F. Haas (ed.), *Proc. 6th Inter. Conf. on Clustering Aspects of Nuclear Structure and Dynamics, Strasbourg* (CRN, Strasbourg, 1995)
8. M. Korolija, Z. Basrak, R. Čaplar (eds.), *Proc. 7th Inter. Conf. on Clustering Aspects of Nuclear Structure and Dynamics, Rab (Croatia)* (World Scientific, Singapore, 2000)
9. K. Ikeda (ed.), *Proc. 8th Inter. Conf. on Clustering Aspects of Nuclear Structure and Dynamics, Nara (Japan)* (Elsevier, Amsterdam, 2003)

10. M. Freer (ed.), *Proc. 9th Inter. Conf. on Clustering Aspects of Nuclear Structure and Dynamics, "CLUSTERS'07", Stratford upon Avon (UK)*. J. Phys.: Conf. Ser., vol. 111 (2008)
11. W. von Oertzen, Nucl. Phys. A **148**, 529 (1970)
12. W. von Oertzen, H.G. Bohlen, Phys. Rep. C **19**, 1 (1975)
13. D. Dehnhard, V. Shkolnik, M.A. Franey, Phys. Rev. Lett. **40**, 1549 (1978)
14. D. Baye, Nucl. Phys. **460**, 581 (1986)
15. B. Imanishi, W. von Oertzen, Phys. Rep. **155**, 29 (1987)
16. W. von Oertzen, Z. Phys. A **354**, 37 (1996)
17. W. von Oertzen, Z. Phys. A **357**, 355 (1997)
18. W. von Oertzen, Nuovo Cimento **110**, 895 (1997)
19. W. von Oertzen, M. Freer, Y. Kanada-En'yo, Phys. Rep. **432**, 43 (2006)
20. W. von Oertzen, M. Milin et al., Eur. Phys. J. A **46**, 345 (2010)
21. Y. Kanada-En'yo, M. Kimura, in *Clusters in Nuclei*, ed. by C. Beck. Lect. Notes Phys., vol. 818 (2010), p. 129
22. H. Horiuchi, K. Ikeda, Cluster model of the nucleus, in *International Review of Nuclear Physics*, vol. 4 (World Scientific, Singapore, 1986), p. 1 and references therein
23. H. Horiuchi, Y. Kanada-En'yo, Nucl. Phys. A **616**, 394c (1997)
24. Y. Kanada-En'yo, H. Horiuchi, Prog. Theor. Phys. **93**, 115 (1995)
25. Y. Kanada-En'yo, H. Horiuchi, Prog. Theor. Phys. Suppl. **142**, 205 (2001)
26. H. Feldmeier, K. Bieler, J. Schnack, Nucl. Phys. A **586**, 493 (1995)
27. T. Neff, H. Feldmeier, R. Roth, Nucl. Phys. A **713**, 311 (2003)
28. H. Horiuchi, K. Ikeda, Prog. Theor. Phys. **40**, 277 (1968)
29. K. Ikeda, N. Tagikawa, H. Horiuchi, Prog. Theor. Phys. Extra **464** (1968)
30. H. Horiuchi, Prog. Theor. Phys. **43**, 375 (1970)
31. H. Horiuchi, K. Ikeda, Y. Suzuki, Prog. Theor. Phys. **52** (1972), Chap. 3
32. T. Ichikawa et al., Phys. Rev. Lett. **107**, 112501 (2011)
33. D. Baye, Phys. Rev. Lett. **58**, 2738 (1987)
34. F. Michel, in *Proc. 5th Inter. Conf. on Clustering Aspects in Nuclear and Subnuclear Systems*, ed. by K. Ikeda, Kyoto, Japan (Physical Society of Japan, Tokyo, 1989), p. 65
35. S. Ali, A.R. Bodmer, Nucl. Phys. **80**, 99 (1966)
36. W. von Oertzen et al., Eur. Phys. J. A **43**, 17 (2010)
37. H.G. Bohlen, W. von Oertzen, M. Milin et al., Eur. Phys. J. A **47**, 44 (2011)
38. N. Keeley, K.W. Kemper, K. Rusek, Phys. Rev. C **64**, 031602(R) (2001)
39. M. Milin, W. von Oertzen, Eur. Phys. J. A **14**, 295 (2002)
40. W. von Oertzen et al., Eur. Phys. J. A **21**, 193 (2004)
41. M. Milin, M. Zadro et al., Nucl. Phys. A **753**, 263 (2005)
42. M. Freer, E. Casarejos et al., Phys. Rev. Lett. **96**, 042501 (2006)
43. H.T. Fortune, R. Sherr, Phys. Rev. C **84**, 024304 (2011)
44. H.T. Fortune, R. Sherr, Phys. Rev. C **84**, 054312 (2011)
45. M. Uroić, D. Miljanić et al., Int. J. Mod. Phys. E **17**, 2345 (2008)
46. R.J. Charity, T.D. Wiser et al., Phys. Rev. C **80**, 024306 (2009)
47. A.N. Kuchera, G.V. Rogachev et al., Phys. Rev. C **84**, 054615 (2011)
48. O.S. Kirsebom et al., Phys. Rev. C **85**, 054308 (2012)
49. N. Curtis et al., Phys. Rev. C **77**, 021301(R) (2008)
50. N. Curtis et al., Phys. Rev. C **82**, 029907(E) (2010)
51. H.G. Bohlen et al., Nucl. Phys. A **722**, 3c (2003)
52. H.G. Bohlen et al., Phys. At. Nucl. **66**, 1494 (2003)
53. H.G. Bohlen et al., Nucl. Phys. A **734**, 345c (2004)
54. M. Majer, R. Raabe, M. Milin et al., Eur. Phys. J. A **43**, 153 (2010)
55. P. Descouvement, Nucl. Phys. A **699**, 463 (2002)
56. Y. Kanada-En'yo, H. Horiuchi, A. Dote, J. Phys. G **24**, 1499 (1998)
57. Y. Kanada-En'yo, M. Kimura, H. Horiuchi, C. R. Phys. **4**, 496 (2003)
58. M. Ito, J. Phys. Conf. Ser. **49**, 206 (2006)
59. N. Itagaki et al., Phys. Rev. C **77**, 067301 (2008)

60. F. Kobayashi, Y. Kanada-En'yo. arXiv:1208.0387
61. H.G. Bohlen et al., Int. J. Mod. Phys. E **17**, 2067 (2008)
62. Y. Kondo et al., Phys. Lett. B **690**, 245 (2010)
63. T. Sugimoto et al., Phys. Lett. B **654**, 160 (2007)
64. Y. Kanada-En'yo, Phys. Rev. C **85**, 044320 (2012)
65. W. von Oertzen, in *Clusters in Nuclei*, ed. by C. Beck. Lect. Notes Phys., vol. 818 (2010), p. 102
66. G. Herzberg, *Molecular Spectra and Molecular Structure; vol. I, Spectra of Diatomic Molecules* (van Nostrand, Princeton, 1950)
67. Y. Kanada-En'yo, H. Horiuchi, Phys. Rev. C **52**, 647 (1995)
68. M. Kimura, N. Furutachi, Phys. Rev. C **83**, 044304 (2011)
69. M. Freer et al., Phys. Rev. C **80**, 041303(R) (2009)
70. M. Itoh et al., Phys. Rev. C **84**, 054308 (2011)
71. M. Freer et al., Phys. Rev. C **84**, 034314 (2011)
72. M. Freer et al., Phys. Rev. C **84**, 034317 (2011)
73. M. Freer et al., Phys. Rev. C **86**, 034320 (2012)
74. F. Hoyle, Astrophys. J. Suppl. Ser. **1**, 12 (1954)
75. M. Chernykh, H. Feldmeier, T. Neff, P. von Neumann-Cosel, A. Richter, Phys. Rev. Lett. **98**, 032501 (2007)
76. D.T. Khoa, D.C. Cuong, Phys. Lett. B **660**, 331 (2008)
77. D.T. Khoa, H.S. Than, D.C. Cuong, Phys. Rev. C **76**, 014603 (2007)
78. A.N. Danilov, T.L. Belyaeva, A.S. Demyanova, S.A. Goncharov, A.A. Ogloblin, Phys. Rev. C **80**, 054603 (2009)
79. A. Bohr, B.R. Mottelson, *Nuclear Structure, vol. I* (Benjamin, Elmsford, 1975)
80. A. Bohr, B.R. Mottelson, *Nuclear Structure, vol. II* (World Scientific, Singapore, 1998)
81. W. Nazarewicz et al., Phys. Rev. Lett. **52**, 1272 (1984)
82. W. Nazarewicz, P. Olanders, Nucl. Phys. A **441**, 420 (1985)
83. P. Butler, W. Nazarewicz, Rev. Mod. Phys. **68**, 349 (1996)
84. W. Bauhoff et al., Phys. Rev. C **29**, 054604 (1984)
85. M. Kimura, Phys. Rev. C **69**, 044319 (2004)
86. Y. Sasamoto et al., Mod. Phys. Lett. A **21**, 2393 (2006)
87. T. Yoshida, N. Itagaki, T. Otsuka, Phys. Rev. C **79**, 034308 (2009)
88. N. Soić, M. Freer et al., Nucl. Phys. A **728**, 12 (2003)
89. M. Milin et al., Nucl. Phys. A **730**, 285 (2004)
90. M. Freer et al., Phys. Rev. C **84**, 034317 (2011)
91. H. Fujimura et al., Phys. Rev. C **69**, 064327 (2004)
92. N. Itagaki et al., Phys. Rev. Lett. **92**, 142501 (2004)
93. N. Itagaki et al., Phys. Rev. C **64**, 014301 (2001)
94. J.A. Maruhn, N. Loebl, N. Itagaki, M. Kimura, Nucl. Phys. A **833**, 1 (2010)
95. J.A. Maruhn, N. Loebl, S. Umar, N. Itagaki, M. Kimura, H. Horiuchi, A. Thosaki, Mod. Phys. Lett. A **25**, 1866 (2010)
96. T. Suhara, Y. Kanada-En'yo, Phys. Rev. C **84**, 024328 (2011)
97. N. Itagaki, W. von Oertzen, S. Okabe, Phys. Rev. C **74**, 067304 (2006)
98. N. Furutachi, M. Kimura, Phys. Rev. C **83**, 021303(R) (2011)
99. H.G. Bohlen et al., Phys. Rev. C **68**, 054606 (2003)
100. H.G. Bohlen et al., Eur. Phys. J. A **31**, 279 (2007)
101. D.R. Tilley, H.R. Weller, C.M. Cheves, R.M. Chasteler, Nucl. Phys. A **595**, 1 (1995), and later additions (2000)
102. W. von Oertzen, Eur. Phys. J. A **11**, 403 (2001)
103. G.L. Morgan et al., Nucl. Phys. A **148**, 480 (1970)
104. H.T. Fortune, Phys. Rev. C **18**, 1053 (1978)
105. M. Gai et al., Phys. Rev. C **43**, 2127 (1991)
106. M. Gai et al., Phys. Rev. C **45**, R2548 (1992)
107. N. Furutachi et al., Prog. Theor. Phys. **119**, 403 (2008)

108. H.T. Fortune, Eur. Phys. J. A **48**, 63 (2012)
109. M. Kimura, Phys. Rev. C **75**, 034312 (2007)
110. H. Horiuchi, K. Ikeda, Prog. Theor. Phys. **40**, 277 (1968)
111. M. Ito, Phys. Lett. B **636**, 293 (2006)
112. M. Ito, N. Itagaki, H. Sakurai, K. Ikeda, Phys. Rev. Lett. **100**, 182502 (2008)
113. M. Ito, N. Itagaki, Phys. Rev. C **78**, 011602(R) (2008)
114. M. Milin et al., Eur. Phys. J. A **41**, 335 (2009)
115. S. Thummerer et al., J. Phys. G **11**, 509 (2003)
116. C. Wheldon et al., Eur. Phys. J. A **26**, 321 (2005)
117. G. Leander, R.K. Sheline, Nucl. Phys. A **413**, 375 (1984)
118. G.V. Rogachev et al., Phys. Rev. C **64**, 051302(R) (2001)
119. N. Curtis et al., Phys. Rev. C **66**, 024315 (2001)
120. V.Z. Goldberg et al., Phys. Rev. C **69**, 024602 (2004)
121. N. Itagaki, M. Kimura, Phys. Rev. C **79**, 034312 (2009)
122. S.Yu. Torilov, M. Brenner et al., Eur. Phys. J. A **47**, 158 (2011)
123. T. Sakuda, F. Nemoto, Prog. Theor. Phys. **62**, 1606 (1979)
124. P. Descouvemont, D. Baye, Nucl. Phys. A **463**, 629 (1987)
125. R.K. Gupta, in *Clusters in Nuclei, vol. 1*, ed. by C. Beck. Lecture Notes in Physics, vol. 818 (2011), p. 223
126. V. Zagrebaev, W. Greiner, in *Clusters in Nuclei, vol. 1*, ed. by C. Beck. Lecture Notes in Physics, vol. 818 (2011), p. 267
127. I. Ragnarsson, R.K. Sheline, Phys. Scr. **29**, 385 (1984)
128. A. Algora, J. Cseh, J. Phys. G **22**, L39 (1996)
129. A. Algora, J. Cseh, J. Darai, P.O. Hess, Phys. Lett. **639**, 451 (2006)
130. Yu.V. Pyatkov et al., Eur. Phys. J. A **66**, 1631 (2010)

# Chapter 6
# Clusterization in Ternary Fission

**D.V. Kamanin and Y.V. Pyatkov**

## 6.1 Searching for New Ternary Decays—Background and Motivation

The present paper is devoted to the observation of a new kind of ternary decay of low-excited heavy nuclei. This decay mode has been called by us "collinear cluster tri-partition" (CCT) in view of the observed features of the effect, that the decay partners fly apart almost collinearly and at least one of them has magic nucleon composition. CCT is observed together with conventional binary and ternary fission. It could be one of the rare fission modes, but at the moment this assumption is not an established fact. For instance, many years have passed between the experimental discovery of the heavy ion radioactivity and working out of a recognized theory of the process.

Nuclear fission, a process where a heavy nucleus decays into two fragments of intermediate mass (e.g. Ba + Kr) has been identified by Hahn and Strassmann in 1938. It was discovered by chemical analysis while irradiating natural Uranium with thermal neutrons [1]. Shortly afterwards Petrzhak and Flerov [2] observed spontaneous fission of the $^{238}$U isotope. The energy release in the fission process was immediately calculated by all leading physicists at that time to be very large, typically 200–205 MeV (e.g. Meitner and Frisch [3]). The large value is due to the larger binding energy per nucleon ($E_B/N$) in the mass range around mass $A = 54$ (iron, $E_B/N = 8.2$ MeV), as compared to the value at the end of the periodic table, ($E_B/N = 7.2$ MeV). This fact could have been noticed four years before

---

D.V. Kamanin (✉) · Y.V. Pyatkov
Flerov Laboratory of Nuclear Reactions, Joint Institute for Nuclear Research, Joliot-Curie 6,
Dubna 141980, Moscow Region, Russia
e-mail: kamanin@jinr.ru

Y.V. Pyatkov
National Nuclear Research University "MEPHI", Kashirskoe shosse 31, Moscow 115409, Russia
e-mail: yvp_nov@mail.ru

C. Beck (ed.), *Clusters in Nuclei, Volume 3*, Lecture Notes in Physics 875,
DOI 10.1007/978-3-319-01077-9_6,

these discoveries, because of the existence of the liquid drop model and the nuclear mass formula of Bethe and Weizsäcker [4]. However, the large collective motion through a large deformation (today called super-deformation) was considered to be unlikely.

Fission of heavy low-excited nuclei into three fragments of comparable masses, so called "true ternary fission", has been intensively investigated soon after the discovery of fission. Swiatecki [5] has shown within the framework of the liquid-drop model (LDM) that fission into three heavy fragments is energetically more favourable than binary fission for all nuclei with fissility parameters $30.5 < Z^2/A < 43.3$. On the basis of a modified liquid-drop model that takes into account the finite range of the nuclear forces the macroscopic potential energy maps for symmetric systems of interest were calculated [6]. These maps demonstrate many important features of the potential energy landscape, including the heights and locations of the binary, ternary, and quaternary fission saddle points. In 1963 Strutinsky [7] has calculated the equilibrium shapes of the fissioning nucleus and has shown, that along with the ordinary configuration with one neck, there is the possibility of more complicated elongated configurations with two and even three necks, at the same time it was stressed, that such configurations are much less probable. Later Diehl and Greiner [8, 9] have shown a preference for prolate over oblate saddle-point shapes for the fission of a nucleus into three fragments of similar size. Such pre-scission configurations could lead to almost collinear separation of the decay partners, at least in a sequential fission process. Actually the Coulomb interaction in the total potential energy is the smallest for linear arrangements of the three fragments. Ternary potential barriers as a function of the distance between the mass centers of the fragments were calculated in Ref. [10]. In the ternary fission path, the isomeric states corresponding to elongated and compact shapes were predicted for heavy systems. Investigating ternary fission of the system $^{238}\mathrm{U} + {}^{238}\mathrm{U}$ the authors of [11] came to conclusion that binary fission is much more probable than ternary fission even among very heavy compound nuclei. The reasons for this are that the LDM potential for ternary fission turns out to be higher than that for binary fission at large deformations and that the formation and rupture of necks for binary fission occur much earlier in the fission process than for ternary fission. However, it was emphasized that very strong shell effects might also lead to earlier ternary neck formation during fission. Results demonstrating a decisive role of shell effects in the formation of the multi-body chain-like nuclear molecules were obtained by Poenaru et al. [12]. We want to refer as well on very recent theoretical articles, devoted to unusual ternary decays of heavy nuclei including CCT [13–16]. The authors analyze the potential energy of different pre-scission configurations leading to ternary decays, and the kinetic energies of the CCT partners [17] are calculated for a sequential decay process. These results, being strongly model dependent can be considered as only the first step in the description of the CCT process.

On the experimental side there have been multiple attempts to find the true ternary fission in low energy fission by means of counting techniques and in radiochemical studies. The schemes of the spectrometric experiments were based on the assumption of comparable angles between all three fragments emitted [18, 19].

Masses of the fragments were calculated in this case based on experimental values of the energies and angles. Contradictory results have been obtained; these were treated as showing the absence of fission fragments in the vicinity of mass fifty both in binary and ternary fission [20]. The latest attempt to find very specific ternary decay mode similar to the CCT in $^{252}$Cf nucleus is reported in series of works [21–24]. Spontaneous cold ternary decay showing the nuclei of $^{96}$Sr, $^{146}$Ba and $^{10}$Be in the exit channel was searched for. The experiment was carried out at the Gammasphere and gamma-gamma coincidences were analyzed. At the first stage of the work the authors came to conclusion that $^{10}$Be nucleus stays at rest after fission but later this conclusion was not confirmed. At the same time almost collinear ternary decays of excited heavy nuclear systems were known from the experiments in Refs. [25, 26] at the early stage of our work.

In the highly excited nuclear systems produced by the nucleus-nucleus collisions in the intermediate energy domain (20–100 MeV/u) the binary fission remains an important exit channel. Nevertheless, the ternary, quaternary, quinary … decays have been observed [27, 28]. The interpretation of this multi-fragment production is still elusive, but all the models put forward so far (dynamically induced density fluctuations, expansion of an initially compressed source, statistical decay and so on) are valid exclusively for hot nuclear matter at the excitations far beyond the region where shell effects manifest themselves.

As was mentioned above, at least one of the CCT products has magic nucleon composition. Shell effects give rise also to two well-known binary decay modes: namely, cluster radioactivity and cold fission. Evident and deep link between all three processes demands to remind briefly the main features of these binary decays.

Cluster radioactivity as a rare spontaneous decay mode of heavy nuclei has been intensively studied in recent years. In this type of radioactivity any emitted nuclear species with masses heavier than $A = 4$ ($\alpha$-particles) and lighter than $A \approx 60$ (fission fragments) are called "clusters". The heavy fragments are grouped in the vicinity of the double magic $^{208}$Pb, and this allows speaking about the known domain of cluster decay as "lead radioactivity". This type of radioactivity is far from being unique. Many other combinations of daughter nuclei are allowed energetically to be emitted; they include the formation of the products of comparable masses. This process is known as cold fission. However, cluster radioactivity is a very rare process: the observed partial life times lie in the interval $10^{11}$–$10^{27}$ s. This corresponds to a branching ratio relative to $10^{-10}$–$10^{-17}$ for those $\alpha$-decays.

In all known cases, except for one, the products of cluster radioactivity are formed in their ground states. From this point of view cluster radioactivity is much closer to alpha-decay than to spontaneous fission, the process in which the both fragments are deformed and strongly excited. For this reason correct comparison of both processes can be done only if cold fission is meant because here the fragments are formed in their ground or low-lying excited states. However, cold spontaneous fission itself is studied even worse than cluster radioactivity. The question of what is the mechanism of cluster radioactivity and whether it resembles either $\alpha$-decay or fission was widely discussed.

The authors of [29] made a survey of mass distributions of cold decays for a series of nuclei and drew some conclusions. Cold decays are distributed over the whole available range of masses. The phenomenon known today as "cluster radioactivity" is only a particular case of their more general family. It is not distinguished neither by the nature of its origin, nor by its probability in comparison with the other modes. One can speak about "lead", "tin" and "calcium" activities depending on the vicinity of $Z$- and $N$-values to the corresponding magic numbers. The most widespread activity is the "tin" one due to the fact that the ratio $82/50$ is close to the average $N/Z$ ratio of the decaying parent nuclei (this provides on the average the maximum $Q$-value). "Tin" activity drifts from very asymmetric one in the parent mass region $A \sim 150$ to symmetric fission for $^{264}$Fm. Another source of enhancement of the decay probability is the formation of fragments having prolate static deformations. Orientation of the big axis along the direction of movement results in lowering of Coulomb barrier and diminishing the path under it. As a result, the authors conclude that one cannot distinguish between cold fission and different types of cluster radioactivity. However, the dynamics of fragment formation in different parts of mass spectra can be different. Alpha-radioactivity and fission usually are described by completely different formalism reflecting a different physical picture of what happens, and these extremes are applied to the description of cluster radioactivity.

Alpha-decay is considered to be a non-adiabatic process. It means a sudden formation of a cluster inside the mother nucleus which then makes attempts to penetrate the barrier. The fission-like process, on the contrary, is described as an adiabatic one. It includes the pre-scission phase where the matter flow takes place and fragments are overlapping. Their final formation happens only after the system goes through a sequence of geometrical shapes whose parametrization is a part of the adopted theoretical approach. The existing data and theoretical calculations indicate that cluster (at least "lead") radioactivity and cold fission have different mechanisms, probable non-adiabatic and adiabatic correspondingly. The transition between both mechanisms takes place at the fragment masses in the vicinity $A = 35$.

We would like to emphasize, that at the early stage of our work the process of "true ternary fission" (fission of the nucleus into three fragments of comparable masses) was considered to be undiscovered for low excited heavy nuclei [30]. Another possible prototype—three body cluster radioactivity—was also unknown. The most closest process to the CCT phenomenon, at least cinematically, is the so called "polar emission" [31], but only very light ions (up to isotopes of Be) have been observed so far. In the analysis of the experiments devoted to the "polar emission", we came to the conclusion that typical CCT fragments could not be detected in the cited works [32]. In fact, *dE*-*E* telescopes (energy-loss, energy) were used to stop the fission fragments (FFs) in the *dE*-detector located on the path of the light charged particles (LCP) flying in the same direction (polar LCP). At the same time this detector must be thin enough to be transparent for the LCP under study. The thickness of the *dE*-detectors, chosen as a compromise, puts a boundary for the mass/charge of the LCP, which could be detected.

Bearing in mind both theoretical and experimental results mentioned above, we came to the conclusion, that collinear tri-partition of low-excited heavy nuclear systems would be a promising field of research. In our first experiments dedicated to this problem [33, 34] some indications of such processes were already observed. At least one of the decay products detected was a magic nucleus. By analogy with known cluster decay (or lead radioactivity), the process has been called "collinear cluster tri-partition" (CCT).

## 6.2 Comparative Study of the CCT in $^{252}$Cf $(sf)$ and $^{235}$U$(n_{th}, f)$ Reaction

In the present section we describe the results of two different experiments devoted to the search for collinear tri-partition of heavy nuclei. In these experiments binary coincidences with two detector systems placed at relative angles of 180° are measured, see Figs. 6.1 and 6.2. Among all known detection methods to measure the masses of nuclear reaction products, the TOF-$E$ (time-of-flight *vs*. energy) method is the only one which uniquely allows the study of multi-body decays. In this method both, the fragment velocities $V$ obtained by means of TOF, and the energy $E$, are measured for each detected fragment individually. The fragment mass $M_{TE}$ is calculated simply using the equation $M_{TE} = 2E/V^2$. For a three-body decay six variables determine the kinematics (i.e., 3 masses and 3 velocity vectors). Adding momentum conservation reduces the number of independent variables to four. In our experiments two masses and two velocities are determined for two fragments observed at a relative angle of 180°. Thus all the results presented below are obtained within the framework of the "missing-mass" approach. With the two-arm spectrometers binary coincidences have been measured, with a special mechanism, which blocks the registration of a third fragment, as explained above and in Fig. 6.1. This means that only two fragments were actually detected in each fission event and their total mass, the sum $M_s$ will serve as a sign of a multi-body decay if it is significantly smaller than the mass of the initial system.

### 6.2.1 *Experiment Ex1*

In the first experiment (Ex1, Fig. 6.1), performed at the FOBOS [35] setup in the Flerov Laboratory of Nuclear Reactions (FLNR) of the Joint Institute for Nuclear Research (JINR) in Dubna, about $13 \times 10^6$ coincident binary fission events of $^{252}$Cf were collected. The TOF of the fragment was measured over a flight path of 50 cm between the "start" detector (label (3) in Fig. 6.1), which is based on micro-channel plates (MCP) placed next to the $^{252}$Cf-source and the "stop" one represented by position sensitive avalanche counters (PSAC, 4). The source activity was 370 fissions/s, it was deposited on a $Al_2O_3$ backing of 50 μg/cm$^2$ thickness and 18 mm

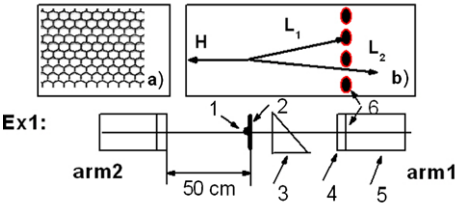

**Fig. 6.1** Scheme of (Ex1) for coincidence measurements of two fragments of the fission decay of $^{252}$Cf. This experiment has been performed at the FOBOS setup [35]. Here: *1*—Cf source, *2*—source backing, *3*—micro-channel plate (MCP) based timing "start" detector, *4*—position sensitive avalanche counter (PSAC) as "stop" detector, *5*—ionization chamber (BIC) with the supporting mesh, *6*—mesh of the entrance window. The front view of the mesh is shown in the insert (**a**), an enlarged mesh section is presented in the insert (**b**). After passage of the two fragments through the source backing, two light fragments $L_1$ and $L_2$, are obtained with a small angle divergence due to multiple scattering. In (**b**) we show that one of the fragments ($L_1$) can be lost hitting the metal structure of the mesh, while the fragment $L_2$ reaches the detectors of the arm 1. The source backing (2) exists only on one side and causes the mentioned angular dispersion in the direction towards the right arm 1

**Fig. 6.2** Scheme (Ex2) of the mini-FOBOS spectrometer which includes a "start" avalanche counter with an internal target (*1*), Bragg ionization chambers (BIC) (*2*) and "stop" position-sensitive avalanche counters (PSAC) (*3*). The target is irradiated by a collimated beam of thermal neutrons (*4*)

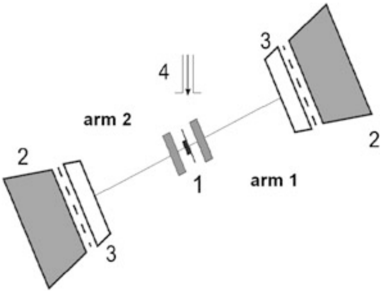

in diameter—(1). Through the measurements of the position of the fragments in the PSAC's, this information provided also the fragment's emission angle with a precision of $1^0$. The energies of those coincident fragments which passed through the PSACs were measured in the Bragg ionization chambers (BIC, label 5 in Fig. 6.1). The entrance windows of the large BIC are made of 1 µm thick aluminized Mylar, with a diameter of 385 mm. To withstand the pressure of the counting gas, the delicate window foil has to be supported by a two-fold structure—a concentric heavy carrier of a transparency of 94 % and an adjacent etched Ni-mesh having a cell dimension of 2.7 mm in diameter and 0.9 mm bulkhead in between the open pores. The thickness of the mesh is about 1 mm. The geometrical structure of the mesh is hexagonal, its front view is shown in the insert (a) of Fig. 6.1, a mesh section is presented in the insert (b). The mesh reduces the total transparency to 75 %. This mesh is a very important peculiarity of the present experiments as explained below (see Fig. 6.1).

## 6.2.2 Experiment Ex2

For a better understanding of the unusual decay channel in $^{252}$Cf $(sf)$ we planned to investigate different fissile systems at different excitation energies up to the threshold of the survival of nuclear shells. One of the reactions we had chosen in an additional experiment was fission induced by thermal neutrons in $^{235}\mathrm{U}(n_{th}, f)$.

The experiment (Ex2) was performed with a beam of thermal neutrons of the IBR-2 reactor in the Frank Laboratory of Neutron Physics of the JINR with the help of the double-armed TOF-*E* mode of the mini-FOBOS [36] spectrometer. The overall statistics processed in this experiment was about $2 \times 10^6$ fission events. The scheme of the setup is shown in Fig. 6.2. The spectrometer is also based on FOBOS detector modules. The start detector is a symmetrical avalanche counter with internal target. The active layer of the target material was prepared by evaporation of 100 µg/cm$^2$ of $^{235}$U on an $Al_2O_3$ backing of 50 µg/cm$^2$ thickness. In this case along with measuring the fission fragment (FF) time-of-flight (TOF) and their energies $(E)$, two more parameters being sensitive to the nuclear charge are added. The drift time of the track formed after stopping of a fragment in the gas volume of the BIC is known to be linked with the fragment's nuclear charge [37]. The corresponding parameter was measured as the time difference between the PSAC signal and the signal from the Frisch grid of the BIC. Special calibration procedures have been worked out for the FF nuclear charge determination [38]. According to the tests carried out before, the charge resolution does not exceed 3.8 units (FWHM) for the FF from the light mass peak, while the mean values for each fixed charge are correctly determined.

The second independent variable, which is also sensitive to the nuclear charge, is the specific energy loss of the FF in the gas volume of the PSAC [35]. This parameter proved to be very useful also for the selection of the CCT events.

In both experiments similar procedures for the TOF-*E* calibration and the calculation of the $M_{TE}$ masses were used. In brief, the mass spectrum of binary decays, which depends on the measured variables and parameters to be determined, was fitted to the known mass spectrum of $^{252}$Cf fission [39]. The data presented in Fig. 6.3 were obtained in the following way. For each fixed experimental $M_{TT}$(TOF, TOF) mass a corresponding mean value of $M_{TE}$ was obtained. ${M_{TT}}^{(1)}$ (primary, i.e., the fragment mass before neutron emission) was calculated as $M^{(1)}{}_{TT} = M_c/(1 + V_1/V_2)$, where $M_c$—the mass of the fissioning system, $V_{1,2}$—velocities of the coincident fragments (indices correspond to the numbers of the spectrometer arms). The values $\langle M_{TE} \rangle$ are compared with their values expected for, i.e., $M_{TT}$—$\nu(M_{TT})$, where $\nu(M_{TT})$—mean number of neutrons emitted from the fragment of the mass $M_{TT}$, taken from Ref. [40]. Thus, Fig. 6.3 demonstrates the absence of shifts (essential nonlinearity) in the calibration of the $M_{TE}$ masses. This point is very important for correct treatment of the data, especially for the mass characteristics and the peculiarities discussed below such as peaks and ridges in the spectra and distributions, respectively.

**Fig. 6.3** Correlation of the mean values of the experimental mass $\langle M_{TE} \rangle$ (post-neutron emission) *vs.* mass, $M_{TT}$, obtained in the present TOF-TOF analysis. The shift due to neutron emission $\nu(M_{TT})$ [40] has been taken into account

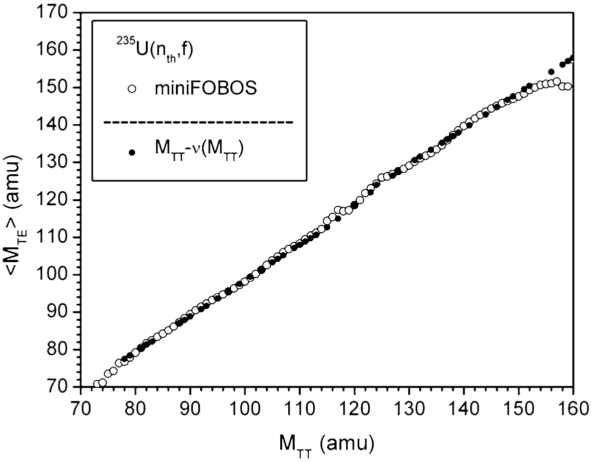

**Fig. 6.4** Contour maps (in logarithmic scale, the steps between colors are approximately a factor 2.5) of the mass-mass distribution of the collinear fragments, detected in coincidence in the two opposite arms of the FOBOS spectrometer in Ex1. The additional bump (7) in arm1 is indicated by an *arrow*. Two large windows *w*1 and *w*2 are used in the later analysis (Sect. 6.3). See text for details

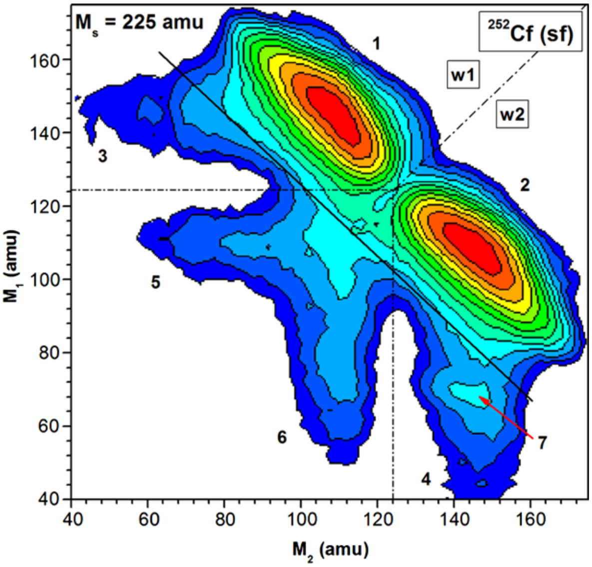

## 6.2.3 *Results of Experiment Ex1, $^{252}$Cf (sf)*

Figure 6.4 shows in a logarithmic scale the two-dimensional distribution ($M_2$–$M_1$) of the two registered masses of the coincident fragments in the experiment (Ex1). In this FOBOS setup $M_1$ is defined as the fragment mass derived from the arm facing to the additional dispersive (scattering) materials. Only collinear fission events with a relative angle of 180 ± 2° were selected, which corresponds to the typical angular spread for conventional binary fission fragments.

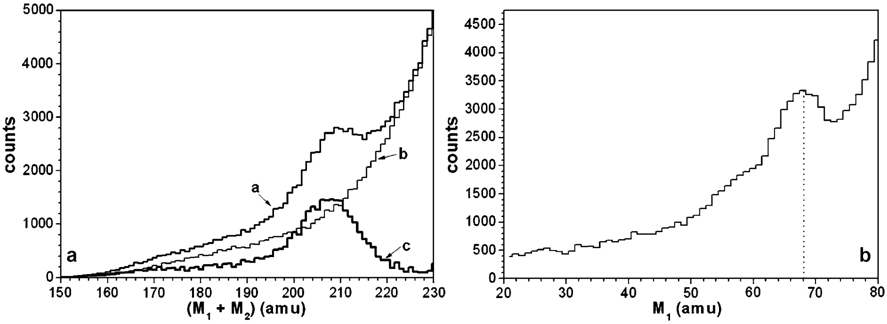

**Fig. 6.5** The bump "7" from (Ex1) in Fig. 6.4 is analyzed. In (**a**) the spectra of the summed masses $M_s$ for the "tails" (4 and 3) shown as spectrum *a* and *b*, respectively, are compared. The result of the subtraction of spectrum *b* from spectrum *a* (difference spectrum) is marked as *c*. On the *right side*, part (**b**), the projection of the bump onto the $M_1$ axis is shown

The "tails" in the mass distributions marked 3–6 in Fig. 6.4 extending from the regions (1) and (2) which are used to mark conventional binary fission, are mainly due to the scattering of fragments on both the foils and on the grid edges of the "stop" avalanche counters and the ionization chambers. Once again we emphasize the small but important asymmetry in the experimental arrangement between the two arms, which consists in location of both the thin source backing (50 μg/cm$^2$ of $Al_2O_3$) at the "rear side" of the target and the "start" detector foil only in arm 1 (Fig. 6.4). An astonishing difference in the counting rates and in the shapes of the "tails" (3) and (4) attracts attention. In the case shown in Fig. 6.4 there is a distinct "additional" bump, marked (7), on top of the latter "tail" (4). The bump is located in the region corresponding to a large "missing" mass. In Fig. 6.4 the line for the measured total mass $M_s = M_1 + M_2 = 225$ amu is shown as a border line separating these interesting events from normal binary fission. Statistical significance of the events in the structure (7) can be deduced from Fig. 6.5, where the spectra of total (summed) masses $M_s$ for the "tails" (4) and (3) are compared. The yield of the events in the difference spectrum *c* is $(4.7 \pm 0.2) \times 10^{-3}$ relative to the total number of events in the distribution shown in Fig. 6.4. It is only a lower limit of the yield due to the reasons discussed below. In order to explain the differences in the "tails" (4) and (3) mentioned above (see also Fig. 6.7), the following scenario is proposed, and the corresponding geometry has been shown in Fig. 6.1 (insert b). We assume that in ternary fission three fragments are emitted collinearly due to two sequential binary decays. Two of the fragments are emitted in one direction but become separated in their velocity vectors with a small angle difference of $\sim 1°$ after passing the scattering media, due to multiple scattering [41]. These media are the backing of the source and the foil of the start detector both located only on the side of tail (4). For instance, for a $^{70}$Ni fragment with the energy 70 MeV the mean angle of multiple scattering in the backing is equal to 0.64° while the tail of the angular distribution extends up to 2°. As a result two fragments continue to fly in the same direction with a small angle divergence.

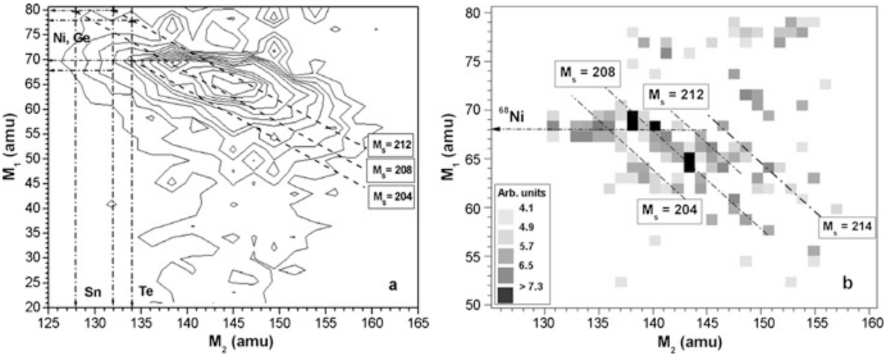

**Fig. 6.6** *Left side*, (**a**): The figure depicts as a 2*D*-contour map ($M_1$ *vs* $M_2$) the difference between the "tails" (4) and (3), for the events measured in Ex1, with the system shown in Fig. 6.1. *Dashed lines* tilted by 45° with respect to the $M_2$ axis correspond to a fixed total mass of the two detected fragments $M_s = M_1 + M_2 = \text{const}$. Part (**b**): the same as in (**a**), however, passed through a second derivative filter which emphasizes local peaks in each section of $M_s = \text{const}$. The ridges correspond to different values of $M_s$ (204, 208, 212 and possibly 214 amu). The *arrows* in the figures mark positions of magic isotopes on the mass axis. Their role in the CCT process is discussed in the text

Thus, if both fragments pass on and enter into the BIC, we register a signal corresponding to the sum of the energies of these two fragments. In this case the event will be treated as binary fission with the usual parameters. In the other cases only the proper energy (mass) of one of the light fragments is measured, because the second one is stopped (lost) in the supporting grid of the ionization chamber. Just the absence of a similar grid is likely the reason why the authors of the work in Ref. [42] have failed to observe collinear ternary decays of $^{252}$Cf (sf) using the time-of-flight method.

For a more detailed analysis of the bump we have constructed the contour map of the two-dimensional mass-mass distribution obtained by subtraction of the "tail" (3) from the "tail" (4) (Fig. 6.6(a)). No additional normalization was used.

This distribution is almost free from experimental background originating from scattered fragments of ordinary binary fission. Some features of this 2*D* plot can be further emphasized by procesing of the distribution with a second derivative filter (Fig. 6.6(b)), such method which is typically used in the search for peaks in gamma spectra, and it is explained in more detail in Refs. [43, 44]. The vertical scale (reversed values of second derivative) represented by the squares is defined in the insert to this figure. The maxima of the peaks extend over certain linear regions of $M_2 = \text{const}$, which are found predominantly as discrete diagonal lines, marked in Fig. 6.6(b). Note that they correspond to the total masses $M_s = \text{const}$ with values of 204, 208, 212 and perhaps 214 amu, respectively. To show the positions of the tilted ridges on the map of the bump they are marked by the dashed lines in Fig. 6.6(a). As can be deduced from the figure, the ridges go through crossing points corresponding to different combinations of two fragments with magic nucleon numbers (marked by the dot-dashed arrows). These marked points could be related to mass values with magic subsystems, well-known from binary fission [45, 46] as follows (corresponding rounded $Q$ values for ternary decays are marked in braces): 204 → $^{70}$Ni ($Z = 28$) + $^{134}$Te{241 MeV} or $^{72}$Ni + $^{132}$Sn ($Z = 50$) {251 MeV}, 208 → $^{80}$Ge + $^{128}$Sn {261 MeV} and for 212 → $^{80}$Ge + $^{132}$Sn {257 MeV}, $^{78}$Ni + $^{134}$Te {228 MeV} or $^{68}$Ni + $^{144}$Ba {217 MeV} and for $M_s = 214 \rightarrow$ $^{82}$Ge + $^{132}$Sn {226 MeV}. It should be reminded that the $Q$ value that corresponds to the most probable binary partition of $^{252}$Cf is about 216 MeV.

Of course, at the moment this interpretation of the tilted ridges is only a hypothesis to be confirmed by the other results shown below.

The ridges discussed are crossed as well by the horizontal ridge (seen via bunching of contour lines in Fig. 6.6(a)). The projection of the bump onto the $M_1$ axis (Fig. 6.5(b)) confirms this conclusion. The effect is linked with the isotopes of $^{68,70}$Ni, which are also magic [46]. Due to this fact we call the bump under discussion as “Ni”-bump.

### 6.2.4 *Results of Experiment Ex2,* $^{235}\mathrm{U}(n_{th}, f)$

The mere fact of the existence of the bump in the total mass as discussed above, as well as the presence of its internal structure was confirmed in an experiment (Ex2) devoted to the $^{235}\mathrm{U}(n_{th}, f)$ [47], in which nuclear charges were measured in addition.

A bump similar to that marked by an arrow in Fig. 6.4 is again well pronounced as shown in Fig. 6.7(a). The yield of the events in the bump is $(5.1 \pm 0.4) \times 10^{-3}$ relative to the total number of fission events detected. As in the previous case the bump is observed only in one spectrometer arm (marked by number 1) facing to the target backing. The projections of the bump onto the $M_1$ axis for both reactions are compared in Fig. 6.7(b). The pronounced peaks in both cases are centered at the masses (68–70) amu, associated with the magic isotopes of Ni. Projections onto the $M_s = \mathrm{const}$ direction are shown in Fig. 6.7(c). Although the total masses of the corresponding two fissioning systems differ by 16 amu the projections of the bump onto this direction are shifted no greater than 6 amu. Such shift of the top yield in the frame of the wide peak could be assigned to the different population of the fission modes based on magic pairs of Sn/Ge or Sn/Ni isotopes in Cf and U* nuclei.

We show the comparison of the spectra of nuclear charges of the measured FF in the two opposite spectrometer arms in Fig. 6.8. The result for the measured charges confirms the previous finding with the mass distributions, namely, the existence of an “additional” bump in the arm with the scattering media. It confirms the hypothesis that the upper boundary of the “additional” bump (Fig. 6.7(a), and (b)) is actually connected with Ni isotopes.

As was mentioned above, the presence of the tilted ridges $M_s = \mathrm{const}$ for the $^{252}$Cf nucleus was revealed using a special mathematical process for the FF mass-mass distribution. This fact has been confirmed independently for the $^{236}$U* system by using selection with an additional parameter, namely, the specific energy losses $dE$ of the FF in the “stop” avalanche counter.

**Fig. 6.7** (**a**) FF mass-mass distribution (logarithmic scale) obtained for the $^{235}\text{U}(n_{th}, f)$ reaction. (**b**) Projections of the bump onto the $M_1$ axis for comparison of the reactions discussed here. (**c**) Projections of the bump onto the direction $M_s = M_2 + M_1 = \text{const}$

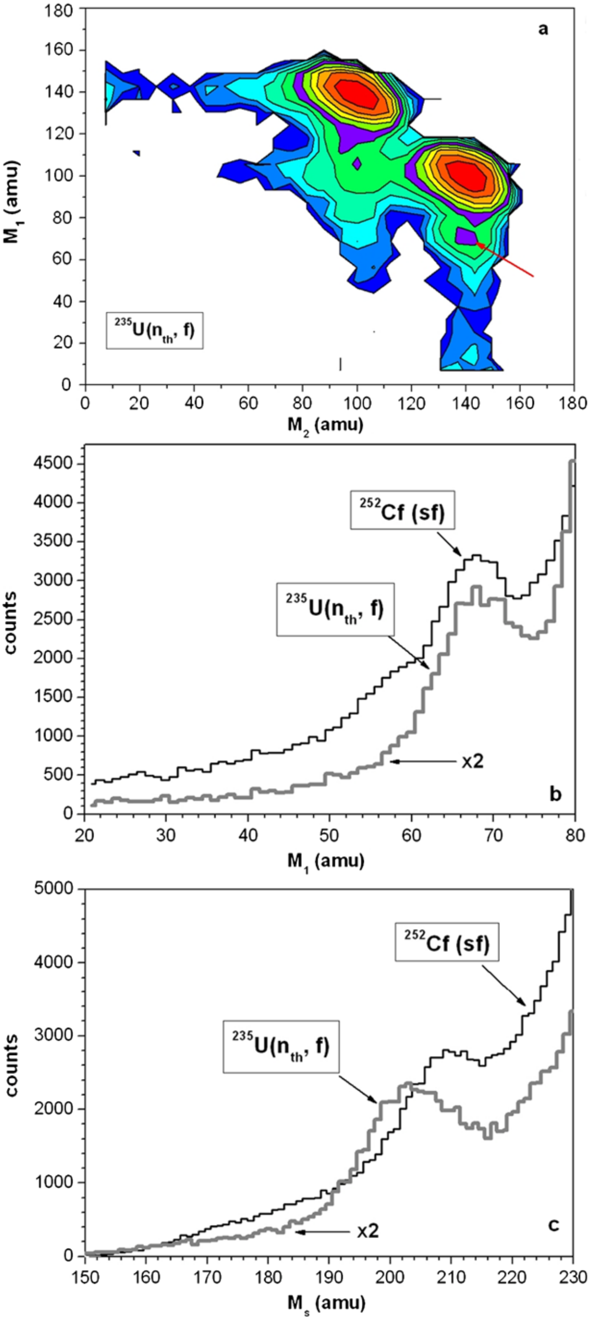

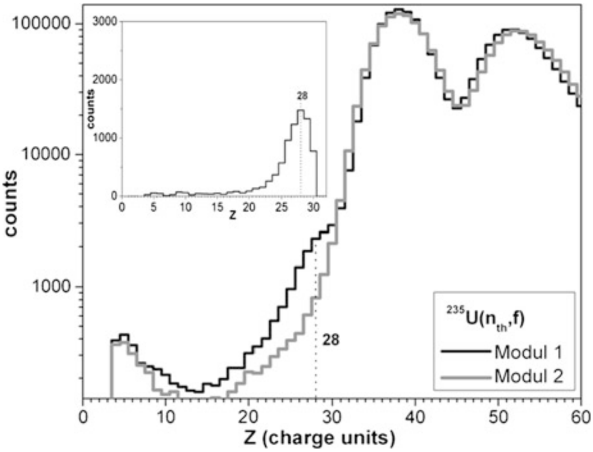

**Fig. 6.8** Nuclear charge spectra from the FF from the reaction $^{235}\mathrm{U}(n_{th}, f)$, the FF are detected in the two opposite spectrometer arms. A difference in the yields (bump) presented in the *upper panel* in a linear scale is visible for the charges around $Z = 28$ (isotopes of Ni)

In Fig. 6.9 we show the mass-mass distribution of those FF, selected by this additional parameter, of an increased energy loss in comparison to FF from the light mass peak of normal binary fission. In this way we can select the events when a "fork" of two fragments of a ternary decay fly into the same first spectrometer arm, i.e., where the bump is observed. Total energy losses of these two fragments in the same counter have values, which are higher compared with the *dE* values for ordinary light fragments. It should be stressed that in this case the experimental variables used for gating (specific energy losses *vs*. velocity) are not distorted due to scattering on the entrance grid of the BIC, being the main source of the background events.

In the bump region a tilted valley structure with reduced event density is clearly seen indicating the presence of ridges with specific total masses, $M_s = \mathrm{const}$ (Fig. 6.9(a)). It is marked by the tilted arrow. A projection of the bump onto this direction is shown in Fig. 6.9(b), the left bracket in the spectrum shows the mass region of potential location of pairs of magic isotopes $^{128,132}\mathrm{Sn}/^{68,70,72}\mathrm{Ni}$. Similarly the right bracket corresponds to pairs $^{128,132}\mathrm{Sn}/^{80,82}\mathrm{Ge}$. At least two peaks centered at the partitions marked in the figure (70/132 and 80/128 amu) are statistically significant. Actually, a parabolic (structureless) fit shown by the dot-dash line gives $\chi^2/f = 2.1$ (chi-square per degree of freedom), while a least squares approximation by the cubic spline (dot line) shows $\chi^2/f = 1.04$.

A peak centered at 68 amu comes out in the projection of the bump onto the $M_1$ axis in Fig. 6.9(c). Further as can be inferred from Fig. 6.9(a) the heavy fragments involved in the bump are bounded by the mass numbers in the region 128–144 associated with magic nuclei of $^{128}\mathrm{Sn}$ and $^{144}\mathrm{Ba}$. This conclusion is confirmed by the projection of the bump onto the corresponding axis (Fig. 6.9(d)), where the boundaries for Sn and Ba are shown. It should be noted that the internal structure of the bump seen in Fig. 6.9(a) is reproduced as well if the selection is made using a gate based on the drift time [48].

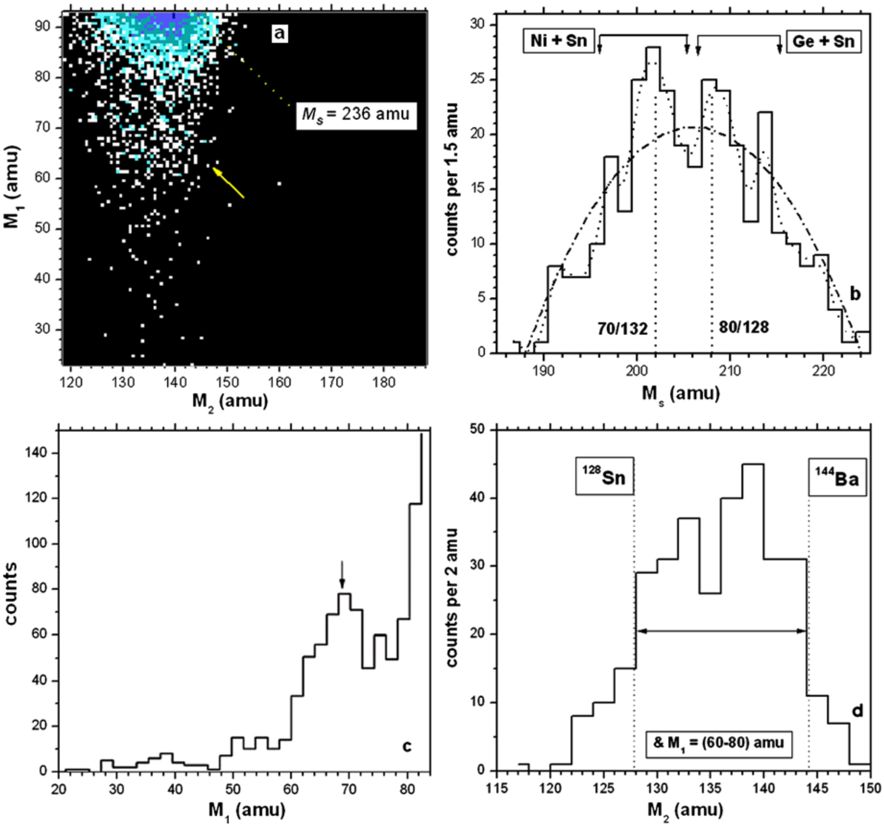

**Fig. 6.9** (**a**) Mass-mass distribution of the fission events from the reaction $^{235}\mathrm{U}(n_{th}, f)$ selected by the additional gate on the velocity-energy-loss, the $V$–$dE$ matrix; (**b**) Projection onto $M_1 + M_2 =$ const direction. Parabolic and spline least squares fits are shown by *dash-dot* and *dot lines*, respectively. (**c**) Projection of the distribution onto $M_1$ axis; and (**d**) Projection onto the $M_2$ axis for the events from the range $M_1 =$ (60–80) amu. See text for details

### *6.2.5 Summary and Conclusions*

The present section has been devoted to the observation of a new multi-body decay channel called by us "collinear cluster tri-partition" (CCT). We observe in the mass-mass distributions (2*D*) the bump linked with large missing masses in the FF mass-mass distribution for cases, where the fragments passes through a dispersive medium providing an angular divergence between the two CCT partners flying towards the same spectrometer arm. The second principal feature of the spectrometer to be stressed is the presence of the blocking structure (grid or mesh) at the entrance to the BIC. Only the sequential action of these two technical details, namely angular struggling and blocking allows the detection of a CCT event, in the frame of the missing mass method. Earlier studies of spontaneous fission of $^{252}$Cf in the series of our experiments performed at different time-of-flight and energy spectrometers [49] gave the same observation when both masses of the coincident fragments were identified in the frame of the velocity-energy ($V$-$E$) method. Bearing in mind, that potentially scattering of fragments at the entrance to the $E$-detector could imitate these effects, we have used another approach with different experimental observables [50], which is methodically independent from FF masses investigated. Such approach was realized in the other experiment Ex2 discussed in the present paper.

We have shown in Ex2 (Fig. 6.9), that the selection of the fission events using $V$-$dE$ (velocity-specific energy losses), confirmed not only the presence of the bump in the FF mass-mass distributions from the $^{235}\mathrm{U}(n_{th,f})$ reaction, but also confirmed its internal structure. In particular an effective cleaning of the bump region from the background in this case, allowed us to observe directly the tilted ridges (and, respectively, the valleys in between). These again were found to correspond to total masses of pairs of magic clusters, namely, (Ni/Sn) or (Ge/Sn). The ridges under discussion are actually linked with pairs of magic clusters, they are the same for the two fissioning systems, namely, in $^{252}$Cf and in $^{236}$U*. Although these systems differ by 16 mass units, the position of the ridges stayed unchanged. In addition to the $dE$ variable being absolutely independent from experimental mass values, an estimation of the nuclear charge ($Z$) via the drift time in the ionization chambers corresponds as well with the experimental fragment mass [38]. Thus the correct position of the bump in the nuclear charge of the fragments (projection on the $Z$ axis in Fig. 6.8), gives clear arguments for the correctness of our assumption on the origin of the bump.

Experimental results suggesting the existence of a new decay mode, the collinear cluster tri-partition (CCT) decay channel, have been obtained [47, 51]. This decay mode manifests itself through a particular bump corresponding to a specific missing mass in the FF mass-mass distributions. One of the decay modes which contribute to the bump can be treated as a new type of cluster decay as compared to the well known heavy ion or lead radioactivity. Key features of both them are summed up in Fig. 6.10. The relatively high CCT yield can be understood if one assumes collective motion through hyper-deformed pre-scission shapes of the mother systems, which is supported by the fact that the linear arrangement realizes the lowest Coulomb potential energies of three clusters. We also emphasize, that the $Q$ values for ternary fission are by 25–30 MeV more positive, again due to the formation of magic fragments, than in binary fission. The ternary fission process must be considered to proceed sequentially, with two neck ruptures in a short time sequence characteristic for binary fissions.

## 6.3 CCT Modes Based on the Deformed Magic Clusters

In the previous sections we have discussed the “Ni”-bump, which is vividly seen in the FFs mass-mass correlation plot without any processing (Fig. 6.4), because it is

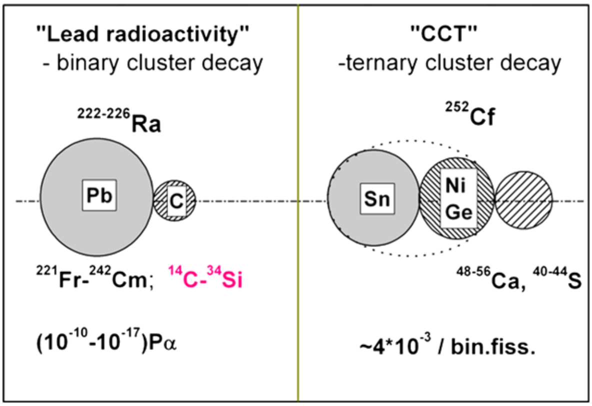

**Fig. 6.10** Cluster scheme for the comparison of the lead radioactivity with collinear cluster tri-partition

located below the loci of binary fission. Special analysis of the data from Ex1 let to reveal the bumps based on deformed magic clusters [51, 52]. Two large windows $w1$ and $w2$ were chosen in the mass-mass distribution from Ex1 (Fig. 6.4). The corresponding projections of the distributions onto the coordinate axis in the "clean" arm2 (box $w1$) and those facing to the source backing, arm1 (box $w2$), are compared in Fig. 6.11(a). The spectra were normalized to the same number of counts. The difference spectrum is shown in Fig. 6.11(b). Some statistically significant peaks are seen. The first one from the left is the projection of the "Ni"-bump onto the $M_1$-axis, this peak was already shown in grater scale in Fig. 6.5. Further structures follow: a wide peak bounded by magic nuclei of $^{82}$Ge and $^{94}$Kr (deformed), and peaks centering, respectively, at $^{98}$Sr and $^{108}$Mo isotopes (both to be magic and deformed).

The origin of the peaks becomes clear from following consideration illustrated by Fig. 6.12. Let us focus our attention on the peak in the vicinity of mass 70 amu (Ni) in the difference spectrum (right part of the "Ni"-bump, Fig. 6.11(b)). The fact that the "Ni-bump" is observed only in one of the spectrometer arms facing the source backing, was treated above as being due to a stopping in the entrance mesh of the ionization chamber of the third light fragment directed in the same arm as the Ni cluster. In contrast, the same pair of fragments directed at the "clean" arm2 predominantly (due to a low angular divergence) gives overlapped energy signals in the "stop" detector and time-of-flight signal corresponding to the faster of them. As a result the calculated mass will be incorrect but registered as an "almost normal" binary one within the experimental mass dispersion. Such events from arm2 play a role of "donors" for the bump events in arm1. In other words the events being actually ternary should move from the locus defined as binary in arm2 to the "Ni"-bump in arm1 (illustration in the upper part of Fig. 6.12). As a result the difference spectrum $Y(w2)$–$Y(w1)$ (low part of Fig. 6.12) must have the peak of positive counts and corresponding negative counting tail for the "donors" fragments in the region of binary fission Fig. 6.12. Evidently the yields of the bump and the "tail" must be equal to each other ($S_1 = S_2$).

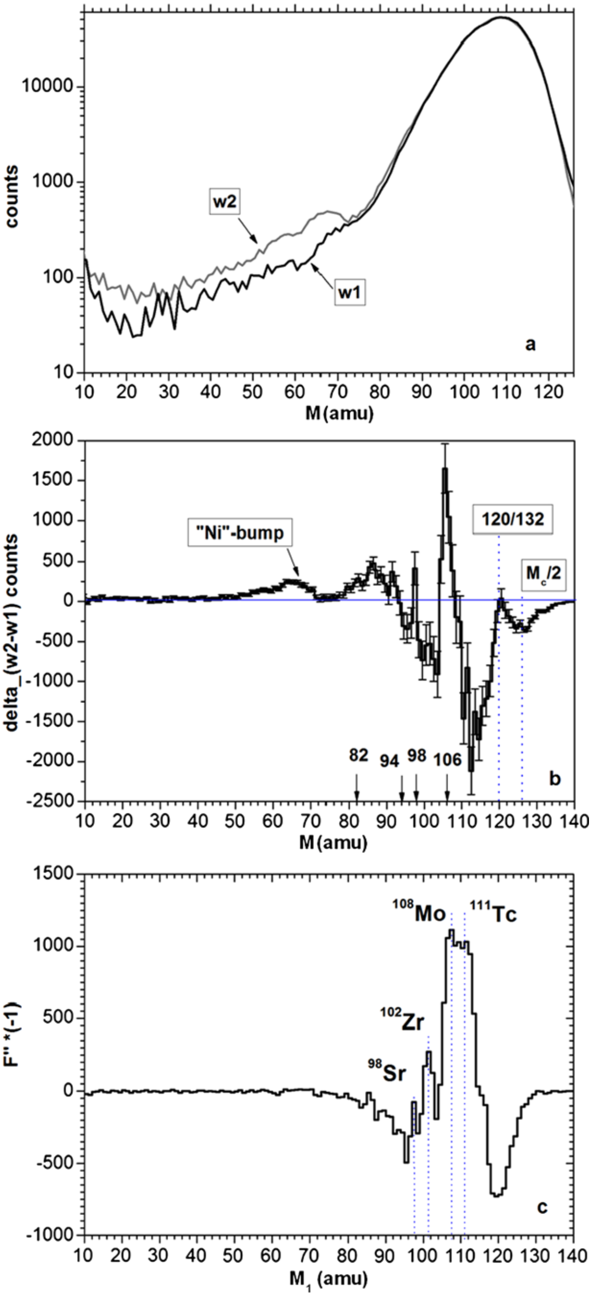

**Fig. 6.11** (**a**) Projections of the events from box *w*1 and box *w*2 (Ex1, shown in Fig. 6.1(a)) onto $M_2$ and $M_1$ axes, respectively; (**b**) difference between these projections and, (**c**) the second derivative of the spectrum being the projection of the events from box *w*2 onto $M_1$ axis. See text for details

In the experiment one observes a superposition of partial contributions from different magic clusters. For instance, the gross central peak in Fig. 6.11(b) lies on the negative "background" (tail) provided by all less massive magic clusters.

**Fig. 6.12** Schematic representation of Fig. 6.8(a) (*upper part* of the figure) for illustrating a reason of forming a negative tail of the "Ni"-bump in the difference spectrum of yields $Y(w2)$–$Y(w1)$ (*lower part*)

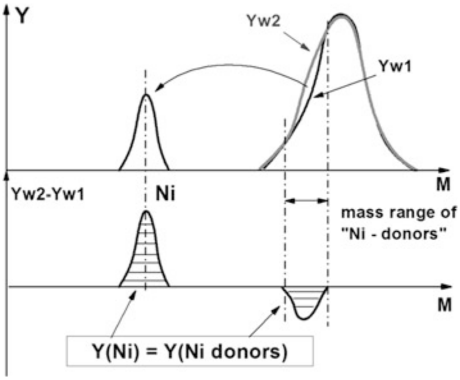

The position of the local peaks in Fig. 6.11(b) could depend on a possible shift in the centers of the spectra in Fig. 6.11(a) due to independent mass calibrations in the opposite arms of the spectrometer. We have two independent evidences for the required quality of the calibrations. The maximal mass of the light fragment in the mass-asymmetric fission mode can not exceed 120 amu due to the known extreme stability of the complimentary heavy fragment (double magic $^{132}$Sn). This is just the feature observed in Fig. 6.11(b): the negative yield in the difference in the spectrum vanishes for the mass partition 120/132 amu. The negative minimum at $M_c/2$ (Fig. 6.11(b)) where $M_c$ is the mass of the fissioning nucleus of $^{252}$Cf, shows, that ternary fragmentation is likely to occur in the region of mass-symmetric fission as well.

Another argument for the quality of the mass calibrations can be inferred from Fig. 6.11(c). The figure shows the second derivative of the mass spectrum linked with the box *w*2 of the data from Ex1, this shows similar peaks as the difference spectrum in Fig. 6.11(b). Thus Fig. 6.11(b) can be treated as a manifestation of a whole sequence of bumps, based on magic spherical and deformed clusters of $^{68-70}$Ni, $^{82}$Ge, $^{94}$Kr, $^{98}$Sr, $^{102}$Zr, $^{108}$Mo, $^{111}$Tc. The yield of the most populated "Mo"-bump ($A = 106$–$111$) is about $8 \times 10^{-3}$ per binary fission, i.e. twice as high as the corresponding value for the "Ni"-bump directly seen in the mass correlation plot (Fig. 6.4(a)).

## 6.4 Ternary Decays with Comparable Masses of the Fragments

When events characterized by approximately equal momenta and velocities were selected in Ex2, the mass-mass distribution of FFs reveals a specific structure in the form of a right angle whose vertex lies on the diagonal of the plot in the vicinity of the points (68, 68) amu (Fig. 6.13(a)). We observed earlier a similar structure (rectangle) in the mass-mass distribution of fragments from the spontaneous fission of the $^{252}$Cf nucleus [52].

The assumption that the sides of the right angle in Fig. 6.13(a) are connected with magic Ni isotopes is confirmed by Fig. 6.13(b). It depicts the distribution of FFs with

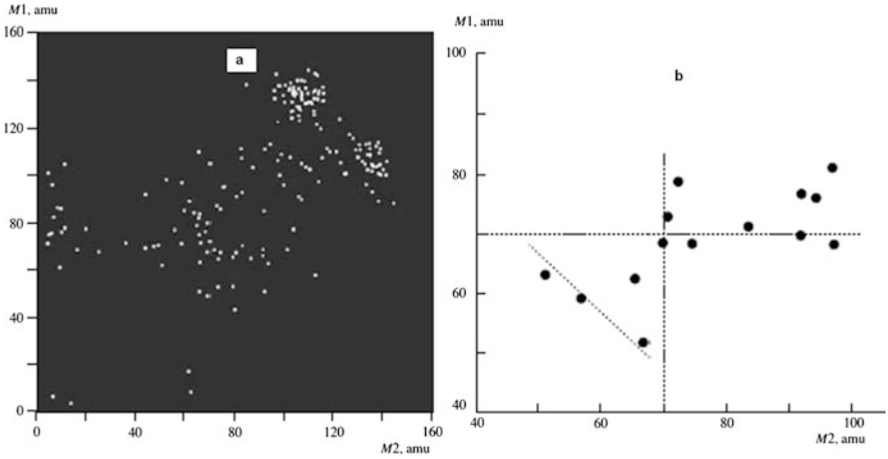

**Fig. 6.13** Mass-mass distribution of genetically related FFs with approximately equal momenta and velocities (**b**) the same but also similar nuclear charges are selected. The events at the vertex of the right angle have charges of $Z \sim 28$; the events lying on the slantwise straight line $M_s = \text{const}$ are discussed in the main body of the text

approximately equal momenta, velocities, and nuclear charges. With allowance for a small shift toward larger values in the charge calibration in arm 1 [53], a charge of about 28 does indeed correspond to the points at the vertex of the angle. Of interest in this figure are also points that lie on the slantwise straight line $M_s = \text{const}$, and the "lost" mass corresponds here to the deformed magic nucleus $^{118}$Pd. The middle of the points corresponds in mass and charge to a symmetric pre-scission configuration of three magic clusters: $^{59}$V–$^{118}$Pd–$^{59}$V.

Note that, although the distribution in Fig. 6.13(b) includes just a few events, the reliability of their analysis is quite high. Indeed, there are no other points in the vicinity of the concentration of points under consideration. Each point results from the measurement of six independent experimental parameters (time-of-flight, energy, and drift time at each arm). Finally, the points are grouped along three specific directions: $M_1$, $M_2 = \text{const}$, and $M_s = \text{const}$.

A less stringent selection permitted revealing a whole family of events similar to the three-cluster configuration discussed above. Figure 6.14(a) shows the distribution of FFs upon momentum and drift time selections. The momentum selection was applied to events in the rectangular window shown in Fig. 6.14(b). It includes events beyond the tails resulting from scattering of FFs by the supporting grid of the BIC entrance window. The second window includes events characterized by an increased value of the parameter $D$ on the $V$-$D$ matrix. The most intense concentrations of points in Fig. 6.14(a) remained from the loci of ordinary binary fission. The points indicated by the arrow and situated on the straight line $M_a = M_b$ stand out among others. They are separately shown in Fig. 6.14(c). The mass distribution of detected fragments in Fig. 6.14(c) gives sufficient grounds to assume that the corresponding pre-scission configurations are three-body chains comprising two or

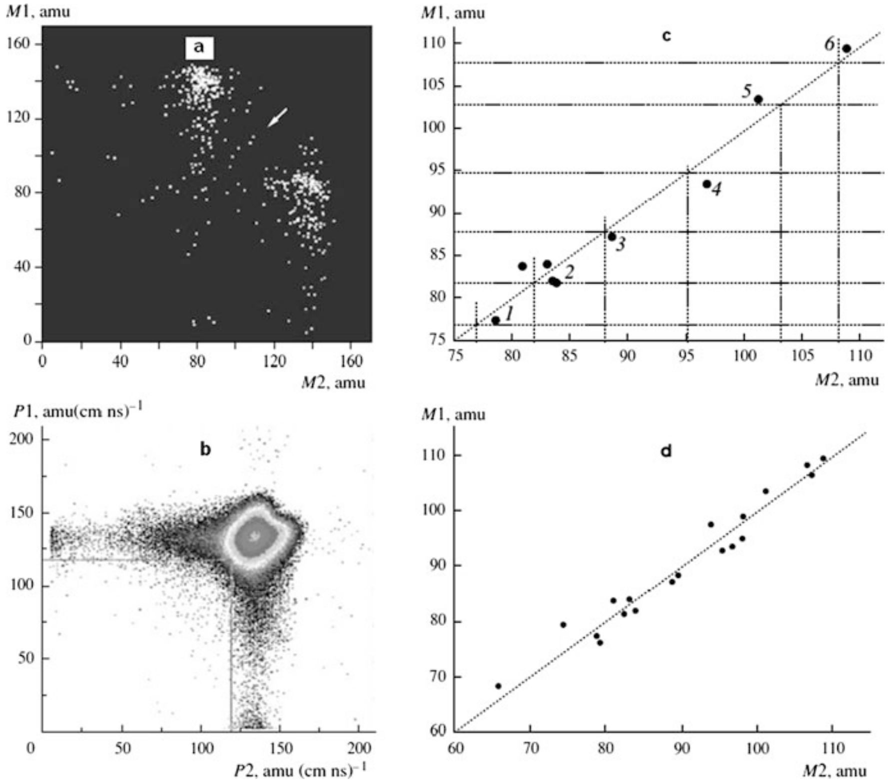

**Fig. 6.14** (**a**) Mass-mass distribution of FFs selected by the momentum and the parameter $D_{exp}$. The arrow points to the group of events with approximately equal masses. (**b**) Window (rectangle) for selection in the momentum *wP* in the momentum-momentum distribution of FFs. (**c**) Events of collinear cluster tripartition with equal masses of detected decay products. The *numbers* label the following cluster configurations: (1) $^{78}\mathrm{Zn}_{30}$–$^{80}\mathrm{Ge}_{50}$–$^{77}\mathrm{Zn}$, (2) $^{82}\mathrm{Ge}_{50}$–$^{72}\mathrm{Ni}_{28}$–$^{82}\mathrm{Ge}$, (3) $^{88}\mathrm{Se}_{54}$–$^{60(2)}\mathrm{Cr}_{24}$–$^{88}\mathrm{Se}$, (4) $^{95}\mathrm{Rb}_{58}$–$^{46}\mathrm{Ar}_{28}$–$^{95}\mathrm{Rb}$, (5) $^{103}\mathrm{Zr}_{40}$–$^{30(2)}\mathrm{Mg}$–$^{103}\mathrm{Zr}$, and (6) $^{108}\mathrm{Mo}_{66}$–$^{20}\mathrm{O}$–$^{108}\mathrm{Mo}$. (**d**) As in Fig. 6.14(c), but for total statistics

three magic clusters. As statistics increase, the population of the region along the straight line $M_a = M_b$ also increases (Fig. 6.14(d)), and the yield of these events was $8 \times 10^{-6}$ (binary fission)$^{-1}$.

## 6.5 CCT with Light Ion Emission

It is known that the drift time of the track formed by the fragment in the chamber gas to the Frisch grid is associated with the nuclear charge of the fragment [37, 54]. The corresponding parameter $D_{exp}$ was measured as the difference between the time signal from the position sensitive avalanche counter and the time reference for the pulse front from the Frisch grid of the Bragg ionization chamber. The mass, energy, and track drift time measured for each fragment were used to find the nuclear charge of the fragment $Z$ with the help of a specially developed procedure [38]. Note that for the investigation of multi-body (not binary) decays, only the mass of the fission fragment calculated via its velocity $V$ (time-of-flight $T$) and energy ($E$) can be used. The determined mass is thus denoted below as $M_{TE}$, unlike the mass $M_{TT}$ calculated via fission fragment velocities.

The main background for the investigated effect is given by fragments scattered on the input grid of the Bragg ionization chamber. These are characterized by lower $M_{TE}$ values but correctly measured velocities and correspondingly, $M_{TT}$ masses. The track drift time in the Bragg ionization chamber, $D_{exp}$, is also measured correctly. Due to the above, it is entirely possible to distinguish between the investigated effect and the scattered events of binary fission. To accomplish this, a formula associating the drift time, mass, and charge of the ion from [38] is used to introduce the additional variable of calculated drift time:

$$D_{calc} = \alpha - \beta\sqrt{E_{BIC} M^{*}_{TT} Z^{-2/3}} + \gamma M^{*}_{TT} Z^{-2/3} \tag{6.1}$$

where $M^{*}_{TT}$ is the mass corrected to the number of emitted neutrons, i.e., the "post-neutron" ($M$) mass; $Z$ is the fragment charge corresponding to the hypothesis of constant charge density ($Z_{UCD}$); $E_{BIC}$ is the fragment energy in the Bragg ionization chamber; and $\alpha$, $\beta$, $\gamma$ are the parameterization coefficients found a priori using charge calibration.

It follows from definition of $D_{calc}$ (6.1) that for scattered events $D_{calc} = D_{exp}$ within resolution, and for events of collinear cluster tri-partition $D_{calc} > D_{exp}$. This can be proved by comparing $D_{calc}$ for a typical light fragment registered correctly and after scattering, respectively. The distribution of $D_{calc}$–$D_{exp}$ for one spectrometer arm obtained in Ex2 is shown in Fig. 6.15(a). The nuclear charge distribution of fission fragments for events beyond the triangular window in Fig. 6.15(a) (i.e., increased values of $D_{calc}$) is shown in Fig. 6.15(b). Arrows mark groups of events with small charges to be further analyzed.

The spectra of masses, charges, velocities, and energies for these ions are shown in Fig. 6.16.

Note first of all that the discussed data are related to almost collinear tri-partition of $^{236}$U* nucleus due to the limited spectrometer aperture, thus the maximum deviation of the lightest fragment from the fission axis cannot exceed 14°. It follows from Fig. 6.15(b) that almost in all analyzed events the light ion (light charged particle) is registered in coincidence with a fragment from the light group of mass distribution of fission fragments observed in conventional binary fission. In this case, the heavy fragment flying in the same direction as the light charged particle either goes beyond the spectrometer aperture (case a) or is lost at the input grid of the Bragg ionization chamber (case b). This follows, e.g., from Fig. 6.17(a) for events marked in Fig. 6.15(b) by vertical arrow. In case *a*, the heavy fragment has not hit the position sensitive avalanche counter and the signal $dE$ is given by the light charged particle only (the lower group of points). If both the light charged particle and the heavy fragment pass through the counter the signal $dE$ is considerably larger (the

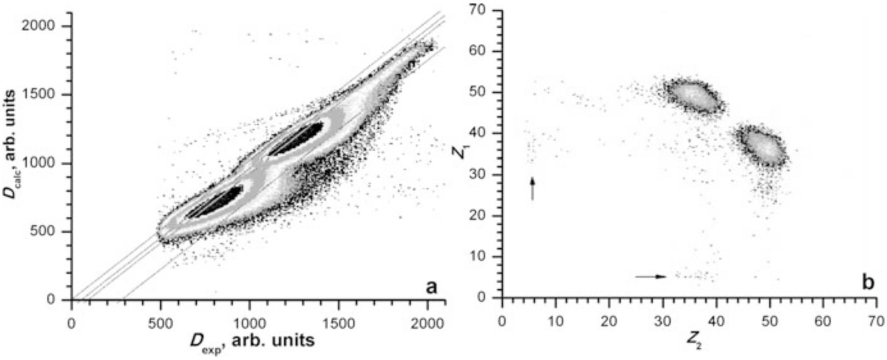

**Fig. 6.15** (**a**) Distribution $D_{calc}$–$D_{exp}$ in one of the spectrometer arms; (**b**) nuclear charge distribution of fission fragments for events beyond the triangular window in (**a**). See the text for detailed description

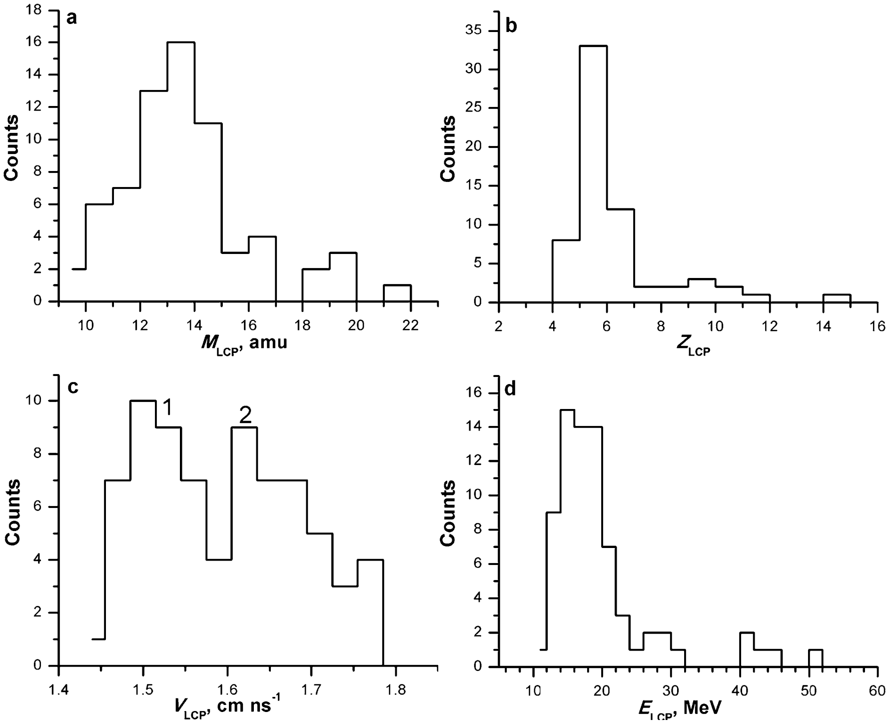

**Fig. 6.16** Spectra of (**a**) masses, (**b**) charges, (**c**) velocities, and (**d**) energies of light ions marked by *arrows* in Fig. 6.15(b)

upper group of points), however, then the heavy fragment is lost at the input grid of the Bragg ionization chamber and only the light charged particle is registered.

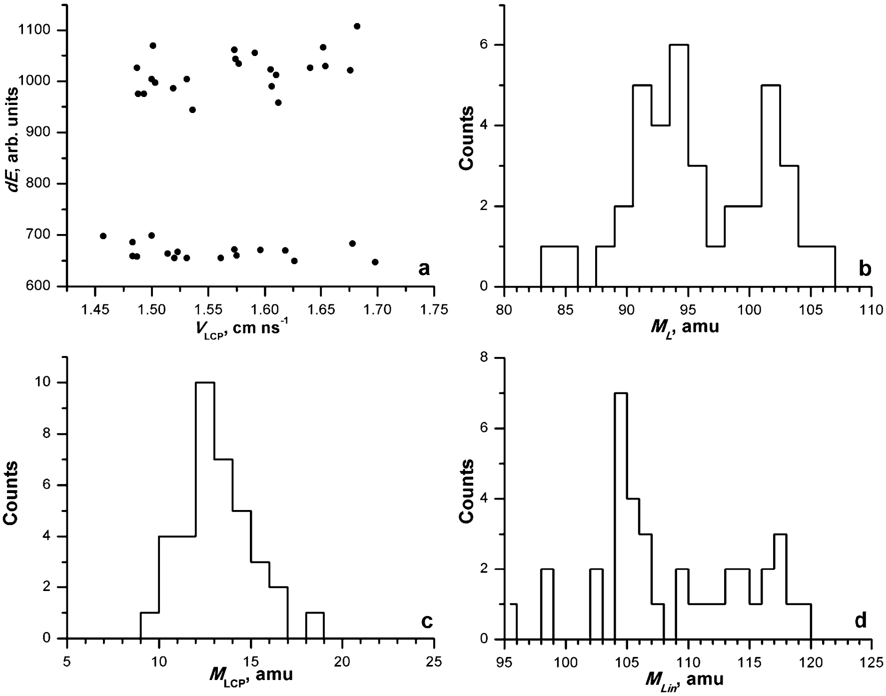

**Fig. 6.17** (**a**) Distribution velocity-energy loss in the position sensitive avalanche counter for fragments in the first spectrometer arm; (**b**) mass spectrum of light fragment registered in coincidence with light charged particle with the velocity $V_{LCP} < 1.6\ \mathrm{cm\,ns}^{-1}$ (peak 1 in Fig. 6.16(c)); (**c**) mass spectrum of such light charged particles; (**d**) mass spectrum of light fragments before light charged particle partition

Two groups of ions can be seen in the velocity spectrum of light charged particles (peaks 1 and 2 in Fig. 6.16(c)). The spectrum of masses ($M_L$) of light fragments measured in coincidence with these light charged particles from the first peak ($V_{LCP} < 1.6\ \mathrm{cm\,ns}^{-1}$) is shown in Fig. 6.17(b). It consists of two peaks associated with magic nuclei $^{94}$Kr and $^{103}$Zr (shell minimum “B” of the map of shell corrections from Ref. [45] and shell minimum for $Z = 40$ from Ref. [55], respectively). The mass spectrum of light fragments ($M_{Lin}$) before the partition of the light charged particle is of interest. To obtain this spectrum, the masses were summed event-wise, $M_{Lin} = M_L + M_{LCP}$. The mass spectrum of the light fragment prior to light charged particle partitioning is shown in Fig. 6.17(d). The central mass peak corresponds to the magic isotopes $^{105}$Zr–$^{106}$Nb (shell minimum “C” from Ref. [45]).

The total spectrum of primary masses of light fragment $M_{Lin}$ is shown in Fig. 6.18 (on the left of the central separating line corresponding to $M_c/2$, where $M_c$ is the mass of the compound nucleus). Along with the peak in a mass region of ~106 amu, the second peak is observed for 111–113 amu; this peak is associated with the deformed magic nuclei $^{111}$Tc and $^{113}$Ru (shell “C” [45] and its experimental manifestation discussed in Ref. [56]). The mass of the lost heavy frag-

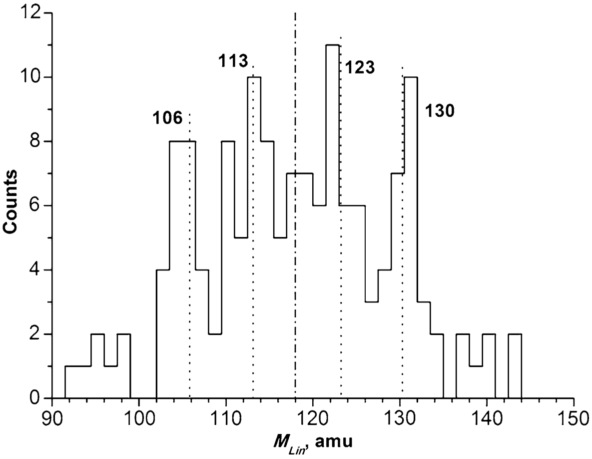

**Fig. 6.18** Masses of fragments at the binary stage of fission; the *dashed-and-dotted line* corresponds to one half the mass of the compound nucleus

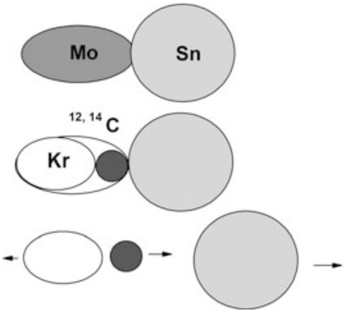

**Fig. 6.19** Illustration of the scenario of collinear cluster tripartition

ment can be reconstructed, $M_H = (236 - M_{Lin})$ amu. The peaks in the spectrum of heavy fragments (Fig. 6.18) correspond to magic $^{123}$Cd (shell "K" [45]) and $^{128,132}$Sn.

The obtained experimental information can be generalized in the context of the following scenario of the two stage decay of $^{236}$U*. Being sufficiently elongated, the system clusterizes, forming the di-nuclear system (Fig. 6.19) consisting of two magic clusters. Upon further elongation, the deformed light magic cluster (Mo) clusterizes into light charged particle (carbon nucleus) and the magic remainder (Kr).

The process of collinear cluster tri-partition according to a similar scenario in $^{236}$U* may take place both in valleys of mass-asymmetric and mass-symmetric forms [57]. To the best of our knowledge, the described effect was not observed earlier in works on the polar emission of light charged particles, this is probably associated with the excessive thicknesses of the *dE* detectors used to identify the charge of light charged particles.

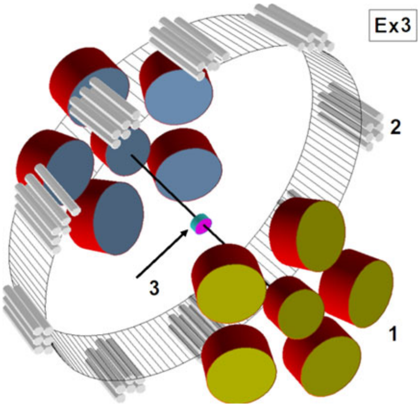

**Fig. 6.20** Layout of the experiment (Ex3) for the neutron coincidences with the modified spectrometer based on FOBOS detector modules (*1*), the "neutron belt" consisting of 140 $^3$He-filled neutron counters (*2*), and the "start" avalanche counter with the Cf source inside (*3*)

## 6.6 Additional Information from the Neutron Gated Data

### 6.6.1 *Experiment Ex3*

Results of two different experiments (Ex3 and Ex4) for the study of fission of $^{252}$Cf (sf) events in coincidence with neutrons are reported in this section [58]. The experiment (Ex3) has been carried out with the modified FOBOS spectrometer also at the FLNR of the JINR. The layout of the experimental set-up is shown in Fig. 6.20. Due to the low yield of the process under study, a compound configuration containing five big and one small standard FOBOS modules in each arm was used. The distance to the source is again 50 cm. Such a scheme of the double-armed TOF-*E* spectrometer allows the measurement of energies and velocity vectors of the coincident fragments and covers ~16 % of the hemisphere in each arm. In order to provide "start" signals for all of the modules only wide-aperture start detectors capable to span a cone of ~100° at the vertex could be used. Another point to be taken into account when choosing appropriate start detectors, arises from the expected decay kinematics (Fig. 6.1, insert b). Among two fragments flying in the same direction only the faster one will be assigned a correct TOF, if the start detector is located at some distance from the decay source. Both problems are solved in the specially designed very compact three-electrode start avalanche counter, in which the central electrode (cathode) is combined with the $^{252}$Cf fission source (330 fissions/s, and a $Al_2O_3$ backing of 50 µg/cm$^2$ thickness).

From the results of our previous experiments we can assume, that there are several CCT modes [33] with the middle fragment of the three-body pre-scission chain with very low velocity after scission. The neutrons emitted from the moving binary fission fragments are focused predominantly [59] along the fission axis. In order to exploit this directivity for revealing the CCT events, the "neutron belt" was assembled in a plane perpendicular to the symmetry axis of the spectrometer, which serves as the mean fission axis at the same time (Fig. 6.20) [60]. The centre of the belt coincides with the location of the fission source. The neutron detector consists of 140 separate hexagonal modules each comprising $^3$He-filled proportional

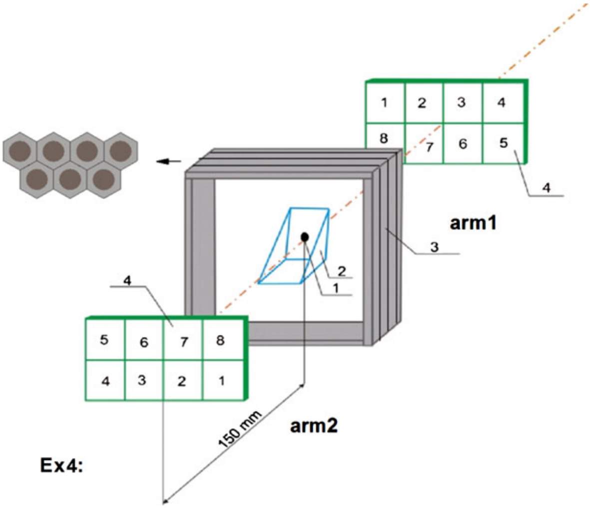

**Fig. 6.21** Scheme of the COMETA set-up of Ex4, which consists of two mosaics of eight PIN-diodes each (*4*), the MCP based start detector (*2*) with the $^{252}$Cf source inside (*1*), and the "neutron belt" (*3*) consisting of 28 $^{3}$He-filled neutron counters in a moderator. The cross section of the belt is marked by the *arrow*

counter, a moderator, a high-voltage input and a preamplifier. The counters operate under a gas pressure of 7 bar, being 50 cm in length and 3.2 cm in diameter. The moderator is made of polyethylene. The neutron counters cover altogether ~29 % of the complete solid angle of $4\pi$. The "neutron belt" consists of two layers of neutron registration modules. At the testing stage we have found that more than 90 % of the neutrons were detected in the two first layers of the counters. For this reason the third layer was omitted in the final version of the set-up.

The registration efficiency for neutrons does not exceed 4 % for those emitted in normal binary fission and it is 12 % for neutrons emitted isotropically. The electronics of the "neutron belt" is operated in slave mode being triggered by the fission event selector. All in all more than $2 \times 10^6$ fission events in coincidence with neutrons were detected.

### 6.6.2 Experiment Ex4

The experiment Ex4 has been performed as the two previous ones at the FLNR of the JINR using the COMETA set-up (Fig. 6.21). It is the double arm TOF-*E* spectrometer which includes the micro-channel plate (MCP) based "start" detector with the $^{252}$Cf source inside, similar to that used in Ex2. Two mosaics of eight PIN diodes each served as the stop detectors and the "neutron belt" comprising 28 $^{3}$He-filled neutron counters are used. Each PIN diode (2 × 2 cm of surface area) provides both energy and timing signals. The actual active area of the PIN diodes is a little bit smaller due to the multi-aperture diaphragm, non-transparent for the FFs, covering the mosaic as a whole. The diaphragm provides ~3 mm demarcation strips between neighbouring diodes. Thus the angle between the fragments $L_1$ and $L_2$ (see Fig. 6.1(b)) must be more then 1° in order them to be detected in neighbouring

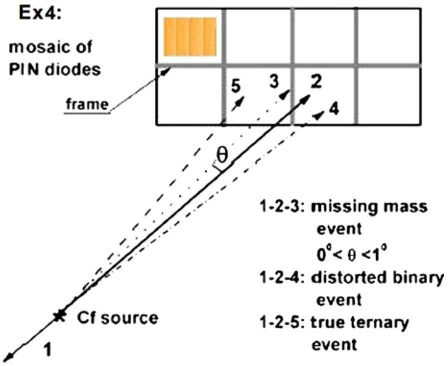

**Fig. 6.22** Geometry in Ex4 with the PIN diodes. Hitting the mosaic by a fork of fragments can give rise to three different types of events. Blocking can occur if the opening angle of the fork lies in the range $0° < \theta < 1°$ (missing mass event marked as 1–2–3). Both fragments of the fork can hit the same PIN diode (event 1–2–4). If $\theta > 1°$ the fragments forming the fork can be detected in two different PIN diodes (true ternary event 1–2–5)

diodes. In this way the structure provides a dead-zone, where one of the fragments can get lost (similar to Ex1, Fig. 6.1(b)). Each flight path is 15 cm.

The use of the Si-semiconductor detectors in TOF-*E* spectrometry of heavy ions (or FFs) is known to have delicate methodological problems due to the "amplitude (pulse-height) defect" [61] and "plasma delay" [62] effects in the *E* and TOF channels, respectively. The first effect involves a nonlinearity in the dependence of the deposited energy on the electrical charge measured, while the latter distorts the TOF used in the calculation of the heavy ion masses. We have worked out an original approach for accounting of the amplitude defect and the correct reconstruction of the FF mass in TOF-*E* measurements [63]. Unfortunately, it is valid only for the case when dispersion of the plasma delay time can be ignored due to a long flight path used. This is not the case here.

To overcome the problem we have used a simplified approach as follows. Two coefficients of the linear time calibration are calculated using the velocity spectrum of the known FFs from the literature. The energy calibration dependence is presented as a parabolic curve passing via three points, namely, through the known centres of the energy peaks for the light and heavy fragments, and the energy of the alpha-particles of the natural radioactivity of $^{252}$Cf nucleus. Such approach gives quite satisfactory results for the reconstruction of the FF masses, at least, in the vicinity of the loci of binary FFs, as shown below.

The neutron belt is located in the plane perpendicular to the symmetry axis of the set-up. According to modelling and previous experiments, the detection efficiency is estimated to be $\sim$5 % and $\sim$12 % for the neutrons emitted in binary fission and from an isotropic source, respectively [64]. The total statistics of binary fission events collected for Ex4 in coincidence with neutrons is about $4 \times 10^6$.

### 6.6.3 Efficiency for the Registration of CCT Events

The registration of the CCT events is based on the double arm time of flight and energy (TOF-$E$) measurements and the particular geometrical blocking effect, already introduced in Refs. [33, 51] which are shown in Fig. 6.1. In this section we give a discussion of the geometrical differences of the three experiments. These are partially contained in the description of each experiment. We summarise that the missing mass approach is linked both to the blocking of parts of the solid angle of the $E$-detectors and the dispersive effect of the backing of the source. For the two collinear (relative angle 180°) fragments, which come from the first neck rupture, as in binary fission, one is reaching the energy detectors undisturbed ($A1$). For the second neck rupture of the other fragment ($A23$), again two fragments ($A2$ and $A3$) are produced collinearly, however, these are dispersed in the backing of the source and in other media (start detectors), into a fork with a certain opening angle. In Ex1 and Ex2 the support grid of the gas-ionisation chambers act as blocking medium over the whole area of the solid angle of the ionisation chambers. In Ex3 these are the narrow regions around the frames defining the solid angle of the $E$-detectors (PIN diodes), see Fig. 6.22. A fork of two fragments, hitting the mosaic detectors can give rise to three different types of events.

- Blocking can occur if the opening angle of the fork lies in the range $0^\circ < \theta < 1^\circ$ (missing mass event marked as 1–2–3 in Fig. 6.22). As a consequence only an area along the border lines of the PIN diodes is available to register CCT events with a missing mass. The opening angle of the fork $\theta$ is expected to be around 1° [54]. In the actual geometry of Ex4 approximately 60 % of the whole area of each PIN is active for the registration of one of the fragments in the fork in such scenario.
- Both fragments of the fork can hit the same PIN diode (event 1–2–4 in Fig. 6.22). In this case the masses of the fragments are not correctly determined. An interesting manifestation of such events will be discussed below in Sect. 6.6.7.
- If $\theta > 1^\circ$ the fragments forming the fork can be detected in two different pin-diodes (true ternary event 1–2–5 in Fig. 6.22).

In order to define the differences in the structures of the $M_1$–$M_2$-plots, we can use an expression which defines the experimentally observed yield $Y_{exp\_CCT}$ of a distinct CCT mode. It can be estimated as follows:

$$Y_{exp\_CCT} \sim Y_{phys} \times P_{miss}. \tag{6.2}$$

Here $Y_{phys}$ is the relative (per binary fission) physical yield of the corresponding collinear ternary decay mode, $P_{miss}$ is the probability that one of the CCT partners will be lost while two others are detected, defining the missing mass approach.

Further for neutrons in coincidence (in Ex3 and Ex4), $P_n$ defines the probability to register $n$ neutrons in coincidence with the FFs from the CCT decay. For this case Eq. (6.2) must be amended as follows:

$$Y^n_{exp\_CCT} \sim Y_{phys} \times P_{miss} \times P_n. \tag{6.3}$$

For Ex1 the opening angle of the fork must be larger than 0.15° in order that one of the fragments gets blocked. For Ex3 this angle is very similar. The blocking structure in these experiments is homogenously distributed over the whole solid angle. For Ex4 this condition is quite different, the blocking medium is determined mainly by the spaces between the adjacent PIN diodes, which is given by the frames. The efficiency to register a blocking event is a factor 3 smaller.

## *6.6.4 Inclusive Data for the Experiments Ex1, 3, 4*

The analysis is based on the presentation and discussion of two-dimensional diagrams of the registered masses ($M_1$ and $M_2$), in which the sum $M_s$ of the two masses can be discussed. The events with total masses $M_s = M_1 + M_2$ will appear as diagonal lines in the mass correlation plot. Projections onto an axis showing either $M_1$ or $M_2$, are also used. Rectangular-like structures bounded by the magic nuclei will be shown as well. These are well seen for higher neutron multiplicities in the neutron gated data (Sect. 6.6.5).

### 6.6.4.1 Experiment Ex1

We repeat shortly the results reported in Sect. 6.2. The most pronounced manifestation of the CCT as a missing mass event is a bump (Fig. 6.4) in the two dimensional mass-mass correlation plot. In this distribution of the fission fragment masses, the bump occurs only in one of the spectrometer arms with dispersive media ($M_1$), whereas it is absent in the analogues variable for the second arm ($M_2$). The bump is marked by the arrow in Fig. 6.4. We see two great peaks due to binary fission, the pronounced vertical and horizontal intensities are due to binary fission fragments scattered on the entrance support grid for the windows of the gas detectors (see Fig. 6.1). Actually this background becomes negligible in Ex4.

### 6.6.4.2 Experiment Ex3

The inclusive results as obtained in the experiment Ex3 (Fig. 6.20) (with lower statistics) confirm the results of Ex1. New aspects are obtained by gating the FF mass-mass distributions by the number of neutrons detected in coincidence (Sect. 6.6.7), see also Ref. [65].

At first we will compare the results of Ex3 without neutron gating, with those obtained in Ex1. The FF mass correlation plot, similar to that obtained in Ex1 (Fig. 6.4 is shown in Fig. 6.23(a). Projections of this distribution both on the $M_1$ axis and on the $M_s$ directions are presented in Fig. 6.23(b), and 6.23(c), respectively. They are compared with the analogous spectra from the experiments Ex1, including the result (Ex2) from the $^{235}\mathrm{U}(n_{th}, f)$ reaction [49].

**Fig. 6.23** (**a**) Contour map of the mass-mass distribution (logarithmic scale, with lines approximately a step factor of 1.5) from a coincidence in the two opposite arms of Ex3. The bump in the spectrometer arm (arm1) facing the backing of the Cf source is marked by the *arrow*. (**b**) Projections onto the $M_1$ axis for comparison with the experiment Ex1, and with the Ex2 results of the $^{235}U(n_{th}, f)$ reaction [49]. Positions of the magic isotopes of Ni are marked by the *arrows* (see text of Sect. 6.6.4.3 for details). (**c**) Projections onto the direction $M_s = M_2 + M_1$. The result for Ex1 is presented by two curves marked by the *arrows 1* and *2* (*dotted*) for the arm1 and arm2, respectively. For Ex3 the yield of arm2 is subtracted

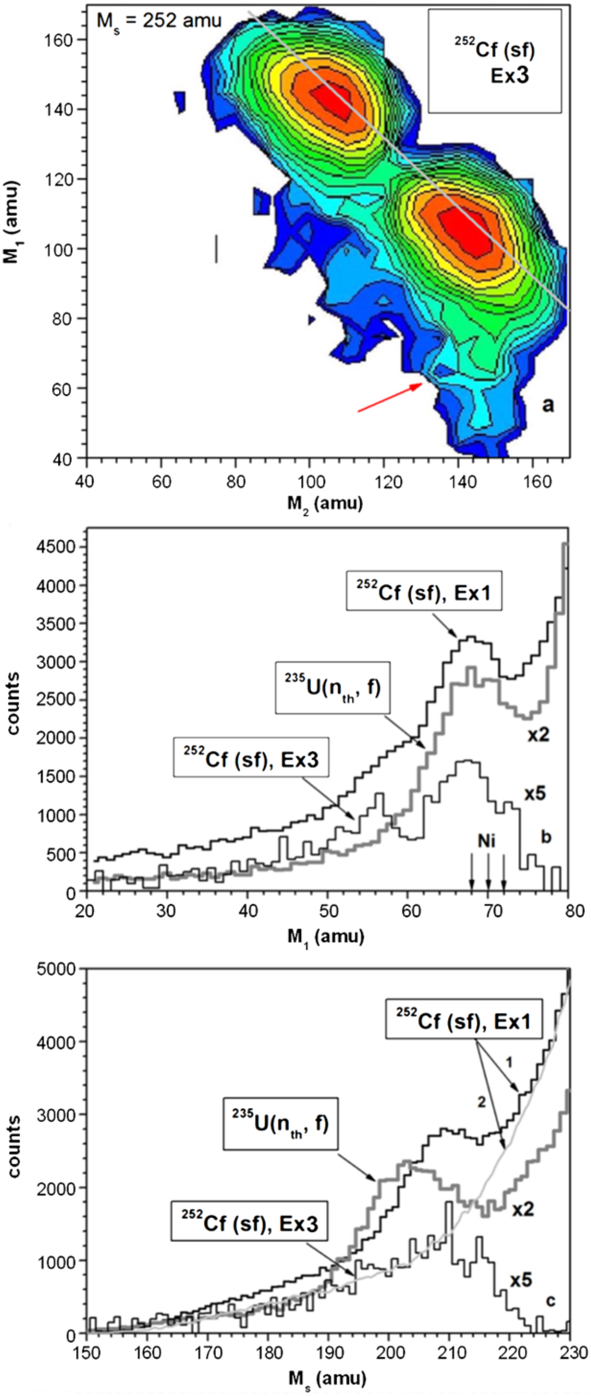

The bump in the projected FF mass correlation data in Fig. 6.23(b) is located around magic isotopes of Ni, these are the isotopes of $^{68}$Ni, $^{70}$Ni and $^{72}$Ni having the magic number of protons $Z = 28$. The first one can be called a "one and a half" magic nucleus due to the neutron sub-shell $N = 40$ [46, 66], while the last one has nucleon composition corresponding to the unchanged charge density hypotheses ($Z_{UCD}$ hypotheses) [67–69]. The middle isotope of $^{70}$Ni showing enhanced yield in far asymmetric fission [46] is likely a compromised version in between two already considered nuclei. This bump will be called below as the "Ni"-bump. The bump marked by the arrow in Fig. 6.23(a) looks less pronounced as compared to that obtained in Ex1 (Fig. 6.4). This can be partially explained by a worse mass resolution due to a larger total thickness of the foils along the flight pass (see Sect. 6.6.6 for details). Projections for Ex3 are shown in the "difference" version, i.e. as a difference of the tail regions in arm1 and in arm2, respectively. The second peak at lower masses in Ex3 looks more pronounced, it corresponds to the complicated two-dimensional structure centered at $M_1 \sim 56$ amu in Fig. 6.27. Overall a good agreement is observed in the position of the peaks in Fig. 6.23(b), and 6.23(c) for all three experiments. The shift of the peak for the $^{235}\mathrm{U}(n_{th}, f)$ reaction in Fig. 6.23(c) has already been discussed in Ref. [54].

#### 6.6.4.3 Experiment Ex4

This methodically quite different experiment confirms our previous observations concerning the structures in the missing mass distributions. In this case there is no tail due to scattering from material in front of the $E$-detectors. Figure 6.24(a) shows the region of the mass distribution for the FFs from $^{252}$Cf (sf) around the "Ni"-bump ($M_1 = 68$–$80$ amu, $M_2 = 128$–$150$ amu). The structures are seen in the spectrometer arm facing the source backing only. No additional selection of the fission events has been applied in this case, the experiment has no background. A rectangular-like structure below the locus of binary fission is bounded by magic nuclei (their masses are marked by the numbered arrows), namely, $^{128}$Sn (1), $^{68}$Ni (2), $^{72}$Ni (3). In Fig. 6.24(b) we show the projection of the linear structure seen at the masses 68 and 72 amu. Peaks seen in Fig. 6.24(b) allow to estimate a mass resolution of the COMETA set-up to be $< 2.0$ amu (FWHM).

Two tilted diagonal lines with $M_s = 196$ amu and $M_s = 202$ amu (marked by number 4) start from the partitions 68/128 and 68/134, respectively. In experiment Ex1 [51], Fig. 6.6, similar sub-structures have been seen for masses $M_s = 204$, 208, 212, 214 amu, where they were revealed indirectly—by applying a method of the second derivative filter to the absolutely statistically reliable distribution. We emphasize the difference in the geometry of the blocking mediums in Ex1 and Ex4, which are decisive for the relative experimental yields of the CCT modes with different angular distributions between the fragments forming the fork (see Sect. 6.6.3). We

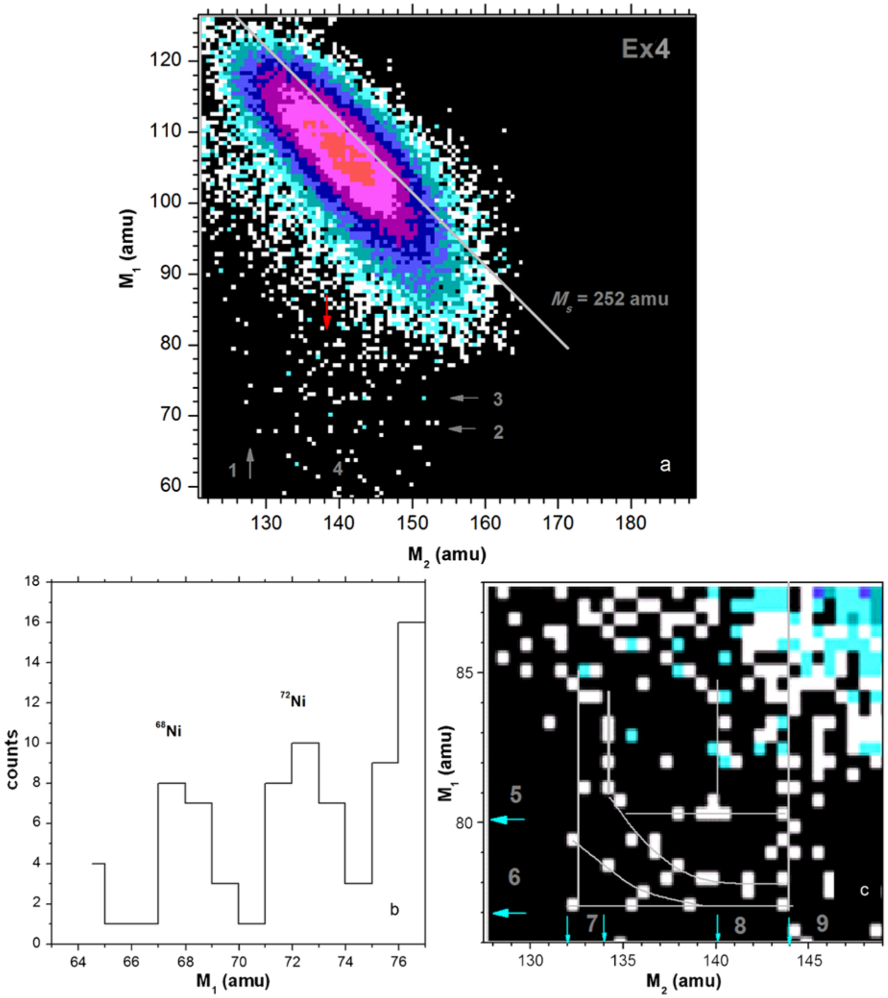

**Fig. 6.24** Results of Ex4: The region of the mass-mass distribution for the FFs from $^{252}$Cf (sf) around the CCT-bump (Figs. 6.4 and 6.23(a)). No additional gates were applied since there is no background of scattered fragments due to the use of PIN-diodes. An internal structure of the "bump" seen as the *horizontal lines* marked by the *arrows 2* and *3* is shown in Fig. 6.24(b) as a projection. A part of the plot just below the locus of binary FFs yielding the rectangular structure marked by the *red arrow* in part (**a**), already seen before, is shown in a larger scale in (**c**). The *lines* are drawn to guide the eye

observe the preference of lighter mass partitions which produces the tilted ridges in Ex4. The positions of the points in the lower part of Fig. 6.24(a) confirm the possible existence of the ridges revealed in Ex1, with the following magic partitions assigned to the starting point of the ridges: 70/134 ($M_s = 204$ amu), 68/140 ($M_s = 208$ amu), 68/144 ($M_s = 212$ amu), 70/144 ($M_s = 214$ amu).

Thus, the comparison of Ex1 and Ex4, which are very different both by the structure of the detectors and the mass calculation procedures used, as well as the statistics collected, still gives a strong confirmation of the existence of tilted ridges $M_s = \text{const}$ linked with magic partitions. As can be inferred from Fig. 6.24(a), the yield of the FFs with the mass 128 amu, which is extremely low in conventional binary fission, is clearly seen. The scattered binary fragments can not give rise to this structure. A part of the plot just below the locus of the binary FFs for a little bit lower statistics is shown in a larger scale in Fig. 6.24(c). The structure is bounded by the magic nuclei of $^{80}$Ge, $^{77}$Zn, $^{132}$Sn, $^{144}$Ba (their masses are marked by the arrows 5, 6, 7, 8, respectively). According to the shell correction map from [55] the nucleon composition of the $^{77}$Zn isotope corresponds to a deformed shell for both neutrons and protons. The stabilizing effect for mass numbers around $A = 76$ in conventional ternary fission is reported in Ref. [70]. The structures observed in Fig. 6.24 agree in most aspects with the rectangular structures seen in the neutron gated data of Ex3.

These observations point to the fact that the CCT decay occurs in a large variety of modes (mass combinations), which could not be distinguished in Ex1 without additional gating due to the large background from scattered FFs.

Likely due to the difference in the parameters of the blocking mediums, the experimental yield of the "Ni"-bump in Ex4 does not exceed $10^{-3}$ per binary fission, i.e. it is much less then in Ex1 and Ex3. At the same time with the absence of scattered FFs in Ex4, we were able to observe the internal structure without any additional cleaning of the FF mass distribution.

### 6.6.5 Results of Neutron Gated Data for the Experiments Ex3 and Ex4

The spectrum of the measured neutron multiplicities is presented in Fig. 6.25. For comparison, a similar spectrum, but measured in a $4\pi$ geometry and calculated for an efficiency of 100 % with corrections from Ref. [65], is shown in the insert (a) of this figure. Actually the experimental neutron-multiplicity spectrum in our experiments is formed as a superposition of several components. Each partial neutron multiplicity (panel a) is transformed according to the binomial law and contributes to the experimental neutron-multiplicity spectrum. During the time gate opened by a fission event for reading the neutron counters, those neutrons from previous fission events as well as neutrons from the background of the experimental hall can give additional contributions to the number of neutrons detected. These two sources have been calculated in the frame of the model of the neutron registration channel [60] and they are shown in Fig. 6.25 (the curves marked as "pile-up" and "background"). The model with the parameters known both from the experiment [71] and from the simulations using the MCNP code [72] reproduces the experimental data very well.

It should be stressed that experimental neutron multiplicities in our work are used for gating of the coincident fission fragments only. Reconstruction of the absolute neutron yields, similar to those shown in the insert of Fig. 6.26 is quite a different task beyond the scope of this work.

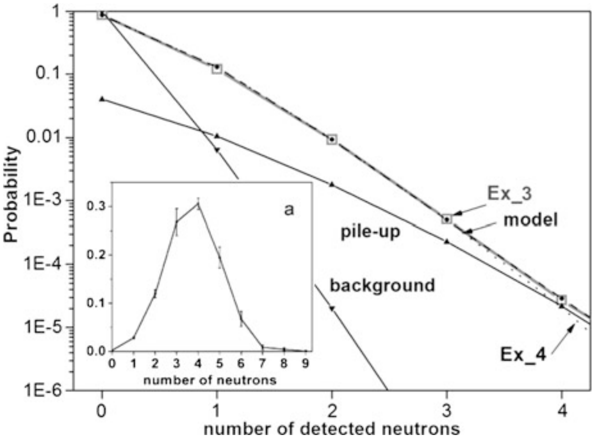

**Fig. 6.25** Neutron multiplicities measured in Ex3 (*gray rectangles*) and Ex4 (*dotted line*) in coincidence with fission fragments. The error bars do not exceed the dimension of the symbol. Calculated multiplicities for Ex3 are shown by a *dashed line* (marked as “*model*”). Contributions of the background and pile-up events in Ex3 are marked as “*background*” and “*pile-up*”, respectively. *Panel-insert* (**a**) depicts the spectrum of neutron multiplicities for $^{252}$Cf ($sf$) from Ref. [65] measured in $4\pi$ geometry and recalculated to a registration efficiency of 100 %

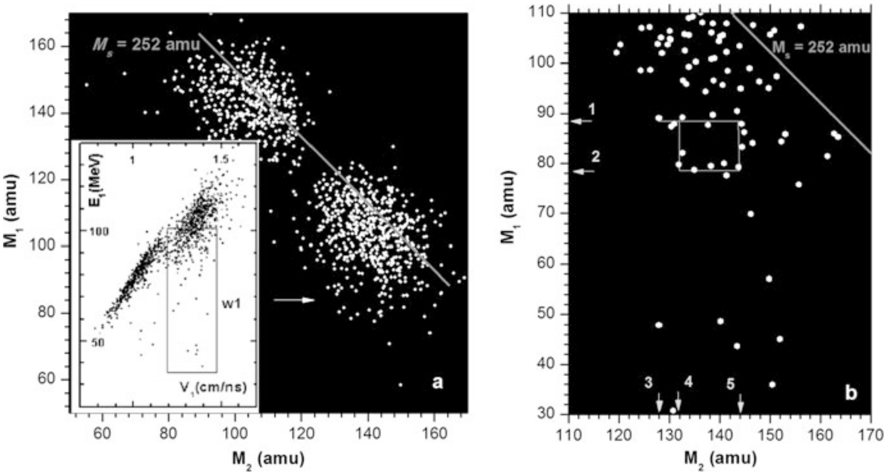

**Fig. 6.26** Results of Ex3 ($n = 3$): (**a**) Mass-mass distribution of the FFs for the multiplicity $n = 3$. The rectangular structure is marked by the *arrow*. (**b**) Mass-mass plot for the events in Ex3 with $n = 3$ and the gate $w1$ in the $V_1$–$E_1$ plot shown in the insert. The rectangular structure in the plot is bounded by the magic numbers in nuclei with the masses $M_2$: 132–144 amu and $M_1$: 78–88 amu, these are marked by the *arrows*. The *lines* are drawn to guide the eye. See text for additional details

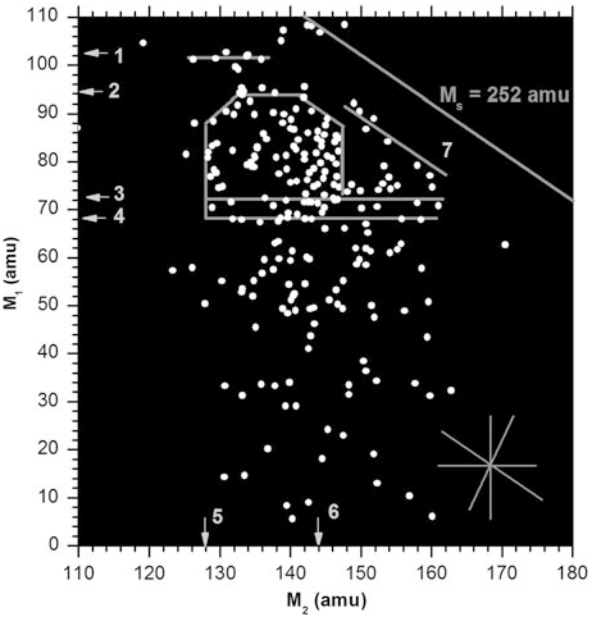

**Fig. 6.27** Ex3: results for neutron multiplicity $n = 2$. The mass-mass distribution of the FFs is accumulated with the additional gate $w1$ as in Fig. 6.26(a) in the $V_1$–$E_1$ plot. This diagram contains no background from scattered particles. *Arrows with the numbers 1–6* mark the positions of masses of magic nuclei, the *line numbered 7* points to events with the loss of a $^{14}$C nucleus, as discussed below. The main intensity corresponds to the masses for the third fragments from 36 down to 20. The *lines* are drawn to guide the eye. See text for more details

### 6.6.5.1 Experiment Ex3

As mentioned before in Sect. 6.6.1, the experiment under discussion with coincident neutrons was motivated by the expectation that the central fragment is connected to an isotropic neutron source of increased (as compared to binary fission) multiplicity linked with the CCT. For this reason a selection of the fission events with an increased number of detected neutrons was studied. Due to restricted statistics collected, we start with the gate set to $n = 3$, where $n$ is the number of detected neutrons.

The corresponding mass distribution is shown in Figs. 6.26(a) and 6.26(b). A rectangular structure is marked by the arrow. It is observed in the same arm as the bump in Figs. 6.4, 6.23(a). The events forming the rectangle and its vicinity lie in the box $w1$ in the $V_1$–$E_1$ distribution presented in the insert. Additional selection with this $w1$ gate reveals the rectangular structure in a more pronounced way (Fig. 6.26b). The rectangle lies well below the line with $M_s = M_1 + M_2 = 252$ amu and it is bounded by the magic isotopes of $^{94}$Kr, $^{80-82}$Ge, $^{128,132}$Sn, and $^{144}$Ba, their masses are marked by the arrows 1–5, respectively.

After the similar procedure for $n = 2$, more events remain and complicated structures appear (Fig. 6.27). A larger concentration of events in the plot appear within the boundaries of masses as marked in the figure (magic isotopes of $^{94}$Kr, $^{128}$Sn, $^{68}$Ni). The extension of the points in the right half of the rectangle likely reflects shell effects around $N = 88$ (neutrons) in the shell correction map [73].

There is negligible background from scattered binary fission fragments in these data, therefore we emphasize the non-random nature of the whole plot. The "tail" of scattered fragments should look like a smooth curve decreasing monotonically from the locus of conventional binary fission (see, for instance, curve 2 in Fig. 6.23(c)). This is not observed here. The most populated rectangular structure is bounded by magic nuclei, as was mentioned before. The bulk of the points below this structure lie, within mass resolution, only along four discreet directions, namely, $M_1$ or $M_2 =$ const, $M_1 + M_2 = M_s =$ const (it means that the missing mass is const) and the line to be almost perpendicular to the latter. In order to have an idea of such different structures these possible directions are shown in the lower right corner of the plot for visual comparison with the data. One of the examples of the lines with $M_s =$ const is marked by the number 7, this line corresponds to a missing $^{14}$C nucleus.

In order to estimate quantitatively the probability of a random realisation of the lines under discussion, special Monte-Carlo testing was performed using a well known formalism of the Hough transformation [74, 75] for formal revealing of lines consisting of several points. The probability of a random realization of such line does not exceed 2 % (see Appendix for the details) and it is even much lower for a more complicated structure like the rectangle in Fig. 6.26(b).

We emphasize once more that the structures visible in Figs. 6.26 and 6.27 are seen in the same spectrometer arm (and only there) as the bump shown in Fig. 6.23. The rectangular structures have been revealed thanks to neutron gating, which effectively suppressed the background from the scattered FFs of binary fission in the region of interest and selects different CCT-modes. Each event is a true triple coincidence with *E*-TOF and a group of neutrons. The neutron number is potentially much larger then 3, because of the lower efficiency for neutron detection.

### 6.6.5.2 Estimation of the CCT Events as a Neutron Source

In our neutron-gated distributions the background due to scattered FFs is negligible, therefore a random generation of linear structures has a low probability. This is important for the interpretation of the structures seen in Figs. 6.26 and 6.27. The structures are the groups of true physical events, and they must be associated with ternary fission events with at least one missing fragment. The fact that the structures appear only with neutron gating means that the neutron source, which produces these events (structures) has parameters, which differ from those of a neutron emission in conventional binary fission.

We try to estimate roughly the neutron multiplicity of the decays for the events shown in Fig. 6.27. Among this matrix 230 events were detected ($1.1 \times 10^{-4}$ per binary fission) in coincidence with two neutrons, and 17 events ($8.0 \times 10^{-6}$ per binary fission) in the same region of the mass correlation plot have the experimental neutron multiplicity three ($n = 3$). We can assume the ternary decay modes to be connected with all the experimental points in Fig. 6.27. The experimental yields for the events $n = 2$ and $n = 3$ are shown in Fig. 6.28 by the triangles.

For further discussion we suppose (model_1): that neutrons are emitted from accelerated fragments moving with the velocities typical for normal binary fission.

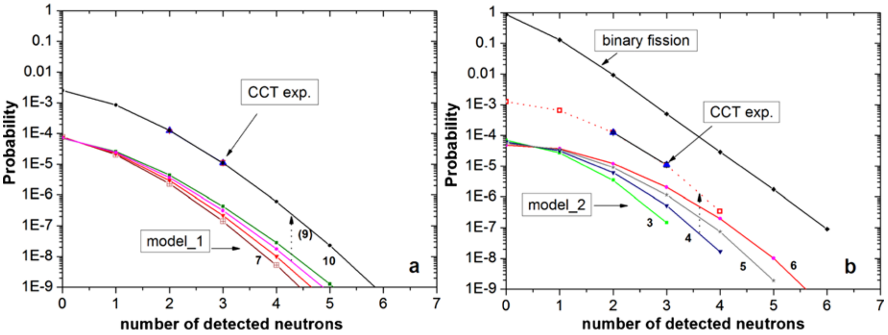

**Fig. 6.28** Comparison of the neutron yields associated with CCT (*error bars* do not exceed the dimension of the symbol) with (**a**) the multiplicity spectra for neutrons emitted from the accelerated fission fragments (model_1) and with (**b**) those for isotropic neutron sources (model_2) of different multiplicities (marked near the curves). Each *curve* is normalised arbitrary to the total yield $10^{-4}$. The model curves, which provide the best agreement of the slopes with those of the experimental observations are marked by the *arrows*. See text for details

The calculations are based on the model of the neutron registration channel presented earlier in Ref. [64]. Using the slope of the experimental curve as a criterion one can try to choose the best result among the model spectra. We obtain a primary neutron multiplicity of $M\_n = 9$. Very elongated pre-scission shapes are needed in order to provide such increased neutron multiplicity [65]. At the same time we observe the velocities of the detected fragments close to corresponding mean values in normal binary fission. In order to overcome the contradiction the neutron source searched for was supposed to be at rest or isotropic (model_2). The results of modelling the multiplicities of such a situation are compared with the experimental data in Fig. 6.28(b). The best agreement is observed for the slope of the curve corresponding to four neutrons emitted from the experimental centre ($n = 4$).

The results of estimations of the neutron multiplicity obtained in the two different models can be judged as follows: one (model_1) failed to reproduce the experimental data, but it does not exclude that a superposition of two sources (models) exists. It is important that at least a certain part of the detected neutron multiplicity is accounted to a neutron source different from those bound to accelerated fragments. In Refs. [76, 77] and others, an isotropic component is observed in addition to the neutrons emitted from the accelerated fragments. In our case the latter will be detected with a factor 3 lower efficiency.

#### 6.6.5.3 Results of Experiment Ex4

The FFs mass-mass distribution for the events selected with the gates within similar approach as used in Ex3 is shown in Fig. 6.29. Namely, we chose $n = 3$ and a selection with the gate in the $V_1$–$E_1$ distribution similar to the box $w1$ in Fig. 6.26(a). Again the rectangular structure is found similar to that seen in Ex3 (Figs. 6.26 and 6.27), however, for a different mass range.

**Fig. 6.29** Ex4 ($n = 3$ and $w1$): Results obtained at the COMETA set-up: mass-mass distribution of the FFs from $^{252}$Cf ($sf$) under the condition that three neutrons ($n = 3$) were detected in coincidence and an additional selection with the gate $w1$ in the ($V_1$–$E_1$) distribution similar to that shown in Fig. 6.26(a) of Ex3

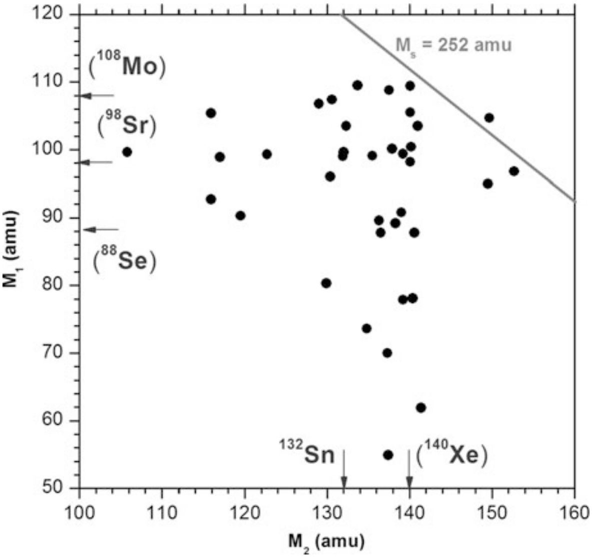

This structure is invisible in the initial ungated distribution, because it is located very close to the locus of the conventional binary fission events, as can be seen from the comparison of Fig. 6.24 with Fig. 6.29. The additional gates help to reveal new CCT-decay modes with very light fragments, $M_3 = 22$ amu and lighter reaching down to binary fission.

As can be inferred from the figure, the rectangular structure seen in its upper right corner is bounded by the nuclei with the masses in the vicinity of known magic nuclei (shown in the brackets). These masses (except of double magic $^{132}$Sn) were calculated based on the unchanged charge density hypothesis for the fission of the $^{252}$Cf nucleus. Actually we know that at least three neutrons were emitted in each fission event presented in the figure. A change in the nuclear composition of the mother system can lead to a shift of the masses of the magic nuclei if neutrons were emitted from the decaying system (pre-scission neutrons). Likely this is what we observe here. For the upper right corner of the rectangle both mass and charge conservation laws are met only if the upper side of the rectangle corresponds to the $^{109}{}_{43}$Tc nucleus while the mass 140 amu corresponds to the isotope composition of $^{140}{}_{55}$Cs.

The structure manifests itself exclusively thanks to the difference of the neutron sources for the fragments appearing in both binary fission and CCT, respectively. These two decay modes must differ in the neutron multiplicity or/and in their angular distributions of the emitted neutrons in order to provide the higher registration efficiency for neutrons linked with the CCT channel. At the same time the excitation energy of the system at the scission point defined as $Eex = Q - TKE$ (where $Q$ is the reaction energy, TKE—is the total kinetic energy of all the decay fragments), is known from our experimental data. It does not exceed $Eex = 30$ MeV. This value of the excitation energy is high enough to allow for the emission of three or four neutrons, which corresponds almost to the mean neutron multiplicity of binary fission. Thus the neutron source linked with the new CCT channels must have a much smaller velocity as compared to conventional binary fragments, or it can be almost at rest in the extreme case [17]. The latter agrees with the hypothesis put forward above that we deal with the pre-scission neutrons at least for very light missing masses.

## *6.6.6 Mass Resolution of the Set-Ups Used*

Experiments Ex1, Ex2 and Ex3 were performed using gas filled detectors while PIN-diodes were used in Ex4. The mass resolution achieved in each experiment is discussed separately.

### 6.6.6.1 Mass Resolution in Ex3

The time-of-flight spectrum of an $^{226}$Ra $\alpha$-source measured at the FOBOS set-up shows a time resolution of 200 ps (irradiating a small central part of the PSAC) and $\sim$400 ps if all the surface of the counter is irradiated (Fig. 4 in [35]). Thus in Ex3 the relative time resolution does not exceed 1 %.

For the energy ($E$) only the residual energy is measured in the BIC of the FOBOS set-up due to the energy losses in the mylar foils along the flight pass with the total depth of about 1 mg/cm$^2$. The mass reconstruction procedure was presented in Ref. [39]. The SRIM code [78] allows to calculate the mean residual energy and its variance for the FF after passing of all foils. The relative uncertainty (FWHM) of the measured residual energy does not exceed 2 % and 3 % for typical light and heavy fragments, respectively. Thus the corresponding mass resolutions (within uncertainty of the time-of-flight) are estimated to be approximately 3 amu for the light peak and 4.5 amu for the heavy one.

At the same time the loci of binary fission events (Fig. 6.23(a)) show much worse mass resolution which is $\sim$6 amu and $\sim$8 amu for the typical light and heavy fragments, respectively, even after "cleaning" by gating within condition $P_1 \approx P_2$, where $P_{1,2}$ are the FFs momenta, i.e. momentum conservation law. Such selection allows to exclude the events connected both with random coincidence of FF with alpha-particle and scattered FFs. The estimation of, mass resolution given before (3 amu and 4.5 amu) is related to an ion of a single mass the and a fixed nuclear charge, while actually in the conventional binary fission we deal with the registration of isobaric chains including normally four or five isotopes [79]. At a fixed mass number $A$ the shape of the fractional independent yield $Y(z)$ being non-Gaussian, differs substantially for different FF energies (Table 3 in Ref. [79]). Modeling using the SRIM code shows that the centers of the residual energy spectra for the adjacent isotopes of an isobaric chain are shifted relative to each other by the distance similar or even larger (for heavy fragments) then their width (for instance, $\sim$1 MeV for $A = 110$ amu at the initial energy of $E = 112$ MeV). Such a shift is a decisive factor for a dramatic increase of the total width of the residual energy spectrum for FFs of fixed mass after passing thick ($\sim$1 mg/cm$^2$) mylar absorber.

It is known as well, that some of the FFs differ essentially by the range and specific energy losses from both the calculated data and the experiments with corresponding unexcited nuclei. A mean value of $q = 3$ charge units was found [80] for the shifted part of the ionic charge state distribution thanks to an Auger cascade linked with the de-excitation of low energy rotational levels.

The procedure of mass reconstruction briefly looks as follows [39]. Let us assume $E_{ch}$ and $V_{in}$ to be the energy of the fragment deposited in the BIC and, respectively, its actual velocity before the BIC entrance. Both are measured in the experiment. The energy $E_{cal}$ of the fragment after crossing of the entrance window of the BIC is calculated applying the table of energy losses [81] for the sequence of masses $M_j$ (in the range 0–250 amu) with the nuclear charge $Z_{UCD}$, assigned to the corresponding fragment at fixed velocity $V_{in}$. In order to restore the fragment mass we examine mass-by-mass descending along the calculated dependence on $E_{cal}$ $(M,\ Z_{UCD}$, at $V_{in} = \text{const})$ until the following condition is met for the first time: $E_{ch} < E_{cal}\ (M,\ V_{in})$. Strictly speaking such procedure is absolutely correct (within energy and velocity resolution) for the fragment having really $Z = Z_{UCD}$ which does not emit neutrons. The uncertainty due to the neutron emission would shift the calculated charge by some percents only. The uncertainty in the nuclear charge increases the dispersion and distorts the shape of the response function but its most probable value stays unbiased as it was shown in Fig. 3 of Ref. [54].

In Ex3 dispersion of the points along the line number 1 in Fig. 6.27 shows that mass resolution does not exceed 3.5 amu (FWHM). Similar resolution is obtained for $M_1 \sim 94$ amu (the upper side of the rectangle in Fig. 6.26(b)). The value obtained (3.5 amu) is very close to that cited before (3 amu) for typical light binary FFs with fixed nuclear charge. It is reasonable to suppose that the better mass resolution observed, just for the CCT partners as compared to conventional binary fragments, is due to an absence of both factors leading to the mass spread mentioned above, namely, dispersion of nuclear charge at fixed mass and an increased dispersion of the ionic charge due to internal conversion.

From the neutron gated data presented here (see Sect. 6.6.8) we draw the conclusion, that the heavy CCT partners detected are borne rather cold and likely without angular momenta. Some of them have magic nucleon composition providing increased stiffness and stability [73].

### 6.6.6.2 Mass Resolution in Ex1

In Ex1 MCP based “start” detectors and thinner foils in the gas filled detectors (total thickness of all the foils along the flight path does not exceed 0.6 mg/cm$^2$) allow a better mass resolution in Ex1 as compared to that in Ex3. For the conventional binary fission events, selected within the condition on the momenta $P_1 \approx P_2$, the mass resolutions are estimated to be 4 amu and 6 amu for the typical light and heavy fragments, respectively.

#### 6.6.6.3 Mass Resolution in Ex4

The time resolution obtained with alpha particles at the COMETA set-up is better than 330 ps [82]. The mean velocity of the Ni-nuclei linked with the lines 2, 3 in Fig. 6.24(a) observed in Ex4 is about 0.75 cm/ns that this gives a relative time resolution of about 2.7 %.

The energy resolution of the semiconductor Si-detectors is mainly defined by the fluctuations of the pulse height defect (PHD). For instance in Ref. [83], the energy resolution of the PIN-diode did not exceeded 1.7 MeV for $^{127}$I-ions at the beam energy of 80 MeV. Assuming the energy resolution to be inversely proportional to the PHD value, we can roughly estimate (Fig. 6 in Ref. [83]) for our case the value of 0.25 MeV. Thus the estimated mass resolution does not exceed 2.5 amu. This value agrees well with our data. In Fig. 6.24(b) we show the projection of the linear structure seen in at the masses 68 and 72 amu. The peaks presented and other structures in Fig. 6.24 correspond to the mass resolution of the COMETA set-up to be $\sim$2.0 amu (FWHM).

Due to the rather short flight pass used in the COMETA set-up, the mass resolution is determined mainly by the relative time resolution. For the typical light fragment from binary fission, which is faster and heavier, than a Ni fragment from the CCT process, the mass resolution is calculated to be $\sim$6 amu. It is very close to the estimation obtained from the width of the main locus of fission fragments in Fig. 6.24(a).

### *6.6.7 Triple Coincidences in Ex4*

Another opportunity, namely the observation of slow fragments from the ternary decay as almost isotropic neutron source is confirmed by the other results of Ex4. The individual detectors of the mosaic of the COMETA set-up allow in principle a triple coincidence, i.e. the direct detection of all three partners of a ternary decay. For the sake of convenience the FFs from such events are labelled as $m_1$, $m_2$ and $m_3$ in an order of decreasing masses in each ternary event. Thus designations $M_1$, $M_2$ (here $m_1$, $m_2$) are different to their previous use. For this case we plot the $m_1$–$m_2$ correlation obtained in Ex4 in Fig. 6.30. The rectangular structures in the centre of the figure are bounded by the same isotopes ($^{108}$Mo, $^{128,132}$Sn, $^{140}$Xe) or similar ($^{110}$Tc, $^{102}$Zr) magic clusters (their masses are marked by the arrows with the numbers 6, 4, 5, 1, 2, respectively) to those mentioned above in Fig. 6.29. Below the rectangle the horizontal line 3 corresponding to magic $^{98}$Sr nucleus is vividly seen. It goes through the thickening of the points 8 centred at the partition of magic deformed nuclei $^{98}$Sr/$^{142}$Xe. The line $M_s = \text{const} = 240$ amu (missing $^{12}$C) goes likely through the same point forming the diagonal of the rectangle with the upper left corner at the partition $^{108}$Mo/$^{132}$Sn. The points marked by number 11 lie in the vicinity of the partition corresponding to magic deformed isotopes $^{116}$Ru/$^{124}$Cd

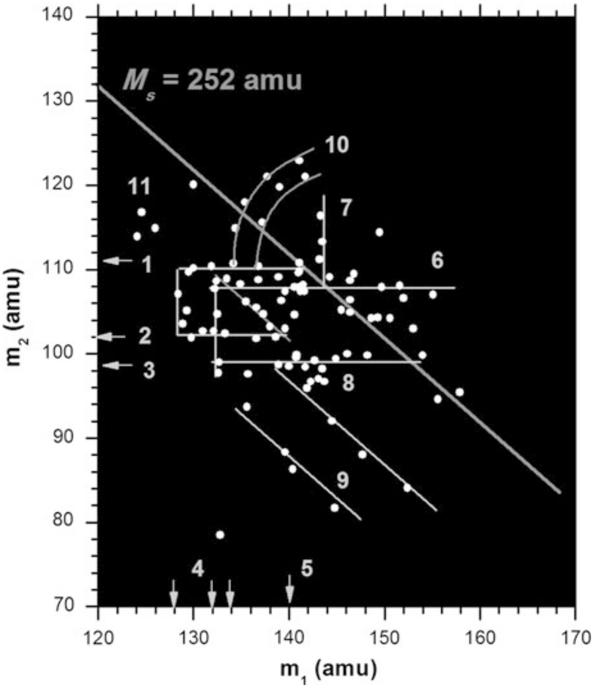

**Fig. 6.30** Ex4, but triple coincidences: Mass-mass correlation plot for the two heaviest fragments $m_1$, $m_2$ obtained in triple coincidences from ternary decay with the condition $m_1 > m_2 > m_3$ (in an order of decreasing masses of the decay partners, see text). Velocities and energies of the third detected partners ($m_3$) do not exceed 0.55 cm/ns and 2 MeV, respectively. The *lines* are drawn tentatively to guide the eye. See text for more details

(nuclei from the shell minima $C'$ and $K'$ in Ref. [73]). Lines 8 and 9 correspond to missing masses 16 and 24 amu, respectively.

For these data one more peculiarity of the distribution should be mentioned, namely, now the region where $M_s > 252$ amu becomes populated. A possible explanation is that a heavy fragment formed in the specific decay mode with e.g. $^{108}$Mo (line 7) in the exit channel, is followed by a much slower light fragment which, hits the same PIN diode as the previous heavy fragment. The faster fragment defines the TOF. However, the measured energy being the sum of two parts will be incorrect, thus leading to an incorrect evaluation of the mass of the heavy fragment. A similar situation can appear in the case of $^{144}$Ba (line 6). Bearing in mind that we really detected three fragments in each event from the distribution in Fig. 6.30 such additional fragment could be the fourth partner of the quaternary decay.

One more remarkable structure consisting of two curves marked by number 10 is connected presumably with a delayed sequential ternary decay. Emission of the light particle provides the "start" signal, and results in a population of a shape isomeric state. Later delayed fission of this isomeric state can occur. Both the heavy fragments formed have distorted (larger) TOFs and, consequently, increased masses.

It should be further mentioned that the velocities and energies of the corresponding lightest central fragments do not exceed 0.55 cm/ns and 2 MeV, respectively. The last number represents also a threshold in the energy channel. Therefore it is not possible to calculate correctly the masses $m_3$ for the events under discussion.

#### 6.6.7.1 Discussion of Sect. 6.6

With the inclusive data from the new experiments we have confirmed the occurrence of the CCT decay observed previously in Ref. [54]. In the neutron gated data we have observed the new unique rectangular structures bounded by magic clusters in the missing mass data (Figs. 6.26, 6.27). We have seen from the COMETA results (Figs. 6.29, 6.30), that not only spherical (Ni, Ge) but also deformed magic clusters ($^{98}$Sr, $^{108}$Mo) can be the constituents of such structures.

At this stage of the study of CCT-decays we are not ready to propose a detailed physical scenario showing different decay modes and to estimate a scenario for the CCT process in the overall picture of clustering effects in nuclei [84–86]. It means that we may have some questionable assignments in the decay channels of the rare CCT process.

With the new experiments, which have a negligible background in arm2 and in arm1, the yield of events in arm1 (facing the source backing) are true missing mass events (each event is a true coincidence). Additional selection of CCT events in this region has been achieved by the selection with a gate in the $V$–$E$ space, and, in addition, with the experimental neutron multiplicities, which implies $Y_{exp\_CCT}(n) \gg Y_{bin}(n)$ in some region of the missing mass space. The neutron source is indeed connected to the ternary fission mode with different mass partitions. Keeping in mind the results of Sect. 6.6.5.3 and 6.6.7, we may assume two different sources of neutrons emitted almost isotropically, namely, from the decaying system before scission (pre-scission neutrons) and from the slow middle fragments of ternary decay. The emission of pre-scission neutrons from the primary nucleus from a strongly deformed shape can be taken as a signature of a complicated fission process.

It has already been stressed, that revealing the CCT mode by means of neutron gating is possible only if the neutron sources connected to the CCT and conventional binary fission, respectively, differ by neutron multiplicity or/and their spatial distribution of the neutrons. The latter can enhance the CCT registration probability due to the geometry of the neutron detectors assembly (neutron belt) used (Figs. 6.20, and 6.21). Possible differences in the neutron energy spectra are not important, because we have experimental evidence that two layers of neutron counters in the moderator are enough for the registration of fission neutrons hitting the neutron belt.

Thus we have observed the rectangular structures seen in Figs. 6.26, 6.27, and 6.29 due to the fact that with the specific neutron assembly used, the probability $Y_{bin}(n)$ decreases (Fig. 6.25) with the increase of neutron multiplicity ($n$) in the corresponding region of the mass correlation plot.

Further comments are needed for the evident difference in the structures seen in Figs. 6.26 and 6.29, respectively, while a similar additional selection gate $n = 3$ was used in both cases. We know (Sect. 6.6.4.3) that the yield $Y_{phys} \times P_{miss}$ is approximately four times smaller at the COMETA set-up as that at the modified FOBOS spectrometer. At the same time both set-ups have very similar values of $P_n$ (Sects. 6.6.1 and 6.6.2), i.e. $Y_{exp\_CCT}(n)$ (formula (3)) was less in Ex4 in general. Keeping in mind that the experimental yield of the different “bumps” increases considerably from the “Ni”-bump to “Mo”-bump [87] it is understandable why we see only “Mo”-bump in Ex4 in the neutron gated data. According to the logic presented, the “Mo”-bump must be seen as well in Ex3 within $n = 3$ gate. This is really so, however, we do not show this part in Fig. 6.26(b) (is above the rectangle), because a complicated superposition of different structures observed there. Additional structures as compared to Ex4 are due to the difference in the blocking mediums in these two experiments.

We comment also on the opening angle of the CCT events and the probability of their registration. We need an opening angle between the two fragments to detect them. Its major part comes from multiple scattering in the backing (and eventually foils) [78]. The originally collinear fragments can have also a primary (intrinsic) angular divergence. That this value is negligibly small can be deduced from the recently discovered ROT effect [88]. The phenomenon is traced to the rotation of the fissioning nucleus while light particles are ejected. The effect has been observed for the first time in fission of the $^{235}$U nucleus induced by cold polarized neutrons. After capture of a polarized cold $s$-neutron, the $^{236}$U$^{*}$ nucleus has the possibility of two spin states 3 and 4, corresponding to two opposite senses of rotation. It was discovered that the angle through which the fission axis rotates with respect to the trajectories of $\alpha$-particles from conventional ternary fission, is very small and barely exceeds $0.2^{\circ}$. This takes place because the rotation after scission is very short-lived and comes to a virtual stop after some $10^{-21}$ s due to the drastic increase of the moment of inertia of the system consisting of two fragments flying apart. Thus, even if a di-nuclear system consisting of two CCT partners has an angular momentum of some units of $\hbar$, it is reasonable to expect a situation comparable with the ROT effect, a negligible angular shift between the fission axis of the initial system and that of the di-nuclear system formed after the first rupture.

In general the CCT-decay is most likely due to a sequential process with two scissions in a short time sequence. As was shown in Ref. [54] the three body chain-like pre-scission configuration which can lead to the CCT in the frame of such sequential process, is linked with the slopes in the potential energy valley of the decaying system. Evidently this fact explains the much lower yield of the CCT as compared to binary fission which is realized via shapes corresponding to the bottom of the same potential valley. The overall relative yield of $3 \times 10^{-3}$ contains a large number of mass combinations, as well the enlarged phase space due to higher $Q$-values and the excited states of the fragments [17].

### *6.6.8 Conclusions to Sect. 6.6*

We have performed studies of fission-decays of $^{252}$Cf with coincidences of the emitted neutrons in two missing mass experiments Ex3 and Ex4. These experiments confirm the observations of the ternary fission process as collinear cluster tri-partition (CCT), which has been observed in previous experiments (Ex1), described in Ref. [54]. The results give new information on the different CCT decay modes (mass partitions):

- The bump discussed earlier in Ex1, Ref. [54] does not show a unique combination of ternary masses. Bearing in mind the results presented in Figs. 6.24, 6.26(b), 6.27, 6.29, and 6.30, we observe a sequence of mass partitions. Most structures are based on pairs of magic nuclei, combined with isotopes like $^{128,132}$Sn.
- Specific linear and rectangular structures are observed in Ex3 and Ex4 with increasing neutron multiplicity (shown in Figs. 6.26(b), 6.27, 6.29). This observation was possible, thanks to a very low background provided by the neutron gating or using mosaics of PIN diodes (with no material in the path of the fragments) in Ex4. These structures provide unique information concerning the evolution of the decaying system near the scission point. Only in this case one can analyse CCT in the multidimensional $\{M_1, M_2, V_1, V_2, E_1, E_2\}$ space event by event. In fact, such analysis is impossible in principle for Ex1 with the high background from scattered binary fission events (subtracted by showing the differences of (arm1–arm2)). These events are within the bump observed in Fig. 6.4. The "background" contains also a sum of different CCT-modes, and as a whole the sum of CCT components is statistically very significant in the absolute scale.
- It should be emphasized that the yields of the "Ni"-bump ($\sim 4 \times 10^{-3}$/binaryFF) and even at heavier masses for the "Mo"-bump [87] ($\sim 10^{-2}$ per binary fission), are attributed to some tens of different partitions forming in fact the corresponding bump. As was mentioned above the yield of a fixed partition, for instance, $^{68}$Ni/$^{128}$Sn (Fig. 6.24) does no exceed $\sim 10^{-5}$/binary fission. Just this yield can reasonably be compared to the probability of known conventional ternary decays with a single light mass isotope emitted.

## 6.7 Experiments on the Heavy Ion Beams

### 6.7.1 *Collinear Multi-Body Decays in the Reaction* $^{238}$U + $^{4}$He *(*40 MeV*)*

Direct detection of all decay partners is desirable for reliable identification of unusual reaction channels, e.g. a spectrometer of high granularity should be used. Such one installed at JYFL (Jyväskylä, Finland) was chosen for studying the reaction $^{238}$U + $^{4}$He (40 MeV) by the international team taking part in HENDES and FOBOS collaborations. The experimental set-up (Fig. 6.31) was assembled as double-arm TOF-*E* (time-of-flight vs. energy) spectrometer with micro-channel plate (MCP) detectors and mosaics of 19 PIN diodes each. Altogether, about 40 millions binary fission events were collected. Besides binary ones, the ternary and quaternary coincidences were also detected in the experiment. Experimental method and data processing are presented in more detail in Refs. [89, 90]. What should be especially mentioned is that fission fragments (FF) mass resolution achieved in the frame of the velocity-energy method does not exceed 2.5 amu (FWHM).

We discuss here only events with the multiplicity three what means that three fragments were detected in coincidence. By convention, $M_a$ denotes below the heaviest mass, $M_b$—the middle one, and $M_c$—the lightest fragment mass in the triplet.

**Fig. 6.31** Scheme of the experimental set-up for $^{238}U + ^{4}He$ (40 MeV) measurements. All distances are shown in millimeters

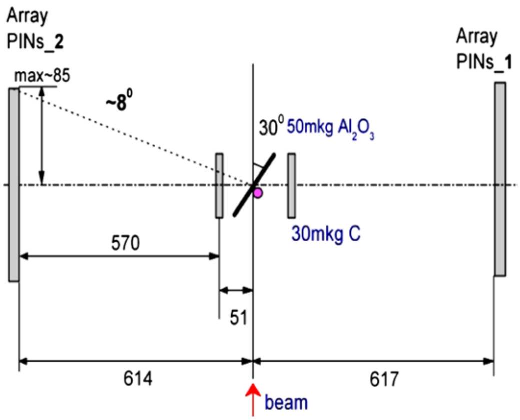

**Fig. 6.32** Ternary events under analysis. See text for details

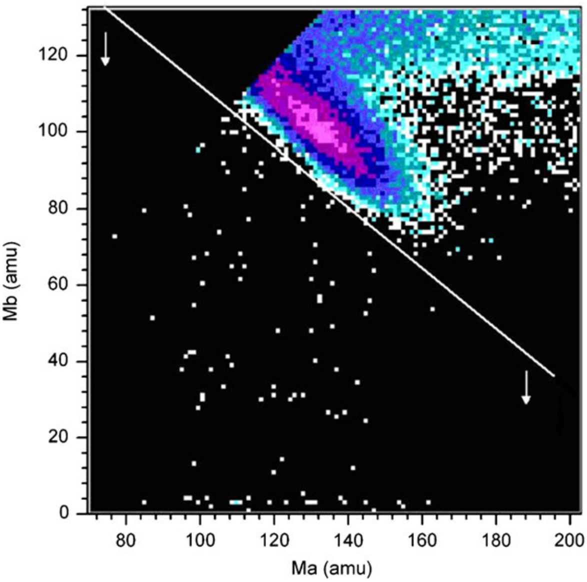

The events under analysis are shown in Fig. 6.32 the white line. The locus and a tail above this line are due to random coincidences. The events with the mass $M_b$ less than 8 amu are also beyond the scope of this report as they were already discussed in our previous publications [91, 92].

It is reasonable to start from the events where a total mass of the detected fragments is equal to the mass of the compound system within the experimental mass resolution. In the following three events the magic or double magic Sn nuclei were detected as the heaviest fragments Table 6.1.

Corresponding light fragment (deformed magic nucleus) was clusterised in the scission point forming dinuclear system. Its brake-up appears to occur due to inelas-

**Table 6.1** Mass conservation law is met in the events presented

| Point number | Decay scheme |
|---|---|
| 1 | $^{128}\text{Sn}+\underbrace{^{32}\text{Mg}+{}^{80}\text{Ge}}_{^{112}\text{Ru}}+\mathbf{2n}$ |
| 2 | $^{132}\text{Sn}+\underbrace{^{68}\text{Ni}+{}^{42}\text{S}}_{^{110}\text{Ru}}$ |
| 3 | $^{130}\text{Sn}+\underbrace{^{72}\text{Ni}+{}^{40}\text{S}}_{^{112}\text{Ru}}$ |

**Table 6.2** Dinuclear molecules based on deformed magic constituents

| Point number | Decay scheme | Point number | Decay scheme |
|---|---|---|---|
| 1 | $\underbrace{^{121}\text{Ag}+{}^{23}\text{F}}_{^{144}\text{Ba}}+\underbrace{^{65}\mathbf{Mn}+{}^{33}\text{Al}}_{^{98}\text{Sr}}$ | 4 | $\underbrace{^{140}\text{Xe}+{}^{25}\text{Ne}}_{^{165}\text{Gd}}+\underbrace{^{62}\mathbf{Cr}+{}^{15}\text{C}}_{^{77}\text{Zn}}$ |
| 2 | $\underbrace{^{113}\text{Ru}+{}^{31}\mathbf{Mg}}_{^{144}\text{Ba}}+\underbrace{^{78}\text{Ni}+{}^{20}\text{Ne}}_{^{98}\text{Sr}}$ | 5 | $\underbrace{^{134}\text{Te}+{}^{30}\mathbf{Ne}}_{^{164}\text{Gd}}+\underbrace{^{50}\text{Ca}+{}^{27}\text{Ne}}_{^{77}\text{Zn}}+\mathbf{n}$ |
| 3 | $\underbrace{^{130}\text{Sn}+{}^{14}\mathbf{C}}_{^{144}\text{Ba}}+\underbrace{^{62}\text{Cr}+{}^{33}\text{Mg}}_{^{95}\text{Rb}}+\mathbf{3n}$ | 6 | $\underbrace{^{110}\text{Tc}+{}^{11}\text{Be}}_{^{121}\text{Ag}}+\underbrace{^{62}\text{Cr}+{}^{58}\mathbf{V}}_{^{121}\text{Ag}}$ |

tic scattering on the material of the start-detector. Such hypotheses is based on the fact that a momentum conservation law is not met in all three events.

In the next set of events the decaying system was also fully clusterised i.e. its mass was exhausted by two magic constituents. Both "initial" clusters undergo fragmentation leading to formation of two dinuclear molecules. In contrast with previous case both "initial" clusters are relatively soft deformed nuclei. Some examples of the events under discussion are presented in Tables 6.2 and 6.3.

The last group combines the events where initial system looks like a chain of three magic clusters. The middle cluster is clusterised in its turn in such a way that one of the constituent shows as well magic nucleon composition. Typical events are shown below in Table 6.3.

Two of them (No. 1, 4) are absolutely identical. It is hard to believe that such astonishing reproducibility could be due to the random coincidences. A presumable scenario which stands behind these events is illustrated by Fig. 6.33.

One sensitive point of the methodic used should be mentioned before coming to the conclusions. As it is shown in Fig. 6.31 the "start" detectors are located at some distance from the target because evidently they can not work properly right

**Table 6.3** Three-body molecules based on magic constituents

| Point number | Decay scheme | Point number | Decay scheme |
|---|---|---|---|
| 1 | $^{98}\mathrm{Sr}+\underset{^{70}\mathrm{Ni}}{\underline{^{42}\mathrm{S}+{}^{28}\mathrm{Mg}}}+{}^{72}\mathbf{Ni}+\underset{\textbf{missed}}{\mathbf{2n}}$ | 5 | $^{120}\mathrm{Pd}+\underset{^{50}\mathrm{Ca}}{\underline{^{32}\mathrm{Mg}+{}^{18}\mathrm{O}}}+{}^{72}\mathbf{Ni}$ |
| 2 | $^{108}\mathrm{Mo}+\underset{^{58}\mathrm{V}}{\underline{^{40}\mathrm{S}+{}^{18}\mathrm{N}}}+{}^{72}\mathbf{Ni}+\mathbf{4n}$ | 6 | $^{95}\mathrm{Rb}+\underset{^{65}\mathrm{Mn}}{\underline{^{42}\mathrm{S}+{}^{22}\mathrm{F}}}+{}^{82}\mathbf{Ge}+\mathbf{n}$ |
| 3 | $^{84}\mathrm{Se}+\underset{^{82}\mathrm{Ge}}{\underline{^{52}\mathrm{Ca}+{}^{30}\mathrm{Mg}}}+{}^{72}\mathbf{Ni}+\mathbf{4n}$ | 7 | $^{142}\mathrm{Xe}+\underset{^{48}\mathrm{Ca}}{\underline{^{34}\mathrm{Al}+{}^{14}\mathrm{N}}}+{}^{52}\mathbf{Ca}$ |
| 4 | $^{98}\mathrm{Sr}+\underset{^{70}\mathrm{Ni}}{\underline{^{42}\mathrm{S}+{}^{28}\mathrm{Mg}}}+{}^{72}\mathbf{Ni}+\mathbf{2n}$ | 8 | $^{126}\mathrm{In}+\underset{^{50}\mathrm{Ca}}{\underline{^{30}\mathrm{Mg}+{}^{20}\mathrm{O}}}+{}^{66}\mathbf{Mn}+\mathbf{n}$ |

**Fig. 6.33** Presumable scenario of one mode of collinear multi-body decay

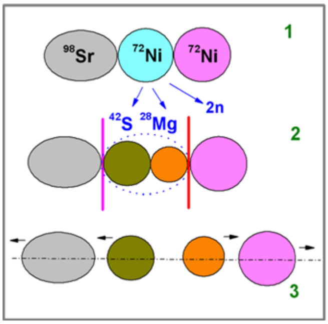

**Before scission: chain of three magic clusters**

**Clustering of the middle nucleus, double rupture (sequential fission) which sets free the constituents ($^{42}$S, $^{28}$Mg) of the middle molecule ($^{72}$Ni)**

**All the partners of the decay fly apart almost collinearly**

in the beam. Such geometry, forcedly used, is decisive for some uncertainties in determining of the fragments' velocities, namely, only faster from two fragments which sequentially hits the same start detector shows correct velocity. We discussed this point in detail in Refs. [89, 90].

#### 6.7.1.1 Conclusions

- Treating of the ternary events from the reaction $^{238}\mathrm{U}+{}^{4}\mathrm{He}$ (40 MeV) proposed is based on the hypothesis that proper i.e. unshifted velocity values were measured. It is hard to believe that stable and strong correlations observed in decay schemes might be due to random coincidences.
- In the frame of such approach two modes of collinear multi-body decay of $^{242}\mathrm{Pu}^{*}$ were revealed. The yield of unusual events (low limit) is about $10^{-6}$/binary fission. Pre-scission shape of the decaying system looks like a chain consisting of two or three magic clusters respectively.

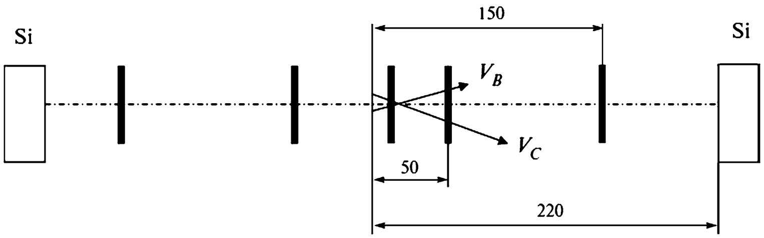

**Fig. 6.34** Scheme of the experimental setup for $^{232}$Th + $d$ (10 MeV) measurements. See text for details

- Formation of long lived "nuclear molecules" (or isomers) based on magic nucleus and light cluster can appear to occur in the scission point.
- Disintegration of such molecule comes from inelastic scattering on the target backing or "start" detector.
- We estimate our results as strong indication of new effect. Bearing in mind principal uncertainties in velocity measurements at HI-beam mentioned above, improved experimental methods are needed in order to exhaust the problem in forthcoming experiments.

## 6.7.2 *CCT in* $^{232}$Th + $d$ *(*10 MeV*) Reaction*

### 6.7.2.1 Experiment and Results

For better understanding of the effect revealed the programme of studying of its manifestations in different nuclear systems in a wide range of excitations was adopted. From the methodical point of view direct detection of all decay partners proves to be more convincing experimental approach reference to "missing mass" method used earlier. Thus much more complicated spectrometer of high granularity is needed. Experimental facility of such kind was used for searching for CCT channel in the reaction $^{232}$Th + $d$ (10 MeV) (Fig. 6.34) [93]. The experiment was performed by the collaboration FLNR (JINR)–ATOMKI (Hungary). Two microchannel (MCP) based timing detectors and mosaic of nine $2 \times 2$ cm$^2$ Si surface-barrier semiconductor detectors in each spectrometer arm were used in order to measure fragments masses in the frame of both the double-velocity and velocity-energy methods. Each Si detector delivered both energy and timing "stop" signals in the events discussed below while "start" signal was taken from the timing detector located at 170 mm from the mosaic. About $5.5 \times 10^6$ fission events were analyzed all in all.

Two different approaches were used for calibration of time-of-flight (TOF) and FF energy. More simple and rough one looks like as follows. Known FF velocity spectrum for $^{252}$Cf $(sf)$ was used for calculating the two coefficients in the linear TOF calibration function. Energy losses in the source backing and timing detectors

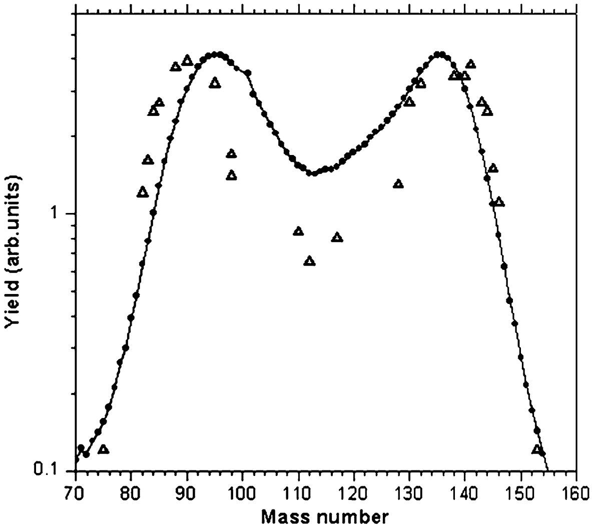

**Fig. 6.35** Comparison of the $M_{TE}$ spectra obtained in this work (*circles*) and $M_{TE}$ spectra from the reaction $^{232}$Th + $d$ (11.5 MeV) [94] (*triangles*). The latter was obtained by radio-chemical method

foils were ignored. In order to determine parabolic calibration dependence "channel-energy" the known positions of the peaks in the double humped energy spectrum of the FF for $^{252}$Cf $(sf)$ and the peak for alphas were exploited. This approach is called below as "3-point" calibration. Resultant spectrum of the FF $M_{TE}$ masses (velocity-energy method) summed over all Si detectors is shown in Fig. 6.35.

As can be referred from the figure both mass peaks of the light ($L$) and heavy ($H$) fragments in the spectrum obtained in our experiment are shifted to the center, but so that $\langle M_L \rangle + \langle M_H \rangle \approx 230$ amu what gives approximately correct post-neutron total mass of fragments.

The second calibration procedure used is based on parameterization of pulse height defect in Si surface-barrier detectors proposed in Ref. [61]. Energy losses of the FF over the flight path are also taken into account. Unknown calibration parameters are calculated by fitting of the experimental $M_{TE}$ quasimass spectrum to the known one for $^{252}$Cf $(sf)$ [90]. Unfortunately, the quality of the Si-diodes let us to exploit them in the run only at relatively low voltage.

Likely this is the reason for overestimated mass values obtained for $^{234}$Pa* (approximately six mass units on total mass) while the FF $M_{TE}$ spectrum for $^{252}$Cf $(sf)$ is reproduced well.

All ternary events analyzed below were calibrated in the frame of "3–point" approach. For the sake of convenience the fragments in each ternary event were resorted in order of decreasing of fragment mass, namely, $M_1$ to be the heaviest, $M_2$ is a middle one and $M_3$ is a lightest. Ternary events detected are shown in Fig. 6.36. Their total yield is about $1.6 \times 10^{-5}$ per binary fission. A bulk of points in the figure lie above the line $M_s = M_1 + M_2 = 234$ amu, i.e. the mass of the compound nucleus. As was shown earlier [90], the measured velocity of the less rapid fragment from the pair of those flying in one direction (Fig. 6.34) will be shifted due to the fact that the faster one gives the "start" signal. This shift in the velocity results in

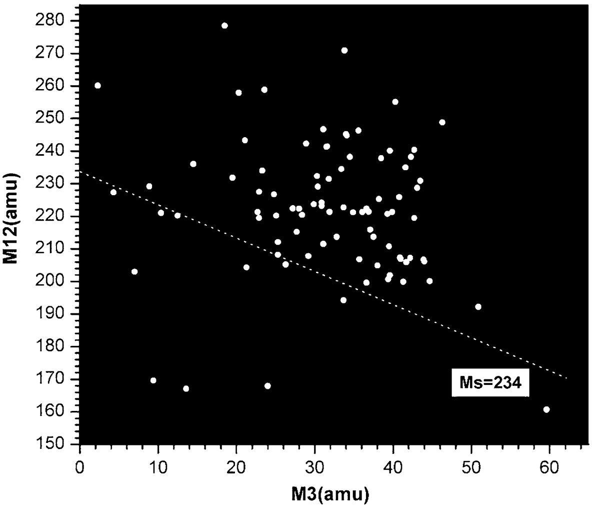

**Fig. 6.36** Ternary events detected in the reaction $^{232}\text{Th} + d$ (10 MeV). Here $M_{12} = M_1 + M_2$

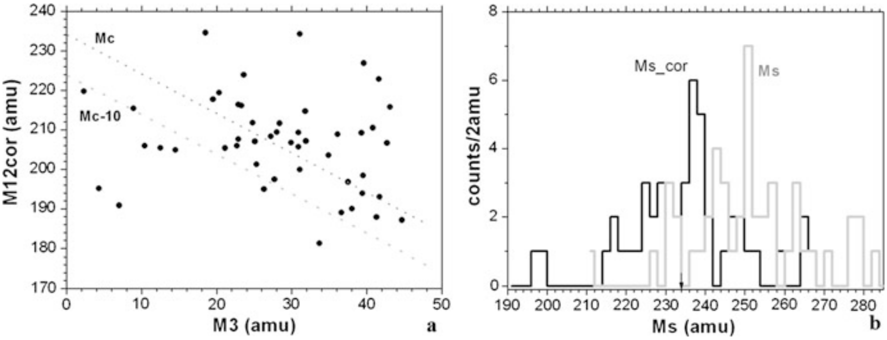

**Fig. 6.37** Scatter plot of ternary events after correction of mass $M_1$—(**a**). The *upper tilted line* corresponds to the mass $M_c$ of the compound nucleus. Comparison of the spectra of total masses of ternary decay products: initial one ($M_s$) and corrected ($M_{s\_cor}$)—(**b**). The mass of compound nucleus is marked by the *arrow*

too high corresponding mass value. Thus the events lying above the tilted line in Fig. 6.36 could be due to this effect. The proper velocity $V_{emis}$ of slower fragment $B$ having experimental velocity $V_{exp}$ can be calculated according to the formula:

$$V_B^{emis} = \frac{22}{\left(\frac{17}{V_B^{exp}} + \frac{5}{V_C}\right)}, \tag{6.4}$$

where $V_C$ is the velocity of the faster partner in the pair.

In all ternary events where the decay partners with the masses $M_1$ and $M_3$ fly in one direction we observe positive difference $V_3 – V_1$. The scatter plot of these events after correction of the mass $M_1$ (the slower fragment) is presented in Fig. 6.37(a). Figure 6.37(b) demonstrates the difference in spectrum of total mass before and after correction, respectively. Position of the main peak in the corrected spectrum is a little bit shifted, namely, $M_{s\_cor} = 237$ amu. It could be connected with the fact that experimental velocities were used for calculations within formula (6.4) instead of unknown proper velocity values which have the fragments on the flight path "target-start detector" (Fig. 6.34).

A "shoulder" of main peak from the left side (Fig. 6.37(b)) is likely due to missing of forth fragment of mass ~10 amu (see the bottom line in Fig. 6.37(a).

Similar procedure of mass correction was applied to ternary events where the fragments of ranks "2" and "3" fly in the same direction (approximately half of all events). All of them show overestimated total mass values even after correction. We suppose a following scenario lies behind. Di-nuclear system (molecule) formed after scission of the initial nucleus knocks out $^{12}$C ion from the target backing. At the same time this inelastic scattering destroys the molecule. As a result three ions fly in the same direction and $^{12}$C ion is the fastest among them. Thus, both $V_3$ and $V_2$ velocities must be corrected according to the formula (6.4) what leads to increasing corresponding masses $M_3$ and $M_2$. Quantitative testing convinced us that such scenario is absolutely realistic. Unfortunately, true energy of the scattered $^{12}$C ion is unknown in each event under analysis preventing one from making proper correction.

The mass spectrum $Y(M_3)$ of the lightest fragments in each detected triplet of fragments under condition $M_s < 242$ amu, which is the right border of the main peak in spectrum of $M_{s\_cor}$ in Fig. 6.37(b), is shown in Fig. 6.38(a). Similar spectrum for all ternary events detected is presented in Fig. 6.38(b). Comparing the spectra one comes to conclusion that the latter could be transformed to the first one by "swapping" the counts from heavier to lighter masses. It is precisely the tendency predicted by the scenario above linked with knockout of fast $^{12}$C ions.

#### 6.7.2.2 Discussion

In the previous sections the island of high yields of the CCT events (two-dimensional bump) in the mass-mass distribution of the FF from $^{252}$Cf (*sf*) and $^{235}$U$(n_{th}, f)$ are discussed. In both cases the bump shows the same internal structure consisting of the ridges $M_s = $ const. While the masses of initial decaying systems differ by 16 amu, positions of the ridges stay in the range (200–212) amu. We supposed that the pairs of magic nuclei (light plus heavy one) of Ni, Ge and Sn stand behind this permanency. Here we observe directly the light fragments calculated in the cited works as "missing" masses amended the total masses of the pairs of magic clusters resulted in the mass of the mother system. It seems quite clear which physics rules the effect. As in well known heavy ion radioactivity (cluster decay) the double magic Pb cluster plays a key role, a pair of magic clusters does the same in the CCT mode under discussion.

The idea put forward is confirmed as well by the results obtained by M.L. Muga and coworkers [95]. Mass spectra obtained in this work for the lightest fragment published by M.L. Muga are compared in Fig. 6.39.

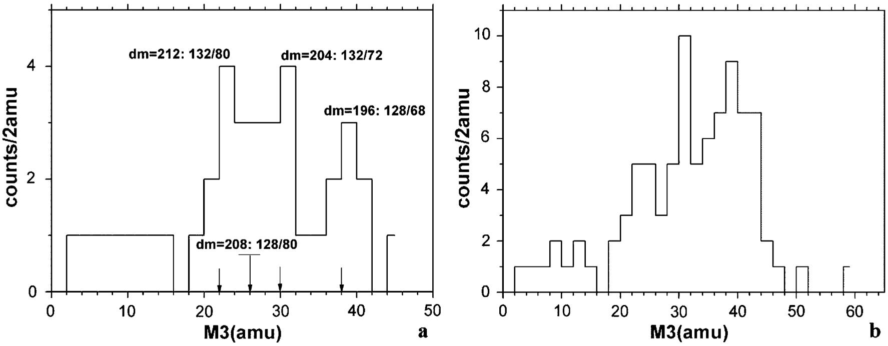

**Fig. 6.38** Mass spectrum of the lightest fragments in each detected triplet of fragments under condition $M_s < 242$ amu (see Fig. 6.37(b))—(**a**). Similar spectrum for all ternary events detected—(**b**). The *arrows* in the figure mark the partitions based on pairs of known magic nuclei of Ni, Ge, Sn

**Fig. 6.39** Mass spectra of lightest fragment in ternary fission of three different fissioning systems [95]. *Triangles* are mark the partitions corresponding to the fixed difference $M_c - M_3 = 212$ amu presumably linked with total mass of magic clusters of $^{132}$Sn and $^{80}$Ge

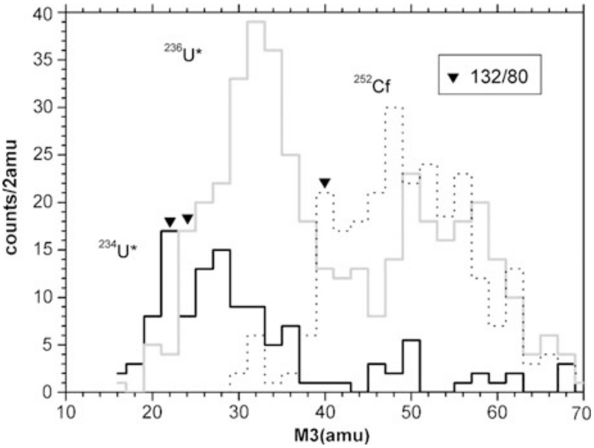

As can be judged from the figure the confines of the gross peaks in the spectrum for $^{234}$U* and this shown in Fig. 6.38(b) are in good agreement. We observe as well the tendency similar to this revealed in our previous data, namely, gross peak in the mass spectrum of the lightest fragments changes its position following the mass of compound nucleus. Really, the sharp rise of the yield in all three spectra presented in Fig. 6.38 starts at the partitions (marked by the triangles) corresponded to the same value of difference $M_c - M_3 = 212$ amu presumably linked with total mass of magic clusters of $^{132}$Sn and $^{80}$Ge.

Ternary decays were detected in Ref. [89] by three Si semiconductor detectors placed at 120° to each other. Estimated yield did not exceed $10^{-6}$/binary fission. The effect for the $^{234}$Pa* is observed in our measurements at the level of $10^{-5}$/binary fission, but these values can be hardly compared due to absolutely different geometry of the experiments. Total angular distribution of the ternary decay partners is also unknown for the moment. We can only remind that in the events identified as ternary decays in the frame of the missing mass approach the two detected fragments fly in the opposite directions (i.e. at 180° to each other) within the angular resolution to be less then 2°. An experimental angular spread of the fragments originated from the ternary decay of $^{234}$Pa* flying in one direction can range from 1° up to 20°. Thus measuring both angular distribution of partners of ternary decay under discussion and its yield stays an actual goal of special forthcoming experiments.

Due to peculiarities of the FF energy calibration used we lack opportunity to analyze accurately mass-energy correlations of ternary decay products in the wide range of masses and energies. By its nature the calibration works well only in the vicinity of three points on the *E–M* plane chosen as reference points. Just imperfection of the calibration forces us to treat the results as "preliminary".

### 6.7.2.3 Conclusions

Basing on direct detection of three coincident reaction products we declare first observation of true ternary fission of $^{234}$Pa* from the reaction $^{232}$Th $+ d$ (10 MeV). The yield of the effect being dependent from the geometry of the experiment is about $10^{-5}$ per binary fission. Experimental angular spread of the ternary decay products flying in one direction can range from 1° up to 20°. Mass spectrum of the lightest fragments in each detected triplet of fragments shows gross peak in the range of (20–40) amu. The spectrum agrees with this followed from our previous experiments aimed at searching for collinear ternary decays performed in the frame of missing mass approach. It is in good agreement as well with the similar spectrum obtained by Muga et al. for $^{234}$U* [95].

Available data confirm our hypotheses put forward earlier that the lightest among the ternary decay partners amends the total mass of pair of magic clusters Ni/Sn or Ge/Sn forming magic "core" up to the total mass of fissioning system. It is reasonable to suppose that as in heavy ion radioactivity (cluster decay) the double magic Pb cluster plays a key role, pair of magic clusters does the same in the CCT mode under discussion. A decisive role of magic pairs of Ni/Sn and Ge/Sn in ternary decay seems to be expectable bearing in mind that they govern in the conventional binary fission as well [96–99].

## 6.8 Clustering in Binary and Ternary Fission—Comparative Analysis

An exceptional role of the shell effects in fission of low excited nuclei is a well-known thesis of the fission theory. The first attempts to create the model of the fission process involving shell aspect were taking place in early fifties of the last century. V.V. Vladimirski [100] was maybe the first who postulated that fission probability has noticeable value only if two cluster structures such as magic cores within the

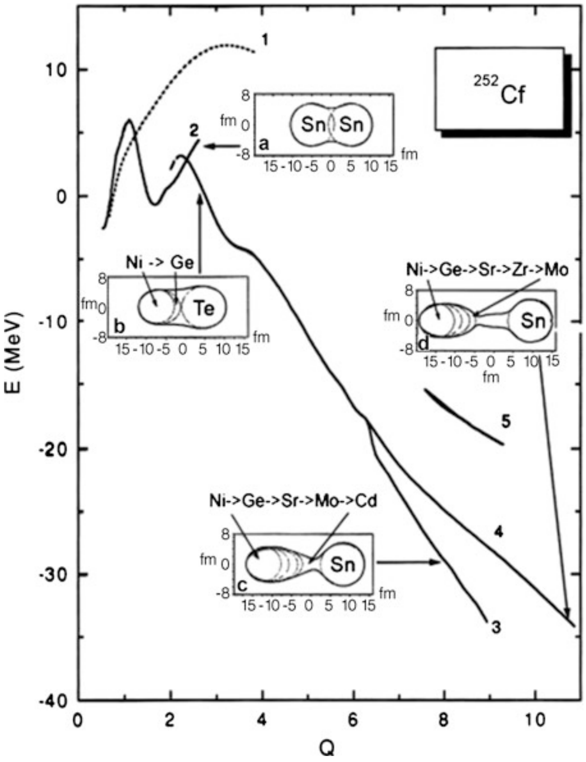

**Fig. 6.40** Potential energy of the fissioning nucleus $^{252}$Cf corresponding to the bottoms of the potential valleys, as a function of *Q*, proportional to its quadrupole moment. The valleys are marked by numbers *1* to *4*. The panels depict the shapes of the fissioning system at the points marked by *arrows*

light and heavy fragment corresponding to the $N = 50$ and $Z = 50$, $N = 82$ shells are not destroyed. A dumbbell-like configuration consisting of two magic clusters connected by a flat cylindrical neck was considered as a typical shape of the fissioning system.

The hypothesis put forward in the past was confirmed for the $^{252}$Cf nucleus by the calculations carried out in Ref. [97] by the Strutinsky method with the Woods-Saxon potential. The nuclear shape was parameterized in the coordinate system based on Cassini ovals. Minimizing the potential energy with respect to the deformation parameters $\alpha_1$–$\alpha_{10}$ one obtains potential energy surface (PES) as a function of elongation and mass asymmetry parameters. The resultant PES shows several separate valleys (Fig. 6.40). In each valley the shape of fissioning system is determined by two geometrically invariable constituents which are close to the magic spherical or deformed nuclei in composition and shape and they are called clusters. The formation of di-cluster configurations of the fissioning system appears to be a crucial factor leading to the multi-valley structure of the PES and to the fission modes which the valleys give rise to. The results obtained provide reliable evidence for the di-cluster mechanism of forming the fission mode, proposed earlier in Ref. [101].

Calculations also based on the Woods-Saxon-Strutinsky model involving many deformation degrees of freedom let one show that the density distribution at the third minimum of the fission barriers of the actinides looks like a di-nucleus. It consists of

**Fig. 6.41** The shape of the nucleus at the bottom of the "symmetric" valley ($Q_2 = 7.52$ a.u., $\eta = 0.074$) (**a**); the same system at the point $Q_2 = 7.52$ a.u., $\eta = 0.208$ (**b**). See text for details

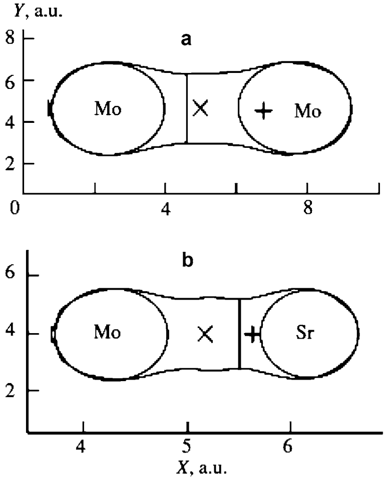

nearly-spherical heavier fragment (around double magic $^{132}$Sn) and well-deformed lighter fragment (from the neutron-rich $A \sim 100$ region) [102].

An image of the most populated fission modes in the measured $M$-TKE (mass-total kinetic energy) distribution was visualized in Ref. [99]. A typical image looks like a trajectory which connects two magic clusters, for instance, $^{132}$Sn and $^{80}$Ge.

Studying super-asymmetric fission the authors of [98] also came to conclusion that a fine structure in the FFs yields at $A = 70$ ($Z = 28$) seen in all analyzed reactions shows that fission is not only determined by the double shell closure in the heavy sphere of the scission point dumbbell configuration around $A = 132$ ($Z = 50$, $N \approx 82$) but also by an effect of the double shell closure of $Z = 28$ and $N \approx 50$ in the corresponding light sphere. Manifestation of the proton shell effect for the mass $A = 70$ at nuclear charge $Z = 28$ was noted in both neutron and proton induced fission of actinides [46, 103].

Direct indication on a deep link between binary fission and CCT was obtained in our work [33]. The elongated prolate configuration with two necks for the fissioning $^{252}$Cf nucleus was demonstrated. This result was obtained in more detailed calculations of the potential energy surface of the $^{252}$Cf nucleus carried out in the framework of the procedure presented in Refs. [97, 104] based on the Strutinsky method. Fig. 6.41 depicts the shape of the fissioning nucleus at the bottom of the "symmetry" valley with the quadrupole moment $Q_2 = 7.52$ a.u. The system that fissions in the vicinity of the bottom of the potential valley constitutes two magic nuclei (clusters) connected by a neck. In Fig. 6.41(a), these clusters are the deformed magic nuclei of $^{108}$Mo ($\beta_2 \sim 0.58$). In the calculations, the shape of the system was varied in such a way that the value of $Q_2$ remained constant while the mass-asymmetry $\eta$ changed starting from the value corresponding to the valley's bottom. By definition, $\eta = (M_1 – M_2)/M_c$, where $M_{1,2}$ is the mass of the system concentrated, respectively, on the left and on the right sides of the varied boundary, which divides the nuclear body into two parts (marked by vertical lines in Fig. 6.41), and $Mc$ is the mass of the fissioning nucleus. As a result, the new shape of the system shown in Fig. 6.41(b)

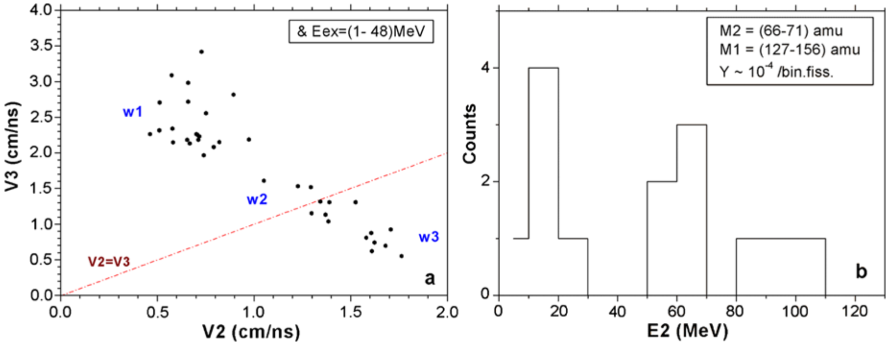

**Fig. 6.42** (**a**) The velocities for the lightest ($V_3$) vs middle-mass ($V_2$) fragments from the ternary decay. (**b**) The energy spectrum of the Ni fragments from the events of the group *w*2 in (**a**)

was revealed for the first time. The energy of the system is only slightly higher (by ~2 MeV) than the corresponding value at the bottom. The distinguishing feature of the shape observed is the double waist which vividly divides the system into three parts of comparable masses namely clusters of $^{108}\mathrm{Mo}_{66}$, $^{98}\mathrm{S}_{38}$, $^{46}\mathrm{Ar}_{28}$. Magic numbers are marked at the bottom of the element symbol. Thus, all three constituents are the magic nuclei. It would appear reasonable to identify the double rupture of such a configuration as true ternary fission (ternary cluster decay).

Thus, the pre-formation of two magic constituents in the body of the elongating fissioning system can be considered as an established fact. Just different pairs of magic clusters give rise to the different fission modes being the key feature of a low energy binary fission. It is reasonable to expect that clusterisation of the nucleons of the "neck" connecting two magic clusters could lead to forming of multi-body chain-like pre-scission configurations. The latter provides multi-body fission and CCT as one of the possible modes of such process.

## 6.9 Perspectives

Our plans on further studying of the CCT process are based on first results of quantitative treatment of the experimental data obtained so far. For instance, the events forming the line $M_1 \approx 68$ amu in the mass correlation plot (Fig. 6.24) were analyzed [105]. The mass and velocity of a "missed" fragment were calculated basing on the mass and momentum conservation laws.

Figure 6.42(a) demonstrates the correlation between the velocities of the two lighter partners of the ternary decay. The FFs from ternary events are labeled by numbers 1–3 in decreasing sequence of their masses. Three different groups of the events are vividly seen in the figure. They are marked by the signs *w*1–*w*3, respectively. The events in each group were analyzed separately. The energy spectrum of the detected Ni ions is shown in Fig. 6.42(b). Their yield does not exceed $10^{-4}$ per binary fission.

**Fig. 6.43** (**a**) The parameters of the events from group *w*3. (**b**) The possible pre-scission quaternary configuration for these events

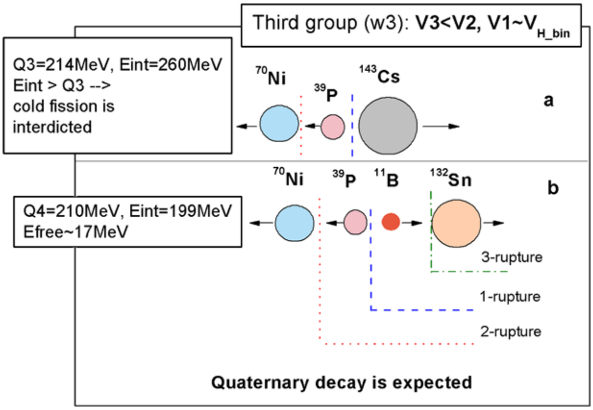

**Fig. 6.44** Mass correlation plot for two heaviest partners of the multi-body decay of $^{252}$Cf (*sf*)

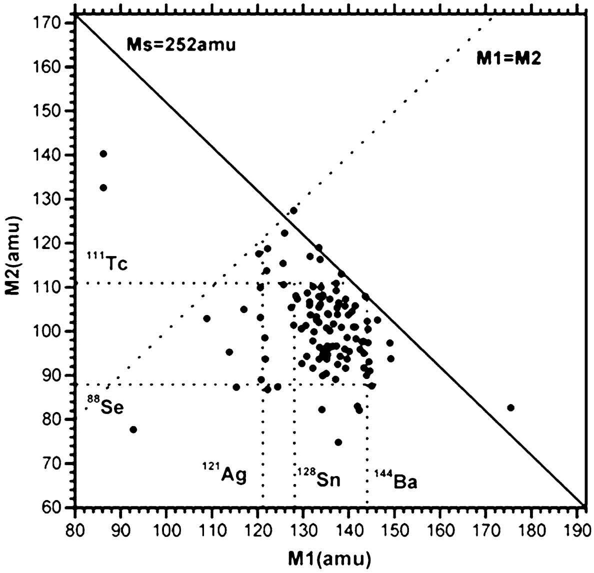

The basic properties of the events joined, for instance, into *w*3-group are presented in Fig. 6.43(a) where $V_1 \sim V_{H\_bin}$ while $V_3 < V_2$. In order to reproduce the experimental velocity correlations the first rupture is supposed to occur between heavy Cs nucleus and di-nuclear system of Ni/P. After full acceleration this system decays making free both its constituents. The interaction energy $E_{int}$ between the nuclei in the chain $^{70}$Ni/$^{39}$P/$^{143}$Cs (taking into account both Coulomb and nuclear components), which converts into the total kinetic energy after scission, exceeds $Q_3$-value (Fig. 6.43(a)). An assumption of the decay via a more elongated quaternary configuration shown in Fig. 6.43(b) overcomes this difficulty.

Thus, the quaternary decay channel is predicted in the frame of the proposed scenario. Another indication of possible realization of quaternary collinear decay we see likely in our data from the COMETA setup where three fragments were actually detected. Corresponding mass correlation plot $m_1$–$m_2$ is shown in Fig. 6.44. It shows clear rectangular structure bounded by the magic clusters. It should be stressed that for the bulk of events the total mass of three detected fragments is essentially less than the mass of the mother nucleus.

We are planning to develop different methodical approaches in order to perform cinematically complete experiment i.e. the direct registration of all (three and more) decay partners. Development of the COMETA setup is in progress. Additional mosaics of PIN-diodes will let to increase essentially the aperture and granularity of the spectrometer.

Digital image of the current impulses from the two CCT partners hit the same PIN-diode during registration gate can be obtained using fast flash-ADC ("double-hit" technique). Both energy and time-reference linked with each impulse will be calculated event by event.

**Acknowledgements** This text presents research results of the work supported in part by the grant of the Department of Science and Technology of South Africa and by a grant of the Federal Ministry of Education and Research (BMBF) of Germany. We would like to thank Prof. W. von Oertzen and Dr. W. Trzaska for fruitful collaboration.

## Appendix

### *A.1 Reliability of Linear Structures in the Scatter Plot of Fragments Masses*

Due to the small number of events in the linear structures discussed in Figs. 6.24(a), 6.26, 6.27, 6.29, 6.30 the question arises whether the structures have a physical reality, i.e. if they are not a random sequence of points. In order to answer this question a special simulation based on Hough transformation was performed.

The Hough transform is a feature extraction technique used in image analysis, computer vision, and digital image processing [74, 75]. The simplest case of Hough transform is the linear transform for detecting straight lines. In the image space, the straight line can be described as $y = mx + b$ and can be graphically plotted for each pair of image points $(x, y)$. In the Hough transform, a main idea is to consider the characteristics of the straight line not as image points $x$ or $y$, but in terms of its parameters, here the slope parameter $m$ and the intercept parameter $b$. For computational reasons, it is better to parametrise the lines in the Hough transform with two other parameters, commonly referred to as $R$ and $\theta$ (Fig. 6.45).

Actually, the straight line on a plane (Fig. 6.45) can be set as follows:

$$x \times \cos(\theta) + y \times \sin(\theta) = R, \tag{6.5}$$

where $R$—the length of the perpendicular lowered on a straight line from the beginning of coordinates, $\theta$—angle between a perpendicular to a straight line and the axis OX, changes within the limits of 0–$2\pi$, $R$ is limited by the size of the entrance image.

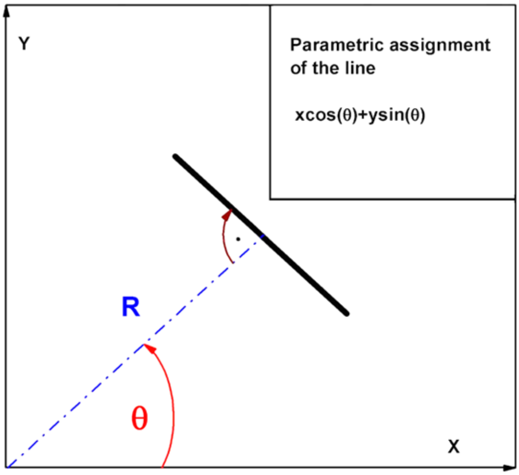

**Fig. 6.45** Parameterization of the line in Hough transform

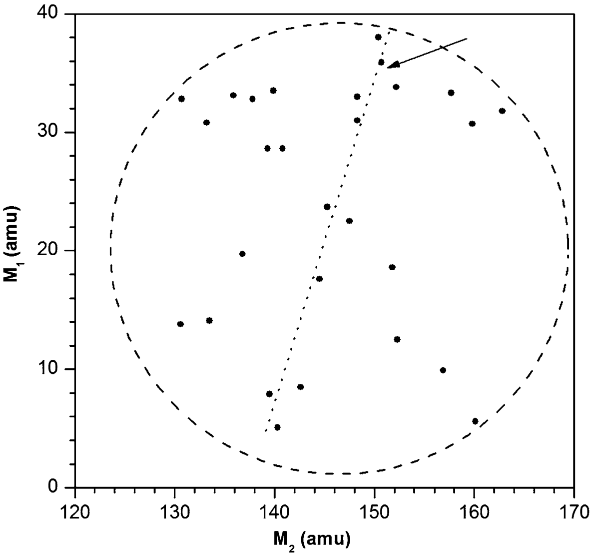

**Fig. 6.46** Part of the distribution shown in Fig. 6.26(a) chosen for estimation of a reliability of the line structures. Monte-Carlo simulation were performed in the circle region marked by the *dash line*. See text for details

In view of step-type representation of entrance data (in the form of a matrix with elements “1”—presence of a point, “0”—it absence), the phase space ($R$, $\theta$) also is represented in a discrete kind. In this space the grid to which one bin corresponds a set of straight lines with close values of $R$ and $\theta$ is entered. For each cell of a grid $(R_i, R_{i+1}) \times (\theta_i, \theta_{i+1})$ (in other words for each Hough transform bin) the number of points with coordinates ($x$, $y$), satisfying to the equation (6.5), where $\theta_i \leq \theta \leq \theta_{i+1}$, $R_i \leq R \leq R_{i+1}$, is counted up. The size of bins is obtained empirically.

Besides the steps on $R$ and $\theta$ ($\Delta R$, $\Delta\theta$) in the real program code realizing Hough transform, there are the additional parameters responsible for the decision—whether all the points, satisfying Eq. (6.5), are necessary to attribute an analyzed straight line.

So, if the distance in pixels (cells of the matrix under analysis) between extreme points of a line segment less than set number *n*—it is rejected. When the code finds two line segments associated with the same Hough transform bin that are separated by less than the set distance *d*, it merges them into a single line segment.

A lower part of the scatter plot shown in Fig. 6.27 below $M_1 = 40$ amu was chosen for the analysis (Fig. 6.46). The straight line (marked by the arrow) united nine points was recognized using Hough transform algorithm at appropriate choice of the principal parameters $(\Delta R, \Delta\theta, n, d)$.

We tried to estimate the probability of a random realization of the line of such length and tilted to the abscissa axis at an arbitrary angle. A sequence of patterns within randomly distributed points inside was generated. Each circular pattern included precisely the same number of points as those in the initial distribution in Fig. 6.46. An area of circular shape was chosen in order to avoid a priori distinguished direction (for instance, diagonal in a rectangular area). Each pattern was processed with the Hough transform algorithm "tuned" earlier on revealing the line under discussion. Among one hundred patterns analyzed only two of them provided a positive answer. In other words, a probability of a random realization of the line under discussion is about 2 %.

Another approach based on the methods of morphological analysis of images [106, 107] was applied as well in order to estimate the probability of random realization of the rectangle seen in Fig. 6.26(b). This probability was estimated to be less than 1 %.

## References

1. O. Hahn, F. Strassmann, Naturwissenschaften **27**, 89 (1939)
2. K.A. Petrzhak, G.N. Flerov, J. Phys. USSR **3**, 275 (1940)
3. L. Meitner, O. Frisch, Nature **143**, 239 (1939)
4. C.F. von Weizsäcker, Z. Phys. **96**, 431 (1935)
5. W.J. Swiatecki, in *Proceedings of the Second UN Conference on the Peaceful Uses of Atomic Energy*, Geneva, vol. 15 (United Nations, Geneva, 1958), p. 651
6. P. Möller, J.R. Nix, Nucl. Phys. A **272**, 502 (1976)
7. V.M. Strutinsky, N.Ya. Lyashchenko, N.A. Popov, Nucl. Phys. **46**, 639 (1963)
8. H. Diehl, W. Greiner, Phys. Lett. B **45**, 35 (1973)
9. H. Diehl, W. Greiner, Nucl. Phys. A **229**, 29 (1974)
10. G. Royer, J. Mignen, J. Phys. G, Nucl. Part. Phys. **18**, 1781 (1992)
11. X.-z. Wu, J.A. Maruhn, W. Greiner, J. Phys. G, Nucl. Part. Phys. **10**, 645 (1984)
12. D.N. Poenaru, W. Greiner, J.H. Hamilton, A.V. Ramayya, E. Hourany, R.A. Gherghescu, Phys. Rev. C **59**, 3457 (1999)
13. R.B. Tashkhodjaev, A.K. Nasirov, W. Scheid, Eur. Phys. J. A **47**, 136 (2011)
14. K. Manimaran, M. Balasubramaniam, Phys. Rev. C **83**, 034609 (2011)
15. K. Manimaran, M. Balasubramaniam, Eur. Phys. J. A **45**, 293 (2010)
16. V.I. Zagrebaev, A.V. Karpov, W. Greiner, Phys. Rev. C **81**, 044608 (2010)
17. K.R. Vijayaraghavan, W. von Oertzen, M. Balasubramaniam, Eur. Phys. J. A **48**, 27 (2012)
18. M.L. Muga, Phys. Rev. Lett. **11**, 129 (1963)
19. P. Schall, P. Heeg, M. Mutterer, J.P. Theobald, Phys. Lett. B **191**, 339 (1987)
20. F. Gönnenwein, Nucl. Phys. A **734**, 213 (2004)

21. P. Singer, Yu. Kopach, M. Mutterer, M. Klemens, A. Hotzel, D. Schwalm, P. Thirolf, M. Hesse, in *Proceedings of the 3rd International Conference on Dynamical Aspects of Nuclear Fission* (JINR, Dubna, 1996), p. 262
22. A.V. Ramayya et al., Phys. Rev. Lett. **81**, 947 (1998)
23. A.V. Ramayya et al., Prog. Part. Nucl. Phys. **46**, 221 (2001)
24. A.V. Daniel et al., in *Proceedings of the International Workshop on the New Applications of Nuclear Fission*, Bucharest, Romania (World Scientific, Singapore, 2004), p. 41
25. S.A. Karamian, I.V. Kuznetsov, Yu.Ts. Oganessian, Yu.E. Penionzhkevich, Yad. Fiz. **5**, 959 (1967)
26. P. Glässel, D.v. Harrach, H.J. Specht, L. Grodzins, Z. Phys. A **310**, 189 (1983)
27. C.-M. Herbach et al., Nucl. Phys. A **712**, 207 (2002)
28. G. Royer, F. Haddad, J. Phys. G, Nucl. Part. Phys. **20**, L131 (1994)
29. A.A. Ogloblin, G.A. Pik-Pichak, S.P. Tretyakova, in *Proceedings of the International Workshop Fission Dynamics of Atomic Clusters and Nuclei*, Luso, Portugal, 2000 (World Scientific, Singapore, 2001), p. 143
30. C. Wagemans, in *The Nuclear Fission Process*, ed. by C. Wagemans (CRS, Boca Raton, 1991). Chap. 12
31. E. Piasecki, M. Sowinski, L. Nowicki, A. Kordyasz, E. Cieślak, W. Czarnacki, Nucl. Phys. A **255**, 387 (1975)
32. S.W. Cosper, J. Cerny, R.C. Gatti, Phys. Rev. **154**, 1193 (1967)
33. Yu.V. Pyatkov, V.V. Pashkevich, Yu.E. Penionzhkevich, V.G. Tishchenko, C.-M. Herbach, in *Proceedings of the International Conference of Nuclear Physics "Nuclear Shells—50 Years"*, Dubna, 1999, ed. by Yu.Ts. Oganessian et al. (World Scientific, Singapore, 2000), p. 144
34. Yu.V. Pyatkov et al., in *Proceeding of the International Symposium on Exotic Nuclei EXON-2001*, Baikal Lake, 2001, ed. by Yu.E. Penionzhkevich et al. (World Scientific, Singapore, 2002), p. 181
35. H.-G. Ortlepp et al., Nucl. Instrum. Methods Phys. Res., Sect. A, Accel. Spectrom. Detect. Assoc. Equip. **403**, 65 (1998)
36. D.V. Kamanin et al., JINR Preprint 15-2007-182, Dubna (2007)
37. A. Oed, P. Geltenbort, F. Gönnenwein, Nucl. Instrum. Methods **205**, 451 (1983)
38. A.N. Tyukavkin et al., Instrum. Exp. Tech. **52**, 508 (2009)
39. Yu.V. Pyatkov et al., JINR Preprint E15-2004-65, Dubna (2004)
40. V.F. Apalin, Yu.N. Gritsyuk, I.E. Kutikov, V.I. Lebedev, L.A. Mikaelian, Nucl. Phys. **71**, 553 (1965)
41. L. Meyer, Phys. Status Solidi B **44**, 253 (1971)
42. A.V. Kravtsov, G.E. Solyakin, Phys. Rev. C **60**, 017601 (1999)
43. M.A. Mariscotti, Nucl. Instrum. Methods **50**, 309 (1967)
44. Yu.V. Pyatkov, V.G. Tishchenko, V.V. Pashkevich, V.A. Maslov, D.V. Kamanin, I.V. Kljuev, W.H. Trzaska, Nucl. Instrum. Methods Phys. Res., Sect. A, Accel. Spectrom. Detect. Assoc. Equip. **488**, 381 (2002)
45. B.D. Wilkins, E.P. Steinberg, R.R. Chasman, Phys. Rev. C **14**, 1832 (1976)
46. D. Rochman, I. Tsekhanovich, F. Gönnenwein, V. Sokolov, F. Storrer, G. Simpson, O. Serot, Nucl. Phys. A **735**, 3 (2004)
47. Yu.V. Pyatkov et al., Phys. At. Nucl. **73**, 1309 (2010)
48. D.V. Kamanin, Yu.V. Pyatkov, A.N. Tyukavkin, Yu.N. Kopatch, Int. J. Mod. Phys. E **17**, 2250 (2008)
49. Yu.V. Pyatkov et al., Rom. Rep. Phys. **59**, 569 (2007)
50. A.N. Tyukavkin et al., Preprint No. R15-2008-88, JINR (Joint Inst. Nucl. Res., Dubna, 2008)
51. Yu.V. Pyatkov et al., Eur. Phys. J. A **45**, 29 (2010)
52. D.V. Kamanin et al., in *Proceedings of the 18th International Seminar on Interaction of Neutrons with Nuclei: "Neutron Spectroscopy, Nuclear Structure, Related Topics"*, Dubna, 2010 (2011), p. 102
53. A.N. Tyukavkin et al., Prib. Teh. Eksp. **4**, 66 (2009)

54. A.A. Alexandrov et al., in *Proceedings of 15th International Seminar on Interaction of Neutrons with Nuclei: "Neutron Spectroscopy, Nuclear Structure, Related Topics"*, Dubna, 2007 (2008), p. 248
55. H. Märton, private communication
56. S.I. Mulgin, K.-H. Schmidt, A. Grewe, S.V. Zhdanov, Nucl. Phys. A **640**, 375 (1998)
57. V.V. Pashkevich, Yu.V. Pyatkov, A.V. Unzhakova, Int. J. Mod. Phys. E **18**, 907 (2009)
58. Yu.V. Pyatkov et al., Eur. Phys. J. A **48**, 94 (2012)
59. C. Butz-Jorgensen, H.H. Knitter, Nucl. Phys. **490**, 307 (1988), and Refs. therein
60. D.V. Kamanin et al., Phys. At. Nucl. **66**, 1655 (2003)
61. S.I. Mulgin, V.N. Okolovich, S.V. Zhdanov, Nucl. Instrum. Methods Phys. Res., Sect. A, Accel. Spectrom. Detect. Assoc. Equip. **388**, 254 (1997), and Refs. therein
62. M. Moszyński, B. Bengtson, Nucl. Instrum. Methods **91**, 73 (1971)
63. Yu.V. Pyatkov et al., in *Proceedings of the 14th International Seminar on Interaction of Neutrons with Nuclei: "Neutron Spectroscopy, Nuclear Structure, Related Topics"*, Dubna, 2006 (2007), p. 134
64. D.V. Kamanin et al., in *Proceedings of the International Symposium on Exotic Nuclei (EXON-2009)*, ed. by Yu.E. Penionzhkevich et al. AIP Conference Proceedings, Sochi, 2009, p. 385
65. J.F. Wild et al., Phys. Rev. C **41**, 640 (1990)
66. O. Sorlin et al., Phys. Rev. Lett. **88**, 092501 (2002)
67. V.K. Rao, V.K. Bhargava, S.G. Marathe, S.M. Sahakundu, R.H. Iyer, Phys. Rev. C **9**, 1506 (1974)
68. V.K. Rao, V.K. Bhargava, S.G. Marathe, S.M. Sahakundu, R.H. Iyer, Phys. Rev. C **19**, 1372 (1979)
69. C. Wagemans (ed.), *The Nuclear Fission Process* (CRC Press, Boca Raton, 1991). Chap. 6
70. F. Gönnenwein, M. Mutterer, Yu. Kopatch, Europhys. News **36**, 11 (2005)
71. A.N. Tyukavkin, PhD thesis, MEPhI, Moscow (2009)
72. MCNP—Monte Carlo N-Particle code. http://mcnp-green.lanl.gov
73. B.D. Wilkins, E.P. Steinberg, R.R. Chasman, Phys. Rev. C **14**, 1832 (1976)
74. http://en.wikipedia.org/wiki/Hough_transform
75. L.G. Shapiro, G.G. Stockman, *Computer Vision* (Prentice Hall, New York, 2001)
76. N.V. Kornilov, F.-J. Hambsch, A.S. Vorobyev, Nucl. Phys. A **789**, 55 (2007)
77. A.S. Vorobyev, O.A. Shcherbakov, Yu.S. Pleva, A.M. Gagarski, G.V. Val'ski, G.A. Petrov, V.I. Petrova, T.A. Zavarukhina, in *Proceedings of the 17th International Seminar on Interaction of Neutrons with Nuclei: "Neutron Spectroscopy, Nuclear Structure, Related Topics"*, Dubna, 2009 (2010), p. 60
78. www.srim.org
79. U. Quade et al., Nucl. Phys. A **487**, 1 (1988)
80. H. Wohlfarth, W. Lang, H. Dann, H.-G. Clerc, K.H. Schmidt, H. Schrader, Z. Phys. A **287**, 153 (1978)
81. FZR 92-09, Mai 1992, Herausgeber: H. Prade, F. Donau.
82. D.V. Kamanin et al., in *Proceedings of the 7th International Conference on Dynamical Aspects of Nuclear Fission (DANF-2011)*, Smolenice Castle (2011 in press)
83. Y.S. Kim, P. Hofmann, H. Daniel, T. von Egidy, T. Haninger, F.-J. Hartmann, M.S. Lotfranaei, H.S. Plendl, Nucl. Instrum. Methods Phys. Res., Sect. A, Accel. Spectrom. Detect. Assoc. Equip. **329**, 403 (1993)
84. D. Poenaru, W. Greiner, in *Cluster in Nuclei, vol. 1*, ed. by C. Beck. Lect. Notes Phys., vol. 818 (2010), p. 1
85. V. Zagrebaev, W. Greiner, in *Cluster in Nuclei, vol. 1*, ed. by C. Beck. Lect. Notes Phys., vol. 818 (2010), p. 267
86. G.G. Adamian, N.V. Antonenko, W. Scheid, in *Cluster in Nuclei, vol. 2*, ed. by C. Beck. Lect. Notes Phys., vol. 848 (2012), p. 165
87. D.V. Kamanin et al., in *Proceedings of the 18th International Seminar on Interaction of Neutrons with Nuclei: "Neutron Spectroscopy, Nuclear Structure, Related Topics"*, Dubna,

2010 (2011), p. 102

88. F. Gönnenwein, M. Mutterer, A. Gagarski, I. Guseva, G. Petrov, V. Sokolov, T. Zavarukhina, Yu. Gusev, J. von Kalben, V. Nesvizhevski, T. Soldner, Phys. Lett. B **652**, 13 (2007)
89. Yu. Pyatkov et al., in *Proc. of the Int. Symposium on Exotic Nuclei "EXON2006"*. AIP Conference Proceedings, Khanty-Mansiysk, Russia, 2006 (2007), p. 144
90. Yu. Pyatkov et al., in *Proc. 14th Int. Sem. on Interaction of Neutrons with Nuclei "ISINN-14"* (JINR, Dubna, 2007), p. 134
91. Yu. Pyatkov (HENDES and FOBOS Collaborations), *Proc. VI Int. Conf. on Dynamical Aspects of Nuclear Fission "DANF2006"* (World Scientific, Singapore, 2008), p. 248
92. Yu. Pyatkov (HENDES and FOBOS Collaborations), *Proc. 15th Int. Sem. on Interaction of Neutrons with Nuclei "ISINN-15"* (JINR, Dubna, 2008), p. 281
93. D.V. Kamanin et al., Phys. Part. Nucl. Lett. **7**, 122 (2010)
94. S.H. Freid, J.L. Anderson, G.R. Choppin, J. Inorg. Nucl. Chem. **30**, 3155 (1968)
95. M.L. Muga, C.R. Rice, W.A. Sedlacek, Phys. Rev. Lett. **18**, 404 (1967)
96. Yu.V. Pyatkov, G.G. Adamian, N.V. Antonenko, V.G. Tishchenko, Nucl. Phys. A **611**, 355 (1996)
97. Yu.V. Pyatkov, V.V. Pashkevich, Yu.E. Penionzhkevich, V.G. Tishchenko, A.V. Unzhakova, H.-G. Ortlepp, P. Gippner, C.-M. Herbach, W. Wagner, Nucl. Phys. A **624**, 140 (1997)
98. I. Tsekhanovich, H.-O. Denschlag, M. Davi, Z. Buyukmumcu, F. Gonnenwein, S. Oberstedt, H.R. Faust, Nucl. Phys. A **688**, 633 (2001)
99. Yu.V. Pyatkov, V.V. Pashkevich, W.H. Trzaska, G.G. Adamian, N.V. Antonenko, D.V. Kamanin, V.A. Maslov, V.G. Tishchenko, A.V. Unzhakova, Phys. At. Nucl. **67**, 1726 (2004)
100. V.V. Vladimirski, JETP USSR **5**, 673 (1957)
101. Yu.V. Pyatkov, R.A. Shekhmametiev, Phys. At. Nucl. **57**, 1182 (1994)
102. S. Ćwiok, W. Nazarewicz, J.X. Saladin, W. Płóciennik, A. Johnson, Phys. Lett. B **322**, 304 (1994)
103. D.M. Gorodisskiy, S.I. Mulgin, V.N. Okolovich, A.Ya. Rusanov, S.V. Zhdanov, Phys. Lett. B **548**, 45 (2002)
104. V.V. Pashkevich, Nucl. Phys. A **169**, 275 (1971)
105. Yu.V. Pyatkov, D.V. Kamanin, W. von Oertzen, A.A. Alexandrov, I.A. Alexandrova, N.A. Kondtayev, E.A. Kuznetsova, O.V. Strekalovsky, V.E. Zhuchko, in *Proc. 20 International Seminar on Interaction of Neutrons with Nuclei "ISINN-20"*, Alushta, Ukraine (JINR, Dubna, 2013), p. 104
106. Yu.P. Pytyev, Pattern Recognit. Image Anal. **3**, 19 (1993)
107. Yu.V. Pyatkov, D.V. Kamanin, O.V. Falomkina, Yu.P. Pyt'ev, B.M. Herbst, W.H. Trzaska, Pattern Recognit. Image Anal. **20**, 82 (2011)